UNIVERSITAT DE BARCELONA

# Giant caloric effects in the vicinity of first-order phase transitions

Enric Stern i Taulats

# Giant caloric effects in the vicinity of first-order phase transitions


UNIVERSITAT DE BARCELONA

**Enric Stern i Taulats**

Departament de Física de la Matèria Condensada, Facultat de Física
Universitat de Barcelona

**PhD Thesis**

PhD advisor: Lluís Mañosa i Carrera

Doctorate in Nanoscience

27 January 2017

A tu, iaia,
que has marxat de vacances …

# Declaration

I hereby declare that except where specific reference is made to the work of others, the contents of this dissertation are original and have not been submitted in whole or in part for consideration for any other degree or qualification in this, or any other university. This dissertation is my own work and contains nothing which is the outcome of work done in collaboration with others, except as specified in the text and Acknowledgements. Work took place between October 2012 and January 2017 under the supervision of Dr. Lluís Mañosa. This dissertation contains fewer than 90,000 words including appendices, bibliography, footnotes, tables and equations and has fewer than 120 figures.

Enric Stern i Taulats
27 January 2017

# Acknowledgements

Els resultats i la feina que amaguen aquestes pàgines deuen una gratitud sincera a moltes persones que l'han fet possible. En primer lloc, a en Lluís Mañosa, el meu director de tesi, a qui li agraeixo la seva paciència i dedicació que ha dut a terme amb gran elegància, uns agraïments que estenc a tot l'equip de treball del departament de Física de la Matèria Condensada de la facultat de Física de la UB, a l'Antoni Planes, l'Eduard Vives i a la Teresa Castán. La seva experiència i saviesa, acompanyada de rigor i bon ambient, han donat lloc a una excel·lent base per al meu desenvolupament.

Una bona part dels estudis s'han realitzat gràcies a una estreta col·laboració amb el grup de Caracterització de Materials, del departament de Física i Enginyeria Nuclear de la UPC. L'humor d'en Josep Lluís Tamarit i el saber fer de la Maria del Barrio han amanit hores de mesures allà a l'última planta del fins fa poc edifici de l'ETSEIB. En particular, voldria agrair a en Pol Lloveras la seva dedicació i la seva iniciativa, ha estat tot un referent per a mi a l'hora de resoldre els problemes que han anat apareixent al llarg del camí.

I would like to thank the people of the Device Materials group of the Department of Materials Science & Metallurgy of the University of Cambridge with whom I had a great and fruitful stay in the last quarter of 2015. Especially, I am really thankful to Xavier Moya who has led big part of my work. His profound scientific proficiency together with his gentleness and always accessible attitude have been absolutely helpful for the development of the work performed and learning scientific skills.

It has been a great pleasure to collaborate with the Nanomagnetism Research Group at the Northeastern University and I am very thankful for the short but fruitful stay in Boston from which I would like to highlight the charmful hospitality of Brian LeJeune and the cooperative attitude of Radhika Barua. I am especially thankful to Laura H. Lewis, who has always been remarkably engaging and helpful to me and has provided great opportunities for my progress.

My stay in Kolkata at the Indian Association for the Cultivation of Science was memorable. I am very grateful to professor Subham Majumdar who guided me for the use of their experimental facilities and to Sabyasachi Pramanick for his clever suggestions and sharing his tricks and his abilities on sample preparation.

My group in Barcelona has received many PhD students and Postdocs researchers who have enriched my background. I must mention Bariş Emre and Suheÿla Yüce with whom we begun to successfully run our first experimental setups. I would like to point out Pablo Camarillo's great background on sample preparation, Pedro Castillo and Dani Soto's experimental patience and meticulous procedures, and Robert Niemann and Tino Gottschall's great ability to overcome scientific problems which make them great researchers. At the roots of my PhD studies I received instruction and smart advices from David González to whom I am also very grateful.

Dels estudis de doctorat em quedo amb molts bons moments que també han donat sentit a aquests anys. De converses amenes als passadissos, dinars al bar de biologia, i unes quantes cerveses que han caigut per aquí i per allà. Els dos danis, l'Alsina i en Pablos, i tota la tropa de doctorands de la facultat i de "físics pel món", tothom bona gent amb qui hem passat, i passarem, bones estones. No puc deixar d'esmentar, tampoc, a l'Aniol, sempre present; a l'hospitalitat d'en Josep, amb qui hem arreglat el país entre vins i formatges allà a la plaça Osca; les aventures amb la Bàrbara, la flama dels companys del Quatre Rius i els somriures compartits al casal El Forn de Girona.

Els estudis de doctorat han estat, també, moments amb la Marta, qui m'ha acompanyat un tros de vida, malgrat que els camins ja s'hagin separat. Dono les meves gràcies més sinceres a la meva família, que sempre m'ha donat suport amb cura i paciència: als meus pares, sempre atents; a l'Anna, en Carles, l'Albert, la Chiara, i, per suposat, a la Júlia i a la Laura, que han vingut al món mentre estudiava els efectes calòrics gegants i que, de ben segur, seran qui més empraran els mètodes de refrigeració alternatius als actuals. I, finalment, a la Muga, que m'ha fet companyia fidelment aquest darrer tram d'escriptura de tesi.

Personalment, aquesta tasca ha estat possible gràcies al finançament concedit per la beca FI-DGR 2013 de l'AGAUR de la Generalitat de Catalunya i, en la seva etapa final, a la beca de col·laboració 2016-1-FFIS-1 de la Universitat de Barcelona. Estic especialment orgullós que el finançament públic permeti desenvolupar tasques com les que he dut a terme, al servei de la ciència i el coneixement.

# Table of contents

# Resum en català

Els materials d'estat sòlid són susceptibles de mostrar una gran resposta tèrmica induïda per un camp extern a l'entorn de transicions de fase de primer ordre [1]. La forta sensitivitat de la temperatura de transició amb el camp aplicat i la calor latent associada amb el canvi de fase poden donar lloc als efectes magneto-, electro-, elasto- i barocalòric gegants [2–5]. Així, els materials que presenten aquests efectes exhibeixen grans canvis isoterms d'entropia i grans canvis adiabàtics de temperatura sota la influència dels camps conjugats als respectius paràmetres d'ordre de les transicions (camp magnètic, camp elèctric, pressió uniaxial i pressió hidrostàtica, respectivament). A més, l'acoblament entre els graus de llibertat estructurals, magnètics i electrònics en el règim de la transició possibilita que la resposta tèrmica sigui induïda per múltiples camps, originant així l'efecte multicalòric [6]. En els darrers anys, l'interès en entendre i elaborar materials calòrics ha crescut excepcionalment, amb l'ull posat en les aplicacions potencials en tecnologies de refrigeració alternatives per a la indústria a gran escala que podrien substituir els mètodes convencionals de compressió de vapor, que empren gasos que contribueixen en gran mesura, i de manera preocupant, a l'efecte hivernacle i l'escalfament global [7].

L'objectiu de la present tesi ha estat l'estudi dels efectes calòrics gegants de diferent tipus i origen. En aquest sentit, s'han elaborat un conjunt de tècniques experimentals que permeten la caracterització de les respostes tèrmiques induïdes per camps externs. D'una banda, les tècniques calorimètriques i termomètriques desenvolupades han permès la mesura de les calors bescanviades i dels canvis de temperatura sota aplicació d'un o més camps externs. En ser tècniques de mesura directa de la resposta tèrmica, d'aquesta manera s'han obtingut uns resultats d'especial rellevància en l'estudi dels efectes calòrics gegants [1]. De l'altra, també han estat rellevants les tècniques que han permès la determinació del comportament dels paràmetres d'ordre de les transicions de fase en funció dels camps aplicats, en especial les tècniques magnetomètriques. A partir d'aquesta caracterització es pot estimar la resposta tèrmica mitjançant les corresponents relacions termodinàmiques.

Primerament es presenten els efectes calòrics gegants que acompanyen la transició magnetovolúmica del $Fe_{49}Rh_{51}$. Els aliatges de FeRh amb composicions properes a l'equiatòmica

presenten una transició de primer ordre al voltant d'una temperatura $T \sim 320$ K entre una fase de baixa temperatura antiferromagnètica i una fase d'alta temperatura ferromagnètica, amb un canvi de volum associat d'un $\sim 1$ % [8, 9]. La present tesi aprofundeix en les característiques de l'efecte magnetocalòric gegant que aquest material exhibeix, el qual ha restat com un dels millors materials magnetocalòrics des de la seva descoberta l'any 1990 [10]. En particular, es caracteritza la magnitud de la resposta tèrmica de manera consistent mitjançant diferents tècniques, així com la seva reproductibilitat sota ciclatge del camp magnètic. De manera similar, es reporta per primera vegada l'efecte barocalòric gegant associat amb l'expansió isotròpica relacionada amb la transició de fase magnetovolúmica. La forta sensitivitat de la transició envers el camp magnètic i la pressió hidrostàtica concedeixen una forta resposta multicalòrica quan els dos camps són aplicats o extrets simultàniament o seqüencialment. Aquesta resposta és analitzada extensament en base a mesures indirectes del comportament de la magnetització en funció de la pressió hidrostàtica i el camp magnètic. En aquesta transició, l'aplicació de cada camp involucra efectes calòrics oposats, en tant que cadascun afavoreix energèticament una fase diferent: mentre que el camp magnètic afavoreix la fase ferromagnètica d'alta temperatura, la pressió afavoreix la fase de menor volum de baixa temperatura. S'analitzen els avantatges en quant a l'amplificació de la resposta tèrmica que suposa l'aplicació de més d'un camp i se'n detallen els efectes restrictius de la histèresi associada a la transició. A tall d'exemple, es proposen cicles termodinàmics amb els dos camps que esquivarien aparentment aquestes irreversibilitats. A més, també s'avalua la resposta multicalòrica sota aplicació d'un camp magnètic i d'un camp uniaxial compressiu, la qual és de menor magnitud ja que és la pressió hidrostàtica la força mecànica que millor s'adapta a les característiques de la transició, que consta d'una expansió isotròpica sense canvi de simetria.

Un altre bloc d'estudi ha estat el dels aliatges de tipus Heusler amb base de Ni-Mn, que presenten unes interessants propietats magnètiques i estructurals. En aquests materials l'ordre ferromagnètic que poden presentar es deu a la hibridització entre els orbitals 3*d* dels àtoms de níquel i manganès, la qual afavoreix l'exclusió energètica dels electrons amb espí minoritari. En conseqüència, emergeix un magnetisme d'electrons itinerants que es mouen en una banda energètica *d* que ha quedat polaritzada en espí, i que és eminentment localitzat als àtoms de manganès [11, 12]. Així, les propietats magnètiques presenten una forta dependència envers els paràmetres estructurals, tals com la distància interatòmica entre els àtoms de manganès. Els efectes calòrics gegants en els aliatges estudiats es manifesten a les rodalies de la transició martensítica que típicament presenten aquests materials, i que pot presentar un fort acoblament magnetostructural [13]. Al llarg de la tesi es descriuen els efectes magnetocalòric i barocalòric d'un conjunt d'aliatges amb propietats magnetostructurals

diverses arranjades en funció de la seva composició particular, com són la temperatura i la histèresi associades a la transició o l'ordre magnètic de cada fase involucrada. El conjunt de resultats experimentals han permès fonamentar una descripció completa de l'efecte calòric i la corresponent reversibilitat en cada material i han aportat una visió sistemàtica i general de les característiques dels efectes calòrics en aquests materials. D'aquesta manera s'han pogut establir conclusions relatives a l'optimització de la resposta tèrmica, en funció de paràmetres importants com la histèresi i la sensitivitat de la transició amb els camps aplicats, la distància de la temperatura de la transició martensítica envers el punt de Curie de la fase d'alta temperatura, la magnitud dels camps aplicats, el canvi d'entropia associat a la transició de primer ordre. A més, també se n'avalua la seva potencial resposta multicalòrica. Així mateix, s'analitzen mètodes que amplifiquen la resposta calòrica com l'elaboració de compostos d'aliatges amb gradients composicionals que exhibeixen un canvi gradual de les temperatures de transició en funció del fragment del compost. En conseqüència, en aquests compostos cada fragment presenta la resposta tèrmica a diferents temperatures i, per tant, presenten un eixamplament del rang de temperatures operacional de l'efecte calòric. Finalment, s'empren les tècniques calorimètriques desenvolupades, conjuntament amb mesures magnetomètriques, per a l'estudi termodinàmic de les transicions de tipus intermartensític que típicament presenten els aliatges de Ni-Mn-Ga en cert rangs composicionals [14]. El mecanisme físic que condueix a aquests fenòmens està actualment sota debat [15] i l'estudi que es presenta indica que poden ser tractats com a transicions de fase.

Finalment, es presenten els efectes calòrics associats amb les perovskites de $BaTiO_3$ i de $Pb(Sc_{0.5}Ta_{0.5})O_3$. En el primer cas, el $BaTiO_3$ és un conegut material d'interès a dia d'avui pel seu ordre ferroelèctric a temperatura ambient. Aquest material presenta un conjunt de transicions de fase de primer ordre amb canvis electrostructurals als $\sim$ 200, 280 i 400 K [16–18]. En primer lloc, s'analitza l'efecte electrocalòric gegant que presenta al seu punt de Curie als 400 K. Aquesta transició és de caràcter displaciu entre una fase d'alta temperatura d'estructura cúbica i amb comportament paraelèctric i una fase de baixa temperatura tetragonal i ferroelèctrica. El canvi volúmic associat a aquesta transició també propicia l'efecte barocalòric quan s'hi apliquen pressions hidrostàtiques, el qual s'analitza en aquesta tesi, així com també l'efecte barocalòric a la transició entre fases ferroelèctriques als $\sim$ 280 K. Així doncs, la concurrència dels efectes calòrics induïts per camps elèctrics i pressions hidrostàtiques a la mateixa transició suggereix el potencial multicalòric de perovskites com el $BaTiO_3$. En el cas del $Pb(Sc_{0.5}Ta_{0.5})O_3$, aquest material presenta una transició a prop de temperatura ambient ($\sim$ 295 K) de característiques fortament dependents del grau d'ordre dels cations de $Sc^{3+}$ i $Ta^{5+}$ [19, 20]. El grau d'ordre i les característiques de la transició de la mostra sota estudi optimitzen la resposta electrocalòrica, la qual és

analitzada en aquesta tesi conjuntament amb la seva reversibilitat i la seva resistència a la fatiga després d'un gran nombre ($10^5$) de cicles de camp elèctric. En ambdós casos es reporta que les mostres de tipus *bulk* poden presentar també efectes calòrics de caràcter gegant induïts per camps elèctrics de magnitud reduïda ($\sim$ 10 kV cm$^{-1}$), en comparació amb les respostes electrocalòriques típicament reportades en les capes fines [1].

# Abstract

Solid state materials are candidates to exhibit a large field-driven thermal response in the vicinity of first-order transitions. The strong sensitivity of the transition temperature with the applied field and the latent heat associated with the change of phase can give rise to the giant magneto-, electro-, baro-, and elastocaloric effects. Furthermore, the coupling between structural, magnetic and electronic degrees of freedom at the transition regime enables the thermal response to be driven by multiple fields and, thus, giving rise to the multicaloric effect. In the last years, the interest in understanding and tailoring novel caloric materials has exceptionally grown in view of their potential application to alternative cooling technologies for large scale industry. The present thesis reports the giant caloric effects encompassing the $Fe_{49}Rh_{51}$ magnetovolumic transition, the magnetostructural martensitic transformation in Ni-Mn based Heusler alloys, and the ferroelectric perovskites $BaTiO_3$ and $Pb(Sc_{0.5}Ta_{0.5})O_3$. The physical conditions for the optimization of the thermal response which yield to an enlarged magnitude and operation range are explored, as well as the corresponding reproducibility upon field cycling and the potential multicaloric character. This evaluation is achieved by means of a complete caloric characterization in which the calorimetric experimental techniques which have been developed in purpose are crucial.

# Nomenclature

| | |
|---|---|
| $A$ | Magnetic vector potential |
| $\alpha$ | Low temperature phase |
| $\beta$ | High temperature phase |
| $\gamma$ | Unit shearing strain |
| $\Delta H_t$ | Total enthalpy change at the first-order transition (latent heat) |
| $\Delta M_t$ | Total magnetization change at the first-order transition |
| $\Delta P_t$ | Total polarization change at the first-order transition |
| $\Delta S_t$ | Total entropy change at the first-order transition |
| $\Delta V_t$ | Unit cell volume change at the first-order transition |
| $\Delta v_t$ | Total specific volume change at the first-order transition |
| $\varepsilon$ | Strain - Emissivity of the surface of a material |
| $\zeta$ | Integration baseline function |
| $\eta$ | Efficiency - Order parameter |
| $\theta$ | Scattering angle in XRD technique |
| $\lambda$ | Wavelength - Eigenvalue of the distortion matrix |
| $\mu$ | Chemical potential - Magnetic moment |
| $\mu_0$ | Vacuum permeability |
| $\mu_B$ | Bohr magneton |
| $\rho$ | Density |
| $\sigma$ | Stress - Stefan-Boltzmann constant |
| $\tau$ | Time constant |
| $\Phi$ | Magnetic flux |
| $\phi$ | Phase of the wave function |
| $\chi$ | Magnetic susceptibility - Transformed fraction |
| $\Psi$ | Wave function |
| $\omega$ | Angular frequency - Fitting parameter for $M(T,p,H)$ curves |
| | Volume expansion at the first-order transition (%) |
| AFM | Antiferromagnetic |

| | |
|---|---|
| $B$ | Magnetic field $B$ |
| BCE | Barocaloric effect |
| BTO | Barium titanate, $BaTiO_3$ |
| C | Cubic crystallographic structure |
| $C$ | Heat capacity - Stiffness - Curie constant |
| $c$ | Speed of light |
| DSC | Differential Scanning Calorimetry |
| $e$ | Electron charge |
| $E$ | Electric field - Energy |
| $E_F$ | Fermi energy |
| ECE | Electrocaloric effect |
| eCE | Elastocaloric effect |
| $f$ | Frequency - Twin variant volume fraction |
| $F$ | Force - Helmoltz free energy |
| FE | Ferroelectric |
| FM | Ferromagnetc |
| $G$ | Gibbs free energy |
| $g_J$ | Landé g-factor |
| $H$ | Magnetic field $H$ - Enthalpy |
| $h$ | Planck constant |
| $\hbar$ | Reduced Planck constant |
| HPDTA | High Pressure Differential Thermal Analysis |
| $I$ | Electric current |
| IR | Infrared |
| $J$ | Exchange integral - Total angular momentum quantum number |
| $j$ | Current density |
| $K$ | Magnetic anisotropy energy density |
| $k$ | Wavenumber |
| $k_B$ | Boltzmann constant |
| $L$ | Orbital angular momemtum |
| $l$ | Length |
| $M$ | Magnetization |
| $M^*$ | Analytical fit of the magnetization curves of $Fe_{49}Rh_{51}$ |
| $m$ | Mass |
| MCE | Magnetocaloric effect |
| mCE | Mechanocaloric effect |

| | |
|---|---|
| $N$ | Density of states |
| NM | Non-modulated structure |
| O | Orthorhombic crystallographic structure |
| $Q$ | Heat |
| $q$ | Electric charge |
| $P$ | Polarization - Power - Radiation per unit area |
| $P_S$ | Spontaneous polarization |
| $p$ | Pressure |
| PE | Paraelectric |
| PM | Paramagnetic |
| PST | Lead scandium tantalate, $Pb(Sc_{0.5}Ta_{0.5})O_3$ |
| $R$ | Electrical resistance - Thermal resistance of a medium |
| RC | Refrigerant capacity |
| $S$ | Entropy - Sensitivity - Elastic compliance - Electron spin |
| $T$ | Temperature |
| $T_A$ | Temperature amplitude of the oscillation in MDSC technique |
| T | Tetragonal crystallographic structure |
| $T_C$ | Curie temperature - Critical temperature |
| $T_t$ | Transition temperature |
| $T_{t_c}$ | Transition temperature upon cooling |
| $T_{t_h}$ | Transition temperature upon heating |
| $t$ | Time - Tolerance factor in perovskite structures |
| $t_p$ | Modulation period in MDSC technique |
| $U$ | Internal energy - Distortion matrix |
| $V$ | Volume - Voltage |
| $v$ | Specific volume - Velocity |
| $W$ | Work |
| $x_i$ | Thermodynamic field |
| $X_i$ | Thermodynamic displacement conjugated to the $x_i$ field - Cofactor condition |
| $Y$ | Electric signal output |
| $\bar{Y}$ | Baseline integration of the HPDTA calorimetric peak |

# Chapter 1

# Introduction

The materials interaction with external stimuli has always been a source of interest in Physics. From the thermodynamic point of view, in a general framework we consider a field as a thermodynamic force with the ability of inducing changes on its thermodynamic conjugate coordinate and thus generating work and an energy exchange. Since an applied field can be responsible of a change of the thermodynamic state of the system, a material may exhibit either a temperature change when the field is applied adiabatically or an entropy change when it is applied isothermally. These thermal effects in solids are called magnetocaloric (MCE), electrocaloric (ECE), elastocaloric (eCE) or barocaloric (BCE) if the applied field which drives the caloric response is a magnetic field, electric field, uniaxial stress or hydrostatic pressure, respectively. Particularly, since the elastocaloric and barocaloric effects are particular cases of mechanically driven caloric effects they are often labelled as mechanocaloric effects (mCE). Interestingly, in some particular conditions these phenomena are remarkably magnified and some materials can exhibit large temperature changes or heat exchanges upon field cycling.

An illustrative example of these thermal phenomena was experienced at the beginning of the eighteenth century by the blind natural philosopher John Gough when he quickly stretched (in other words: when he adiabatically applied a positive stress) an Indian rubber while lipping it and realised that the material exhibited a sudden boost of its temperature and cooled down [1, 21]. John Gough was perhaps the first in evaluating the interdependence between the thermal response of a material with the elastic properties described by its length and the applied stress. Analogously, in 1881 E. Warburg reported that pure iron heats up with the application of a magnetic field and cools down upon its withdrawal [22]. However, it is in 1917 when P. Weiss and A. Piccard give a first satisfactory thermodynamic approach to what they called *the novel magnetocaloric phenomenon* in the analysis of the temperature change of nickel when a magnetic field is applied in the vicinity of its Curie temperature at 354ºC

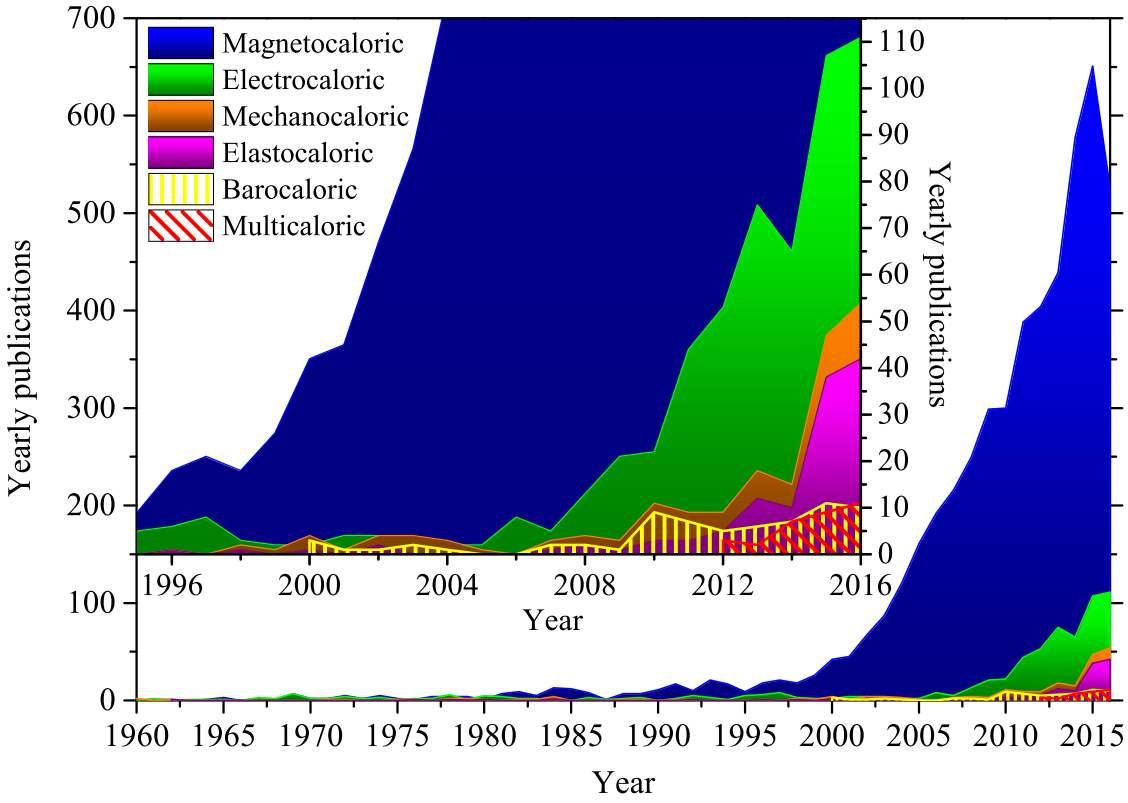


Fig. 1.1 Number of publications per year and per type of caloric effect according to Scopus bibliographic database.

[23]. The electrocaloric effect was first reported in 1930 in the Rochelle salt [24, 25] which prompted research on this field even though the highest electrocaloric temperature change ever measured in this material is very low ($\sim 0.003$K) [26]. In 1962 a larger electrocaloric effect is reported at the Curie temperature of $BaTiO_3$ [27].

The first consolidated application based on these thermal phenomena appears around 1920s when P. Debye and W. Giauque indepedently proposed the so-called *adiabatic demagnetization* technique, a new method for achieving very low temperatures in paramagnetic salts [23]. The idea is to cool the paramagnet down to the liquid helium limit and perform an isothermal magnetization. Consequently, the temperature of the sample does not change but the magnetic entropy is decreased due to the alignment of the spins. The second step consists in the adiabatic withdrawal of the magnetic field (adiabatic demagnetization). The gain of entropy of the magnetic moments during this step is balanced by the reduction of the lattice entropy due to the lower temperatures [28]. The technique is first implemented in 1933 [29] and is still used nowadays.

A few years later, in 1976, G. Brown reported [30] the great performance of Gd for *magnetic heat pumping near room temperature* by application of a 7 T magnetic field around its Curie point which is around room temperature. The concurrence of the second-order transition in Gd prompts large reversible temperature changes in a thermodynamic cycle with an approach to the Carnot efficiency, i.e. a cycle which approaches the thermodynamic limit by absorbing the same amount of entropy from the hot reservoir than the absorbed from the Gd source so that there is no heat loss and energy is completely transformed to work[1]. In 1997 V. K. Pecharsky and K. A. Gschneidner discover the giant magnetocaloric effect in $Gd_5(Si_2Ge_2)$ [2] representing an inflection which greatly prompts the research on materials exhibiting giant caloric effects. The value of this work lies in the fact that materials exhibiting caloric effects of giant magnitude can also be found at room temperature in case of concurrence of a first-order magnetostructural transition which incorporates its associated latent heat to the caloric effect.[2] Hence, with these ideas in mind the feasibility of implementing new materials for room temperature solid state refrigeration based on thermodynamic cycles with novel variables became a reality. Figure 1.1 illustrates the number of published articles per field each year in the last decades according to the Web of Science. The magnetocaloric effect is notably leading the research on solid state caloric materials since the late nineties. The inflection point in the case of electrocaloric materials is found in the late 2000's with the remarkable contribution of Mischenko et al. and the discovery of the giant electrocaloric effect in PZT thin films near the ferroelectric Curie temperature ($T_C \sim 222$ºC) in 2006 [3]. In 2008, E. Bonnot et al. reported [4] the large entropy change induced by uniaxial stress in Cu-Zn-Al and in 2010, L. Mañosa et al. reported the giant barocaloric effect in Ni-Mn-In [5]. These two manuscripts reporting the caloric effects arising in the vicinity of the martensitic transitions of both shape-memory alloys boosted the research on elastocaloric and barocaloric materials, respectively. Interestingly, since the recent years the scientific community is investing efforts into the development and characterization of multicaloric materials. Particularly, the multicaloric effect refers to the thermal response which is driven by the sequential or simultaneous application of multiple applied fields. Indeed, the coupling between different degrees of freedom (magnetic, structural, and electronic) at the transition regime of these materials and the high sensitivity of these transitions to multiple fields are convenient factors for the development of multicaloric

[1] As said, the Carnot cycle represents an ideal cycle and gives an upper threshold for the efficiency because a system converting all the supplied heat into work would violate the second law of thermodynamics.

[2] V. K. Pecharsky and K. A. Gschneidner were the first in coining the expression "giant" magnetocaloric effect. It is important to note here that an earlier work by Nikitin et al. [10] already reported the large magnetocaloric response in $Fe_{49}Rh_{51}$ although that work had a minor impact.

materials. These materials are candidates of exhibiting promising results due to the advantage of tuning the caloric performance with more than one field.

There is no doubt that the need of finding new commercial cooling methods adds up a clear applicational perspective which pushes forward the interest in the research on caloric materials. Actually, the development of new refrigeration methods and the progress of this technology along history has always been associated with clear advances in social welfare and prosperity. Even more, this relationship is expected to be reinforced in future. An average US citizen spends $\sim 25$ % of the energy consumption for food refrigeration and air conditioning [7]. The large scale use of vapour compression technology has implied the use of CFC and HCFs gases which have been recently banned in most countries and have been on the spot since the Montreal Protocol (1989) for being severe ozone-depleting substances. However, their alternative (HFCs) has been proven to seriously contribute to the greenhouse effect and global warming. In addition, after living 160 years of its own history conventional vapour-compression technology has become a highly developed industry which is reaching its energetic efficiency limits [7, 31]. With this in hand, research and industry are aimed nowadays at exploring more efficient, environmentally friendly and economically competitive cooling methods and, thus, overcoming the crucial challenges such as increasing the cooling capacity or the energy efficiency and decreasing the materials costs, the environmental impact and the magnitude of the applied fields for the new cooling methods.

Figure 1.3 illustrates a set of thermodynamically equivalent cooling cycles in conventional electrocaloric, magnetocaloric and elastocaloric systems (from top to bottom, respectively). Each thermodynamic process enumerated with roman numerals is described as follows:

I At the first step the field ($E$, $H$ or $\sigma$) is adiabatically applied to the solid and the forward first-order transition is field-driven. Thus, a large change on its conjugate displacement ($P$, $M$ or $\varepsilon$, respectively) is induced and the solid heats up to a high temperature.

II The hot reservoir absorbs heat from the solid at constant field and the solid cools down.

III The field is adiabatically removed and the reverse first-order transition is driven. The solid cools down.

IV At this point the cold reservoir further cools down due to the heat exchange with the solid which is at a lower temperature. The solid warms up to the initial state and the thermodynamic cycle can be repeated.

In thermodynamic terms a conventional vapour-compression cycle can be considered as an analogous case to the previously described cycle considering that in this case the conjugate


Fig. 1.2 Compendium of pictures taken in the 1950's related to the old ice factory which was settled in Carrer Ciutadans in Girona (Catalonia). In those days, it was common to buy the ice for daily use and keeping the food in proper conditions for a longer durability. Since then the cooling technology and its efficiency has progressed at high speeds.

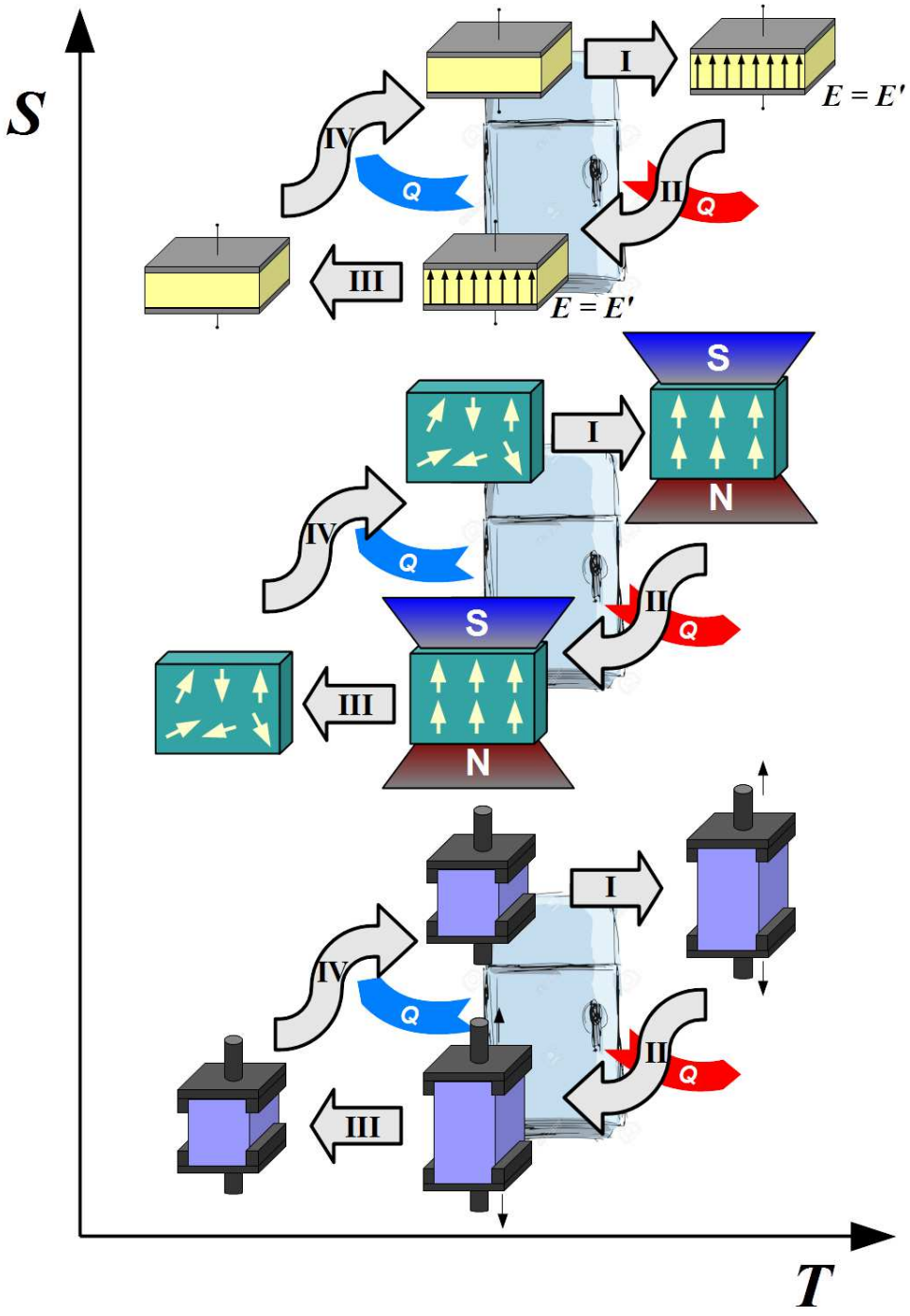


Fig. 1.3 Sketch of different thermodynamically equivalent refrigerating cycles as a function of the corresponding pair of conjugate variables: electric field $E$ and polarization $P$ (top), magnetic field $H$ and magnetization $M$ (middle), and stress $\sigma$ and strain $\varepsilon$ (bottom). In all cases the cycles correspond to the performance of a material exhibiting a conventional giant magnetocaloric effect. The vertical axis is indicative of the entropy change of the system whereas the horizontal axis indicates the temperature change. Horizontal arrows refer to adiabatic processes. Red arrows specify a heat loss of the system which is transferred to the heat sink. Blue arrows specify a heat income which is transferred from the cold reservoir.

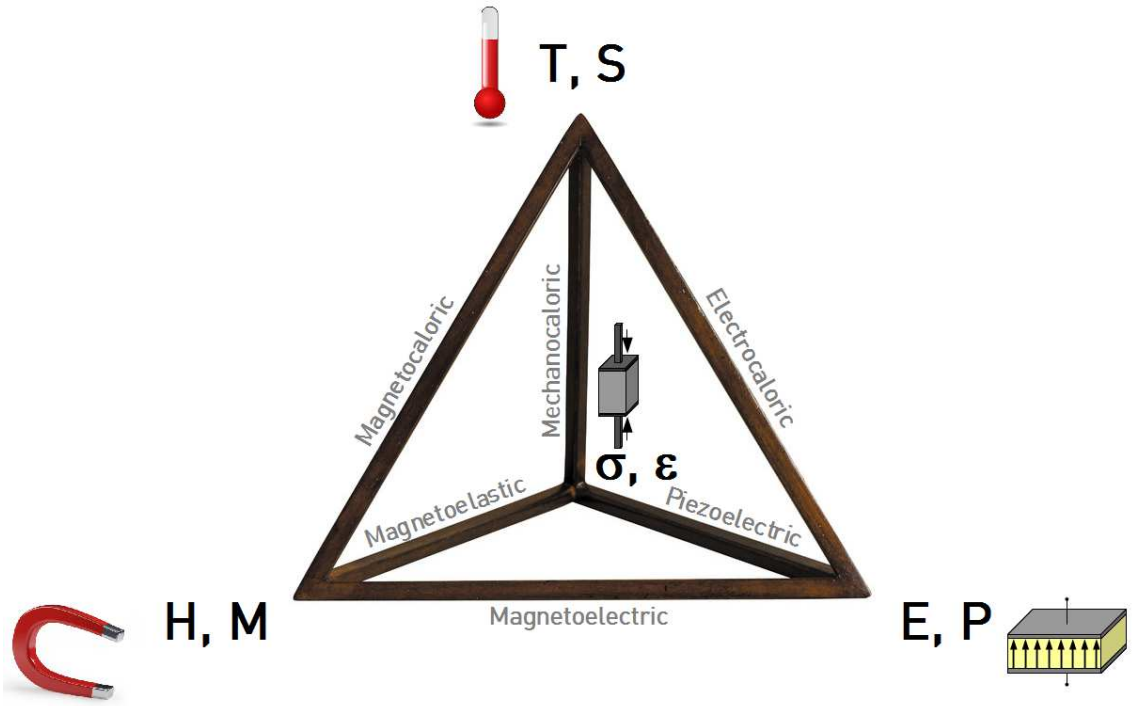


Fig. 1.4 Diagram illustrating the relationship between mechanical, electric, magnetic and thermal properties in a solid.

variables are pressure and volume and the system is a gas which liquefies and evaporates along the cycle.

Although refrigeration can be classified as one of the most prominent applications, it is worth mentioning the great potential of the use of these materials in other fields. Their functional or multifunctional properties classifies them as smart materials. Figure 1.4 sketches the relationship between fields and displacements from which a list of interesting properties can arise such as shape-memory or magnetic shape-memory properties, magnetostriction or piezoelectricity and, thus, interesting applications such as electronic devices, sensors, actuators or energy harvesting devices.

There is an increasingly large list of caloric materials which belong to different material families. They all have the ability to exchange substantial heat $Q$ with the application of fields and exhibit large adiabatic temperature changes $\Delta T$. In this regard, figure 1.5 taken from reference [1] maps the magnitude of $\Delta T$ and $Q$ values for a broad list of caloric materials. Nevertheless, the caloric performance of a material cannot be solely described by these two magnitudes because the phenomenon is far more complex. For instance, we can comment here the films displaying a ferroelectric transition which facilitate the application of extremely large values of the electric field due to their thin thickness. They are candidates to exhibit

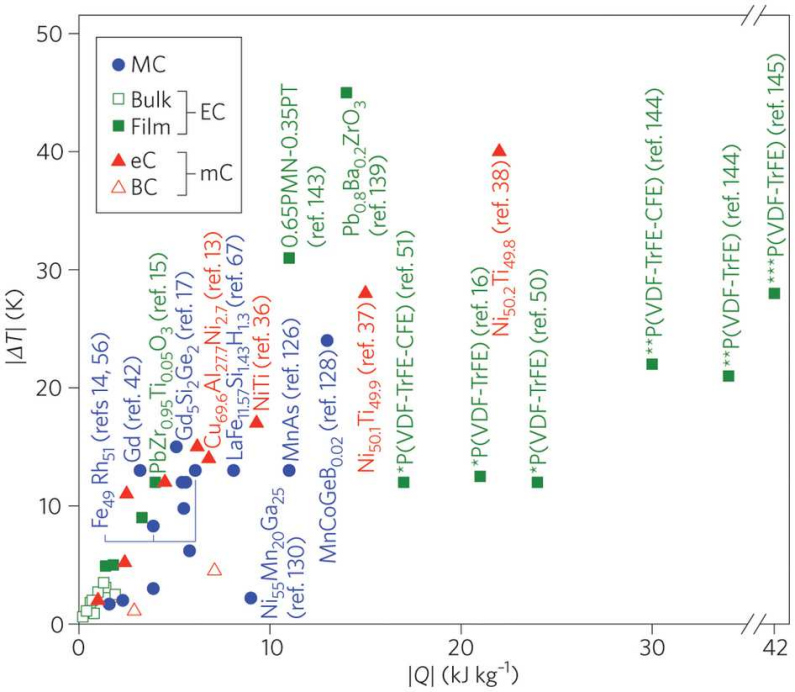


Fig. 1.5 Map of the $\Delta T$ and $Q$ values exhibited by the main caloric materials near and away from room temperature taken from 1.5. Blue circles stand for the MCE driven by changes of magnetic fields $|\Delta\mu_0 H|$ in the range of [1, 5] T, green squares stand for the ECE (open symbols refer to bulk materials with applied electric fields in the range of $|\Delta E| \in [4, 160]$ kV cm$^{-1}$ and solid symbols to films, with $|\Delta E| \in [480, 3500]$ kV cm$^{-1}$), open red triangles to the eCE effect driven by applied uniaxial stresses $|\Delta\sigma| \in [0.1, 0.9]$ GPa and solid red triangles to the BCE effect driven by $\Delta p \in [0.2, 0.26]$ GPa.

great electrocaloric response as corroborated by figure 1.5. In addition, their typical low density strongly magnifies the exchanged heat per sample mass. However, these facts may lead to an overestimation of the caloric effect when considered to real life applications, which require limited values of the applied field and a list of defined properties of the materials with which the thin films may or may not fit.

## 1.1 Dissertation contents

This dissertation is focused on the field-driven giant caloric effects in solid state materials arising in the vicinity of first-order phase transitions and is organized as follows. The second chapter introduces the main concepts for the physical analysis of the giant caloric effects that will be employed during the dissertation, which include a description of the thermodynamics related to caloric phenomena and phase transitions. The third chapter describes the main

experimental techniques which have been developed and are employed along the study. It will be shown that calorimetry under applied fields, thermal imaging and magnetometric measurements take especial relevance. Then, a variety of materials displaying the proper conditions for the enlargement of these caloric responses will be analysed. In common, significant emphasis has been devoted to the reproducibility of the phenomena, the nature of the multicaloric response when more than one field is applied and the different mechanisms allowing an optimization of the caloric effect at the phase transition. The chosen materials are representative of a plural selection of the different families of caloric materials and are listed below:

- **Chaper 4: FeRh**. Since the report of the giant magnetocaloric effect in FeRh in the early 1990s [10, 32] in the vicinity of its first-order transition at $\sim$ 320 K, the near equiatomic Fe-Rh alloy has always persisted as one of the model magnetocaloric materials due to its great caloric performance. The material's interplay with different stimuli (magnetic field, hydrostatic pressure, uniaxial compression) and the consequent thermal response is thoroughly evaluated when the fields are applied either independently or simultaneously as well as the reproducibility of the several caloric and multicaloric effects.

- **Chapter 5: Ni-Mn based Heusler compounds**. This family of alloys typically undergo a first-order martensitic transition which is at the origin of the magnetic shape-memory and superelastic effects [13]. This magnetostructural transition involves a shear strain distortion with a relatively large volume change which make these materials great candidates to exhibit large magneto- and mechanocaloric effects which are evaluated along this chapter.

- **Chapter 6: $BaTiO_3$**. This widely applied ferroelectric material at room temperature exhibits a displacive ferroelectric-paraelectric (FE-PE) transition at $T_C \sim 125$ ºC at which the giant electrocaloric and barocaloric effects take place [16]. The sixth chapter of the dissertation discusses these thermal responses in the vicinity of the Curie point.

- **Chapter 7: $Pb(Sc_{0.5}Ta_{0.5})O_3$**. The electrocaloric performance of this ceramic material is evaluated. It exhibits a room temperature first-order transition from a paraelectric phase to a ferroelectric phase involving a large change on its pyroelectric coefficient. Its high temperature PE phase presents a perovskite structure, A(B' B")$O_3$, in which B atoms (Sc, Ta) display a certain degree of disorder and the long-range FE interaction appears below the transition [19].

Finally, chapter 8 collects the main conclusions of the thesis and the future perspectives are outlined.

# Chapter 2

# Fundamentals

Along this dissertation we will continuously deal with physical concepts like heat, entropy, temperature, heat capacity, susceptibilities, work or phase transitions. In this regard, the present chapter describes the thermodynamics which provide the proper framework for the description of the caloric effects in solids. From the thermodynamic point of view, there is great analogy in the description of each type of caloric effect characterized by each pair of conjugate variables $(x_i, X_i)$, where $x_i$ is the generalized force (intensive variable) and $X_i$ is its conjugate displacement (extensive variable). The description given along the first sections of this thesis will generally be written in a general form, by any pair of conjugate variables $(x_i, X_i)$[1]. Table 2.1 outlines the variables involved in each type of caloric effect and includes the different expressions related to the work $W$ which are described in section 2.2.3. It is worth remembering that the BCE and the eCE are particular cases of the mCE. A description of the conjugate variables related to the mechanocaloric effect are given in the appendix A.

## 2.1 Thermodynamics

Let us define a system under the influence of a certain set of fields $x_i$ with conjugate displacements $X_i$ such as magnetic field $H$ and magnetization $M$, electric field $E$ and polarization $P$, uniaxial stress $\sigma$ and strain $\varepsilon$ or hydrostatic pressure $p$ and volume $V$. A differential change in its internal energy $U$ is given by

[1]For the sake of simplicity and as usual in the published reports on caloric materials, the notation of the thesis will usually omit the tensor character of the applied fields and the conjugate displacements unless required for the particular description. For instance, in the case of the MCE or the ECE the variables $(\mathbf{x}, \mathbf{X})$ are vectors and this simplification usually implies the assumption that the given value of the applied field $x$ is the component parallel to the conjugate displacement $X$ so that the dot product is $\mathbf{x} \cdot \mathbf{X} = xX$.

Table 2.1 Characteristic fields and conjugate displacements of the magneto-, electro-, mechano-, elasto- and barocaloric effects and the associated expressions for the magnetic, electric and mechanical work for a given infinitesimal change in conjugate displacement.

| Caloric effect | Field $x_i$ | Conjugate displacement $X_i$ | Work $dW$ |
|---|---|---|---|
| MCE | Magnetic field, $\mathbf{H}$ | Magnetization, $\mathbf{M}$ | $\mathbf{H}\cdot d\mathbf{B}$ $-\mu_0\mathbf{M}\cdot d\mathbf{H}$ |
| ECE | Electric field, $\mathbf{E}$ | Polarization, $\mathbf{P}$ | $\mathbf{E}\cdot d\mathbf{D}$ $-\mathbf{P}\cdot d\mathbf{E}$ |
| mCE | Stress, $\boldsymbol{\sigma}$ | Strain, $\boldsymbol{\varepsilon}$ | $V\boldsymbol{\sigma}\cdot d\boldsymbol{\varepsilon}$ |
| eCE | Uniaxial stress (along $\hat{x}$), $\sigma_{\hat{x}}$ | Strain (along $\hat{x}$), $\varepsilon_{\hat{x}}$ | $V\sigma_{\hat{x}}d\varepsilon_{\hat{x}}$ |
| BCE | Hydrostatic pressure, $-p$ | Volume, $V$ | $-pdV$ |

$$dU(S,X_i) = TdS + \sum_{i=1}^{n} x_i dX_i \tag{2.1}$$

which is a function of the entropy $S$ and the displacements $X_i$ [33]. $T$ is the temperature of the system and is presented as the conjugate field of entropy $S$. The above equation implies that $\left(\frac{\partial U}{\partial S}\right)_{x_i} = T$ and $\left(\frac{\partial U}{\partial X_i}\right)_{x_{j\neq i}} = x_i$ and since $U$ is an exact differential, the following expression is accomplished:

$$\frac{\partial^2 U}{\partial x_i \partial x_j} = \frac{\partial^2 U}{\partial x_j \partial x_i} \tag{2.2}$$

which leads to

$$\left(\frac{\partial S}{\partial x_i}\right)_{T,x_{j\neq i}} = \left(\frac{\partial X_i}{\partial T}\right)_{x_i} \tag{2.3}$$

Equation (2.3) is one of the **Maxwell relations**. The entropy $S$ and displacements $\{X_i\}$ appear as the natural variables of the internal energy $U$. Hence, $U$ can be convenient for describing a thermodynamic process in which $S$ and $\{X_i\}$ are kept constant. Legendre transforms of these variables lead to the definition of new thermodynamic potentials with different natural variables, i.e. enthalpy $H = U + \sum_{i=1}^{n} x_i X_i$, the Helmoltz free energy $F = U - TS$ and the Gibbs free energy $G = F - \sum_{i=1}^{n} x_i X_i$. The whole set of Maxwell relations are

derived by considering the symmetry of the second derivatives of these new thermodynamic potentials with respect to their natural variables just like it has been shown in (2.3). The corresponding Maxwell relations read:

$$\left(\frac{\partial S}{\partial x_i}\right)_{T,x_{j\neq i}} = \left(\frac{\partial X_i}{\partial T}\right)_{x_i} \tag{2.4}$$

$$\left(\frac{\partial S}{\partial X_i}\right)_{T,X_{j\neq i}} = -\left(\frac{\partial x_i}{\partial T}\right)_{X_i} \tag{2.5}$$

$$\left(\frac{\partial X_i}{\partial x_j}\right)_{T,x_{k\neq j}} = \left(\frac{\partial X_j}{\partial x_i}\right)_{T,x_{k\neq i}} \tag{2.6}$$

Maxwell relations are useful expressions which relate the interdependence of the set of variables which can describe thermodynamically the system. Equations (2.4) and (2.5) are called the *caloric Maxwell relations* [6] since they relate the entropy variation with respect to field $x_i$ or displacement $X_i$ to the temperature derivatives of $x_i$ and $X_i$. Equation (2.6) relates the field-induced ($x_i$) changes in non-conjugate displacements ($X_{j\neq i}$) when the other fields are kept constant. Therefore, as we will see equation (2.6) can become especially convenient for analysing the multicaloric effect in materials exhibiting a cross-coupled response to conjugate displacements under the application of multiple fields.

Considering the expression (2.4) and the heat capacity at constant fields $C = T\left(\frac{\partial S}{\partial T}\right)_{x_{i=1,\dots,n}}$ it is convenient now to write the differential entropy change of the system as:

$$dS = \left(\frac{\partial S}{\partial T}\right)_{x_{j=1,\dots,n}} dT + \sum_{i=1}^{n}\left(\frac{\partial S}{\partial x_i}\right)_{T,x_{j\neq i}} dx_i = \frac{C}{T}dT + \sum_{i=1}^{n}\left(\frac{\partial X_i}{\partial T}\right)_{x_{j=1,\dots,n}} dx_i \tag{2.7}$$

In the physical case in which only the field $x_i$ is modified while the other fields $\{x_{j\neq i}\}$ are kept constant the isothermal field-driven entropy change is written as

$$\boxed{\Delta S(0 \to x_i') = \int_0^{x_i'}\left(\frac{\partial X_i}{\partial T}\right)_{x_{j=1,\dots,n}} dx_i} \tag{2.8}$$

and the adiabatic temperature change is

$$\boxed{\Delta T(0 \to x_i') = -\int_0^{x_i'}\frac{T}{C}\left(\frac{\partial X_i}{\partial T}\right)_{x_{j=1,\dots,n}} dx_i} \tag{2.9}$$

Both (2.8) and (2.9) display a direct dependence on the terms $\left(\frac{\partial X_i}{\partial T}\right)_{x_{j=1,\ldots,n}}$ which are called *caloric response functions*. These functions clearly tune the magnitude of the thermal response. The convenience of phase transitions for the enhancement of the caloric response becomes now evident since in these cases the temperature derivative of the associated order parameter $X_i$ is expected to be greatly enlarged at the transition temperature range. The phenomenon is more pronounced in first-order phase transitions in which the order parameter $X_i$ displays an abrupt change. In the case of the expression (2.9) the heat capacity $C$ appears as a denominator inside the integral. In relation to this, low heat capacities $C$ also endorse a larger temperature change. For the *indirect* computation of the caloric effects in which these expressions are employed, it is important to note that this quantity can have a significant temperature and field dependence over the range of variables over which the transition takes place.

### 2.1.1 The multicaloric effect

A multicaloric effect is defined as the thermal effect which emerges in a material in response to the simultaneous or sequential application of more than one field. Equations (2.8) and (2.9) are frequently used when analysing magneto-, electro-, elasto- and barocaloric effects in materials, i. e. when the associated field of each caloric effect is applied while keeping the others constant. Let us explore now the expressions for the entropy change $\Delta S(T, 0 \rightarrow x_1', 0 \rightarrow x_2')$ in a material in which the multicaloric response is driven by two fields ($x_1$, $x_2$). Although only two fields are considered here, the following analysis can be generalised to the case in which more fields are applied.

First of all, one has to consider the fact that entropy is a state function and the total entropy change $\Delta S(T, 0 \rightarrow x_1', 0 \rightarrow x_2') = S(T, x_1', x_2') - S(T, 0, 0)$ can be computed irrespective of the path from the initial state[2] to a state in which the entropy is $S(T, x_1', x_2')$ under equilibrium conditions as illustrated in figure 2.1.

We can begin our analysis by dividing the entropy change in the following contributions [6]:

$$\boxed{\Delta S\left(T, 0 \rightarrow x_1', 0 \rightarrow x_2'\right) = \Delta S\left(T, 0 \rightarrow x_1', 0\right) + \Delta S\left(T, x_1', 0 \rightarrow x_2'\right)} \tag{2.10}$$

[2]For the sake of clarity and for a simpler notation, we consider an initial state in which the value of the fields is $(x_1 = 0, x_2 = 0)$. It is worth noting that the description can be generalized to any initial state $(x_1, x_2)$ with independence of the sign of the changes $\Delta x_1$ and $\Delta x_2$ by a suitable modification of the limits of integration in each case.

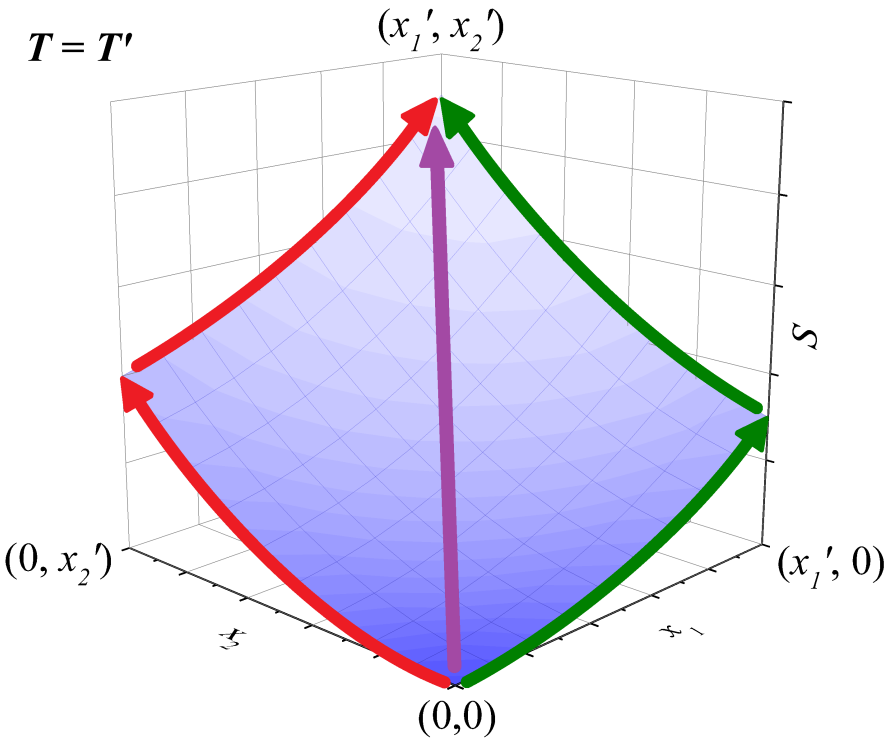


Fig. 2.1 Illustrative diagram of the total entropy $S$ of a system as a function of the ($x_1$, $x_2$) plane under isothermal conditions. Entropy is a state function and the computation of $\Delta S\,(T,0\rightarrow x_1',0\rightarrow x_2') = S\,(T,x_1',x_2') - S\,(T,0,0)$ is independent of the path from one state to the other under equilibrium conditions as illustrated by the green, purple and red arrows.

The second term of the above expression can be specified differently by considering the following subtraction of entropy quantities :

$$\Delta S\left(T,\delta x_1',0\rightarrow x_2'\right) - \Delta S\left(T,0,0\rightarrow x_2'\right) = \frac{\partial}{\partial x_1}\Delta S\left(T,\delta x_1',0\rightarrow x_2'\right) dx_1 \tag{2.11}$$

where $\delta x_1' \rightarrow 0$. The above expression can be generalized for any change $\delta x_1' \rightarrow x_1'$ by integration:

$$\Delta S\left(T,x_1',0\rightarrow x_2'\right) - \Delta S\left(T,0,0\rightarrow x_2'\right) = \int_0^{x_1'} \frac{\partial}{\partial x_1}\Delta S\left(T,x_1,0\rightarrow x_2'\right) dx_1 \tag{2.12}$$

The second term in (2.10) can be derived by use of equations (2.12) and (2.8). Accordingly, this term can be expressed as:

$$\Delta S\left(T,x_1',0\rightarrow x_2'\right)=\Delta S\left(T,0,0\rightarrow x_2'\right)+\int_0^{x_1'}\frac{\partial}{\partial x_1}\Delta S\left(T,x_1,0\rightarrow x_2'\right)dx_1$$
$$=\int_0^{x_2'}\left(\frac{\partial X_2}{\partial T}\right)_{x_1=0,x_2}dx_2+\int_0^{x_1'}\frac{\partial}{\partial x_1}\int_0^{x_2'}\left(\frac{\partial X_2}{\partial T}\right)_{x_1',x_2}dx_2dx_1 \tag{2.13}$$

The expression of the entropy change is given by rearranging the terms in equation (2.10) with the terms of (2.8) and (2.13):

$$\boxed{\begin{aligned}&\Delta S\left(T,0\rightarrow x_1',0\rightarrow x_2'\right)=\int_0^{x_1'}\left(\frac{\partial X_1}{\partial T}\right)_{x_2=0,x_1}dx_1\\&+\int_0^{x_2'}\left(\frac{\partial X_2}{\partial T}\right)_{x_1=0,x_2}dx_2+\int_0^{x_1'}\int_0^{x_2'}\left(\frac{\partial^2 X_2}{\partial x_1\partial T}\right)_{x_1',x_2}dx_2dx_1\end{aligned}} \tag{2.14}$$

Interestingly, a third term on the right hand side of equation emerges. This term is a double integral of $\left(\frac{\partial^2 X_2}{\partial x_1\partial T}\right)_{x_1',x_2}$ over the whole $(x_1, x_2)$ space and its role on the final result will be especially evaluated in section 4.4. Again, the fact that entropy is a state function together with the interdependence between fields $(x_1,x_2)$ and conjugate displacements $(X_1,X_2)$ certifies that the calculus of $\Delta S\left(T,0\rightarrow x_1',0\rightarrow x_2'\right)$ cannot be based on the simple sum of the caloric effects associated with the variation of each field independently by departing from the initial state $[\Delta S(T,0\rightarrow x_1',0)+\Delta S(T,0,0\rightarrow x_2')]$. In fact, the lack of this coupling term would convert the right hand side of equation (2.14) into the sum of two terms referring to thermodynamically unconnected path (see figure 2.1).

Alternatively, as follows from (2.8) the equation (2.10) can also be expressed as:

$$\Delta S\left(T,0\rightarrow x_1',0\rightarrow x_2'\right)=\int_0^{x_1'}\left(\frac{\partial X_1}{\partial T}\right)_{x_2=0,x_1}dx_1+\int_0^{x_2'}\left(\frac{\partial X_2}{\partial T}\right)_{x_1=x_1',x_2}dx_2 \tag{2.15}$$

which can be convenient when computing the values of $\Delta S$ if $X_2$ is known as a function of temperature and $x_2$ at a certain value of the applied field $x_1=x_1'$. In this case, (2.15) is the simple sum of the caloric effects associated with each one independently because they refer to thermodynamically connected states as expressed in the right hand side of equation (2.10) and illustrated by the green arrows in figure 2.1.

In view of the cross-response between fields $(x_1,x_2)$ and conjugate displacements $(X_1,X_2)$, the entropy change associated with the application or removal of $x_2$ can be written in terms

of the non-conjugated field $X_1(T,x_1,x_2)$. With this purpose, we use the Maxwell relation (2.5) to obtain:

$$\Delta S\left(T,0,X_1(0)\rightarrow X_1(x_2')\right) = -\int_{X_1(0)}^{X_1(x_2)} \left(\frac{\partial x_1}{\partial T}\right)_{X_1,X_2} \tag{2.16}$$

considering that $X_2$ is kept at a constant value $X_2'$, $\left(\frac{\partial x_1}{\partial T}\right)_{X_1} = -\left(\frac{\partial x_1}{\partial X_1}\right)_T \left(\frac{\partial X_1}{\partial T}\right)_{x_1}$, and $dX_1 = \left(\frac{dX_1}{dx_2}\right) dx_2$, the previous expression (2.16) can be expressed as:

$$\boxed{\Delta S\left(T,0,X_1(0)\rightarrow X_1(x_2')\right) = \int_0^{x_2} \frac{\left(\frac{\partial X_1}{\partial x_2}\right)_{T,x_1}}{\left(\frac{\partial X_1}{\partial x_1}\right)_{T,x_2}} \left(\frac{\partial X_1}{\partial T}\right)_{x_1,x_2} dx_2} \tag{2.17}$$

Interestingly, the expression (2.17) allows the entropy change driven by $x_2$, i.e. $\Delta S(T,0,0\rightarrow x_2')$, to be expressed in terms of the non-conjugated displacement $X_1$.

## 2.2 Phase transitions

As previously mentioned, from the above expressions it is clear that the caloric response functions $\left(\frac{\partial X_i}{\partial T}\right)_{x_i}$ have a strong connection with the magnitude of the caloric effect and the conditions for their enhancement are met in the vicinity of phase transitions, i. e. where the materials display large changes in conjugate displacements over a particular temperature region.

Thermodynamically, a phase is a homogeneous region of matter at a certain thermodynamic state which displays a set of macroscopic properties and uniformly distributed physical features. A phase transition occurs when the equilibrium state of a system changes qualitatively under the influence of a driving field $x_i$ or temperature $T$ and the system evolves from one phase with a certain characteristic group of macroscopic properties to another. These macroscopic changes are often linked to symmetry elements that appear or disappear during a phase transition.

The **order parameter** is the quantity which measures the degree of order of a certain physical property across the boundaries of the phase transition and it can take the form of a scalar, a vector, a tensor, a pseudo-scalar, etc. The thermal average of the order parameter vanishes on one side of the transition and takes a non-zero value on the other side. Let us define a transition which occurs at the temperature $T_C$ with an order parameter $\eta$. $\eta$ takes the

value $\eta_0$ (different from zero) at one of the transition boundaries when the system is fully at the highly ordered phase (low symmetry phase). The set of symmetry transformations in which $\eta_0$ is invariant is called $\eta_0$ group. We consider now a small variation of this magnitude $\delta\eta$ at the transition point and, hence, the order parameter takes now the value $\eta = \eta_0 + \delta\eta$. $\delta\eta_0$ group has less symmetries and is a subgroup of $\eta_0$ group. Since $\eta$ is a function of both terms it has the same symmetries as $\delta\eta_0$ which is less symmetric [34, 35].

At this point, it is worth to mention the Neumann principle which is expressed as follows [36]:

> If a crystal is invariant with respect to certain symmetry operations, any of its physical properties must also be invariant with respect to the same symmetry operations, or otherwise stated, the symmetry operations of any physical property of a crystal must include the symmetry operations of the point group of the crystal.

In relation to this, **ferroic transitions** refer to those phase transitions which result in a new macroscopic property which couples to an external field and a ferroic material is any material which exhibits one or more ferroic phase transitions. In the special case of **multiferroic transitions** the transition results in more than one macroscopic property which couple to more than one field [37].

Usually the high-symmetry phase, i.e. the *disordered* phase with respect to a certain order parameter (the phase in which $\eta = 0$), corresponds to the high temperature phase which has a higher absolute entropy in comparison with the low temperature phase. However, in some cases this might not be accomplished and the loss of entropy related to the loss of symmetry described by the order parameter $\eta$ can be balanced by a gain of entropy from other entropic contributions related to other degrees of freedom. Actually, this will be the situation of some materials under study along the dissertation which display a high temperature ferromagnetically ordered phase and a low temperature phase with a more disordered magnetic state (paramagnetic or antiferromagnetic).

Interestingly, systems exhibiting phase transitions with symmetry changes of very different physical origins may be described in an equivalent manner. For instance, the tensor character of the order parameter, symmetries of the system and the space dimension can be common features in phase transitions of different kinds with independence of their differences at the microscopic level or at finite scales. A general description of these phenomena can be given in the framework of *critical phenomena* and can be valid in either physical, chemical or biological systems. This is explained in view of the unique features of the system arising at the critical point $T_C$, where the correlations which coordinate the value of the order parameter

Table 2.2 Behaviour of the entropy $S$, the order parameter $X_i$, and the heat capacity at constant temperature $C_p$ in first- and second-order phase transitions.

| | $S = \left(\frac{\partial G}{\partial T}\right)_{x_i}, X_i = \left(\frac{\partial G}{\partial x_i}\right)_T$ | $C_p = \left(\frac{\partial^2 G}{\partial T^2}\right)_P$ |
|---|---|---|
| First-order phase transition | Discontinuous | Divergence |
| Second-order phase transition | Continuous | Discontinuous |

become arbitrarily large, limited only by the size of the system. This is in contrast with the situation above and below $T_C$, where the correlations are limited to the value of a certain correlation length. Phase transitions with the same scale-free symmetric properties belong to the same *universality class* and share the same *critical exponents* for the power-laws describing the main thermodynamic quantities in the vicinity of $T_C$ [38].

### 2.2.1 Classification of phase transitions

**First-order phase transitions** or **discontinuous phase transitions** are defined to be those that involve a non-zero latent heat and have an associated sudden jump in the entropy of the system ($\Delta S_t$). In contrast, a phase transition is called *continuous* when the change does not involve any associated latent heat and the entropy and the order parameter change continuously[3]. Table 2.2 and figure 2.2 illustrate the behaviour of the characteristic parameters at $T_C$ in first- and second-order transitions (continuous transitions).

The Gibbs free energy ($G = H - TS$) becomes a convenient thermodynamic potential for the description of phase transitions because its minimization clarifies the spontaneity of a

[3]In relation to this, we can introduce the **Ehrenfest classification of phase transitions** which defines the order $n$ of the phase transition as the order of the lowest derivative of $G$ which shows a discontinuity upon crossing the coexistence curve between phases $\alpha$ and $\beta$ in a phase diagram. Hence, a phase transition is of order $n$ if it accomplishes:

$$\left(\frac{\partial^m G_\alpha}{\partial T^m}\right)_{x_i} = \left(\frac{\partial^m G_\beta}{\partial T^m}\right)_{x_i}, \quad \left(\frac{\partial^m G_\alpha}{\partial {x_i}^m}\right)_T = \left(\frac{\partial^m G_\beta}{\partial {x_i}^m}\right)_T; \qquad m = 1, 2, ..., n-1. \tag{2.18}$$

$$\left(\frac{\partial^n G_\alpha}{\partial T^n}\right)_{x_i} \neq \left(\frac{\partial^n G_\beta}{\partial T^n}\right)_{x_i}, \quad \left(\frac{\partial^n G_\alpha}{\partial {x_i}^n}\right)_T \neq \left(\frac{\partial^n G_\beta}{\partial {x_i}^n}\right)_T \tag{2.19}$$

However, this classification fails in classifying the transitions which show divergences in the derivatives of $G$. This is the case for magnetic transitions with a susceptibility of the form $\chi = \frac{1}{(T - T_C)^\gamma}$. For this reason, a more rigorous method of classifying the phase transitions is distinguishing the **discontinuous** (or first-order phase transitions) and the **continuous** transitions.

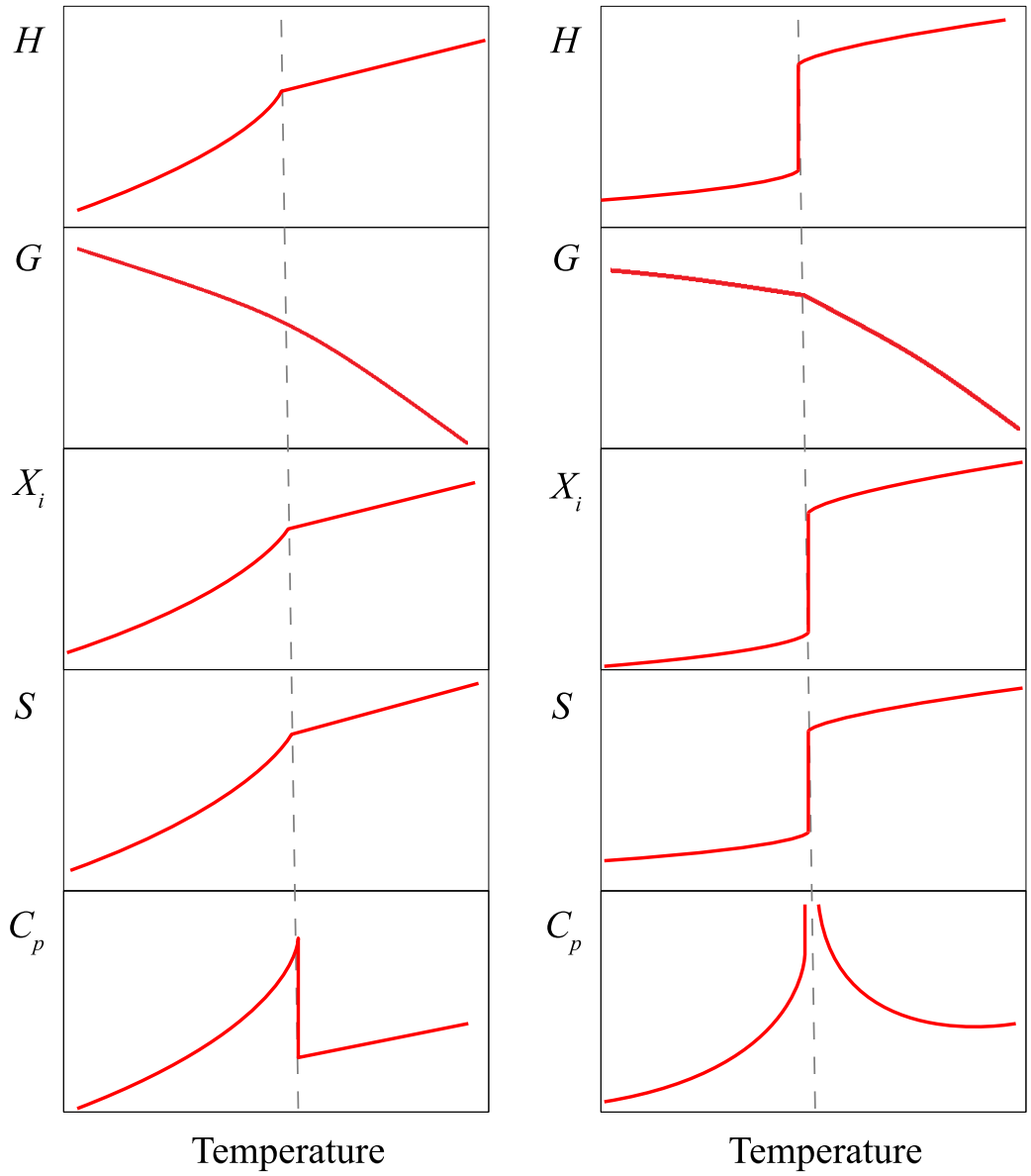


Fig. 2.2 Behaviour of relevant parameters involved in second-order phase transitions (left panels) and first-order phase transitions (right panels). From top to bottom, each diagram plots the temperature dependence of the enthalpy ($H$), the Gibbs free energy ($G$), the displacement $X_i$, the entropy ($S$), and the heat capacity at constant pressure $C_p$ in the vicinity of the transition temperature $T_C$, which is indicated by the dashed grey lines.

thermodynamic process. For instance, a nucleation process of an ordered crystal becomes spontaneous when the Gibbs free energy is minimized and thermal fluctuations provide sufficient energy for overcoming any activation free energy barrier, i. e. the maximum energy along the transformation path relative to the energy of the initial state. The natural variables for the Gibbs free energy are the temperature $T$, the fields $\{x_i\}$, and the set of extensive quantities $\{N_i\}$ referring to the number of particles of each phase which are also included below in the thermodynamic analysis.

If the system is in equilibrium, the Gibbs free energy is in a minimum and $dG = 0$. The differential form of $G$ can be written as:

$$dG = \sum_{j=\alpha}^{\beta} \left( -S^j dT + \mu^j dN^j - \sum_{i=1}^{n} X_i^j dx_i \right) = 0$$

In the occurrence of a first-order phase transition from a low temperature phase $\alpha$ to a high temperature phase $\beta$ in which there is a coexistence of two phases of the same substance in equilibrium at given conditions of constant $T$ and $x_i$,

$$dG = \mu^\alpha dN^\alpha + \mu^\beta dN^\beta = 0 \quad \rightarrow \quad \mu^\alpha = \mu^\beta \tag{2.20}$$

where $dN^\alpha = -dN^\beta$ because we have considered that the total number of particles $N = N^\alpha + N^\beta$ is fixed. $\mu^\alpha$ and $\mu^\beta$ are the chemical potentials for each of the two phases and at the phase transition they have equal values. When there is coexistence of the two phases, each phase must have the same Gibbs free energy ($G^\alpha = G^\beta$) or otherwise the mixed system would not be stable and the only remaining phase would be the one with the lowest value of $G$. We can consider now an infinitesimal change in the imposed conditions ($T$, $x_i$) in which the coexistence of the two phases is still stable so that the system moves along the *coexistence line* in the phase diagram. Both phases must still have the same Gibbs free energy. Consequently, $dG^\alpha = dG^\beta$ and

$$-S^\alpha dT - {X_i}^\alpha dx_i = -S^\beta dT - {X_i}^\beta dx_i$$

$$\boxed{\frac{dx_i}{dT} = -\frac{\Delta S_t}{\Delta X_{it}}} \tag{2.21}$$

where $\Delta S_t = S^\beta - S^\alpha$ and $\Delta X_{it} = X^\beta - X^\alpha$ are the transition entropy change and the change in conjugate displacement at the transition, respectively. Equation (2.21) is the **Clausius-Clapeyron equation** in a general form and defines the phase coexistence curve in a $x_i - T$ diagram.

If the process is endothermic (exothermic), the particles have an entropy change $\Delta S_t$ due to a heat $Q$ absorption (release) as:

$$Q = \Delta H_t = T\Delta S_t \tag{2.22}$$

which is identified as the latent heat of the transition and it has a direct correspondence with the enthalpy change of the transition $\Delta H_t$ since the absorbed (released) heat occurs at constant temperature and field.

In particular, the Clausius-Clapeyron equation takes the following form when specifying each pair of conjugate variables which will be of our interest in this dissertation:

$$\frac{\mu_0 dH}{dT} = -\frac{\Delta S_t}{\Delta M_t}; \qquad \frac{dE}{dT} = -\frac{\Delta S_t}{\Delta P_t}; \qquad \frac{dp}{dT} = \frac{\Delta S_t}{\Delta V_t}; \qquad \frac{d\sigma}{dT} = -\frac{\Delta S_t}{\Delta \varepsilon_t} \tag{2.23}$$

which are frequently used expressions for the description of caloric effects.

Actually, as will be clarified in the following subsection, the expressions (2.21) and (2.23) can be considered as the previously presented Maxwell relations written in (2.4), (2.5), and (2.6) for the particular case of an ideal first-order transition in which the displacement $X_i$ exhibits a discontinuity at the transition [13].

### 2.2.2 First-order transitions for caloric effects

Giant caloric effects can arise from the possibility of field-inducing the large entropy change associated with a first-order transition. Following the description of an ideal first-order transition, the discontinuity in $X_i$ of magnitude $\Delta X_{it}$ exhibited at the transition temperature $T_t$ (see figure 2.2) can be expressed in terms of a Heaviside step function $h(T - T_t)$:

$$X_i = X_{i0} + \Delta X_{it} h(T - T_t) \tag{2.24}$$

where $X_{i0}$ is the value of $X_i$ close to $T_t$ in the $\alpha$ phase.

Introducing this expression into equation (2.8) and assuming that $\Delta X_{it}$ is independent of the field $x_i$, the following expression for the entropy change is obtained [13]:

$$\Delta S = \begin{cases} -\Delta X_{it} \dfrac{dx_i}{dT_t} & \text{for } T \in [T_t(0), T_t(x_i)] \\ 0 & \text{for } T \notin [T_t(0), T_t(x_i)] \end{cases} \tag{2.25}$$

Table 2.3 Sign of the main parameters related to conventional and inverse calorics effects. The change in the displacement $X_i$ within the first-order transition $\Delta X_{it}$, the sensitivity of the transition to the applied field $\frac{dT_t}{dx_i}$, the field-induced isothermal entropy change $\Delta S$, and the adiabatic temperature change $\Delta T$.

| Caloric effect | $\Delta X_{it}$ | $\frac{dT_t}{dx_i}$ | $\Delta S$ | $\Delta T$ |
|---|---|---|---|---|
| **Conventional** | - | + | - | + |
| **Inverse** | + | - | + | - |

Considering equations (2.21) and (2.25) it is clear that under these particular conditions there is a direct correspondence between the Clausius-Clapeyron equation and the Maxwell relations. In addition, it is worth noting that the field-driven entropy change coincides with the transition entropy change $\Delta S = \Delta S_t$, which usually sets an estimate of the maximum boundary of the magnitude of the caloric effect in real materials.

As it has been shown, the Clausius-Clapeyron equation becomes an important tool for relating key parameters of the caloric effect. On the one hand, a caloric effect of giant magnitude will require large values of $\Delta S_t$. On the other hand, the transition temperature $T_t$ must also display a sufficiently strong sensitivity with the applied field $x_i$ which leads to an enhancement of the interval at which the caloric effect takes place $[T_t(0), T_t(x_i)]$. In particular, this requires sufficiently high values of $\frac{dT_t}{dx_i}$ which are achieved for large values of $\Delta X_{it}$.

From the thermodynamic point of view, we can distinguish two kinds of caloric effects as a function of the sign of $\Delta X_{it}$: the **conventional caloric effect** for $\Delta X_{it} < 0$, and the **inverse caloric effect** for $\Delta X_{it} > 0$. From equations 2.8, 2.9, and 2.21 it is straightforward to certify that the two types of caloric effects have opposite features, as indicated by the table 2.3. A conventional caloric effect is associated with a shift of $T_t$ towards higher values under the influence of the field $x_i$. Hence, the low temperature phase ($\alpha$) is energetically favoured upon application of $x_i$, which yields to a loss of entropy in the system ($\Delta S < 0$) if the transition $\beta \rightarrow \alpha$ is field-driven ($0 \rightarrow x_i'$). In contrast, in an inverse caloric effect the application of $x_i$ favours the high temperature phase $\beta$, resulting in a shift of $T_t$ towards lower values and a gain of entropy ($\Delta S > 0$) as the field is applied, which drives the $\alpha \rightarrow \beta$ transition. Figure

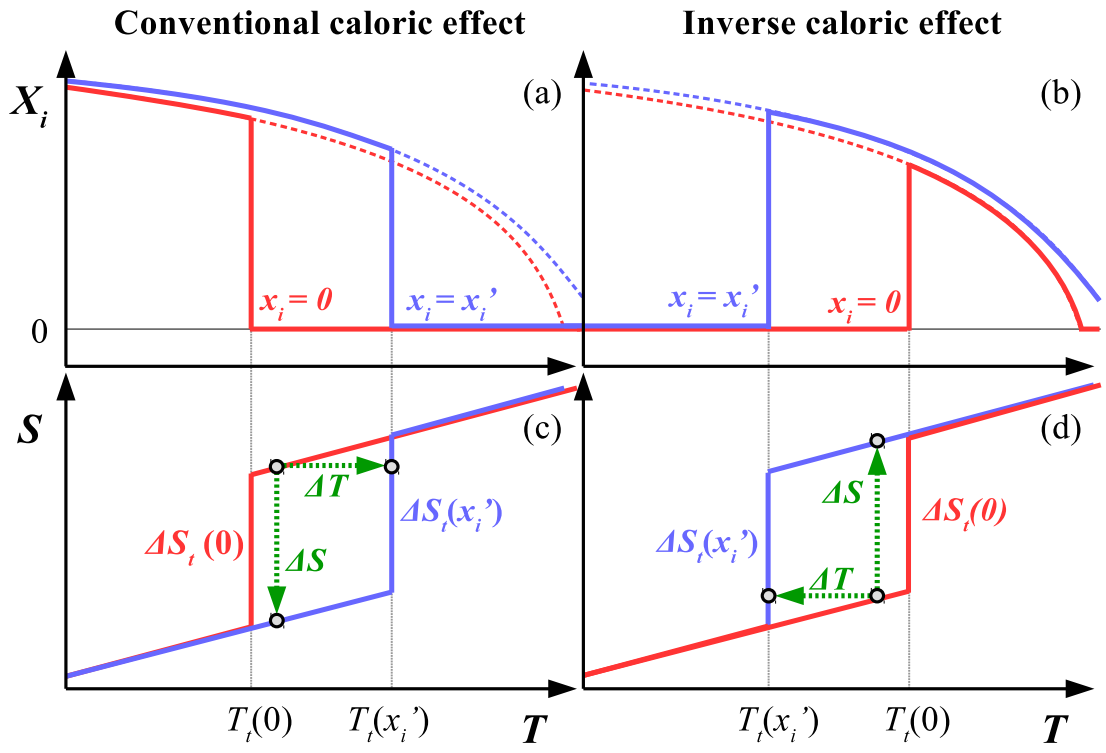


Fig. 2.3 Diagrams illustrating the behaviour of the displacement $X_i$ in absence of fields (solid red line) and under the influence of the conjugate field $x_i = x_i'$ (solid blue line) in the case of a material exhibiting a conventional caloric effect (a) and an inverse caloric effect (b) in the vicinity of an ideal first-order transition. The corresponding diagrams of the entropy curves are illustrated in (c) and (d), respectively. Green arrows indicate the adiabatic temperature change and the isothermal entropy change values upon application of field $0 \rightarrow x_i'$.

2.3 displays the behaviour of $X_i$ of an illustrative system[4] in the occurrence of a conventional (a) and an inverse (b) caloric effect, and the associated entropy curves $S(T,x_i)$ in (c) and (d). In panel (b) the system also exhibits a second-order transition in the high temperature region, as evidenced by the curve at $x_i = 0$ and the continuous variation of $X_i$ toward zero.

At this point, it is worth mentioning the different contributions which come into play to the total entropy $S$ of a magnetic system for the simplified case in which they can be separated as a sum of independent terms [39, 40]:

$$S(T,x_i) = S_m(T,x_i) + S_l(T,x_i) + S_e(T,x_i) \tag{2.26}$$

where $S_m$, $S_l$, and $S_e$ are the magnetic, lattice and electron contributions, respectively. As mentioned in the beginning of this section, in the occurrence of a phase transition $\alpha \rightarrow \beta$ a material can loose entropy from a particular degree of freedom upon heating if it is compensated by the other entropic contributions so that the total entropy change increases, as required. In fact, this explains qualitatively why materials can exhibit inverse caloric effects in which, for example, a material is able to cool down ($\Delta T < 0$) or gain entropy ($\Delta S > 0$) when hydrostatically compressed [41] or by application of a magnetic field [42], even though there is a reduction of the lattice contribution or the magnetic contribution to the total entropy upon driving the transition, respectively.

So far we have considered the simplified case of an ideal first-order transition. First-order transitions typically take place with hysteresis, which is a characteristic feature of this class of transitions. As the field $x_i$ is applied or removed in the vicinity of a first-order transition the system does not transform at the equilibrium point where $\Delta G = 0$ and follows metastable states which yield to irreversibilities. This is illustrated in figure 2.4 which plots the Gibbs free energy of an indicative system undergoing a first-order phase transition between $\alpha$ and $\beta$ phases, which minimize the energy for low and high values of the fields $(x_1, x_2)$, respectively. In particular, when the transition is thermally driven this out-of-equilibrium phenomena yield to supercooling and superheating processes and the transition does not occur at the same temperature $T_t$ upon cooling and heating, but at $T_{tc} < T_t$ and $T_{th} > T_t$, respectively. Furthermore, first-order phase transitions in real materials usually do not occur abruptly and spread over a temperature range. This is explained by a number of factors, such as composition gradients, impurities or lattice defects. With regard to the thermal response upon field cycling, these factors are drawbacks to be minimized as they reduce the caloric performance of a given material. Their consequences will be discussed in detail along the thesis.

[4] The plots are inspired for the typical case described in chapter 5 of a Heusler alloy exhibiting a martensitic transition, in which $(x_i, X_i) = (H, M)$.

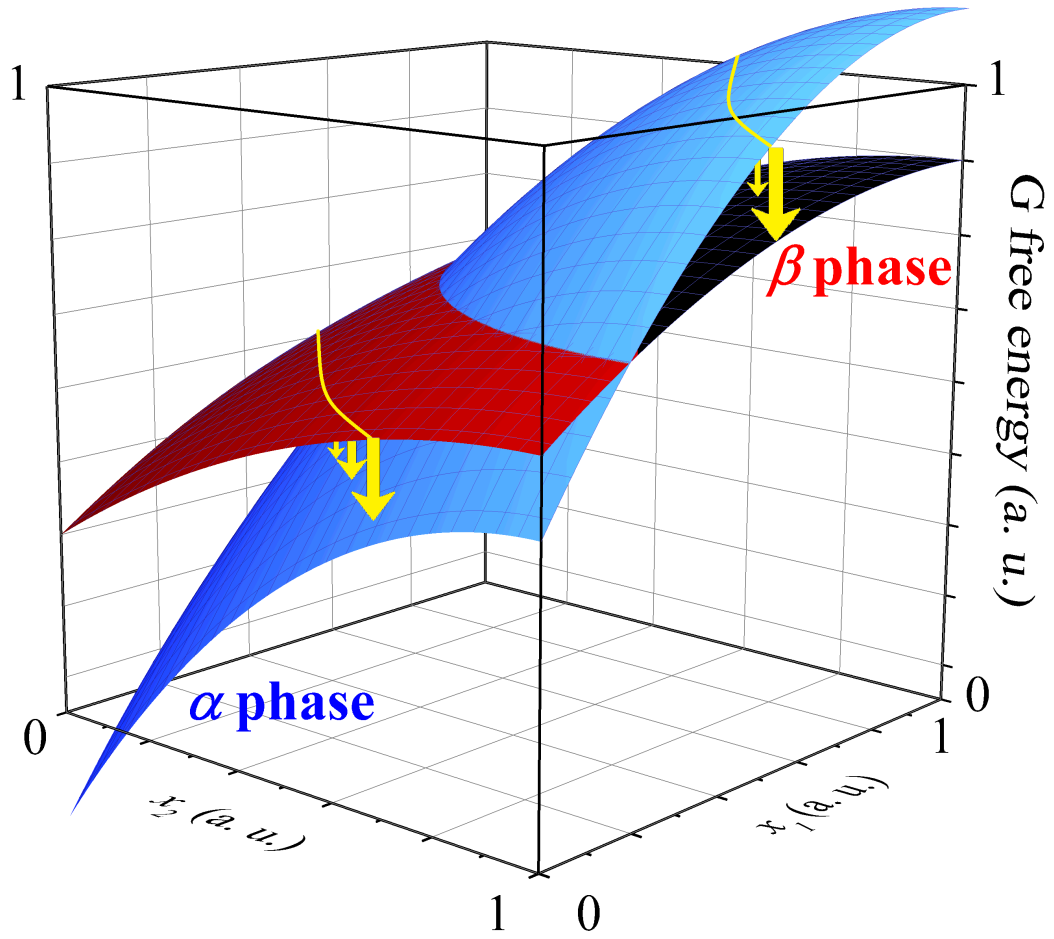


Fig. 2.4 Diagram of the Gibbs free energy $G(x_1, x_2)$ of an illustrative physical system undergoing a field-driven first-order phase transition. The energy of the $\alpha$ and $\beta$ phases are plotted by the blue and red surfaces. Upon applying or removing each field the phase transition does not occur at the intersection of the two surfaces at which $\Delta G = 0$, but at the yellow $(x_1, x_2)$ curves.

In comparison to first-order transitions, the features associated with second-order transitions typically yield to caloric effects of lower magnitude over a larger temperature interval due to the minor values of the caloric response functions $\left(\frac{\partial X_i}{\partial T}\right)_{x_i}$ and the broader temperature region at which the conjugate displacement $X_i$ varies. Interestingly, the lack of hysteresis in this class of transitions drastically reduces the irreversible contributions. As will be seen, materials displaying first-order transitions which are close to the limit of being second-order can be excellent candidates to exhibit giant caloric effects, as they still have an associated latent heat and display a reduced hysteresis.

### 2.2.3 Parameters for the characterization of giant caloric effects

A complete characterization of a field-driven giant caloric effect requires the knowledge of a number of parameters which quantify the thermal response from different perspectives. In addition to considering $\Delta S$, $\Delta T$, and the exchanged heat $Q$ values which quantify the caloric response in absolute terms, it is usually convenient to refer to the **caloric strength** for a proper comparison with the caloric performance of other reported materials with independence of the magnitude of the applied field. The caloric strength stands for the normalization of these values as a function of the applied field, i.e. $\frac{|\Delta S|}{|\Delta x_i|}$, $\frac{|\Delta T|}{|\Delta x_i|}$, and $\frac{|Q|}{|\Delta x_i|}$. As previously explained, the caloric effect arising in the vicinity of a first-order transition tends to saturate at certain values when the applied field is large enough. Once the caloric effect saturates, larger values of the applied will generally yield to an underestimation of the caloric strength since they will not increase the magnitude of $\Delta S$, $\Delta T$, and $Q$.

The **work** performed by the applied field on the system which is required for driving the thermal response is a key feature. The previously presented table 2.1 lists the expressions of the various forms of work related to each pair of conjugate variables. For the case of the MCE, we can distinguish two procedures for driving the caloric response. On the one hand, we can consider the *electrical work* needed for the generation of the applied magnetic field by varying the current through a solenoid in which the sample is located at its bore ($dW = \mathbf{H} \cdot d\mathbf{B}$). On the other hand, the *mechanical work* refers to the change of the applied magnetic field achieved by the relative motion of the sample with respect to a permanent magnet ($dW = -\mu_0 \mathbf{M} \cdot d\mathbf{H}$). In the case of the ECE, the electrical work refers to the typical case in which the electric field is generated by varying the charge of a capacitor through which the sample is enclosed ($dW = \mathbf{E} \cdot d\mathbf{D}$). In contrast, the mechanical work refers to the less likely procedure consisting on the variation of the electric field by the relative motion of the sample with respect to the capacitor ($dW = -\mu_0 \mathbf{P} \cdot d\mathbf{E}$) [43]. In the case of the mCE, the general expression for the mechanical work is given by $dW = V\boldsymbol{\sigma} \cdot d\boldsymbol{\varepsilon}$. In the particular

cases[5] of the application of an uniaxial stress $\sigma_{\hat{x}}$ along the $\hat{x}$ direction (eCE) it is expressed as $V\sigma_{\hat{x}}d\varepsilon_{\hat{x}}$; and for the application of a hydrostatic pressure (BCE), $dW = -pdV$.

In this connection, it is convenient to define the **efficiency** [44], $\eta = \dfrac{|Q|}{|W|}$, which stands for the fraction between the exchanged heat under isothermal conditions and the energetic cost of driving the caloric effect represented by the value of the work $W$ [43, 44].

The **refrigerant capacity** (RC) (also referred as the relative cooling power, RCP) provides an estimate of the transferred heat from the cold end ($T_{cold}$) to the hot end ($T_{hot}$) during a cooling cycle of a refrigerator [45] and is calculated as [46]:

$$\mathrm{RC}(T,x_i) = \int_{T_{cold}}^{T_{end}} \Delta S(T,x_i)dT \tag{2.27}$$

In this regard, the RC value is commonly estimated as $\mathrm{RC} = \Delta S \cdot \delta T_{FWHM}$, where $\Delta S$ stands for the peak value of the field-driven entropy change and $\delta T_{FWHM}$ is its full width at half maximum. The value of $\Delta T_{FWHM}$ can be considered to be a good approximation of the temperature span between the cold and the hot reservoirs ($T_{hot} - T_{cold}$). It is worth mentioning that the behaviour of the $\Delta S$ peak can significantly differ upon field cycling, as it is going to be discussed in this thesis. These non-reversible phenomena are usually omitted in the scientific publications. To avoid confusion in this respect it is convenient to define the *effective refrigerant capacity*, $\mathrm{RC}_{\mathrm{eff}}$, which takes into account these hysteresis losses and strictly refers to the reversible component of the RC [47, 48].

[5] The appendix A provides a description of the variables related to the mCE and the particular conditions associated with the eCE and the BCE.

# Chapter 3

# Experimental techniques

The experimental methods for characterizing the giant caloric effects are aimed at evaluating the temperature change $\Delta T$, the entropy change $\Delta S$ and the heat exchange $Q$ in the vicinity of a first- or second-order transitions by application of one or multiple fields. We can classify these experimental methods depending on the measurement technique used for the characterization of the thermal response.

- **Direct methods** involve the direct evaluation of the thermal response and require especially designed experimental systems for the quantification of $\Delta T$, $\Delta S$ and $Q$. Direct methods are highly convenient since they provide the most reliable evaluation of the caloric response and they are very helpful for the development of physical models which fit the experimental data. However, the particular experimental design in each case can be especially challenging. Usually one has to deal with problems like solving the heat leaks between sample and surroundings, ensuring a proper thermal contact or tracking the sample temperature and the heat exchanges in the required thermodynamic conditions when the applied field is scanned either adiabatically or isothermally.

- **Quasi-direct methods** provide estimates of $\Delta T$, $\Delta S$ and $Q$ values from heat flux and/or heat capacity measurements. The caloric effect is not directly measured from a field driven thermal response and is usually estimated from the subtraction of the entropy curves which have been built from calorimetric data: $\Delta S(T, 0 \rightarrow x_i') = S(T, x_i') - S(T, 0)$ [41, 49, 50]. In this regard, we may also distinguish at this point the reports providing the values which are obtained from the heat capacity $C$ data by the use of the following approximation[1]:

$$\Delta S \sim \int_{T_s}^{T_f} \frac{[C(T,x') - C(T,0)]dT}{T} \tag{3.1}$$

where $T_s$ and $T_f$ bound the temperature range at which the caloric effect takes place by application of the field $0 \rightarrow x'$.

- **Indirect methods** rely on the field and temperature dependences of the order parameter $X_i$ at the transition temperature range and the consequent thermodynamic analysis for the derivation of $\Delta T$, $\Delta S$ and $Q$ values. They involve the application of the Maxwell relations or the Clausius-Clapeyron relation if the transition is first-order as described in the previous chapter. However, the singular behaviour of $X_i$ at the phase transition requires an accurate measurement of its temperature and field dependence and particular attention must be paid to the use of the thermodynamic relations in hysteretic regimes [51]. In addition, the expressions for $\Delta T$ obtained by Maxwell relations require information on the temperature and field dependence of the heat capacity $C(T, x_i)$ as indicated by equation (2.9).

## 3.1 Calorimetric techniques

In the present thesis, the development of especially designed calorimetric techniques has taken an important role since they represent an optimal tool for the characterization of the thermal response in solids. Calorimetry is devoted to measure the exchanged heat between a sample and its surroundings under the influence of external stimuli. In this sense, the different varieties of calorimetric techniques enable the measurement of heat flow rates, specific heat, latent heat as well as transition temperatures and other related parameters which characterize the phase transitions and the thermal properties.

As expected, the history of calorimetric techniques is directly linked to the progress of the theory of heat. One of the first set-up for the measurement of heat was built by Antoine Lavoisier and Pierre-Simon Laplace in the winter of 1782-83. In short words, their ice calorimeter was basically a vessel with different shells filled with ice which covered an inner vessel in which a hot object was placed. The measurement of heat was inaccurately performed by weighting the drained water from the melted ice and, thus, making use of the latent heat of its fusion [52]. Previously, the Scottish chemist Joseph Black realized that the transfer of heat to ice at its melting point and to water at its boiling point does not cause any temperature increment and, hence, he concluded that this transferred energy must be stored in matter in the form of latent heat. To be precise, he based his reasoning on the fact that something expected did not happen. He expected that any small heat quantity transmitted to ice had to entirely melt the system and raise its temperature somehow, but he realized that most of the ice remained at 0 ºC with some additional melted water. "The dog that did not bark" when it was expected to do so, he argued [53]. Calorimetric techniques began to take

relevance in the mid eighteenth century with the experimental contributions of James Joule in understanding heat as a form of energy which can have different physical origins and not of matter [52].

Up to now, a long list of calorimeters have been designed and they can be classified in several ways according to different criteria. However, it is very difficult to establish a simple criterion for classifying the calorimeters because in every classification there are given calorimeters which do not match to a particular category or match with more than one designated category [54, 55]. In our case, we will classify them in two groups as a function of their operating methods [56]. On the one hand, several calorimeters work by continuously scanning temperature and measure the heat flux between the sample and a thermal block. These are the *scanning calorimeters*. Calorimeters of this kind have been developed for this dissertation with the particular availability of measuring the heat flow under the application of externals fields $x_i$. On the other hand, other devices keep the thermal block under isothermal conditions and small amounts of heat are supplied to the sample while its temperature is being measured (adiabatic calorimetry, relaxation calorimetry, and ac calorimetry). Additionally, in some cases the device combines both operating methods, which is the case for the modulated differential scanning calorimeters (MDSC) described in section 3.8.

### 3.1.1 Differential Scanning Calorimetry

The present chapter describes a set of Differential Scanning Calorimetry (DSC) devices which have been inspired with the ideas described in [56, 57]. The main concepts of the developed DSC technique are explained in this section and the particular features of each calorimeter are described in the following sections.

A differential method is an experimental method in which the measured quantity is compared with a quantity of the same kind with slightly different magnitude so that the difference between the two values is evaluated. DSC devices are especially designed with symmetry considerations (twin-type design) so that the two measuring sensors can reasonably be at approximately the same physical conditions. This measurement method involves that perturbations like temperature variations must affect both values similarly, at least at a first approximation, because they are compensated when the differential value is obtained [58].

If the temperature of the calorimeter ($T_0$) is linearly scanned ($T_0(t) = T_0(t=0) + \dot{T}_0 \cdot t$, where $\dot{T}_0 = \dfrac{dT_0}{dt}$ is the scanning rate), the contributions taking part in the measured heat flow $\dfrac{dQ}{dt}$ can be separated as:

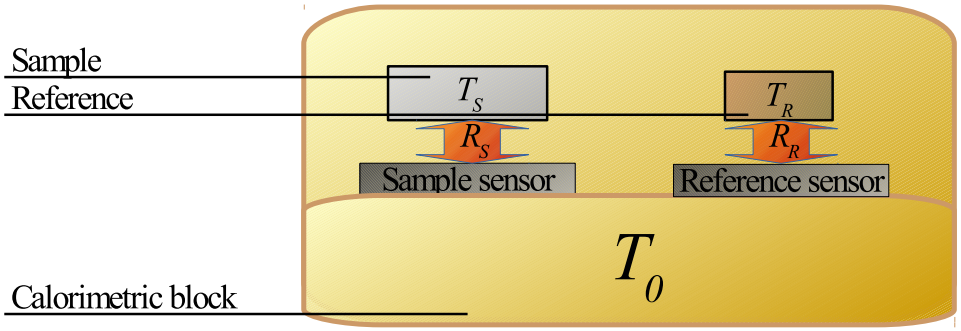


Fig. 3.1 Sketch of a DSC setup illustrating the calorimetric block at temperature $T = T_0$, the sample at $T_S$ and the reference at $T_R$. $R$ stands for the thermal resistance of the medium.

$$\frac{dQ}{dt} = \frac{dQ_0}{dt} + \frac{dQ_{C_p}}{dt} + \frac{dH_t}{dt} \tag{3.2}$$

where $\frac{dQ_0}{dt}$ refers to an unavoidable asymmetric term of the calorimeter which has to be minimized, $\frac{dQ_{C_p}}{dt}$ is the difference in heat capacity contributions between the sample and an inert reference, and $\frac{dH_t}{dt}$ is the enthalpy contribution if the sample exhibits a first-order transition. Our analysis will always be restricted to the quasi-static approximation so that the sample has to be able to follow the temperature profile of the calorimetric block and there are no temperature gradients among the sample. In this sense, care must be taken sometimes because the thermal diffusivity of the sample and its size can hinder the experiment performance if the temperature is scanned too fast, which might be the case when measuring with commercial calorimetric equipments which can achieve fast rates as well as for the temperature-modulated DSC (MDSC) discussed in section 3.8.

Let us specify the origin of the measured heat flow in the purpose-built calorimeters step by step. As illustrated in figure 3.1, in our case the differential method consists in the measurement of the temperature difference $T_S - T_R$ between the sample under study ($T_S$) and an inert reference ($T_R$) while temperature of the calorimetric block ($T_0$) is scanned at a rate $\dot{T}_0 = \frac{T_0}{dt}$ and the other fields are kept constant.[1] By assuming thermal Ohm's law the heat flow $\frac{dQ}{dt} \equiv \dot{Q}$ in response to a temperature gradient $\Delta T$ can be expressed as: $\dot{Q} = \frac{\Delta T}{R}$, which

[1] Please note that the analysis here is restricted to calorimetric runs driven by temperature scans, although that the developed devices have the availability to perform calorimetric runs driven by either electric field or magnetic field as discussed at the end of the present section.

states a proportionality relation between both quantities defined by thermal resistance $R$ of the medium.

If the sample exhibits a first-order transition with a certain enthalpy change $\Delta H_t$, the equations for the thermal balance will be written as:

$$\frac{dH}{dt} = C_S \frac{T_S}{dt} + \frac{T_S - T_0}{R_S} \tag{3.3}$$

$$0 = C_R \frac{dT_R}{dt} + \frac{T_R - T_0}{R_R} \tag{3.4}$$

where (3.3) refers to the heat flow between the sample and the calorimetric block and (3.4), to the heat flow between the reference and the block. $R_S$ and $R_R$ are the corresponding thermal resistances in each medium; and $C_S$ and $C_R$, the heat capacities of the sample and the reference, respectively.

We can assume that both sample and reference have the same thermal resistance $R_S \sim R_R \equiv R$ and that $\frac{dT_S}{dt} \sim \frac{dT_R}{dt} \sim \dot{T}_0$ if the temperature scan is performed at moderate rates. With this in hand, subtraction of (3.4) from (3.3) leads to the following expression for the temperature difference between sample and reference:

$$T_S - T_R = R \left[ \frac{dH}{dt} + (C_R - C_S)\, \dot{T}_0 \right] \tag{3.5}$$

The differentially connected calorimeter sensors provide an electric output $Y$ which is proportional to the expression in (3.5) as $Y = B(T_S - T_R)$, where $B$ is the device proporcionality factor. The particular sensitivity $S = BR$ of the calorimeter calibrates the electric output into heat flow as $\dot{Q} == \frac{dQ}{dt} = \frac{Y}{S}$. With this in hand, equation (3.5) is rewritten as

$$\dot{Q} = \frac{dH}{dt} + (C_R - C_S)\, \dot{T}_0 \tag{3.6}$$

It can be convenient to rescale the heat flow as $\frac{dQ}{dT} = \frac{\dot{Q}}{\dot{T}_0}$, where $\dot{T}_0 = \frac{dT}{dt} = \frac{dT_0}{dt}$. Equation (3.6) is rewritten as:

$$\frac{dQ}{dT} = \frac{dH}{dT} + (C_R - C_S) \tag{3.7}$$

where $\frac{dH}{dT} = \frac{dH}{dt} \dot{T}_0^{-1}$. In particular, expression (3.7) has discarded any dependence on the heating or cooling rate of the measurement. This independence on the scanning rate can be helpful when comparing thermograms and identifying the thermal events.

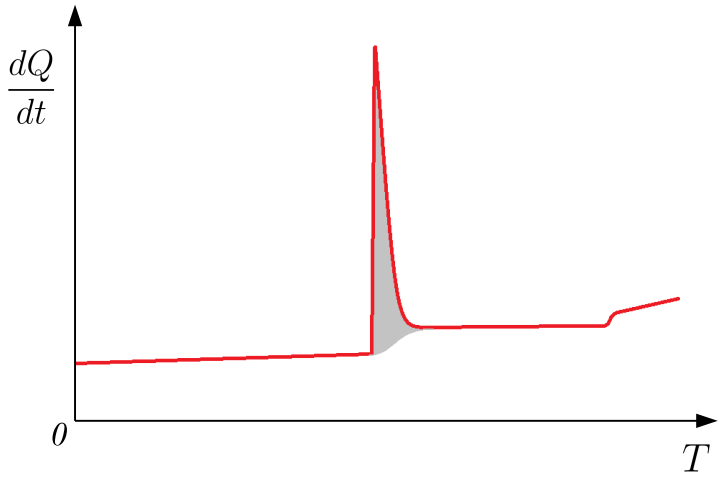


Fig. 3.2 Illustrative thermogram (red line) displaying two thermal events: a first-order transition (peak) and a second-order transition at high temperatures associated with the change of baseline drift in the thermogram . The grey area inside the peak computes for the transition enthalpy and entropy changes by the baseline integration expressed in equations (3.10) and (3.11).

In the absence of first-order transitions, $\frac{dH}{dt} = 0$ and the obtained heat flux is drift from the zero in dependence of the difference between heat capacities $C_R - C_S$. Since the reference is taken so that $C_R$ does not exhibit any abrupt change within our calorimeter operating range, the resulting thermograms will reveal clear information related to the enthalpy change of the first-order transitions and any change on $C_S$. In general, the quantity $C_R - C_S$ will not vary significantly as a function of temperature and, hence, it is expected that the thermograms show a plateau-like signal in temperature regimes away from the influence of any transition.

Second-order transitions can be identified by a feature on the thermograms due to the corresponding jump in $C_S$ as illustrated on the right hand side in the thermogram of figure 3.2. If a first-order transition takes place at a certain temperature while temperature is scanned, the factor $\frac{dH}{dt}$ takes relevance and the resulting thermogram displays a calorimetric peak as depicted in figure 3.2. In any case, the evaluation of a heat capacity change $\Delta C_S^{\alpha\to\beta} = {C_S}^{\beta} - {C_S}^{\alpha}$ at a phase transition involving the phase change $\alpha \to \beta$ can be done by a simple subtraction between the signal drift values above ($\dot{Q}^{\beta}$) and below ($\dot{Q}^{\alpha}$) the phase transition:

$$\Delta C_S^{\alpha\to\beta} = \frac{\dot{Q}^{\beta} - \dot{Q}^{\alpha}}{\dot{T}_0} \tag{3.8}$$

DSC runs allow the computation of the enthalpy and entropy change of a first-order transition by a proper integration of the first term on the right hand side in (3.6). Since $\frac{dQ}{dT}$ data in thermograms are drift from the zero, a proper baseline correction must be performed to separate the $(C_R - C_S)$ term and any asymmetric contribution of the calorimeter which is not related to the first-order transition. An accurate estimate of the behaviour of this term in the temperature range at which the integration takes place is to consider a sigmoid fit for the junction of the baseline which linearly extrapolates the trend of $\frac{dQ}{dT}$ data at the temperature range where $\frac{dH}{dt} = 0$ before and after the transition. The s-shape of the sigmoid function suits conveniently the dynamics of the transition and tailors the baseline to the corresponding change in $C_S$ due to the phase change $\alpha \rightarrow \beta$, which can be expressed as:

$$C_S = {C_S}^{\alpha}(1-\chi) + {C_S}^{\beta}\chi \tag{3.9}$$

where $\chi$ is the transformed fraction function. This function is bounded by $0 \leq \chi \leq 1$ and gives the portion of the sample which has transformed when a phase transition takes place[2], being $\chi = 0$ at a state in which the sample is fully at the low temperature phase ($\alpha$), and $\chi = 1$ at a state in which it is fully at the high temperature phase ($\beta$). Thus, if $\zeta(T)$ refers to the particular baseline function which excludes these contributions, the transition enthalpy change $\Delta H_t$ can be computed as[3]

$$\Delta H_t = H_{T_f} - H_{T_s} = \int_{T_s}^{T_f} \left( \frac{dQ}{dT} - \zeta \right) dT \tag{3.10}$$

where $\zeta \sim C_R - C_S$, and $T_s$ and $T_f$ are the starting and ending temperatures which set out the boundaries of the temperature range where $\frac{dH}{dT} \geq 0$. $H_{T_f}$ and $H_{T_s}$ are the reference enthalpy values to given states at $T_s$ and $T_f$, respectively.

The transition entropy change $\Delta S_t$ is computed analogously by considering that $dS = \frac{\delta Q}{T}$ which yields to the following expression:

$$\Delta S_t = S_{T_f} - S_{T_s} = \int_{T_s}^{T_f} \frac{1}{T} \left( \frac{dQ}{dT} - \zeta \right) dT \tag{3.11}$$

where $S_{T_s}$ and $S_{T_f}$ are the reference entropy values to given states at $T_s$ and $T_f$, respectively. Particularly, if the ending temperature $T_f$ of the integral is replaced by any other arbitrary

[2]Please note that $\chi$ is usually the fraction by weight because entropy and enthalpy is commonly expressed in mass units.

[3]In general, $\zeta$ function is omitted in the expressions of the literature when stated that the integration is performed by the baseline subtraction.

value $T'$ within the transition temperature range the expression (3.11) can be used to track the transition entropy change referenced to $S_{T_s}$:

$$S_{T'} - S_{T_s} = \int_{T_s}^{T'} \frac{1}{T}\left(\frac{dQ}{dT} - \zeta\right) dT \tag{3.12}$$

The entropy change $S_{T'} - S_{T_s}$ emerges from the sample fraction which transforms from the phase $\alpha$ to the phase $\beta$ and, thus, it can be expressed as $S_{T'} - S_{T_s} = \chi(T')\Delta S_t$, At this point we can easily compute the transformed fraction $\chi$ as:

$$\chi(T') = \frac{S_{T'} - S_{T_s}}{\Delta S_t} = \frac{\int_{T_s}^{T'} \frac{1}{T}\left(\frac{dQ}{dT} - \zeta\right) dT}{\Delta S_t} \tag{3.13}$$

The current analysis has been focused so far under the consideration that temperature is the only scanning field which drives the transition. The vast majority of calorimeters are designed with this purpose. However, the completion of the objectives set for this dissertation has required the development of calorimeters with the availability to work under the influence of other fields $\{x_i\}$. Thus, calorimetric techniques can be conceived with other scanning field than temperature while the rest of the stimuli (including temperature) are kept constant.

Actually, the isothermal conditions in which the $x_i$ scans are performed must be considered as quasi-isothermal. The application (or removal) of the field does produce modest temperature gradients in the setup which are, in fact, needed for the measurement of the heat flow. In this case, the field is scanned at rate $\frac{dx_i}{dt}$ and the equations for the thermal balance written in (3.3) and (3.4) remain valid. We assume again that the thermal resistances are the same $R_S \sim R_R \sim R$ and we rewrite expression (3.6) as:

$$T_S - T_R = R\left[\frac{dH}{dt} + C_R\frac{dT_R}{dt} - C_S\frac{dT_S}{dt}\right] \tag{3.14}$$

We use the sensitivity $S(T,x_i)$ of the calorimeter for the $T_S - T_R \rightarrow Y \rightarrow \dot{Q}$ conversion. The calorimeter must be previously calibrated and an accurate evaluation of the field and temperature dependence of sensitivity $S(T,x_i)$ is required. Now, equation (3.14) is transformed to:

$$\dot{Q} = \left[\frac{dH}{dt} + C_R\frac{dT_R}{dt} - C_S\frac{dT_S}{dt}\right] \tag{3.15}$$

In absence of any transition both sample and reference typically exhibit a marginal field induced thermal response and the last two terms in equation (3.15) are significantly low in comparison to the $(C_R - C_S)\dot{T}_0$ term in equation (3.6).

Again, it is useful to express the heat flow $\dot{Q}$ in equation (3.15) as $\frac{dQ}{dx_i} = \frac{dQ}{dt}\left(\frac{dx_i}{dt}\right)^{-1}$ which allows a better comparison between thermograms with independence of the scanning rate $\frac{dx_i}{dt}$. Therefore, equation (3.15) is now written as

$$\frac{dQ}{dx_i} = \frac{dH}{dx_i} + C_R\frac{dT_R}{dx_i} - C_S\frac{dT_S}{dx_i} \tag{3.16}$$

If a phase transition takes place a baseline integration of the peak is performed by analogy with the previously explained case in which temperature is scanned. The field driven $x_{is} \rightarrow x_i{}'$ enthalpy and entropy changes are expressed as

$$H_{x_i{}'} - H_{x_{is}} = \int_{x_{is}}^{x_i{}'} \left(\frac{dQ}{dx_i} - \zeta\right) dx_i \tag{3.17}$$

$$S_{x_i{}'} - S_{x_{is}} = \int_{x_{is}}^{x_i{}'} \frac{1}{T}\left(\frac{dQ}{dx_i} - \zeta\right) dx_i \tag{3.18}$$

where $\zeta \sim C_R\frac{dT_R}{dx_i} - C_S\frac{dT_S}{dx_i}$ and $x_{is}$ is the starting field at which the transition take place.

### Construction of the entropy curves $S(T, x_i')$

Interestingly, calorimetry under applied fields can provide an accurate estimate of the entropy curves $S(T,x_i')$ as a function of temperature at selected values of the applied field $x_i$. With equations (2.7), (3.12) and (3.13) in hand and heat capacity $C_S$ data, each entropy curve can be built from the thermogram obtained by scanning temperature at constant applied field $x_i$ (*isofield measurements*) as expressed in the following expression:

$$S(T,x_i') - S(T_0,x_i') = \begin{cases} \displaystyle\int_{T_0}^{T} \frac{C_S^{\alpha}}{T} dT & T \leq T_s \\ \displaystyle S(T_s,x_i') + \int_{T_s}^{T} \frac{1}{T}\left[\left((1-\chi)C_S^{\alpha} + \chi C_S^{\beta}\right) + \frac{dQ}{dT}\right] dT & T_s < T \leq T_f \\ \displaystyle S(T_f,x_i') + \int_{T_2}^{T} \frac{C^{\beta}}{T} dT & T_f < T \end{cases} \tag{3.19}$$

where $S(T_0,x_i')$ is the entropy at a given state at $T_0$ and field $x_i = x_i'$ which is used as a reference value for the entropy curve construction. Three temperature ranges are distinguished from the expression (3.19). On the one hand, in regions above and below the boundaries of the transition temperature range specified by $\left[T_s, T_f\right]$ the entropy is computed by integrating

$dS = \frac{C}{T}dT$ as expressed in (2.7). On the other hand, the entropy curve within the transition range must account for the additional entropic contribution expressed in (3.12).

### Measurement protocols for isothermal calorimetric measurements

The present section has outlined so far the computational methods of relevant parameters when characterizing the field induced caloric effects in solids obtained from calorimetric techniques under applied fields $\{T, x_i\}$. The special conditions forced by the metastabilities inherent to first-order transitions and the corresponding irreversibilities have direct consequences on the caloric response of the studied systems. Accordingly, one has to follow a detailed measurement protocol for a proper characterization of the thermal response of the solid.

Particularly, isothermal measurements in which the applied field is swept require a specific protocol which takes into account the thermal history of the samples for a proper separation of the reversible and irreversible contributions to the caloric effects which depend on how the field and temperature loops are applied, as illustrated in figure 3.3. The protocol involves the realization of specific thermal excursions which bring the system to a specific state at which the measurement starts. The two experimental protocols shown in figure 3.3 depend on whether the caloric effect is conventional or inverse which define the thermal excursions to be performed before the field $x_i$ is isothermally cycled. A general description is made by considering a material exhibiting a first-order phase transition from a low-temperature $\alpha$ phase to a high-temperature $\beta$ phase in which $X_i$ is the associated order parameter. As explained in section 2.2.2, the effect is conventional (inverse) if $X_i$ is maximized in the $\alpha$ phase ($\beta$ phase). The field induced changes in the conjugate displacement ($\Delta X_i$) are illustrated in figure 3.4 in each case. As shown in this figure, the magnitude of $\Delta X_i$ clearly depends on the metastabilities path and its value upon first application of the field can significantly differ from the subsequent scans. Therefore, the magnitude of the caloric effect is also expected to significantly vary upon cycling. With this in hand, two protocols are specified as follows:

- **Protocol 1**. A thermal excursion in absence of applied field, $x_i = 0$, to a temperature in which the system is fully at the phase in which $X_i$ is minimized.
- **Protocol 2**. A thermal excursion at applied field, $x_i = x_i'$, to a temperature in which the system is fully at the phase in which $X_i$ is maximized.

Subsequently, the sample is brought at moderate heating or cooling rates to the desired temperature at which the isothermal measurement is performed. After thermal stabilization, the first scan of the field $x_i$ starts at $t_s$ as shown in figure 3.3. The scanning rate must

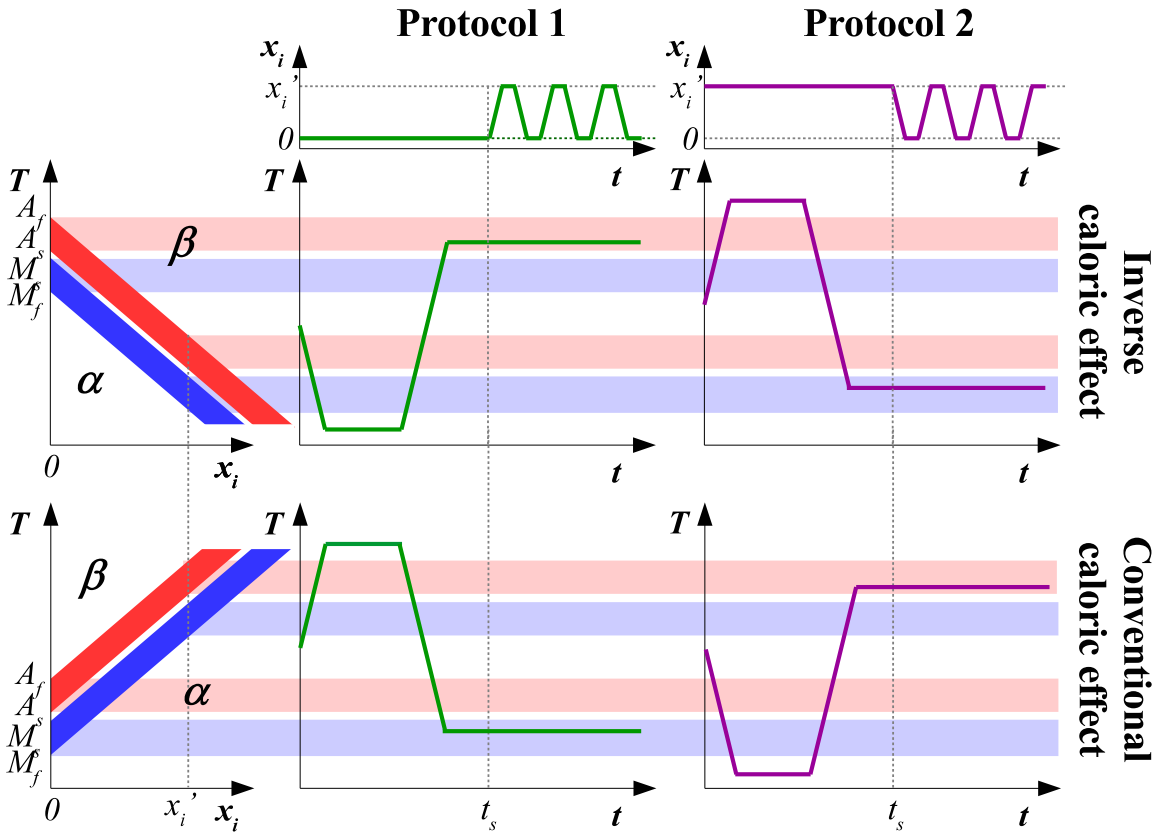


Fig. 3.3 Schematics of the protocols followed for isothermal calorimetric measurements for a material displaying either an inverse caloric effect (second row of charts) or a conventional caloric effect (third row). The first row illustrates the profile of the applied field $x_i$ for protocol 1 (left, green lines) and 2 (right, purple lines). On the left hand, the field dependence of the transition temperatures is plotted in each case. The region at which the forward transition takes place is bounded by $M_s(x_i)$, and $M_f(x_i)$ values and is painted blue whereas the red area depicts the region bounded by $A_s(x_i)$ and $A_f(x_i)$ for the reverse transition. The regions at $x_i = 0$ and at $x_i = x_i'$ are extrapolated as a guide to the eye for the plots displaying the temperature profile in each protocol. $t_s$ is the starting time of the first field scan in each protocol.

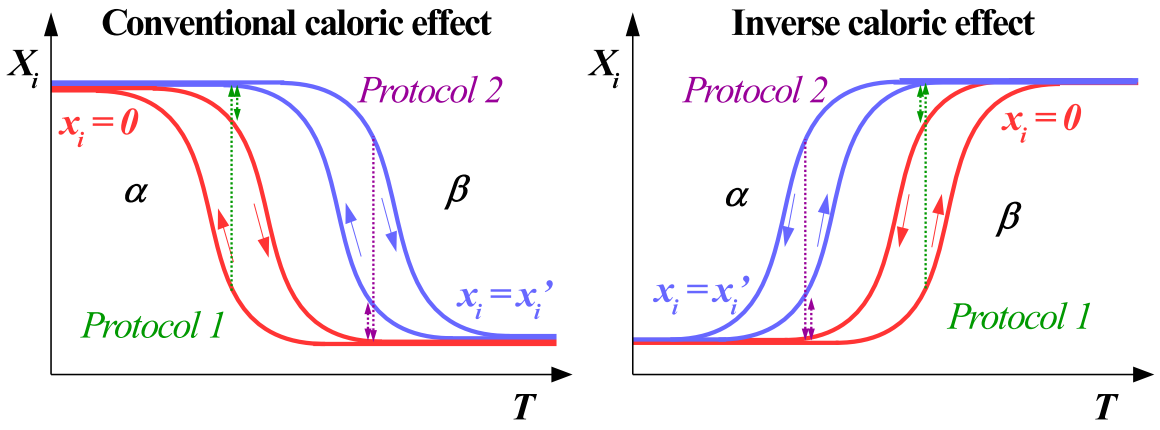


Fig. 3.4 Schematics of the protocols followed for isothermal calorimetric measurements for a material displaying either a conventional caloric effect (left) or an inverse caloric effect (right). Both plots illustrate the behaviour of the transition order parameter $X_i$ upon heating and cooling (as indicated by the arrows) at zero field (red) and at applied field $x_i = x_i'$ (blue). Dotted lines illustrate the change in $X_i$ as a consequence of the application or removal of the field $x_i$ in protocol 1 (green) and protocol 2 (purple).

be sufficiently low to ensure the quasi-isothermal conditions and avoid adiabaticities, but sufficiently high for ensuring a minimum heat exchange magnitude so that the calorimeter is sensitive enough for its measurement.

### 3.1.2 Calorimeter design

As previously stated, sample and reference need to be in the same conditions for a proper measurement of the heat flux obtained from a differential method. This involves special symmetry considerations for the design of a calorimeter in order to ensure similar field scanning rates, similar heat transfer conditions or that external perturbations affect similarly both sample and reference enclosures. The general features of the purpose-built calorimeters are listed as follows:

- The structure of the calorimeter is built from a relatively massive copper block which ensures a proper thermal inertia of the system. The block covers the whole set-up for better thermal homogeneity and minimization of air convection. Copper is a proper thermal conductor and minimizes temperature gradients.
- The inert reference is a copper specimen with a mass similar to that of the sample.

Table 3.1 Typical parameters of the operational performance of the devices for DSC under applied magnetic fields $H$ (first row) and under applied electric fields $E$ (second row): temperature and field operational range, temperature scanning rate, field scanning rate, sensitivity at 300 K, and typical sample mass.

| Field | Operational range | | $\frac{dT}{dt}$ (K/min) | $\frac{dx_i}{dt}$ | $S$(300 K) (mV/W) | Sample mass (mg) |
|---|---|---|---|---|---|---|
| $H$ | 200 - 420 K | 0 - 6 T | 0.5 | 0.2 T/min | 300 | 10 - 1000 |
| $E$ | 200 - 420 K | 0 - 1100 V | 0.5 | 0.5 V/min | 300 | 10 - 200 |

- Both sample and reference are placed on a pair of differentially connected batteries of thermocouples which act as temperature sensors. One face of each thermobattery is in contact with the calorimetric block and the other face holds either the copper reference or the sample. The thermal contact conditions are improved with silicone heat conductive paste. As a result of the thermoelectric effect, each thermobattery provides a voltage output ($V_S$ and $V_R$ for sample and reference, respectively) in proportion to the temperature gradient between both faces, $V_S \propto T_S - T_0$ $V_R \propto T_R - T_0$. The thermobatteries are connected differentially so that the final voltage output is $Y = V_S$ - $V_R = B(T_S - T_R)$. The sensitivity $S = BR = \frac{Y}{\dot{Q}}$ is a characteristic feature of the calorimeter and is obtained by calibration procedures.
- The calorimeter temperature $T_0$ is read with a Pt-100 platinum resistance embedded in the calorimetric block.

With this in hand, the following sections describe the special details of each developed calorimeter.

## 3.2 DSC under magnetic field and electric field

The present section is aimed at describing two calorimeters of similar features with the ability to work under applied magnetic field and electric field, respectively. The DSC measurements under magnetic field have been performed with a calorimeter which is an upgraded version of that described in [56] and is presented in [50]. The device is sketched in figure 3.5 and some parameters related to its operational performance are listed in table 3.1.

The calorimeter is placed on top of a closed copper container through which a cryogenic fluid circulates. The fluid temperature and flow are controlled by a Lauda proline thermal bath. The ensemble of the calorimeter and container is placed into a Dewar flask which is located into the bore (100 mm diameter) of a 6 T Cryogen-Free Magnet from Cryogenic Ltd. Height and centering are adjusted so that the sample stays in the region where the field produced by the magnet is calibrated and constant. The thermobatteries, the sample and the reference are tightly kept in place by Teflon tape in vertical position so that sample minimizes the demagnetizing fields caused by application of the magnetic field. The multimeters which read the Pt100 resistance and the calorimetric signals are computer controlled by means of a Labview software.

The differential scanning calorimeter under electric fields has a similar structure to the previously described device. The setup is sketched in figure 3.6. Some parameters related to its operational performance are listed in table 3.1.

Samples for DSC under electric fields are especially required to have a plate shape so that the proper thermal contact with the thermobattery is ensured. The two sample surfaces are covered with a thin layer of silver paint in order to build the pair of electrodes to apply voltage. Thin copper wires are soldered on each face and connected to a Keithley 2410 source-meter which acts as a $\Delta V = 1100$ V voltage supply. In this case, the thermobatteries lay horizontally on the calorimetric block and a proper thermal contact is ensured by applying a slight compression with a pair of thermally and electrically insulating Teflon screws. Considering the set-up as a capacitor of parallel plates, the applied electric field in the sample can be approximated to be homogeneous, perpendicular to sample's plane and of magnitude $E = \dfrac{\Delta V}{d}$. The calorimetric block is placed in a tailor-made tinplate container which is located in the silicone oil cistern of a *Lauda Proline* thermal bath which enables thermal control of the setup.

### 3.2.1 Setup calibration

The calibration of both setups consists in determining the sensitivity $S$ which converts the electric output $Y$ to the absorbed or released heat flow $\dot{Q}$ as a function of the significant parameters $(T, H, V)$ determining its behaviour over the whole calorimeter operational range. In both cases, the sensitivity has been determined to be independent of the applied field (magnetic field and electric field) and to solely depend on temperature.

The calibration is performed by dissipating a known amount of heat ($P$) on the sample thermobattery. The procedure consists in attaching a strain gauge film on the thermobattery surface which dissipates heat due to Joule effect ($P = I_s \Delta V_s$) at different temperatures within

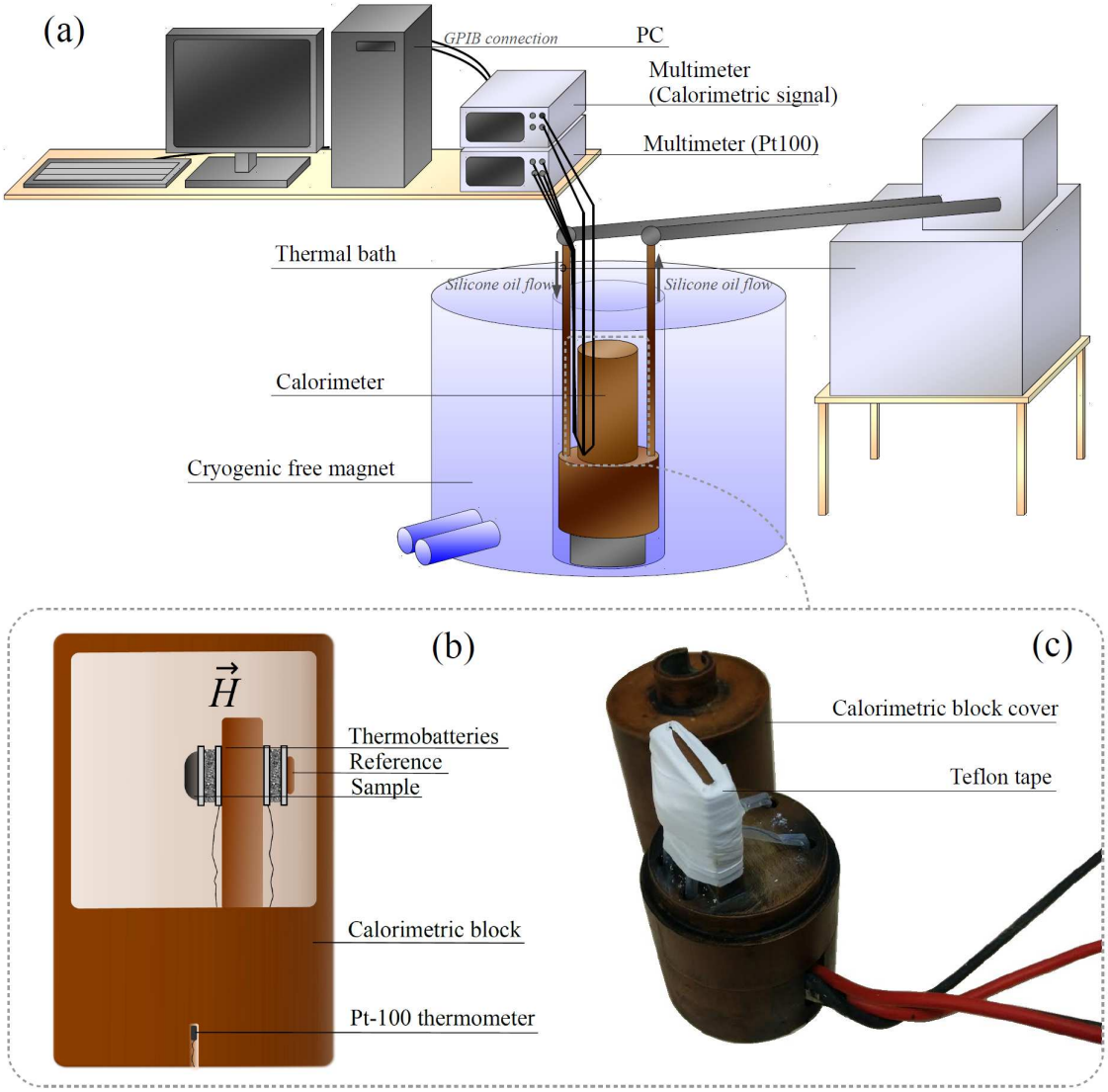


Fig. 3.5 Different views of the differential scanning calorimeter under magnetic field. (a) General view of the experimental set-up. A sketch of the device which is placed at the bore of a 6T cryogen free superconducting magnet is shown in (b), and the corresponding picture in (c) which shows how the sample and the reference are mounted with the use of the Teflon tape.

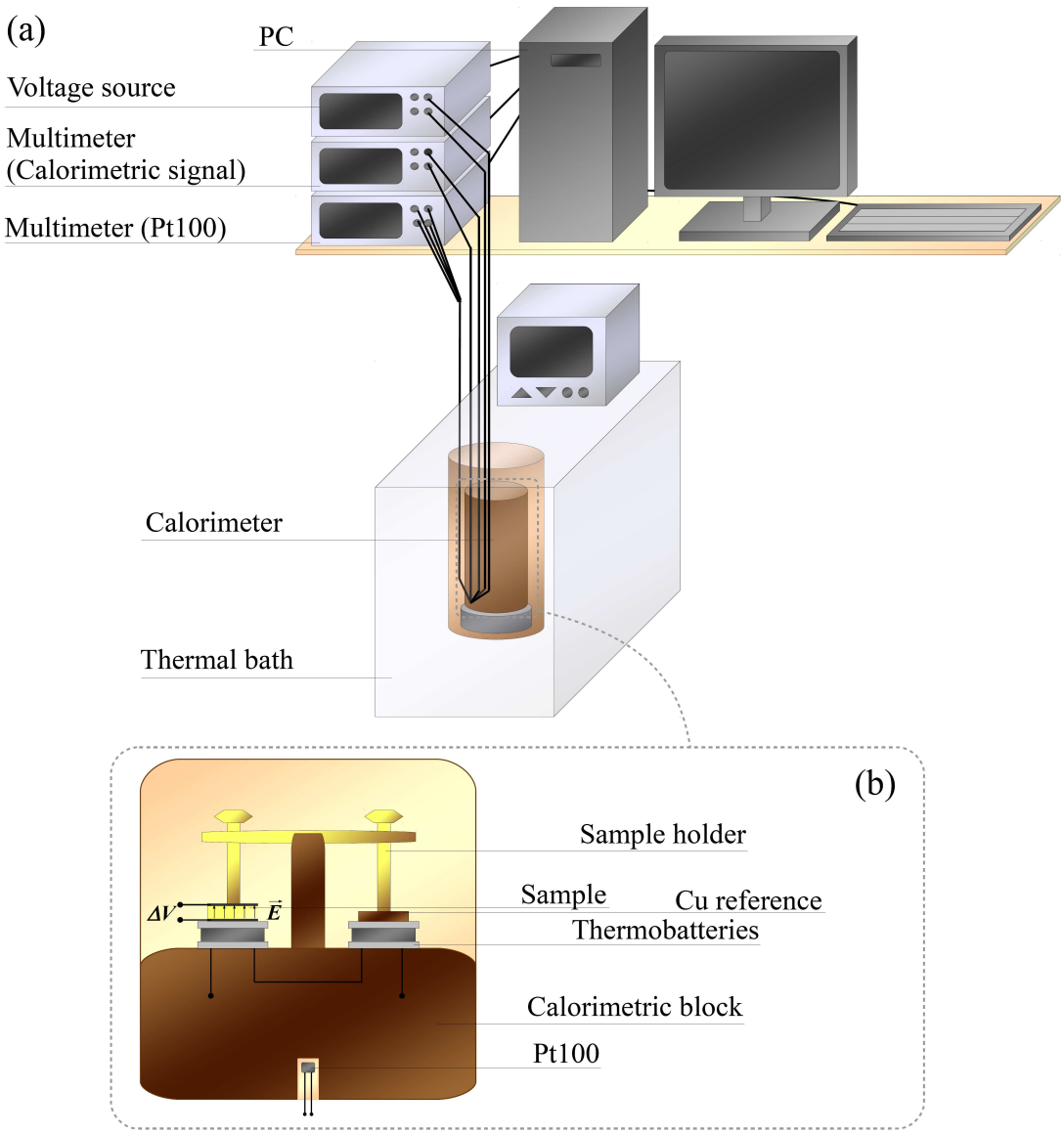


Fig. 3.6 Different views of the differential scanning calorimeter under electric field. (a) General view of the experimental set-up. (b) Sketch of the calorimeter.

the calorimeter operational range. A proper thermal contact is ensured by adding a tiny amount of silicone heat transfer paste. Keeping in mind that the strain gauge electrical resistance significantly changes on temperature, an electrical circuit is mounted so that the current $I_s$ circulating through the strain gauge is known and its potential drop is measured as illustrated in figure 3.7 (a). With this purpose, the current is computed by tracking the potential drop ($\Delta V_r$) in a reference resistance ($R_r = 100\Omega$) connected in series to the strain gauge at room temperature ($I_s = \frac{\Delta V_r}{R_r}$). The dissipated current is applied for periods of $\sim 300$ s at each temperature in which the calorimeter is calibrated and, consequently, the electric output $Y$ displays a plateau, as seen in figure 3.7 (b). The height of this plateau $\Delta V_p$ in reference to a baseline extrapolated from the region at which the electric circuit is open is directly associated with the heat flow being dissipated by the strain gauge and the sensitivity value at the corresponding temperature can then be computed as $S = \frac{\Delta V_p}{P}$.

The response time of the calorimeter can be defined as the delay between the time a thermal event occurs and the corresponding stabilization of $Y$. In our case, the thermal event is the constant dissipation of heat, $P$, and the signal stabilizes at $Y = SP$. Actually, this stabilization takes place exponentially ($Y = SP(1 - e^{-\frac{t}{\tau}})$ and can be parametrized by the time constant $\tau$ which is the elapsed time needed for obtaining a factor of $1/e$ of the stabilized signal. For both calorimeters $\tau \sim 4$ s over the whole operational range. The inset in figure 3.7 (b) illustrates the response time employed by the calorimeter to return to the signal baseline corresponding to the zero heat flow situation in which the calibration electric circuit is open. Usually, the low rates at which the field is scanned (see table 3.1) allows omission of the correction related to the response time of the calorimeter. However, this effect must be taken into account when these rates are considerably increased.

## 3.3 Calorimetry and dilatometry under magnetic field and uniaxial compressive stress

An experimental setup has been built for the analysis of the cross-coupled response in materials displaying magnetostructural transitions which are candidates of being multicaloric materials. As explained in the previous chapter, these first-order transitions are expected to be sensitive to both magnetic field or the type of mechanical stress which best fits the structural symmetry changes of the order parameter at the first-order transition. In this regard, this setup can simultaneously perform both calorimetry and dilatometry measurements under applied magnetic fields and uniaxial compressive stresses. In this case, the samples are required to fit

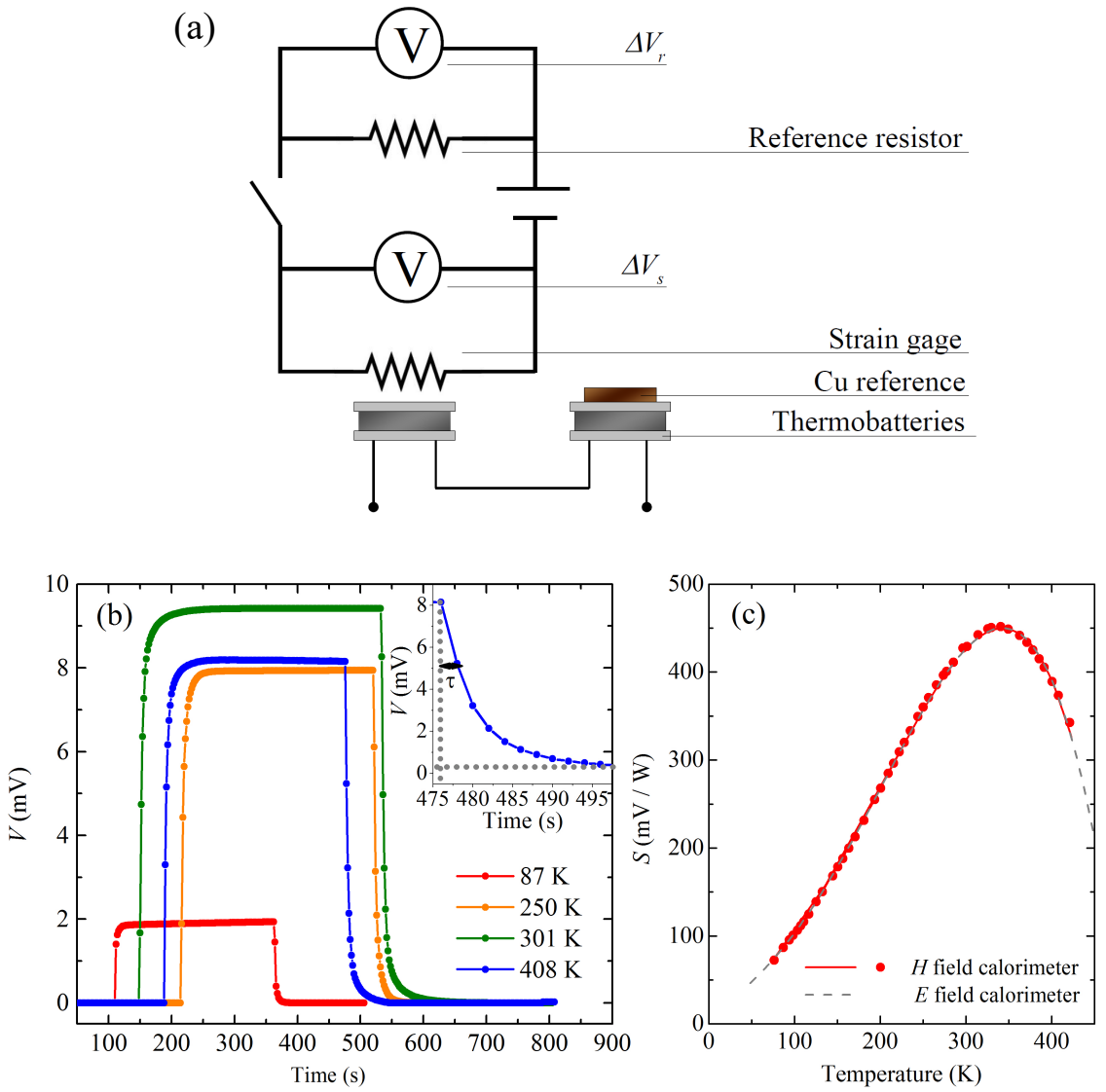


Fig. 3.7 (a): Sketch of the electrical circuit for the calibration of the calorimeters which operate under applied electric fields and magnetic fields. The strain gauge is attached on the sample thermobattery and a reference resistance is used for tracking the current circulating through it. The electrical circuit is closed for $\sim$ 300 s at each measurement temperature. (b): Illustrative examples of the electric output $Y$ as a function of time at selected temperatures measured on the calorimeter which operates under applied magnetic fields. Each peak corresponds to the measurement of the thermal response due to the strain gauge dissipated heat. The inset shows a magnified view of the peak at 408 K at the time the electric circuit has been opened again so that the response time and the corresponding time constant $\tau$ of the calorimeter can be visualized. (c): Plot of the sensitivity values of the calorimeter operating under magnetic field (red symbols) as a function of temperature and the corresponding fourth order polynomial fit (red line). The grey dashed line indicates the sensitivity of the calorimeter operating under magnetic field.

Table 3.2 Typical parameters of the operational performance of the device for the simultaneous measurement of calorimetry and dilatometry under applied magnetic field and uniaxial compressive stress. The first three values stand for the operational range in terms of temperature, magnetic field and applied force, respectively, followed by the typical values of the temperature scanning rate, magnetic field scanning rate, sensitivity at 300 K, and sample mass.

| $T$ (K) | $\mu_0 H$ (T) | $F$ (N) | $\frac{dT}{dt}$ (K/min) | $\frac{d\mu_0 H}{dt}$ (T/min) | $S$(300 K) (mV/W) | Sample mass (mg) |
|---|---|---|---|---|---|---|
| 220 - 360 | 0 - 6 | 1500 | 0.5 | 0.2 | 80 | 200 - 3000 |

the right prism shape or cylindrical shape in order to ensure appropriate application of the uniaxial compressive stress through the bases and avoid additional components of the stress.

Figure 3.8 shows different views of the purpose-built setup which is coupled to the bore (100 mm diameter) of the 6 T Cryogen-Free Magnet (Cryogenic Ltd) from which the applied magnetic field is controlled. As seen in figure 3.8 (b), the system has a low friction mobile platform sustained by three holding bars from which the platform slides vertically. The volume between the mobile platform and the top aluminium plate is reserved for the lead ingots which apply the weight to the system. A central bar is the only pillar sustaining the mobile platform and, hence, it concentrates the force applied by the lead ingots. The other edge of this central bar includes a high strength plastic disk of polyether ether ketone (PEEK). The hard, robust, and thermally insulating properties of this disk are required because it is in contact with one edge of the sample under study and it must avoid heat losses and support the stresses caused by the applied weight. The sample receives a compressive stress which is directly provided by the applied weight. The opposite face of the sample is sustained by a vessel which lies on the base of the magnet joint cylinder shown in figure 3.6 (b). This cylinder is coupled with the bore of the magnet in which the magnetic fields are applied and hangs from an extension plate which is placed at the top surface of the magnet. Thus, this plate is responsible of supporting the total weight of the setup and ensures proper stability of the junction between the magnet and the purpose-built experimental setup. Particularly, the sample lies on a hard aluminium disk which is a suitable material for the heat transfer between the sample and the thermobattery and for resisting the applied stresses caused by the applied weight. Thus, the hard aluminium disk covers a small enclosure in which the thermobattery is placed and shields the thermobattery from the applied stress. The thermobattery measures the

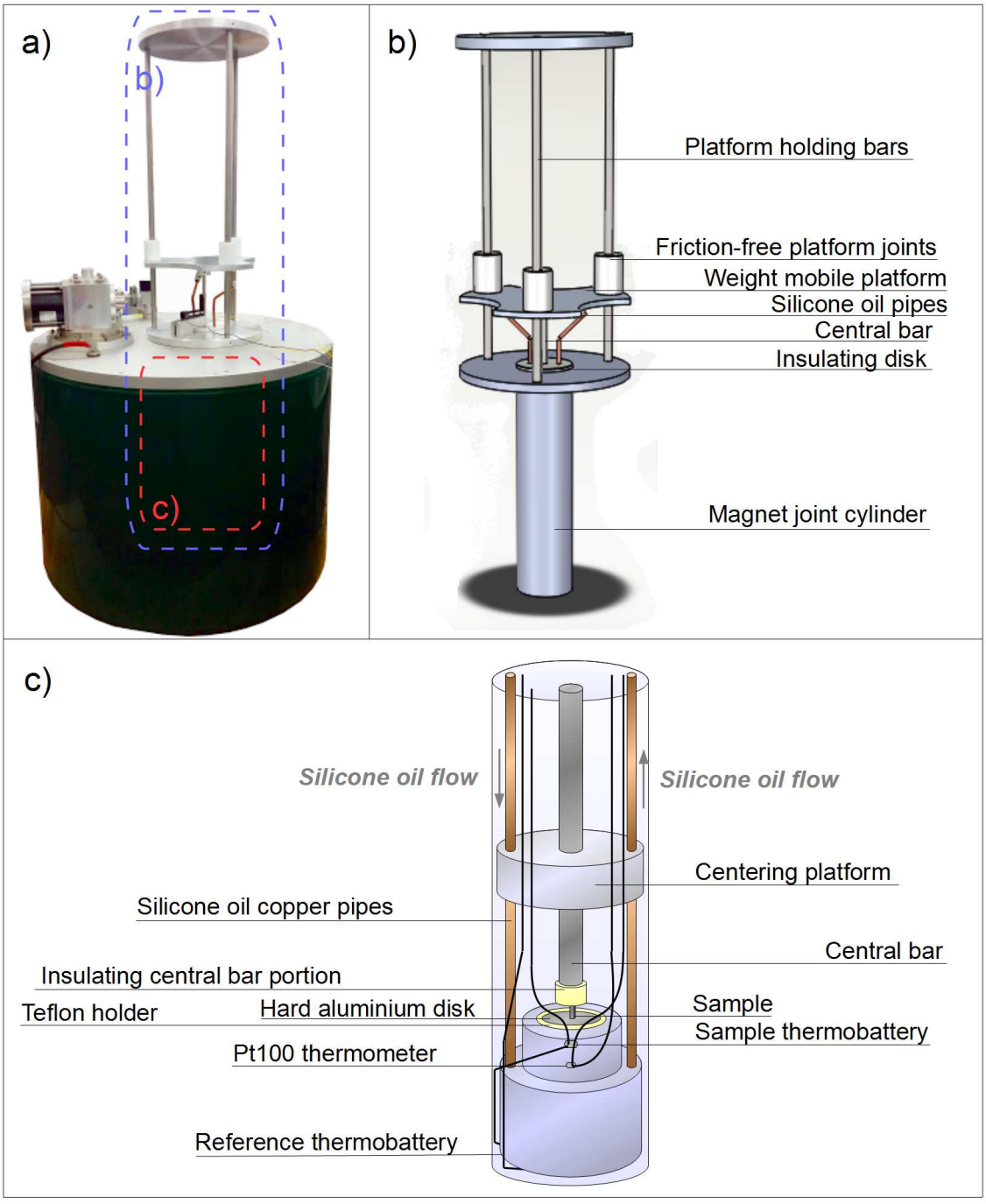


Fig. 3.8 Panel (a) shows a picture of the cryogenic-free magnetic in which the purpose-built experimental setup is coupled on its bore. Panel (b) and (c) show different sections of the setups.

small temperature gradients in the disk related to the calorimetric phenomena as described in section 3.1.1. The dimensions of the hard aluminium disk must be sufficiently thin and small for reducing the heat losses and improving the calorimetric sensitivity and sufficiently thick for preventing its bending due to the stress applied by the sample (in our case, the diameter and the thickness are 15 mm and 2 mm, respectively. The other face of the thermobattery is in contact with the vessel which acts as the calorimetric block. The thermal control of the calorimetric block is achieved by the silicone oil which circulates inside the vessel and is pumped through the copper pipes from the Lauda Proline 890C thermal bath. At the center of the vessel base the reference thermobattery is stack at its surface with the use of a tiny amount of glue. A piece of copper is fixed at the opposite face of the thermobattery which acts as the inert reference. A Pt100 thermometer which measures the block temperature is embedded into a 1 mm diameter hole drilled in the vessel and filled with silicone heat transfer paste for a proper thermal contact.

A linear variable differential transformer (LVDT) is an inductive transducer which outputs an electric signal as a function of the mobility of a core which induces a current through the coil. The dilatometry measurements are performed by attaching an LVDT from Solartron Metrology [see figure 3.9 (a)] which lies on a fix platform mounted on the magnet surface. An LVDT is an inductive transducer which outputs an electric signal as a function of the mobility of a core which induces the current through the coil. As shown in figure 3.9 (b), the sensor is in contact with the mobile platform and measures its vertical linear displacement which has a net contribution from the dilation or contraction of the sample. The LVDT is excited by applying 10 V with an AC voltage source and its output signal is directly related to the displacement of the sensor with respect to its equilibrium position.

### 3.3.1 Setup calibration

The calibration of this setup is performed in analogy with the method described in section 3.2.1 for the previous devices. In this case, the sensitivity depends on the temperature $T$ and the applied compressive force $F$ but it is independent of the applied magnetic field $H$. The value of the applied stress is known in each case by $\sigma = -\frac{F}{A}$, where $A$ refers to the area of the sample face in which the pressure is applied. A resistance is embedded in a copper parallelepiped specimen of dimensions $4 \times 4 \times 6$ mm$^3$ which is placed at the sample site and pressed by the central bar at the same conditions as a sample. The procedure is then similar to the one illustrated in figure 3.7 (a). The resistance dissipates a known heat flow ($P$) because its potential drop is measured as well as the drop in a reference resistance so that the current circulating through the calibration resistance can be derived. The calibration

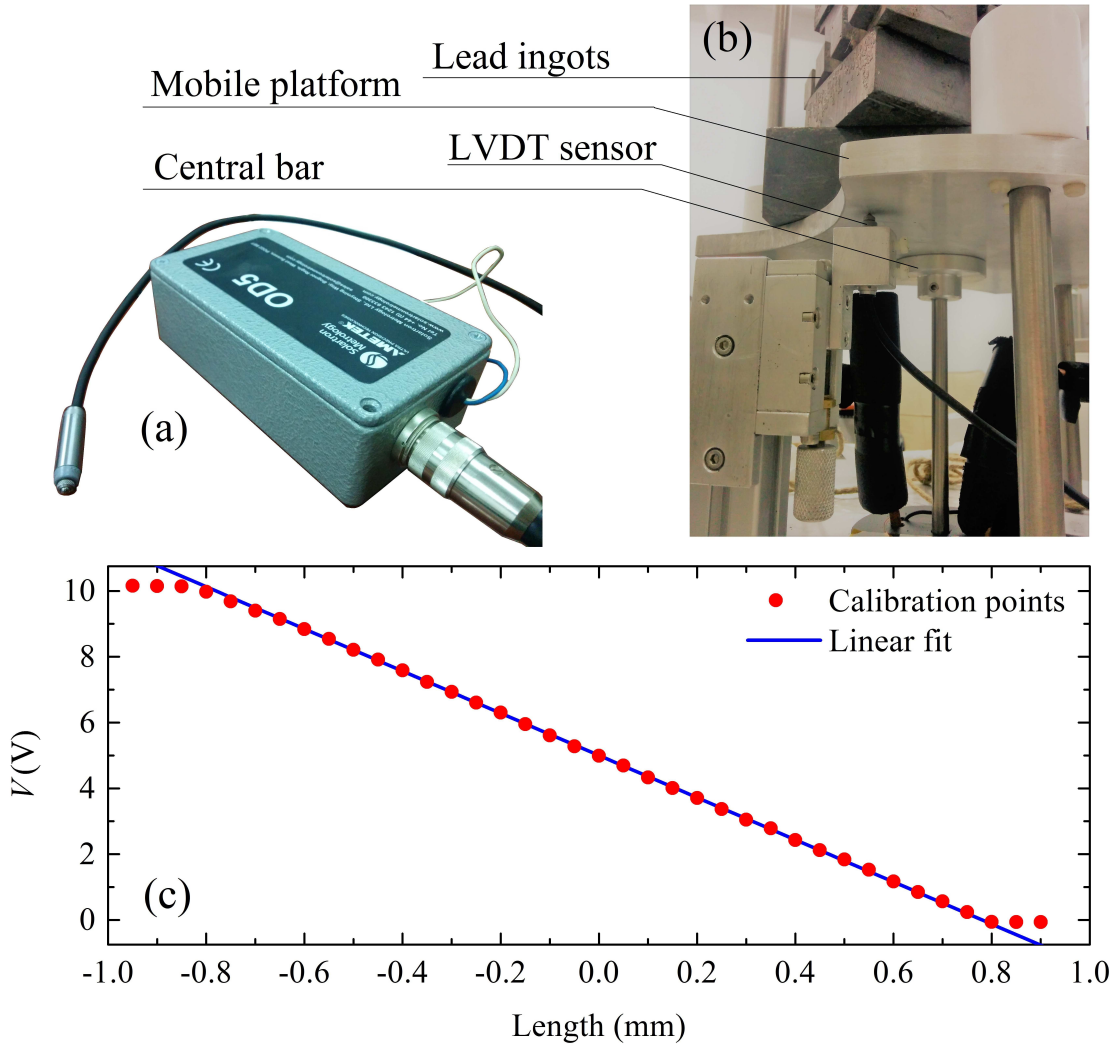


Fig. 3.9 (a) Image of the LVDT sensor from Solartron Metrology. (b) Image of the structure at which the LVDT is mounted. The sensor is in contact with the mobile platform and is sensitive to its vertical displacements. (c) Electric output of the LVDT sensor as a function of the length measured by the micrometer for its calibration. Red symbols show the experimental points and the blue line is the corresponding linear fit: $X(mm) = (-0.1560 \pm 0.0004)V + (-0.780 \pm 0.002)$.

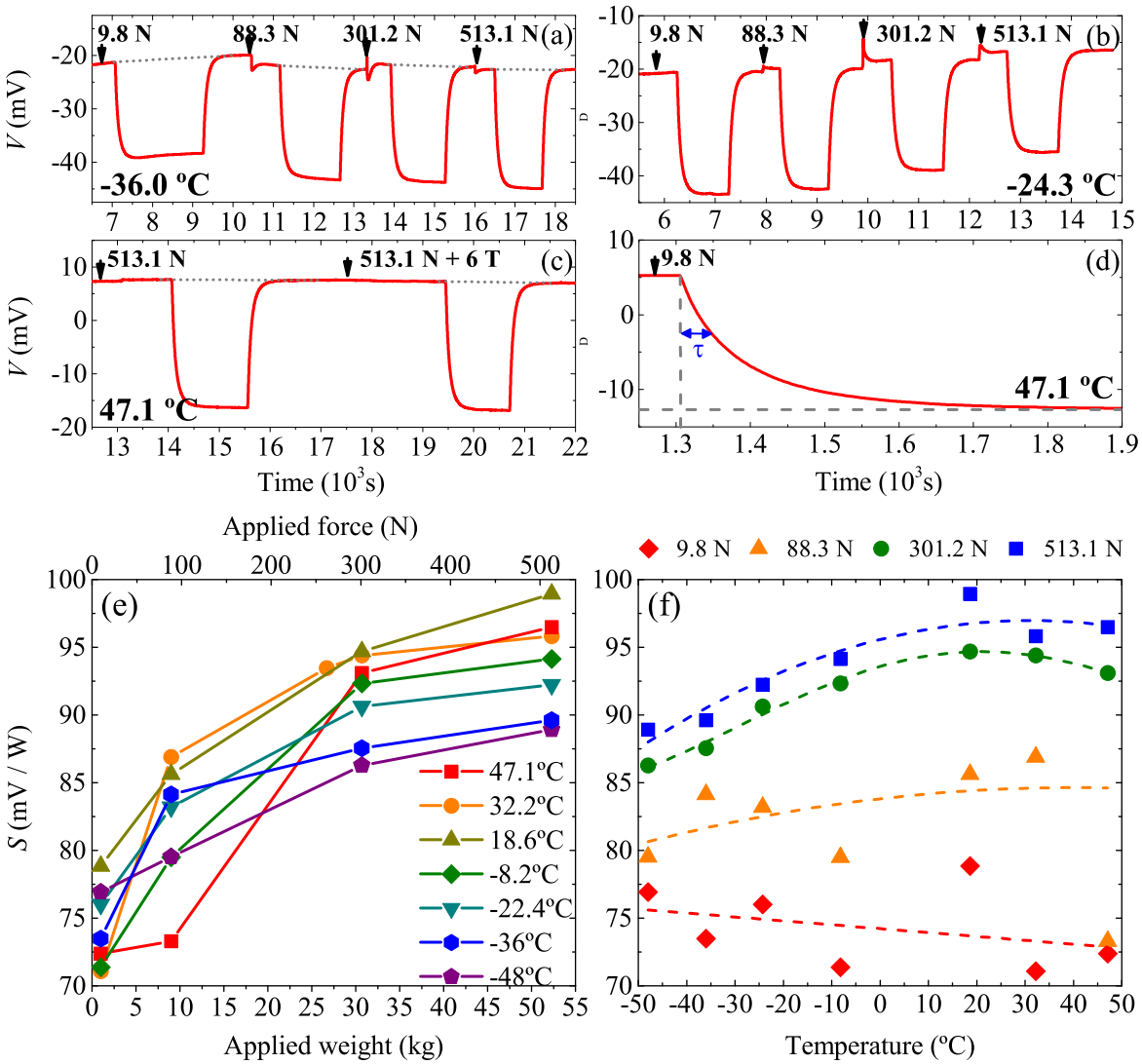


Fig. 3.10 Calibration of the setup designed for calorimetry under magnetic field and uniaxial compressive stress. Plots in (a) and (b) show illustrative examples of the calibration measurements at -36.0 ºC and -24.3 ºC in which the heat is dissipated at different values of the applied compressive stress. Panel (c) compares the obtained electric signal at 0 and 6 T under the same applied stress (513.1 N) and illustrates the independence of the sensitivity with the applied magnetic field. Panel (d) illustrates the response time of the calorimetric signal and the corresponding time constant ($\tau \sim 40s$) upon dissipating the heat at 9.8 N. Bottom panels depict the sensitivity values as a function of the applied weight and force at selected temperatures (e) and as a function of temperature at selected values of the applied compressive stress (f). In panel (f), symbols correspond to experimental data and dashed lines to polynomial fits for the $S(T,F)$ characterization: $S(T,513.2N) = 95.6+0.0893T-0.00143T^2, S(T,301.2N) = 93.6+0.103T-0.00219T^2-1.36\cdot10^{-5}T^3-1.98\cdot10^{-7}T^4, S(T,88.3N) = 83.8+0.0413T-5.16\cdot10^{-4}T^2, S(T,9.8N) = 74.2-0.0288T$.

is then performed by closing the electric circuit shown in figure 3.7 (a) under isothermal conditions at temperature values within the operation range for $\sim$ 900 s. In this case, a longer dissipation time is required because the thermal mass of the hard aluminium disk which is set between the thermobattery and the sample results in a greater calorimeter time constant ($\sim$ 40 s). The dissipation procedure is repeated after adding lead ingots and, thus, increasing the applied stress. Figure 3.10 (a) - (d) show illustrative examples of the obtained calorimetric signal at selected temperatures. Negative plateaus are associated with the exchanged heat ($P$) during the dissipation process and their height values $\Delta V_p$ are obtained by subtracting with respect to the grey dotted baselines. Figure 3.10 (e) and (f) show the sensitivity values ($S = \frac{\Delta V_p}{P}$) as a function of the applied force and temperature, respectively.

The calibration of the LVDT is performed by mapping the voltage output of the sensor with the corresponding displacement by means of a micrometer as shown in figure 3.9 (c). As expected, the sensor exhibits great linearity within its operation range, i.e. $\pm$ 0.8 mm around its equilibrium position.

## 3.4 High Pressure Differential Thermal Analysis

Calorimetric measurements under hydrostatic pressure have been carried out by means of the High Pressure Differential Thermal Analysis (HPDTA) experimental system at the Physics and Nuclear Engineering department of the Polytechnic University of Catalonia. This system is capable to perform calorimetry measurements under applied hydrostatic pressure (0 - 2.5 kbar) over a broad temperature range (180 - 470 K). A sketch of this system can be seen in figure 3.11 and a detailed description can be found in [59]. The sample is placed in an hermetically sealed enclosure at a certain value of the applied pressure. A second enclosure is used for the reference thermocouple. Both enclosures are surrounded by a calorimetric block which acts as thermal bath. Chromel-alumel thermocouples are injected into both enclosures in order to read the calorimetric signal. Specifically, the sample thermocouple is embedded into a hole of 1 mm diameter and 3 mm length which is previously drilled in the sample with the purpose of a better experimental confidence. A differential connection between these two thermocouples outputs the calorimetric signal. In addition, the temperature of the block is read by a calibrated differential connection between the reference thermocouple and a third thermocouple which is in contact with ice at the melting point. Silicon oil is used as the compressor fluid and pressures up to 2.5 kbar can be applied by means of a hand pressure pump. There is no experimental need to keep the reference thermocouple under the same applied pressure as the sample because no change in the calorimetric output has

Table 3.3 Relevant parameters characterizing the HPDTA setup: temperature and pressure operating range, typical temperature scanning rate, typical sensitivity value at 300 K, and typical sample mass for the measurements.

| $T$ (K) | $p$ (kbar) | $\frac{dT}{dt}$ (K/min) | $S$(300 K) (mV/W) | Sample mass (mg) |
|---|---|---|---|---|
| 250 - 450 | 0 - 2.5 | 1 | 1 | 200 - 4000 |

been detected. Moreover, there is also no need to couple an inert sample to the reference thermocouple for the same reasons.

A resistor surrounding the calorimetric block is responsible for the thermal control. A Labview software is aimed at the temperature control of the setup by reading the block temperature with a Pt-100 thermometer and constantly adjusting the resistor voltage to monitor the heating rate. Alternatively, the thermal control of the setup can be monitored by means of a circuit of pipes surrounding the calorimetric block through which a silicone oil is pumped by a Lauda Proline RP 890 thermal bath. In this regard, the HPDTA setup allows the performance of isofield calorimetric measurements in which the temperature is scanned at constant values of the applied pressure.

### 3.4.1 Setup calibration

The electric output given by DTA technique is proportional to the temperature difference between the sample and the reference and its conversion to the heat flow values is given by the setup sensitivity $S$, i.e. $Y = S\dot{Q} \propto T_S - T_R$, which has a particular dependence on temperature and pressure. In addition, the setup output exhibits a strong dependence on the particular thermal contact between the thermocouple and the sample. The type of pressurizing oil which is employed for the measurements is chosen as a function of the temperature range of the desired experiment.

The calibration procedure is performed by means of a family of samples with compositions $Cu_{68.3}Zn_{14.2}Al_{17.5}$, $Cu_{67.0}Zn_{22.2}Al_{10.7}B_{0.1}$, and $Cu_{70.6}Al_{26.5}Ni_{2.7}B_{0.2}$. These samples exhibit a shear strain martensitic transition with negligible volume change and are of special interest because their transition temperature and the corresponding enthalpy and entropy changes are not sensitive to the applied hydrostatic pressure. The following description is focused on a silicone oil with an operating temperature range restricted at $T \in [290, 450]$ K.

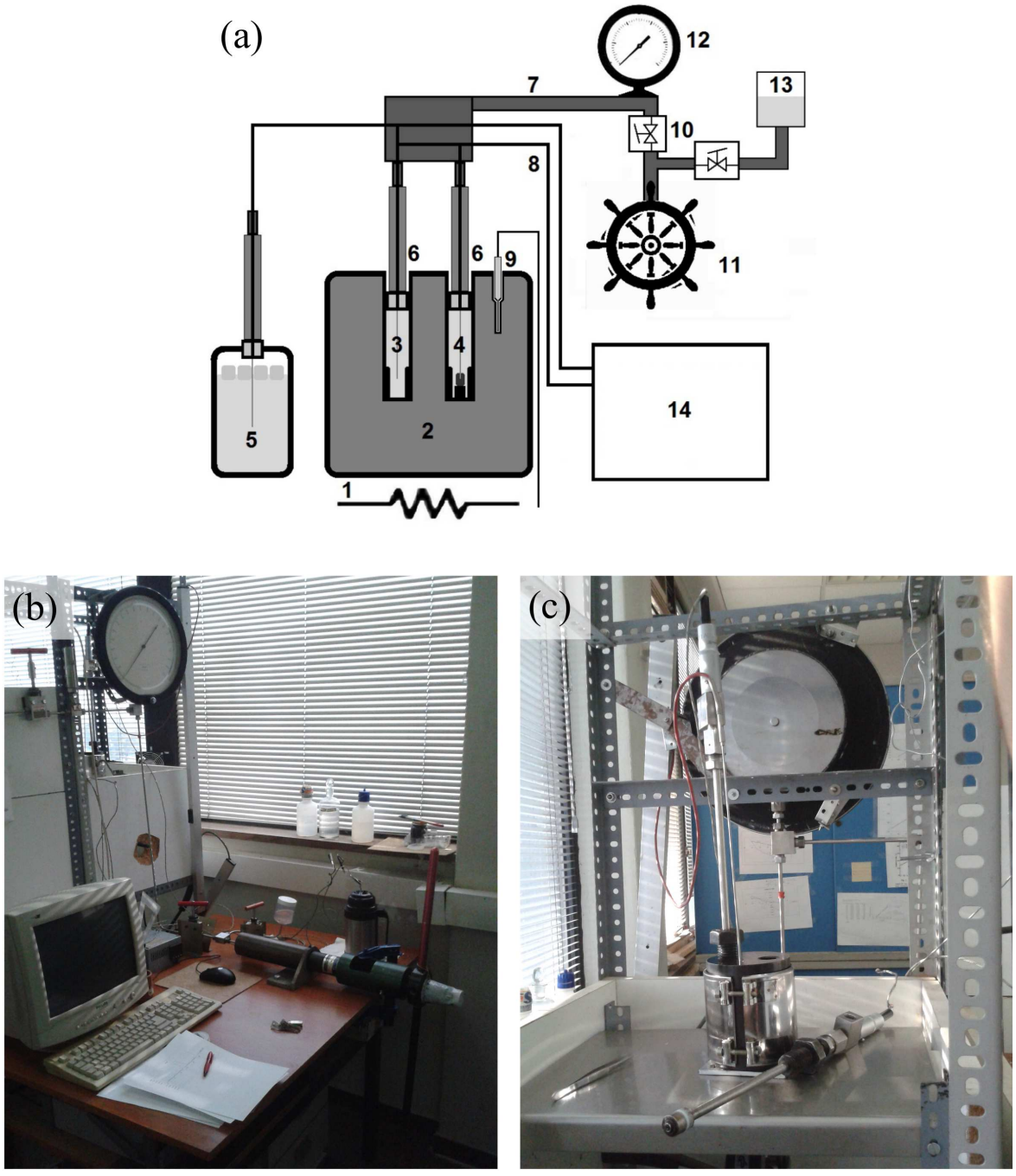


Fig. 3.11 (a) Sketch of the experimental system. 1- Resistor. 2- Calorimetric block. 3- Reference enclosure with a thermocouple connection. 4 - Sample enclosure with a thermocouple connection. 5- Ice deposit with a thermocouple connection. 6- High pressure Bridgman seals. 7- Capillaries for the high pressure liquid conduction. 8- Thermocouple wires. 9- Pt-100 thermometer for the resistor temperature control software. 10- Valves. 11- Pressure pump. 12- Manganin manometer. 13- High pressure liquid reservoir. 14- Data acquisition system. (b) View of the hand pressure pump, the manganin manometer screen, and the computer which monitors the experimental output and input. (c) View of the calorimetric block which is covered by the resistor which monitors its temperature.

Due to the fact that the oil has an influence on the thermal contact between the sample and the thermocouple, the calibration is repeated analogously if the type of oil is changed with appropriate samples transforming at the corresponding temperature range.

A set of thermograms at each transition temperature range have been measured for each calibration sample at selected values of the applied pressure. Considering equation (3.10) and the correspondence $\frac{dQ}{dT} = \frac{Y}{S\dot{T}}$, the expression for the transition enthalpy change as a function of the baseline integration of the calorimetric peak, $\int_{T_s}^{T_f} \frac{Y}{\dot{T}} dT = \bar{Y}$, is expressed as

$$\Delta H_t = \int_{T_s}^{T_f} \frac{Y}{S} \frac{dT}{\dot{T}} = \frac{\bar{Y}}{S} \tag{3.20}$$

where the sensitivity is approximated as a constant value at the transition temperature range between $T_s$ and $T_f$. The analysis relies on the fact that the first-order transition exhibited by the calibration samples is unaffected by the applied pressure and the enthalpy change remains constant over the pressure operating range[4] ($\Delta H_t(p=0) = \Delta H_t(p=p') \equiv \Delta H_t$) so that any change of the integrated signal in each family of thermograms $\bar{Y}$ is due to a pressure dependence of the sensitivity, as stated by (3.20). Panels (b), (c), and (d) in figure 3.12 show the set of thermograms at applied pressure for each sample and (e), (d), and (f) show the corresponding integrated values $\bar{Y}$ and their linear regressions. The sensitivity pressure dependence at the corresponding temperature region at which the transition occurs is directly obtained by reescaling the linear fits $S(T,p) = \frac{\bar{Y}(p)}{\Delta H_t}$, where $\Delta H_t(p=0)$ is previously obtained from calorimetry at atmospheric pressure, performed by an independent setup as shown in figure 3.12 (a).

In each case, the obtained expression for $S(T,p)$ is only valid for each set of thermograms because each time the sample is changed the thermal contact is modified so that the overall magnitude of the sensitivity is affected. However, the general trend of the sensitivity indicates that its relative change at certain value of the applied pressure $p'$, i.e. $\frac{S(p=p')}{S(p=0)}$, remains unaffected by the new thermal contact conditions. With the aim of describing the sensitivity in a generalized form, we define the *normalized sensitivity* as:

$$S^*(p) = \frac{S(p)}{S(p=0)} \tag{3.21}$$

[4] As usual along the dissertation and for simplicity, values at atmospheric pressure (p $\sim$ 1 bar) are considered to be at zero pressure (p = 0), which is a justified approximation since the range of the applied pressures includes values larger than $\sim$ 2.5 kbar.

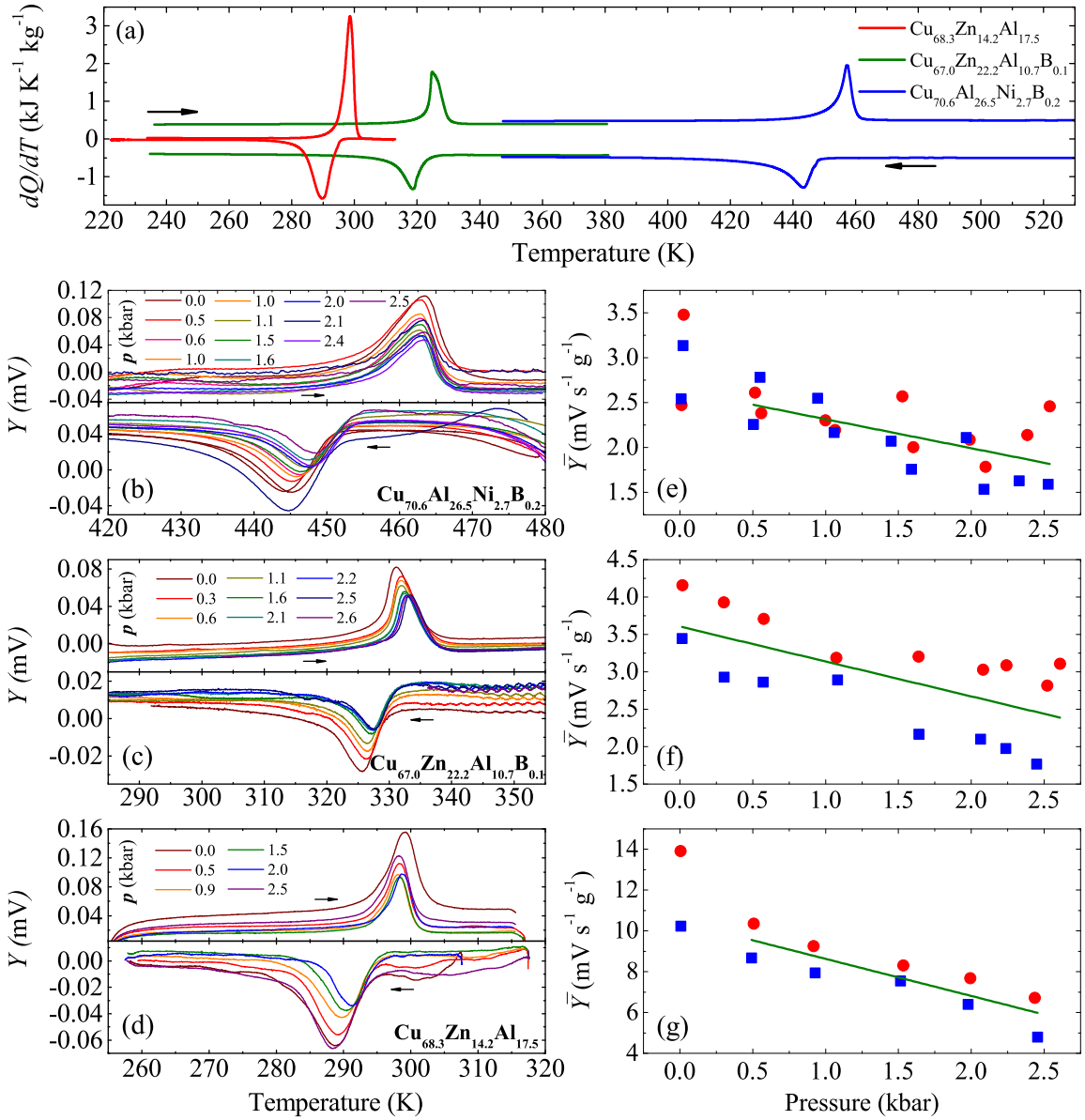


Fig. 3.12 (a) Conventional DSC measurements at atmospheric pressure on the calibration samples for the silicone oil pressure transmitter in HPDTA technique. A commercial TA Q2000 device has been used for the $Cu_{67.0}Zn_{22.2}Al_{10.7}B_{0.1}$ and $Cu_{70.6}Al_{26.5}Ni_{2.7}B_{0.2}$ samples, and the $Cu_{68.3}Zn_{14.2}Al_{17.5}$ sample has been measured with the calorimeter described in [57]. Left panels (b), (c), and (d) illustrate the thermograms at applied pressure for each sample obtained by HPDTA technique and the right panels (e), (f), and (g) display the corresponding values of $\bar{Y}$ for each sample, respectively, where red circles stand for the heating curves and blue squares refer to the cooling curves. The green line refers to the corresponding linear fits.

where $S^* = 1$ for $p = 0$. We can approximate the behaviour of $S^*(p,T)$ as a function of pressure and temperature by the expression:

$$S^*(p,T) = 1 + a(T)p \tag{3.22}$$

where $a(T)$ is the linear rate at which $S^*$ varies with pressure which is obtained experimentally by $a = \dfrac{S(p=p')}{S(p=0)} = \dfrac{\bar{Y}(p=p')}{\bar{Y}(p=0)}$. It is worth noting the temperature dependence of this parameter, so that each family of thermograms obtained from each calibration sample shown in figure 3.12 can be used for obtaining the value of $a(T)$ at a given temperature. From our calibration, we can establish that

$$S^*(p) = \begin{cases} 1 + (0.71 - 1.8 \cdot 10^{-3} T)p & \forall T \in [270, 323] \\ 1 + (0.15 - 5.7 \cdot 10^{-5} T)p & \forall T \in [323, 450] \end{cases} \tag{3.23}$$

where we have assumed a linear temperature dependence in $a$. Figure 3.13 illustrates the behaviour of the normalized sensitivity expressed in (3.23) within the operation range of the silicone oil. As shown, it is weakened with increasing values of the applied pressure.

Once the general expression of the normalized sensitivity has been established, the sensitivity to be used under the particular conditions of the desired experiment is obtained by rescaling $S^*$ with the values of $\bar{Y}$ and $\Delta H_t(p=0)$ of the sample under study:

$$S(T,p) = \frac{\bar{Y}(p=0)}{\Delta H_t(p=0)} S^*(T,p) \tag{3.24}$$

## 3.5 Thermal imaging

A significant source of error when measuring the exchanged heat and temperature changes on caloric materials may be related to the thermal contact. For example, one has to take into account the heat loss between the sample and the environment, the loss of adiabaticity if the sample is poorly insulated or the thermal influence of the sensor on sample's temperature. With this in hand, the characterization of giant caloric effects with non-contact direct methods becomes highly convenient because they are expected to display an improved accuracy.

A non-contact thermometry setup for the measurement of the electrocaloric effect based on fast infrared (IR) imaging technique has been developed during my stay at the Department of Materials Science and Metallurgy of the University of Cambridge. A sketch of the setup is shown in figure 3.14. A Peltier thermobattery is responsible for the temperature control of the sample and is settled on the top of a big metallic block from which the heat flux from the

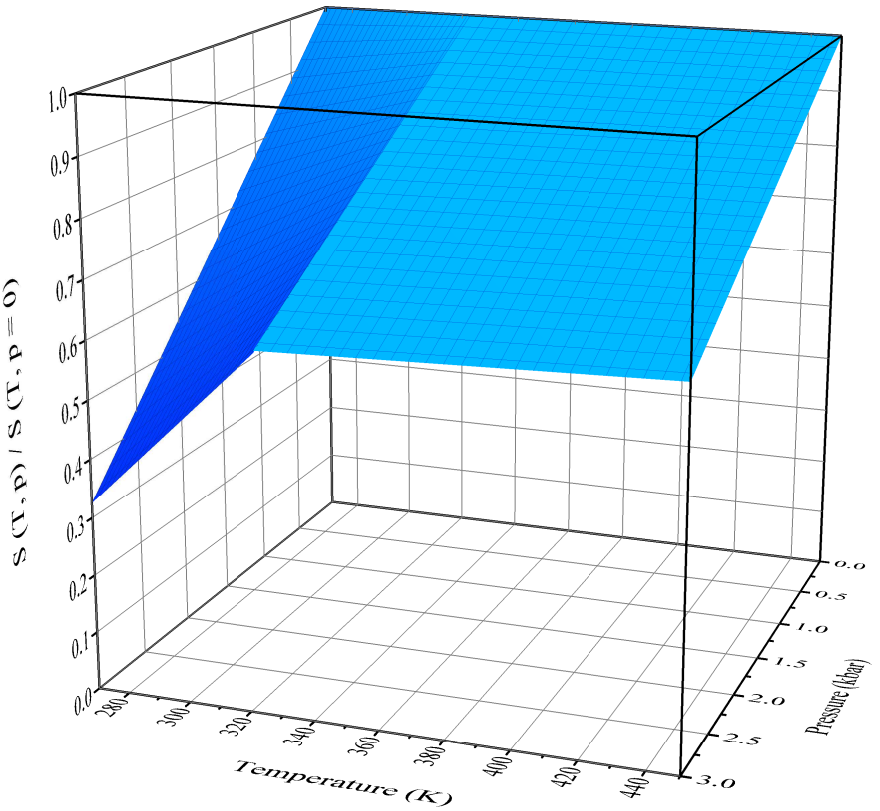


Fig. 3.13 Normalized sensitivity $S^*(p) = \dfrac{S(T,p)}{S(T,p=0)}$ of the HPDTA setup as a function of temperature and pressure for the silicone oil with operation range $T \in [270, 450]$ K.

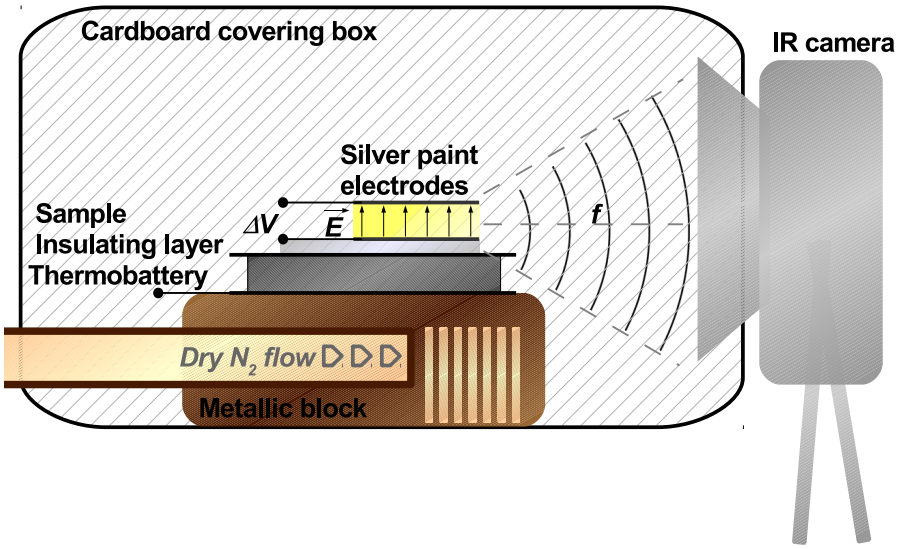


Fig. 3.14 Sketch of the main components of the setup for infrared imaging.

peltier element is dissipated. With this purpose, a constant flow of dry nitrogen circulates through the metallic block and prevents from overheating the setup.

The sample is plate shaped and is covered by a thin layer of silver paint on both faces. Each silver paint layer is a sample electrode and is connected to a voltage supply which applies a potential drop $\Delta V$ to the sample. With the approximation of a capacitor of flat, parallel metallic plates, the value of the applied electric field is $E = \frac{\Delta V}{d}$. The sample is placed on top of a plastic sheet with a poor thermal conductivity which improves the adiabatic conditions when the sample is cycled under electric field. The insulating layer and the sample set is placed on top of the Peltier element which is located at the focal point of the infrared camera (FLIR ©, model SC7500-MB). In particular, the camera records images of the face of the sample which is between both electrodes and tracks its emission at the infrared spectrum. A small piece of black tape is stuck on this sample face for the temperature calibration as explained in section 3.5.1. A cardboard box covers the whole experimental setup and significantly reduces the undesirable environmental radiation coming from other emission sources of the lab.

The imaging process is done at high frequency (0.5 kHz) so that the setup is sensitive enough for the measurement of the height of the peak of the adiabatic temperature change due to the sudden application of the electric field ($\sim 10^{-2}$ s) and its decay as the sample thermalize with its surroundings, typically with a time constant $\tau \sim 5$ s under these experiment conditions. Research IR Max software provided by FLIR is responsible of part of the data analysis and a first calibration of the output signal provided by each pixel of the camera which is converted to the temperature values. The software averages the temperature values given by the pixels in the regions of interest of the output images, i.e. the surfaces of the black tape and the sample, and provides the corresponding values $T_{bt}$ and $T_s$, respectively. The field of view of the camera is the area from which the camera is recording its infrared emission and depends on the lens of the camera and the focal plane dimensions. The spatial resolution of the camera, i.e. the smallest detectable object, is constrained by the field of view of a particular pixel or, in other words, by the division of the field of view in area elements determined by the number of pixels per line and per row. Ideally, none of the sample face dimensions being recorded by the camera should be lower than one order of magnitude than any of the two dimensions of the spatial resolution. In our case, this is accomplished if the thickness of the sample is greater than $\sim 100$ $\mu$m.

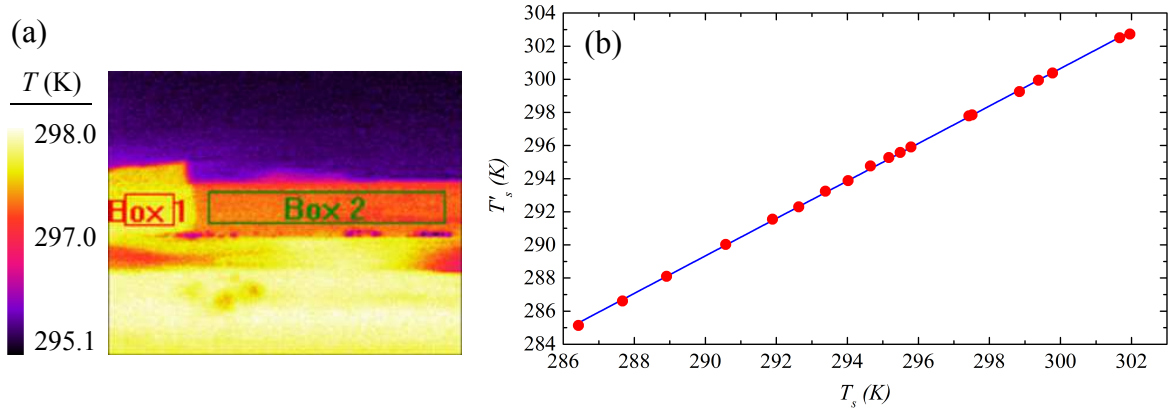


Fig. 3.15 Illustrative example of the temperature calibration of the PST sample described in chapter 7 which consists in associating the measured black tape temperature $T_{bt}$ as the real temperature of the sample $T_s'$ when they reach thermal equilibrium. The picture in (a) is a temperature image of the sample (box 2) and the black tape (box 1) obtained by the IR camera. The corresponding temperature scale is on the left hand side. The red circles in (b) display the black tape temperature as a function of the measured sample temperature $T_s$ and the blue line is the corresponding linear fit, $T's = (1.131 \pm 0.004)T_s - 38 \pm 1$.

### 3.5.1 Setup calibration

The net rate flow of radiation $P$ per unit area emitted by a black body is determined by the Stefan-Boltzmann law which reads $\frac{P}{A} = \frac{\pi^2 k_B^4}{60\hbar^3 c^2} T^4 = \sigma T^4$ [60], where A is the area of the body, $k_B$ is the Boltzmann constant, $\hbar$ is the reduced Planck constant, $c$ is the speed of light and $\sigma \sim 5.670$ W m$^{-2}$ K$^{-4}$ is the Stefan-Boltzmann constant.

A black body isotropically emits as an ideal emitter over all the light frequency spectrum and it absorbs all incoming radiation, showing neither reflection nor transmissivity. The physical bodies are defined as grey bodies when they do not absorb all incident radiation and emit less total radiation than a black body. In this regard, the emissivity $\varepsilon = \frac{P_G}{P_B}$ is the parameter which compares the radiation emission of a grey body $P_G$ with the black body emission $P_B$ at the same temperature. Hence, $\varepsilon = 1$ for a black body and $\varepsilon < 1$ for a grey body. In general, the emissivity depends on the light frequency and the direction, although the emissivity of the materials is usually tabulated as a constant value over the whole IR spectrum. Analogously, we can define the reflectivity $\varphi$ and the transmissivity $\gamma$ as the parameters quantifying the fraction of IR light reflected or penetrated by the sample, respectively. The sum of each contribution corresponds to the total radiation collected by the sensor, i.e. $\varepsilon + \varphi + \gamma = 1$. In general, in the infrared spectrum the transmissivity of the bodies is zero, $\gamma = 0$.

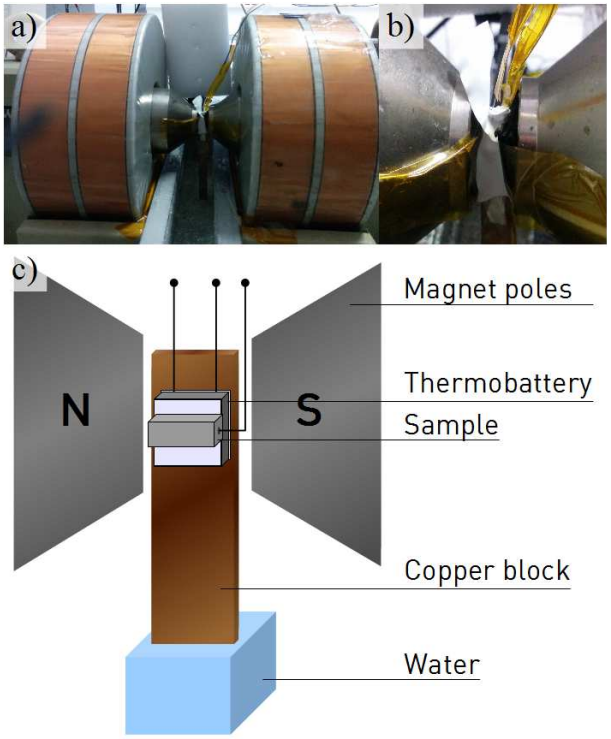


Fig. 3.16 Pictures (a) and (b) display different views of the magnet in which the setup for the thermometry with a fine gauge K thermocouple is placed between the poles. Panel (c) is a skecth of the different components of the experimental setup.

As previously mentioned, FLIR Research IR Max software executes a first calibration procedure and converts the IR radiation collected by each pixel to the corresponding temperature values emitted by a black body. However, our sample might not emit as a black body and the piece of black tape which has a high emissivity value ($\varepsilon > 0.9$) is used for subsequent temperature calibration. The recorded images provide the average temperatures of the black tape and the sample considered as a black body, $T_{bt}$ and $T_s$. Both the sample and the black tape piece are kept in thermal equilibrium so that they reach the same temperature $T'_{bt} = T'_s$. Considering that the measured black tape temperature corresponds to its physical temperature, i.e. $T_{bt} = T'_{bt}$, the calibration is then performed by linearly mapping $T'_s = T_{bt} = a_1 T_s + a_2$ as shown in figure 3.15.

## 3.6 Thermometry with a fine gauge K themocouple

When some specific conditions are met, contact thermometry may also provide good estimates of the temperature change by adiabatic application of an external stimuli. In our case, we have

built a setup for the measurement of the magnetocaloric adiabatic temperature change which is sketched in figure 3.16. The temperature sensor is a fine gauge K thermocouple (0.075 mm diameter) embedded into a hole drilled to the sample. A good thermal contact between the sample and the thermocouple is improved by a small amount of silicone heat transfer paste. The sample is in contact with one of the faces of a Peltier module which monitors the operating temperature. The opposite face of the Peltier module is in contact with the top end of a copper bar which acts as a heat sink. The bottom end of the copper bar is submerged in an ice water reservoir to avoid the overheating of the bar and the Peltier module. A micro-Hall sensor is attached next to the sample to measure the magnetic field. The ensemble is wrapped together with Teflon tape and it is placed into the gap (1.2 cm) of an electromagnet where fields up to 2 T can be applied at rates $\sim 1.5$ T s$^{-1}$. The operating temperature is fixed with a voltage supply which tunes the current through the Peltier element. The output from the thermocouple and Hall sensor is read at a rate of 2.5 Hz by two multimeters, which are connected to a computer.

The accuracy of the measurement depends on the following conditions:

- Adiabatic conditions are met when the ratio between the characteristic time constant associated with the application (or removal) of the field ($\tau_1$) and the time constant associated with the exchanged heat between sample and surroundings ($\tau_2$) is $\frac{\tau_1}{\tau_2} \ll 1$. In our case, the samples under study have shown good adiabaticity $\frac{\tau_1}{\tau_2} < 10^{-2}$.

- The thermal mass of the thermocouple has an influence on the measurement which can be responsible of an underestimation of the $\Delta T$ values due to the exchanged heat with the thermocouple when the sample is heated or cooled. A more accurate temperature output is ensured by minimizing time constant $\tau_3$ related with the thermalisation between the sensor and the sample. This process competes in time with the previously mentioned thermalisation of the sample with its surroundings with time constant $\tau_2$ caused by the adiabatic application of the magnetic field. In our case, $\frac{\tau_3}{\tau_2} \ll 1$ as desired by using the fine gauge K thermocouple. The use of this low-mass sensor has been proved to increase the values of the $\Delta T$ up to 15 % in comparison with the values obtained by a conventional K thermocouple. Accordingly, the ratio between the thermocouple mass $m_K$ and the sample mass $m_S$ must fulfill the relation $\frac{m_K}{m_S} \ll 1$ for the relative minimization of the exchanged heat which cause the temperature change at the thermocouple. In our case, this is accomplished for $m_s > 0.5$ g.

## 3.7 Measurement of $C_p$ by DSC

As seen in the previous sections, the analysis of the heat flow signal obtained by DSC technique hinders the distinction of the heat flow which accounts for the sample heating or cooling which is proportional to its particular heat capacity $C_p$. In contrast, the differential method of this technique allows particularly good sensitivity when the thermal reaction contributions exhibited by the sample are separated.

Although DSC does not explicitly provide actual $C_p$ values of the sample, there are accurate methods for its characterization which require a especial protocol of DSC measurements. In this section, the method for obtaining the sample $C_p$ values is provided and follows the description given in reference [61]. It relies on the fact that DSC measurement is repeated three times in similar conditions so that a clear separation of the $C_p$ contribution is obtained.

A first blank DSC run is performed which consists in a temperature scan without any sample at the sample holder of the calorimeter. A second temperature scan at the same heating or cooling rate as the previous measurement is performed, but in this case the sample under study is placed at its sample holder. Finally, the same measurement is performed with a sapphire sample ($\alpha$-aluminium oxide / $\alpha$-alumina) from which the heat capacity values are well reported elsewhere [62].

According to equation (3.6) the measured heat flow at the blank measurement (I), at the run with the sample (II), and at the run with the sapphire sample (III) corresponds to:

$$\dot{Q} = \begin{cases} C_R \dot{T}_0 & (I) \\ (C_R - C_S)\dot{T}_0 & (II) \\ (C_R - C_\alpha)\dot{T}_0 & (III) \end{cases} \tag{3.25}$$

where $C_R$, $C_S$, and $C_\alpha$ are the heat capacities of the reference, the sample under study, and the sapphire sample, respectively.

Figure 3.17 illustrates representative examples of a set of measurements (I), (II), and (III). Taking into account the expressions in (3.25), it is convenient to introduce $y$ and $y'$ as

$$y = \dot{Q}_{II} - \dot{Q}_I = -C_S \dot{T}_0 \tag{3.26}$$

$$y' = \dot{Q}_{III} - \dot{Q}_I = -C_\alpha \dot{T}_0 \tag{3.27}$$

because their fraction leads to the desired values of $C_S$:

$$C_S = C_\alpha \frac{y}{y'} \tag{3.28}$$

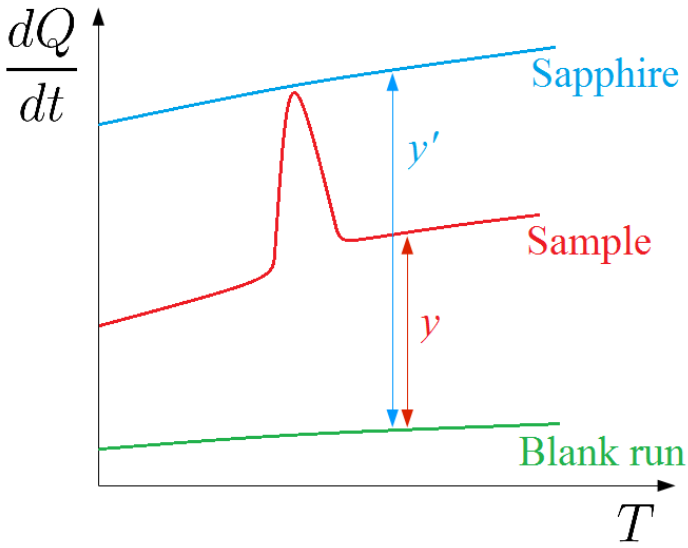


Fig. 3.17 Sketch of the heat flow measured at a blank measurement (I), at a run with the sample (II), and at a run with the sapphire sample, adapted from [61]. $y$ and $y'$ have been computed by subtracting the blank signal (I) from (II) and (III), respectively.

The performance of this method requires excellent reproducibility of the experiments conditions. In this sense, the commercial calorimetric equipments provided by Thermal Analysis (TA) like the DSC Q2000 setup available at the lab of the University of Barcelona can easily ensure a proper repetition of the temperature scans at approximately the same conditions.

## 3.8 Temperature-Modulated Differential Scanning Calorimetry

Temperature-modulated differential scanning calorimetry (MDSC) is an alternative version of the conventional DSC [58]. This method works with the same principles of conventional DSC, i.e. the measurement of the heat flow is performed differentially between a sample and an inert reference, but a sinusoidal temperature modulation[5] is superimposed to the linear heating or cooling ramp which leads to a gain of additional information. The MDSC measurements performed for this dissertation have been done with a Thermal Analysis (TA)

[5]This technique can also employ non-sinusoidal temperature modulations from which a sophisticated analysis of its signal provides further information on the thermal phenomena arising at the sample, although the simplest and most used modulation is the sinusoidal one [58].

Table 3.4 Typical parameters related to the TA MDSC Q2000 measurement performance: sample mass, underlying linear temperature scanning rate, modulation period and modulation amplitude.

| $m$ (mg) | $\alpha$ (K min$^{-1}$) | $t_p$ (s) | $T_A$ (K) |
|---|---|---|---|
| 10 - 100 | 1 - 10 | 30 - 100 | 0.1 - 2 |

Q2000 DSC setup which has the availability to perform both conventional and modulated techniques.

In a temperature modulated DSC with a sinusoidal function, the temperature of the calorimeter behaves as:

$$T(t) = T_0(t=0) + \alpha t + T_A \sin(\omega t) \tag{3.29}$$

where $\alpha$ is the *underlying* linear heating or cooling rate, $T_A$ is the temperature amplitude of the oscillation around the underlying linear scanning rate $T_u = T_0 + \alpha t$ and $\omega = \frac{2\pi}{t_p}$ is its angular frequency ($t_p$ is the period). Temperature varies with time as

$$\frac{dT}{dt} = \alpha + T_A \omega cos(\omega t) \tag{3.30}$$

The calibration procedure in TA Q Series equipments includes a subtraction of the heat flow obtained in blank measurements, i.e. a run without sample. This allows the direct determination of the heat exchange at the sample. In this sense, equation (3.6) can be directly rewritten as

$$\dot{Q} = C_S \frac{dT}{dt} + \frac{dH}{dt} \tag{3.31}$$

According to the right hand side terms in equation (3.31), the analysis of the measured heat flow can be divided into two cases depending on whether or not the sample exhibits any exothermic or endothermic process involving a latent heat ($\frac{dH}{dt} \neq 0$).

### 3.8.1 Absence of thermal events, $\frac{dH}{dt} = 0$

In absence of any thermal event involving an absorption or release of latent heat, the second term in the right hand side of equation (3.31) vanishes. The introduction of equation (3.30) in (3.31) leads to:

$$\dot{Q} = C_S\alpha + C_S T_A \omega \cos(\omega t) \tag{3.32}$$

The first term on the right hand side in equation (3.32) is related to the *underlying* linear heating (or cooling) of the sample ($\dot{Q}_u$) and is usually referred as the *total heat flow*. The second term is the *periodic* component of the heat flow ($\dot{Q}_p$). For a conventional DSC scan, the measured heat flow would directly be the underlying term. Thus, the presence of the periodic term adds up additional information on the calorimetric events of the sample.

In general, the heat capacity $C_S$ has a very weak temperature dependence and we can consider that it remains constant over the temperature interval scanned covering a period of modulation ($t_p$). With this in hand, the time average of the integration over a period of time $t_p$ of the heat flow expressed in (3.32) leads to the underlying term:

$$\frac{\int_{t_0}^{t_0+t_p} \dot{Q}dt}{T} = \frac{C_S}{T}\int_{t_0}^{t_0+t_p} \alpha dt + \frac{C_S T_A}{T}\int_{t_0}^{t_0+t_p} \omega\cos(\omega t)dt = C_S\alpha = \dot{Q}_u \tag{3.33}$$

A Fourier analysis of the measured heat flow allows the separation of the signal in the terms $\dot{Q}_u$ and $\dot{Q}_p$. The heat capacity can be obtained from the measured amplitude $A$ of the periodic term:

$$C_S = \frac{A}{T_A\omega} \tag{3.34}$$

Interestingly, the heat capacity is obtained from the periodic term and not from the underlying term from which it would be obtained in a conventional DSC run. This independence on the underlying term drastically reduces the error in the obtained values for $C_S$ because the error associated with this term is directly related to the subtraction of the blank baseline at the calibration process which has relatively large error bars.

### 3.8.2 Occurrence of thermal events, $\frac{dH}{dt} \neq 0$

When the sample exhibits an endothermal or exothermal event involving a latent heat, equation (3.31) is rewritten as:

$$\dot{Q} = C_S\alpha + C_S T_A \omega \cos(\omega t) + \frac{dH}{dt} \tag{3.35}$$

The last term in the previous equation is a function of temperature and time, i. e. $\frac{dH(T,t)}{dt}$. This term generally varies slowly with time and temperature and we can perform a Taylor

expansion to the first term around the mean temperature $T_u = T_0 + \alpha t$ which yields to the new expression

$$\begin{aligned}\dot{Q} &= C_S\alpha + C_S T_A \omega \cos(\omega t) + \frac{dH(T_u,t)}{dt} + \frac{d^2H(T_u,t)}{dT\,dt}(T - T_u) \\ &= C_S\alpha + \frac{dH(T_u,t)}{dt} + C_S T_A \omega \cos(\omega t) + \frac{d^2H(T_u,t)}{dT\,dt} T_A \sin(\omega t)\end{aligned} \tag{3.36}$$

where we have used $T - T_u = T_A \sin(\omega t)$ from equation (3.29). From equation (3.36) we can distinguish again the periodic ($\dot{Q}_p$) and the non-periodic ($\dot{Q}_u$) components which can be separated by Fourier analysis. These terms are written as:

$$\dot{Q}_u = C_S\alpha + \frac{dH(T_u,t)}{dt} \tag{3.37}$$

$$\dot{Q}_p = C_S T_A \omega \cos(\omega t) + \frac{d^2H(T_u,t)}{dT\,dt} T_A \sin(\omega t) = \dot{Q}_A cos(\omega t + \delta) \tag{3.38}$$

The term $\dot{Q}_u$ is the calorimetric signal which would be obtained if there was no temperature modulation ($T_A = 0$). The periodic contribution $\dot{Q}_p$ has been rearranged to solely one term in which the amplitude $\dot{Q}_A$ and the phase shift $\delta$ correspond to:

$$\dot{Q}_A = \sqrt{(C_S\alpha)^2 + (C_S T_A \omega \cos(\omega t))^2} \tag{3.39}$$

$$\delta = \arctan\left(\frac{d^2H(T_u,t)}{dT\,dt}(C_S\omega)^{-1}\right) \tag{3.40}$$

The sign of phase shift $\delta$ depends on whether the thermal event is entothermic or exothermic and the amplitude $\dot{Q}_A$ is always greater than the underline term ($\dot{Q}_A > \dot{Q}_u$) because the temperature derivative of the heat flow related to the thermal event comes into play.

The value of the heat capacity $C_S$ given by (3.34) is often referred to the *reversing heat capacity* and computed from the so-called *reversing heat flow*, which is the heat flow that is continuously absorbed and released by the sample upon the modulation. The *non-reversing heat flow* is calculated by subtracting the reversing heat flow from the total heat flow and gives the values of the *non-reversing heat capacity*. In the presence of irreversible processes the corresponding thermal contributions upon the modulation process are included in the non-reversing heat capacity.

## 3.9 SQUID magnetometry

The present section briefly outlines the principles of the magnetometry by means of Superconducting Quantum Interference Devices (SQUIDs), which are the most sensitive magnetometers and are based on superconducting loops containing Josephson junctions. The basics of this magnetometry technique has been considered to be summarized here because relevant magnetization measurements performed by SQUIDs are presented along the present dissertation. A detailed description of this technique can be found in [63, 64].

Let us consider a particular type-I superconductor which behaves as in ideal diamagnet with a critical temperature $T_C$ delimiting the superconducting phase. If the temperature of the system is $T < T_C$, the current through it is carried by pairs of electrons which are attracted due to a phonon-mediated interaction which push these particles to have a lower energy than the Fermi energy. These pairs are known as Cooper pairs or BCS pairs and are treated as single particles with twice the mass of an electron $2m_e$, twice their charge $q = 2e$ and the velocity $\mathbf{v}$ of the center of mass of the pair.

In a normal conductor the coherence length (i. e. the average length an electron travels before scattering) of a conduction electron is small because the electrons are scattered due to the impurities or the phonons in a solid. In contrast, the average maximum distance in which a Cooper pair travels is much longer and the particle is not scattered for distances with typical values between 1000 and 1 nm. In terms of the Ginzburg-Landau theory, this is defined as the *coherence length* of the superconductor and it specifies the distance over which the wave function $\psi = \psi e^{i(\mathbf{p}\cdot\mathbf{r})/\hbar}$ which describes the probability of finding the Cooper pair varies. $\mathbf{p}$ stands for the momentum of the particle and $\mathbf{r}$ is the position of its center of mass.

We can imagine now a superconducting ring with a current $I$ circulating through it [65]. The momentum of a Cooper pair is

$$\mathbf{p} = \hbar\mathbf{k} \tag{3.41}$$

where $\hbar$ is the reduced Planck constant, $|\mathbf{k}| \equiv \dfrac{2\pi}{\lambda}$ is the wavenumber of the particle and $\lambda$ is its wavelength. If the particle is under the influence of a magnetic field $\mathbf{B} = \nabla \times \mathbf{A}$, where $\mathbf{A}$ is the magnetic vector potential, the momentum is expressed as

$$\mathbf{p} = m\mathbf{v} + q\mathbf{A} \tag{3.42}$$

If we impose that there is an integer number $n$ of wavelengths within the ring, and we write together equations (3.41) and (3.42), the integration of the resulting equation over the whole ring being under consideration results in

$$2\pi n = \frac{m}{\hbar}\oint \mathbf{v}d\mathbf{r} + \frac{q}{\hbar}\oint \mathbf{A}d\mathbf{r} \tag{3.43}$$

Considering the Stokes' theorem and the definition of the magnetic flux $\Phi$ across the surface $\mathbf{S}$ defined by the ring, i.e. $\oint \mathbf{A}d\mathbf{r} = \int_S \nabla \times \mathbf{A}d\mathbf{S} = \int_S \mathbf{B}d\mathbf{S} = \Phi$, we have:

$$n\frac{h}{q} = \frac{m}{q}\oint \mathbf{v}d\mathbf{r} + \Phi \tag{3.44}$$

from which we can conclude that the magnetic flux $\Phi$ over a superconducting ring is a quantised magnitude. Accordingly, a magnetic flux quantum is $\Phi_0 = \frac{h}{q} = \frac{h}{2e} \sim 2.07 \cdot 10^{-15}$ Wb. For a more general case in which we have a density $n_s$ of superconducting charge particles and a current of particles with velocity $\mathbf{v}$, the supercurrent density is defined as $\mathbf{j} = qn_s\mathbf{v}$ and equation (3.44) can be rewritten as:

$$n\frac{h}{q} = \mu_0\lambda_L\oint \mathbf{j}d\mathbf{r} + \Phi \tag{3.45}$$

where $\lambda_L \equiv \sqrt{\frac{m}{\mu_0 q^2 n_s}}$ is the London penetration depth and is the distance to which the magnetic field penetrates into the superconductor. It usually takes very low values due to the Meissner effect. As a consequence of this ideal diamagnet behaviour, the current density is concentrated near the surface. We can take an integration path deep in the interior of the ring so that the first term on the right is negligibly small and approximate the magnetic flux as $\Phi = n\frac{h}{q} = n\Phi_0$.

The state determined by a uniform current density can be described collectively by the wave function $\Psi$ which is formed from the superposition of the wave functions $\psi_i$ of each Cooper pair. This wave function $\Psi$ maintains its *phase coherence* over long distances and, thus, the phase difference $\Delta\phi_{AB}$ between two points $A$ and $B$ through which a superconducting current circulates is kept constant in time. The application of a magnetic field $\mathbf{B}$ modifies the phase difference between $A$ and $B$ and adds up an additional term $[(\Delta\phi)_{AB}]_\mathbf{B}$ at the expression of the phase difference: $(\Delta\phi)_{AB} = [(\Delta\phi)_{AB}]_i + [(\Delta\phi)_{AB}]_\mathbf{B}$, where $[(\Delta\phi)_{AB}]_\mathbf{B} = \frac{2\pi}{\Phi_0}\int_A^B \mathbf{A}\,.\,d\mathbf{l}$. [65]

The phases $\phi_1$ and $\phi_2$ of two independently isolated superconducting regions with wavefunctions $\Psi_1$ and $\Psi_2$ are unrelated. The *Josephson Tunnelling* appears when there exists a weak link (an insulating barrier) between both superconductors called as the *Josephson junction* and the Cooper pairs are able to tunnel across the gap. In this circumstances, the wavefunctions of each superconductor become coupled and the Josephson current $I_J$ which crosses the junction is expressed as:

$$I_J = I_C \sin(\Delta\varphi) \tag{3.46}$$

where $I_C$ is the critical current and

$$\Delta\varphi = \phi_2 - \phi_1 - \frac{2\pi}{\Phi_0}\int_A^B \mathbf{A}d\mathbf{l} \tag{3.47}$$

$\phi_2$ and $\phi_1$ in (3.47) are the phases in the two superconducting electrodes. The DC Josephson effect refers to the Cooper pairs tunneling across the weak junction in absence of any external electromagnetic field. In this case, the current is bounded by the $\pm I_C$ values as described by (3.46). In the case of the AC Josephson effect a voltage $V$ is fixed across the junctions causing a linear variation of the phase and an AC current with the *Josephson frequency* $f_J = \dfrac{V}{\Phi_0}$.

A SQUID is a magnetic flux-voltage converter which consists of a loop of superconductor with one or more Josephson junctions. As denoted by (3.47) and (3.46), the current oscillates with the magnetic flux penetrating the Josephson junctions because it modifies the phase difference and as a result the SQUID can be sensitive to measure magnetic fields. The two main SQUID types are the Direct Current SQUID (DC SQUID) which have two Josepshon junctions at the superconducting loop and the Radio Frequency SQUID (RF SQUID) which have one Josephson junctions [66].

Concretely, we can focus on the measuring mechanisms of an RF SQUID like the commercial Quantum Design MPMS 5XL SQUID shown in figure 3.18 (a) and (b) in order to explain the performance of the SQUIDS with an illustrative example. The magnetic sample is mounted at the sample holder attached at the end of the sample rod and centered in the middle of a superconducting detection coil. The detection coil acts as a gradiometer and is able to detect magnetic flux gradients across the coil. The rod is actuated by a drive mechanism and makes the sample oscillate along the detection coils. Hence, the captured oscillatory flux induces a current which circulates through the SQUID input coil and induces a magnetic flux which is converted to a voltage output by the SQUID loop containing the Josephson juntion. The output voltage has an oscillatory character described by the Josephson effect and by a proper calibration taking into account the frequency of the sample motion a high sensitivity measurement of the sample magnetic moment can be obtained.

The setup incorporates a superconducting magnet which is responsible of magnetizing the sample and allow either the *isofield operation* consisting on measuring the sample magnetic moment while performing temperature scans at constant field and the *isothermal operation* consisting in magnetic field scans at constant temperature. The magnetic field operation

range is between $H = 0$ and $H = 5$ T and the measuring temperatures are between $T = 1.7$ K and 400 K. The maximum sensitivity of the sample moment is in the range of $10^{-9}$ emu.

## 3.10 Magnetometry under applied pressure

Indirect methods for the characterization of caloric effects require a detailed characterization of the behaviour of the order parameter as a function of the driving forces. Magnetometry under magnetic field and applied hydrostatic pressure appears to be an interesting experimental method for the indirect analysis of the multicaloric effect driven by both magnetic field and hydrostatic pressure because it can provide an entire map of the magnetization as a function of temperature, pressure and magnetic field $M(T, p, H)$ in the vicinity of the transition. The measurements of SQUID magnetometry under applied pressure have been performed in collaboration with Laura H Lewis and Radhika Barua by use of the setup available in the Department of Chemical Engineering, Northeastern University, Boston, USA.

The experimental system consists on the previously described Quantum Design MPMS 5XL SQUID shown in figure 3.18 (a) and (b) with the particular feature that the specially designed enclosure in which the sample is placed at the SQUID is responsible of the application of the hydrostatic pressure and enables the measurement of the sample magnetization as a function of $(T, p, H)$.

This enclosure is an easyLab ®Mcell 10 High-pressure Cell Module and moves accordingly with the MPMS oscillation needed for the magnetic moment measurement. In turn, its non magnetic CuBe composition ensures a proper sensitivity for the magnetic moment measurement. The components of the pressure cell are sketched in figure 3.18 (c). The sample (with maximum dimensions of 1.5 x 1.5 x 5 mm) is placed in a cylindrical PTFE sample holder filled with the pressure-transmitting fluid which applies the hydrostatic pressure up to values of 10 kbar (1 GPa). The enclosure is pressurized with a hydraulic press ram which enables the application of a known force on a tungsten carbide piston pushing onto the ceramic pistons. Consequently, the PTFE sample holder reduces its volume and increases its inner pressure.

### 3.10.1 Setup calibration

The calibration is performed by considering the shift of the Sn superconductor transition temperature as a function of the applied pressure. A calibration tin sample can be placed together with the measuring sample inside the PTFE sample holder. Once both samples are pressurized the desired measurement can be performed and the corresponding pressure can

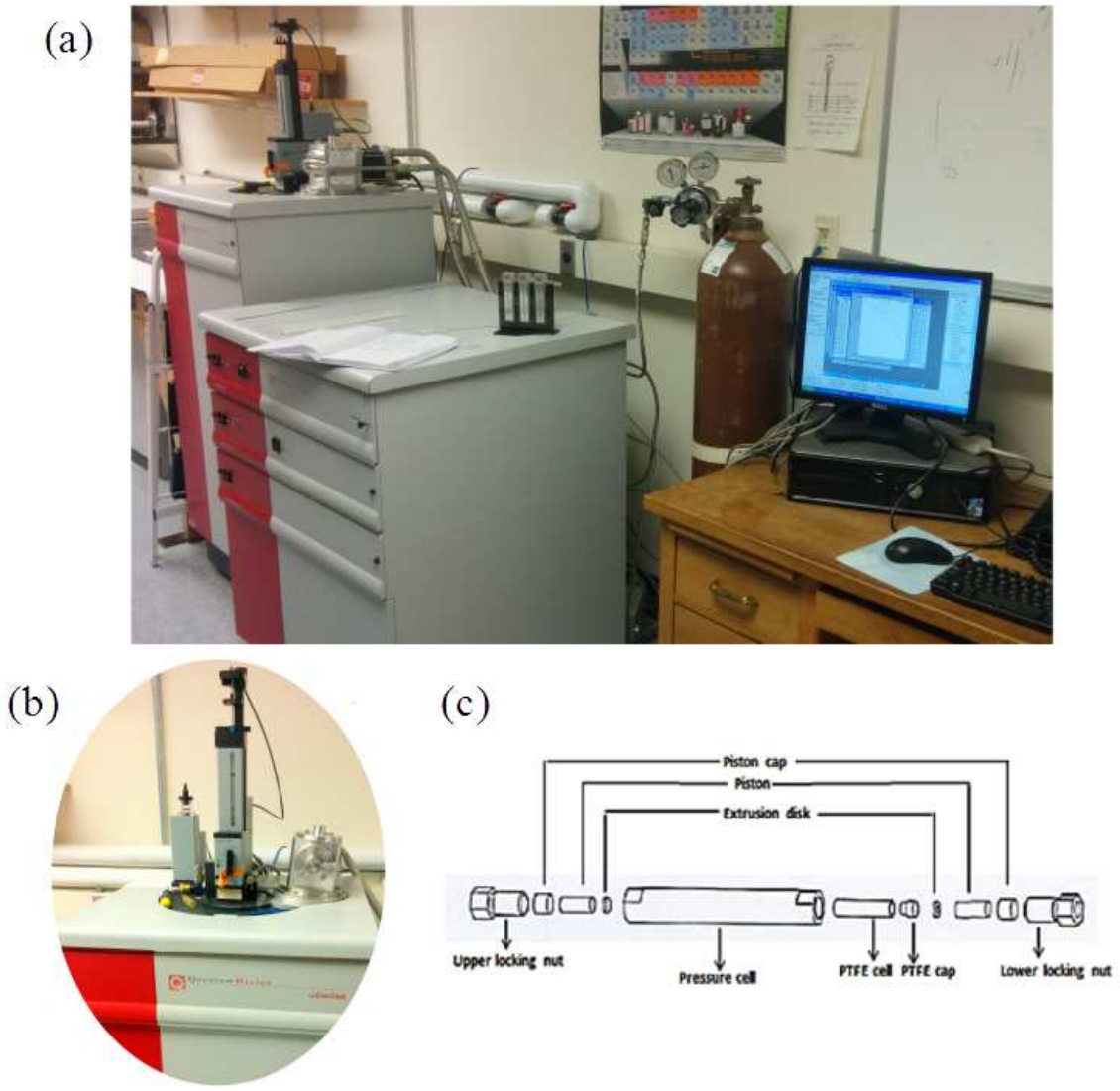


Fig. 3.18 (a): A general picture of the Quantum Design MPMS 5XL SQUID magnetometer at the Department of Chemical Engineering of the Northeastern University (Boston, USA). In the foreground, the computer with the software for monitoring the experiment and the data collection. On its left hand side, the component of the SQUID setup containing the power distribution unit and the control units related to the performance of the experiment which takes place inside the dewar unit which is the taller setup tower behind this component. This last unit has the sample probe and the superconducting magnet which reaches fields up to 5 T inside the solenoid. Picture (b) shows the top section of the dewar tower which contains the probe with the sample and its rotator, and the superconducting solenoids. The sketch in (c) illustrates the components of the CuBe piston clamp pressure cell (Mcell 10 manufactured by Almax EasyLab ®.

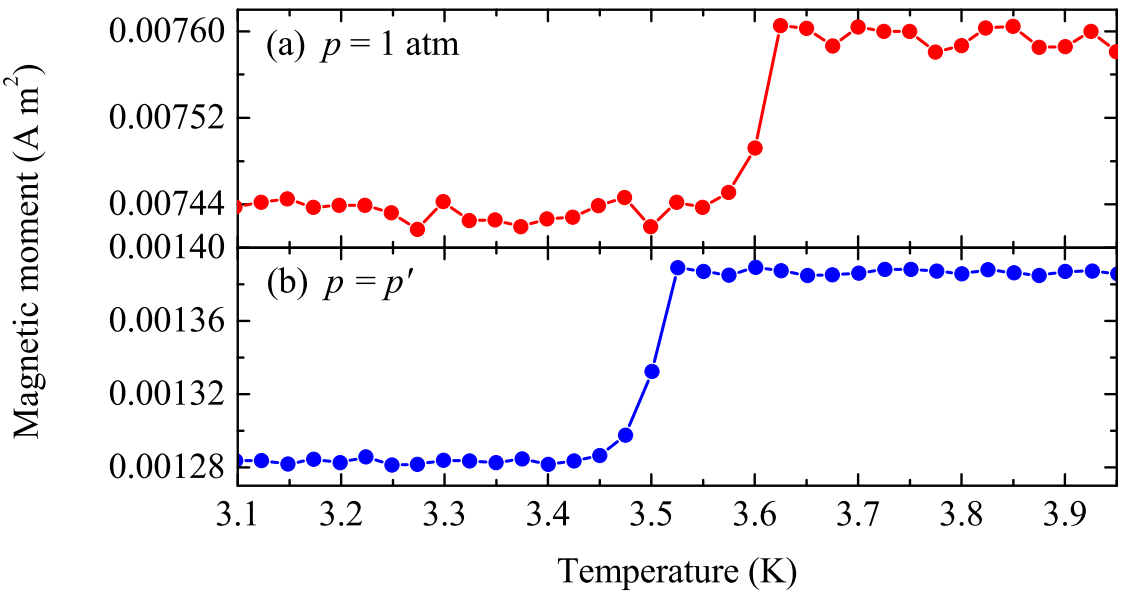


Fig. 3.19 Sn calibration for the magnetometry measurements under applied pressure. Panel (a) displays a cooling run for an unpressurized sample cell ($p \sim 1$ atm). The measured superconductor transition takes place at $T' = 3.624$ K. Panel (b) displays a cooling run for a pressurized sample cell at $p = p'$ with $T' = 3.525$ K.

be known by accurately measuring the magnetic moment on a cooling temperature scan at temperatures below 4 K as shown in figure 3.19. At a certain value of the temperature $T'$ a magnetic moment drop is detected which coincides the Sn superconductor transition due to the Meissner effect. $T_C(p)$ exhibits a temperature shift with the applied pressure $p = p'$ at which the cell has been pressurized. The value of the applied pressure $p'$ is thus known by comparing the measured $T'$ with the reported values of the Sn superconductor transition temperature as a function pressure [67].

# Chapter 4

# Giant caloric effects in $Fe_{49}Rh_{51}$

## 4.1 The FeRh system

The near equiatomic $Fe_{1-x}Rh_x$ $(0.47 \leq x \leq 0.53)$ intermetallic compound exhibits a first-order transition from a low temperature AFM phase to a high temperature FM phase at temperatures within the interval 300 K $\leq T_t \leq$ 370 K. Figure 4.1 shows the phase diagram of Fe-Rh and depicts a narrow region of interest where the rhodium atomic composition is comprised between 48 and 55 % values.

Within this composition range Fe-Rh solidifies in the CsCl structure ($Pm3m$ space group) and orders ferromagnetically below a Curie temperature around 680 K. Upon further cooling, this alloy undergoes a magnetic phase transition from a ferromagnetic (FM) ($\alpha'$ phase) to an antiferromagnetic (AFM) ($\alpha''$ phase) state. This transition is first-order, strongly composition dependent, and does not involve breaking the crystal symmetry. In the FM state Fe atoms have a $\sim 3\mu_B$ moment and Rh atoms $\sim 1\mu_B$, while in the AFM state there is no appreciable magnetic moment in Rh atoms and Fe atoms have $\sim 3\mu_B$ moment with opposite sign on successive layers of (111) iron planes [8]. The first-order phase transition involves a significant latent heat (with associated entropy change), and due to a strong magnetostructural coupling the volume of the unit cell increases by $\sim 1\%$ at the AFM to FM transition. A sketch of the FM and AFM structures is illustrated in figure 4.2. The rest of the phase diagram shown in figure 4.1 is covered by the presence of $\alpha$ phase (body centered cubic, space group: $Im3m$), $\gamma$ phase (face centered cubic, space group: $Fm3m$), $\delta$ phase (body centered cubic, space group: $Im3m$) and the liquid phase $L$ [68].

Although the magnetic transition in Fe-Rh was discovered in the late 1930s [9], the physical origin of the mechanisms giving rise to this transition is still a source of active debate [69–74]. In recent years there has been renewed attention on the study of Fe-Rh due to its potential technological interest. On the one hand, the AFM-FM phase transition which

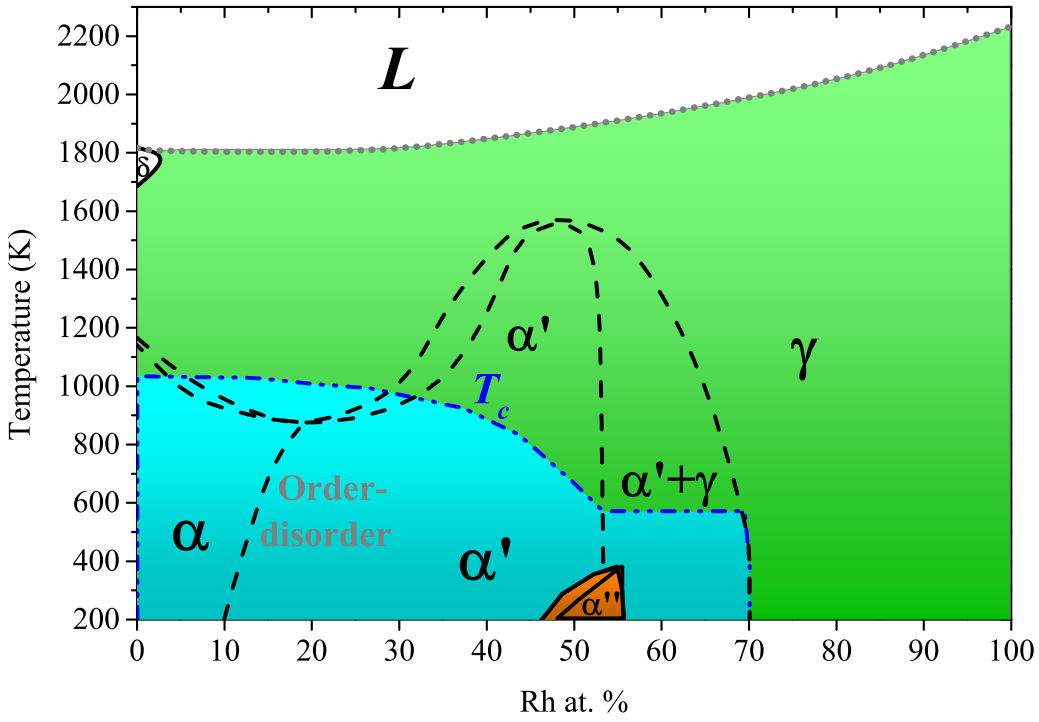


Fig. 4.1 Phase diagram of $Fe_{100-x}Rh_x$ system as a function of the atomic percent of rhodium. The green region is paramagnetic, the blue region is ferromagnetic and the orange is antiferromagnetic. This figure has been adapted from ref. [68].

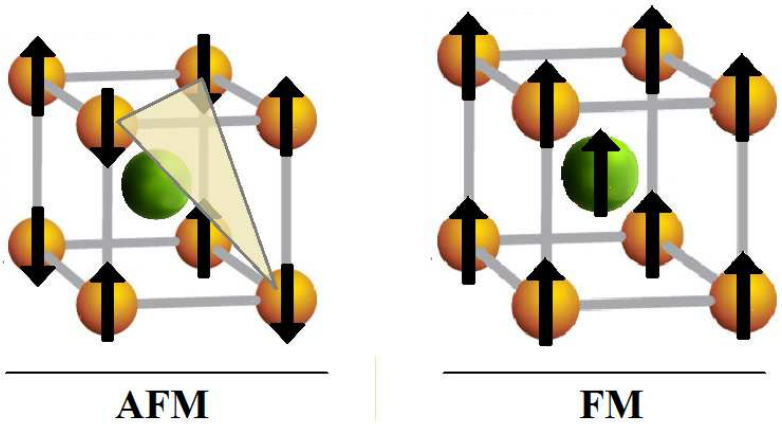


Fig. 4.2 Sketch of the AFM (left) and FM (right) atomic structures and their corresponding magnetic spin configurations indicated by the black arrows. Both phases have the same CsCl structure, but the volume of the FM cell is $\sim 1$ % larger. The larger green atoms represent the Rh atoms which settle at the central position and Fe atoms are represented by orange balls at the corners. The yellow triangle painted at the AFM structure indicates the (1,1,1) plane containing the Fe atoms with parallel spin configuration.

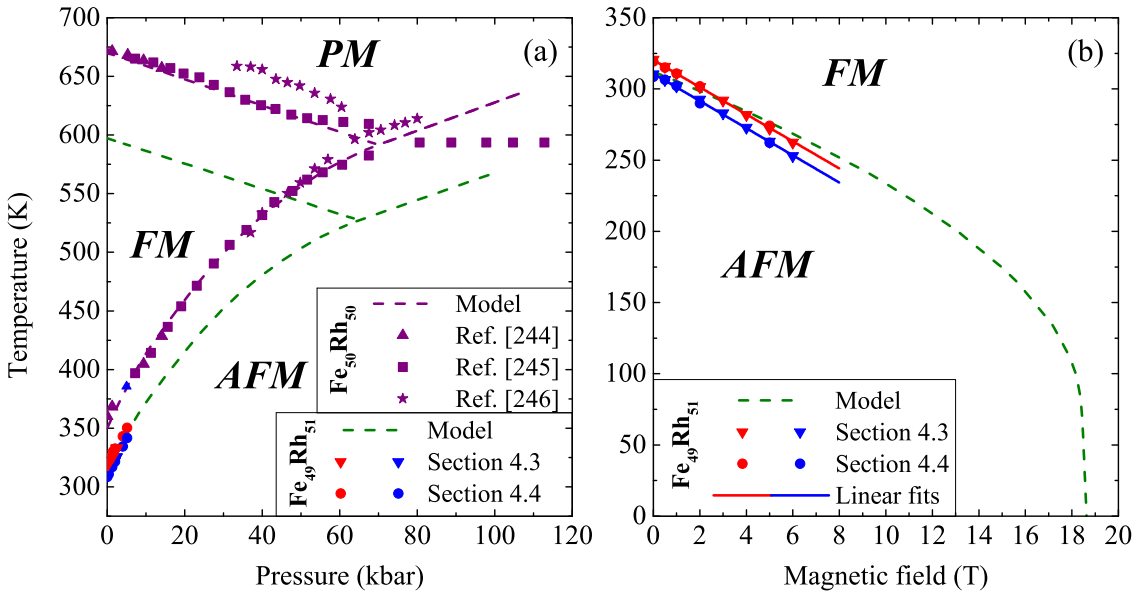


Fig. 4.3 Phase diagram of Fe-Rh. Transition temperature as a function of pressure (a) and magnetic field (b) for $Fe_{50}Rh_{50}$ and $Fe_{49}Rh_{51}$. Results from the mean field model described in the appendix B of the dissertation are denoted by dashed lines while symbols correspond to the experimental data presented in sections 4.3 and 4.4.

occurs at temperatures close to ambient has been found to be useful in thermally assisted magnetic recording devices [75]. On the other hand, the latent heat of the transition gives rise to a large entropy change when the transition is driven by an external field, which results in giant caloric effects suitable for solid state refrigeration near room temperature.

## 4.2 Motivation

In 1990 Nikitin et al. reported *The magnetocaloric effect in $Fe_{49}Rh_{51}$ compound* [10] which signified the first paper reporting a *giant* magnetocaloric response. Since then, this material has remained as a model magnetocaloric material due to the great sensitivity of the transition to applied magnetic fields and its magnetocaloric perfomance. However, FeRh was considered to be of no practical use because the effect was believed to be irreversible in an alternating magnetic field and even to disappear after a few cycles [46, 76, 77]. Later studies indicated that reproducibility could be achieved for 5 T fields provided that the sample was subjected to a proper combination of isothermal and adiabatic processes [78]. With regards to mechanocaloric effects, studies of the AFM-FM transition under uniaxial stress showed that this alloy also exhibited an elastocaloric effect [32]. Both magnetocaloric and elastocaloric effects were found to be inverse. In Fe-Rh, the symmetry-adapted strain-tensor component

describing the structural change accompanying the AFM-FM transition is a dilational strain (volume change), which couples to hydrostatic pressure. It is therefore expected that the transition will be more sensitive to hydrostatic pressure than to uniaxial stress, and there is indeed evidence of a strong dependence of the transition temperatures to hydrostatic pressure as shown in figure 4.3 (a) [79, 80]. These facts point to the existence of a large barocaloric effect at the AFM-FM pressure-induced transition. Moreover, since pressure increases the stability of the low-volume (AFM) phase in such a way that the AFM-FM transition temperature shifts to higher values with increasing pressure, it can be anticipated that the associated barocaloric effect will be conventional.

As illustrated in the phase diagram shown in figure 4.3 the strong hydrostatic pressure and magnetic field sensitivity of the transition the first-order transition exhibited by the near equiatomic Fe-Rh system has the proper elements for a large field-driven caloric response. Understanding the physical mechanisms which drive this response and studying in depth its caloric performance under the influence of external stimuli is of great interest. This chapter is aimed at describing the caloric effects in Fe-Rh driven by mechanical stresses (hydrostatic pressure and uniaxial compression) and magnetic field by taking advantage of the unique experimental techniques described in section 3.

First, an independent characterization of the magneto- and barocaloric effects is presented which is based on a complete characterization of the field driven entropy change and the adiabatic temperature change by means of direct and quasi-direct techniques[1]. Second, the caloric response is then analysed when both pressure and magnetic field are applied either simultaneously or sequentially so that the multicaloric effect emerges. Third, the magnetocaloric effect is analysed when magnetic fields are applied under the additional influence of compressive uniaxial stress.

[1]The corresponding results have been published in references [81, 82].

## 4.3 Barocaloric and magnetocaloric effects in Fe-Rh

### 4.3.1 Sample details

A polycrystalline sample of nominal composition $Fe_{49}Rh_{51}$ was prepared in collaboration with the Indian Association for the Cultivation of Science (IACS) settled in Kolkata (India) by arc melting the pure metals under argon atmosphere in a water-cooled Cu crucible. For homogeneity, the sample was remelted several times. Next, the ingot was vacuum sealed in a quartz tube and annealed at 1100 ºC for 72 h followed by a furnace cooling to room temperature.

From the ingot a 3.3 mm $\times$ 3.0 mm $\times$ 5.6 mm parallelepiped sample (504.36 mg mass) was cut for calorimetric measurements under pressure and for the measurement of the adiabatic temperature change driven by magnetic fields. A 1 mm diameter and 2 mm length hole was drilled in that sample to host the thermocouple in both cases. A second thinner sample (190.1 mg mass) with 1.1 mm thickness and a flat surface of 5.5 mm $\times$ 6.4 mm was cut for calorimetric measurements under applied magnetic field. A long shaped portion of 112.2 mg was cut from the ingot and it was used for magnetization measurements.

### 4.3.2 Experimental details

- **Calorimetric measurements under hydrostatic pressure** were carried out by means of the custom-built calorimeter described in section 3.4. The thermal signal was measured by a chromel alumel thermocouple embedded into the sample. Calorimetric runs are performed by scanning temperature at typical rates 2 K $min^{-1}$ (heating) and 1 K $min^{-1}$ (cooling) while hydrostatic pressure was kept constant. From the calorimetric curves at selected values of pressure, the entropy change (referenced to a given state at $T_0$ above the phase transition) is computed as described in 3.1.1.

- **Calorimetric measurements under magnetic field** were carried out by means of the custom-built high-sensitivity differential scanning calorimeter (DSC) described in section 3.2. This device allows both isofield measurements performed by scanning the temperature (typical rates 0.5 K $min^{-1}$) and isothermal measurements performed by scanning the magnetic field (typical rates 0.16 T $min^{-1}$). From these measurements quasi-direct (isofield data) and direct (isothermal data) computations of the entropy change are performed as described in section 3.1.1.

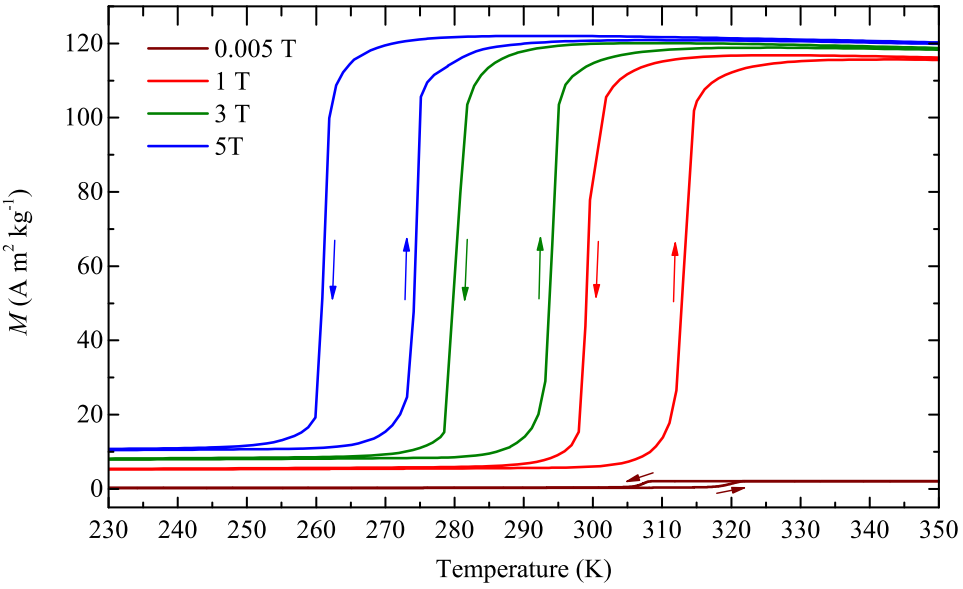


Fig. 4.4 Temperature dependence of the magnetization for cooling and heating runs under applied magnetic field (0.005, 1, 3, and 5 T).

- **The magnetocaloric temperature change** was measured by means of the setup described in section 3.6 based on the fine gauge K thermocouple (0.075 mm diameter) embedded into the hole drilled to the sample.
- **Magnetization measurements** were carried out in a Physical Property Measurement System (PPMS, Quantum Design) provided by the Institut de Ciència de Materials de Barcelona (ICMAB), Barcelona (Catalonia).

### 4.3.3 Results and discussion

The temperature dependence of magnetization $M(T)$ measured during cooling and heating runs across the AFM-FM transition is shown in figure 4.4 for selected values of the magnetic field. It is found that $M(T)$ remains almost temperature independent in both AFM and FM phases and sharply changes at the AFM to FM transition on heating and at the FM to AFM transition on cooling, with a thermal hysteresis which compares well to that derived from calorimetric data.

#### The barocaloric and magnetocaloric entropy change in $Fe_{49}Rh_{51}$

Figure 4.5 shows the isofield calorimetric curves (sweeping temperature) at selected values of hydrostatic pressure without magnetic field and the top panel in figure 4.6 shows the

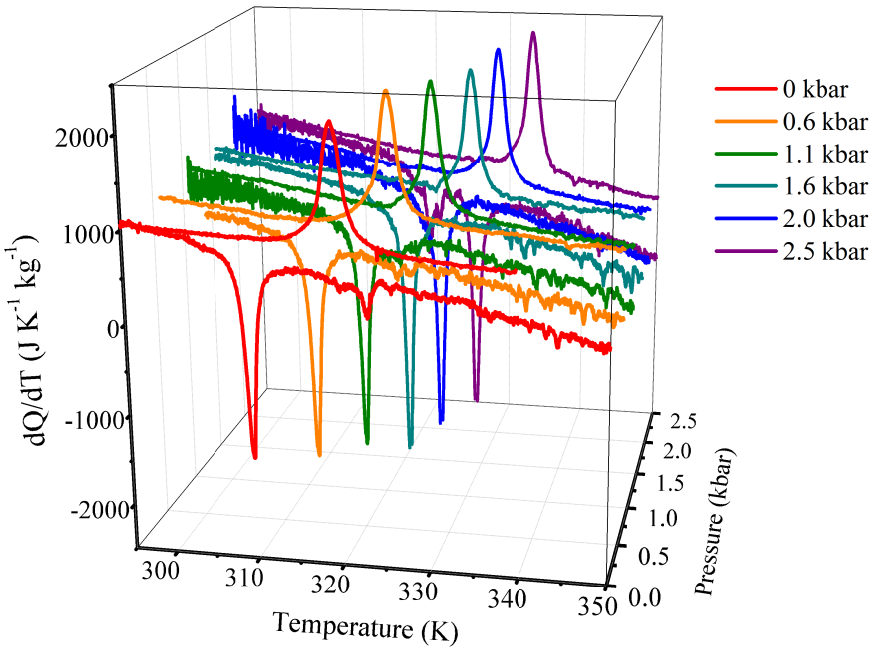


Fig. 4.5 Isofield calorimetric curves recorded at selected values of hydrostatic pressure. Positive peaks refer to heating runs and negative peaks to cooling runs.

isofield calorimetric curves at selected values of magnetic field at atmospheric pressure. The magnetostructural transition gives rise to a large exothermal peak on cooling and endothermal peak on heating. The transition is sharp (it spreads over less than 5 K) and takes place with a thermal hysteresis width of 10 K. The transition shifts to higher temperatures with increasing pressure while it shifts to lower temperatures with increasing magnetic field. This behaviour is consistent with pressure stabilizing the lower volume AFM state and magnetic field stabilizing the larger magnetization FM phase.

As previously mentioned, the reproducibility in the magnetocaloric effect has been a controversial issue [46, 76–78]. Isothermal DSC with magnetic field enables direct determination of the magnetic-field-induced entropy change and it is a unique tool to study the reproducibility of the magnetocaloric effect upon field cycling [83, 84]. We have performed calorimetric measurements at selected values of the temperature while magnetic field was swept. The measurement protocol is described in detail in section 3.1.1 and reference [50]. Figure 4.6 (bottom) shows the isothermal calorimetric signal (sweeping magnetic field) recorded on the first application (positive peaks) and first removal (negative peaks) of a 6 T field at selected values of temperature. Increasing the field drives the sample from AFM to FM phase with the absorption of latent heat (endothermal process) while the sample transforms from FM

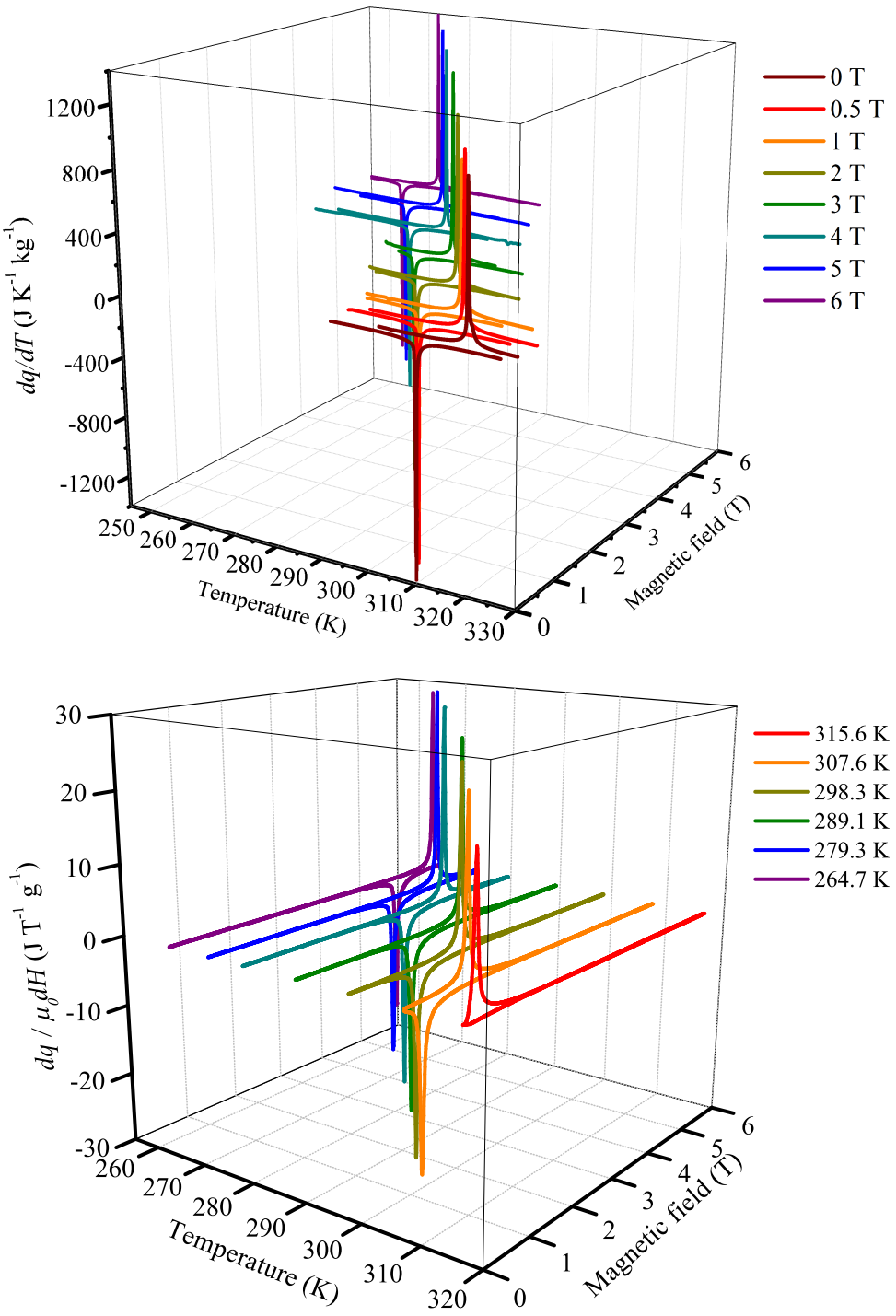


Fig. 4.6 Top panel: Isofield calorimetric curves recorded at selected values of magnetic field. Positive peaks refer to heating runs and negative peaks to cooling runs. Bottom panel: set of illustrative isothermal calorimetric curves collected upon application (positive peaks) and removal (negative peaks) of magnetic field. A previous thermal excursion towards either the high temperature phase or the low temperature phase has been performed before each isothermal measurement following the protocol described in section 3.1.1

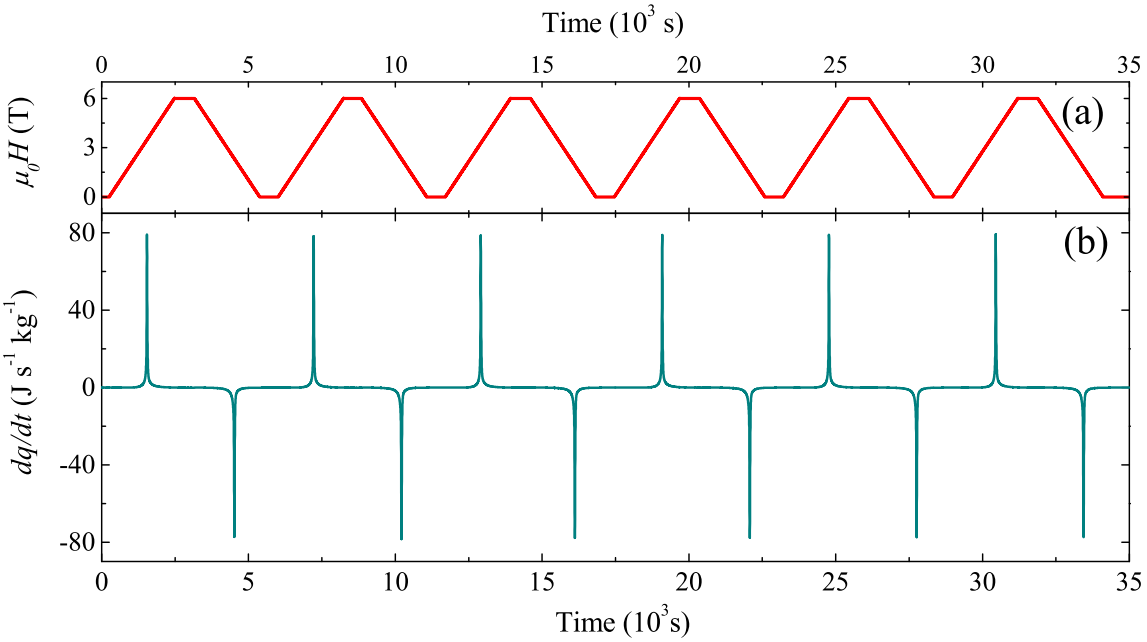


Fig. 4.7 (a) Applied magnetic field and (b) recorded isothermal calorimetric curves as a function of time. Data correspond to isothermal field cycles between 0 and 6 T at a temperature of 289.1 K.

to AFM upon removal of the field and releases the latent heat (exothermal process). An illustrative example of the recorded calorimetric signals upon isothermal successive magnetic field cycles between 0 and 6 T is shown in figure 4.7. The good reproducibility exhibited by calorimetric curves demonstrates an excellent reversibility of the magnetocaloric effect.

Figure 4.8 shows the temperatures of the calorimetric peaks for $[T_{tc}(p,H)]$ forward (FM to AFM) and $[T_{th}(p,H)]$ reverse (AFM to FM) transitions plotted as a function of applied pressure and magnetic field. At this range of the applied pressure and magnetic field, data exhibit a very good linear behaviour. For the forward transition the linear fits are

$$T_{tc}(p,0) = (309.7 \pm 0.1) + (6.4 \pm 0.1)p \tag{4.1}$$

$$T_{tc}(0,H) = (311.2 \pm 0.3) + (-9.6 \pm 0.1)\mu_0 H \tag{4.2}$$

whereas for the reverse transition:

$$T_{th}(p,0) = (319.0 \pm 0.4) + (5.4 \pm 0.2)p \tag{4.3}$$

$$T_{th}(0,H) = (320.6 \pm 0.1) + (-9.7 \pm 0.1)\mu_0 H \tag{4.4}$$

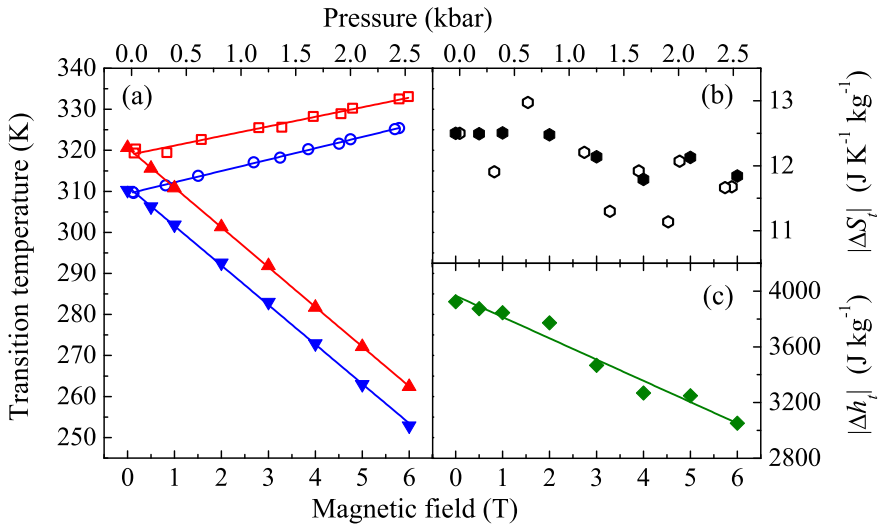


Fig. 4.8 (a) Temperature of the calorimetric peak as a function of pressure (open symbols) and magnetic field (solid symbols). Blue symbols (down triangles and circles) stand for cooling runs while red symbols (up triangles and squares) stand for heating runs. Solid lines are linear fits to the data. (b) Averaged values (between heating and cooling) for the transition entropy change as a function of pressure (open symbols) and magnetic field (solid symbols). (c) Averaged values (between heating and cooling) for the transition enthalpy change as a function of magnetic field. The line is a linear fit to the data.

Thermal hysteresis is not significantly affected by the magnetic field and it marginally decreases with increasing pressure. At much higher pressures (>50 kbar) the pressure dependence of the transition temperature is expected to weaken as the sample approaches the triple point as depicted in figure 4.3 [79].

The entropy ($\Delta S_t$) and enthalpy ($\Delta H_t$) changes corresponding to the AFM-FM transition are derived by numerical integration of calorimetric curves as described in section 3.1.1. Averaged (heating and cooling) values are shown in figures 4.8(b) and 4.8(c) respectively. The values at zero field and atmospheric pressure $\Delta S_t = 12.5 \pm 1$ J K$^{-1}$ kg$^{-1}$ and $\Delta H_t = 3900 \pm 150$ J kg$^{-1}$ are in agreement with previously reported data [85]. It is worth noting that for the studied magnetostructural transition, $\Delta H_t$ is to a very good approximation the energy difference ($E$) between AFM and FM phases.

Isofield calorimetric curves at selected values of hydrostatic pressure and magnetic field enable us to determine the isothermal entropy changes (quasidirect method) associated with the barocaloric and magnetocaloric effects. Quasi-direct results are plotted in figure 4.9 with solid lines. The barocaloric effect has been found to be conventional and the magnetocaloric effect is inverse. That is, while isothermal application of pressure reduces the total entropy, the magnetic field increases the total entropy of the alloy. The conventional and inverse

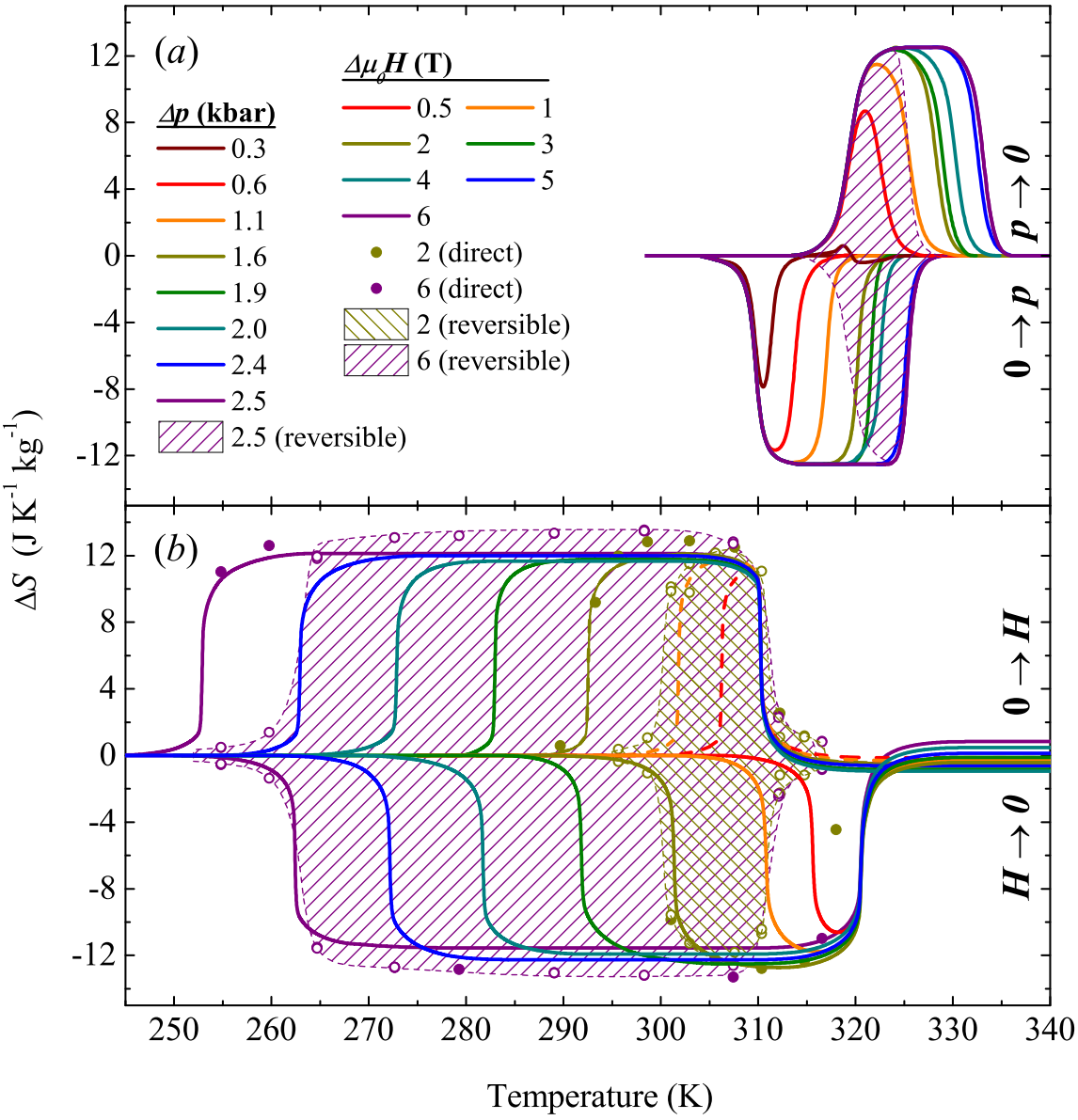


Fig. 4.9 (a) Pressure-induced entropy change (barocaloric effect) and (b) magnetic-field-induced entropy change (magnetocaloric effect) as a function of temperature for selected values of hydrostatic pressure and magnetic field. Coloured lines refer to the quasi-direct determination of the entropy change and the corresponding values of pressure and magnetic field change are displayed in the legend written in (a). The dashed area illustrates the reversibility region of the entropy change upon cycling the sample at 2.5 kbar (purple) (a) and at 6 T (purple) and 2 T (dark yellow) (b). In (b) symbols represent the field-induced entropy values computed from isothermal thermal curves (direct method). Solid symbols correspond to the first application (or removal) of the field and open symbols correspond to successive field cycling.

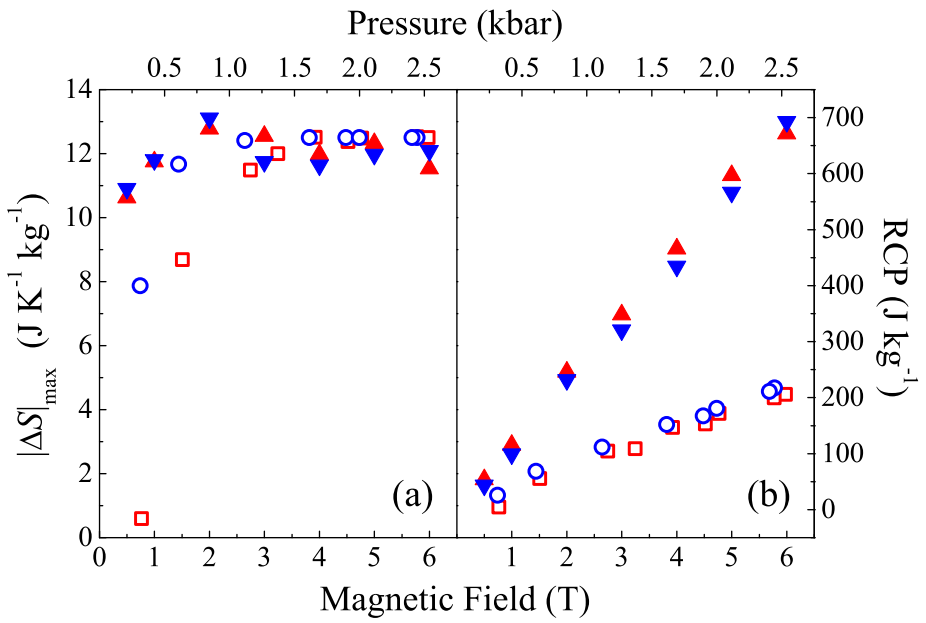


Fig. 4.10 Absolute value of the maximum entropy change (a) and relative cooling power (b) as a function of pressure (open symbols) and magnetic field (solid symbols). Blue symbols (down triangles and circles) stand for cooling runs and red symbols (up triangles and squares) stand for heating runs.

natures of barocaloric and magnetocaloric effects are consistent with pressure stabilizing the low-temperature AFM phase and magnetic field stabilizing the high-temperature FM phase. In the case of the magnetocaloric effect, integration of isothermal calorimetric curves provides a direct determination of the field-induced entropy change ($\Delta S$). Direct results for 2 and 6 T are plotted in 4.9 (b) as symbols (dark green and purple, respectively). There is good agreement between the two sets of data. The reproducibility of $\Delta S$ has been studied by isothermal calorimetric measurements under cyclic variation of magnetic field like the measurement plotted in figure 4.7. $\Delta S$ values are computed from numerical integration of these curves and are constant upon successive field cycling within experimental error. Data for all studied temperatures at 2 and 6 T are indicated as open symbols in figure 4.9.

The pressure-induced entropy change and magnetic-field induced entropy change increase in magnitude as pressure and magnetic field increase, respectively, until a saturation value is reached. This behaviour gives rise to a plateau in the $\Delta S$ vs $T$ curves. Both barocaloric and magnetocaloric effects saturate to the same value, which is coincident with the transition entropy change $|\Delta S_t|$. This result shows that both caloric effects have the same origin, and the giant values for the pressure-induced and field-induced entropy changes are a consequence of the magnetostructural transition which involves a large entropy change $\Delta S_t$. The saturation

value for the barocaloric and magnetocaloric effects is reached for low values of pressure and magnetic field, as illustrated in figure 4.10 (a) which shows $\Delta S_{\max}$, the absolute value of the maximum in the $\Delta S$ vs $T$ curves depicted in figure 4.9, as a function of pressure and magnetic field.

As described in section 2.2.3, the performances of a given material for solid-state refrigeration are typically analysed in terms of the relative cooling power RCP = $|\Delta S|_{max} \times \delta T_{FWHM}$, where $\delta T_{FWHM}$ is the temperature width at half maximum of the $\Delta S$ vs $T$ curves (figure 4.9). The RCP provides an estimate of the amount of heat that can be transferred in a field cycle between cold and hot reservoirs. These values are shown in figure 4.10 (b) for the barocaloric and magnetocaloric effects.

Reversibility of a given caloric effect is expected to be restricted within a certain temperature range which depends on the magnitude of the applied external field. This region can be determined from experiments carried out both on cooling and heating [50] and is indicated as a shaded area in figure 4.9. In the case of a conventional caloric effect (as the barocaloric effect here) this region is bounded by the transition temperature of the reverse (AFM to FM) transition at atmospheric pressure and the transition temperature of the forward (FM to AFM) transition under applied pressure. For an applied pressure of 2.5 kbar the region where barocaloric effect will be reproducible extends from 319 to 325 K. For an inverse caloric effect (such as the magnetocaloric here) the reversibility region is bounded by the reverse (AFM to FM) transition temperature under applied field and the forward (FM to AFM) transition temperature at zero field. The magnetocaloric effect is reversible within 294 and 306 K for 2 T and within 257 and 306 K for 6 T.

The isothermal entropy changes associated with the barocaloric and magnetocaloric effects saturate for pressures $\sim$ 1 kbar and fields $\sim$ 1 T to a value which coincides with the total transition entropy change (see figure 4.10). Such a tendency towards saturation has not been found in other giant magnetocaloric materials. For instance, in Gd-Si-Ge, the entropy change shows a monotonic increase with increasing magnetic field [86] while in some magnetic shape memory alloys the entropy change increases up to a maximum value and decreases upon further increasing magnetic field [87]. These different behaviours can be understood by taking into consideration that the entropy change contains contributions from the latent heat (transition entropy change) and also intrinsic contributions from both high-temperature and low-temperature phases [88]. For the particular case of Fe-Rh the fact that magnetocaloric and barocaloric data saturate to a value which coincides with the transition entropy change indicates that the intrinsic magnetic and elastic contributions of the AFM and FM phases are small. In the magnetic case, the importance of these intrinsic contributions is given by the value $\left(\frac{\partial M}{\partial T}\right)_H$ in each phase. As shown in figure 4.4, $M$ vs $T$

curves are almost flat in both AFM and FM phases, for different values of magnetic field, and the estimated intrinsic contributions to $S$ are one order of magnitude lower than that from the magnetostructural transition. In the FM state, such a weak temperature dependence is due to an almost saturated FM order since the transition takes place well below the Curie point. In the AFM, neither temperature nor magnetic field significantly affect the AFM order. This could be attributed to a large magnetocrystalline anisotropy.

For the barocaloric effect, the intrinsic contribution is given by

$$S = \int_0^{p'} \beta V dp \tag{4.5}$$

where $\beta = \frac{1}{V}\left(\frac{\partial V}{\partial T}\right)_p$ is the thermal expansion and $V$ is the specific volume. By using reported data for $\beta$ and $V$ [72], we estimate that for $p' = 2.5$ kbar this contribution amounts to $\sim 0.6$ J kg$^{-1}$K$^{-1}$ in the AFM phase and to $\sim 0.5$ J kg$^{-1}$ K$^{-1}$ in the FM phase. These values are small compared to the contributions arising from the transition entropy change.

Although a dependence of the transition entropy change on pressure and magnetic field falls within experimental errors, data show a tendency to slightly decrease with increasing pressure and magnetic field [figure 4.25 (b)]. Previous indirect measurements from magnetization data indicated a larger decrease in the isothermal $S$ with increasing magnetic field [76]. By contrast, the energy difference between AFM and FM phases shows a marked decrease as magnetic field increases [figure 4.25 (c)], with an average rate $\frac{d\Delta E}{d\mu_0 H} \backsimeq -150$ J kg$^{-1}$ T$^{-1}$. It is worth noting that recent adiabatic calorimetry experiments [72] did not find any magnetic field dependence of the specific heat of AFM and FM samples which would point to a magnetic-field-independent transition enthalpy change. Probably the different behaviour must be ascribed to a highest sensitivity of differential scanning calorimetry in determining enthalpy changes, and also to the fact that specific heat data correspond to two different samples while present experiments are carried out on a single specimen. It is acknowledged that the features of the AFM/FM transition in Fe-Rh are extremely sensitive to composition [74].

### The barocaloric and magnetocaloric temperature change in $Fe_{49}Rh_{51}$

Taking into account that in Fe-Rh magnetic field stabilizes the high temperature FM phase (as heating does) which results in an inverse magnetocaloric effect, the protocols described in section 3.1.1 were followed to carry out the adiabatic temperature measurements associated with the magnetocaloric effect. Hence, a previous thermal excursion towards a full AFM

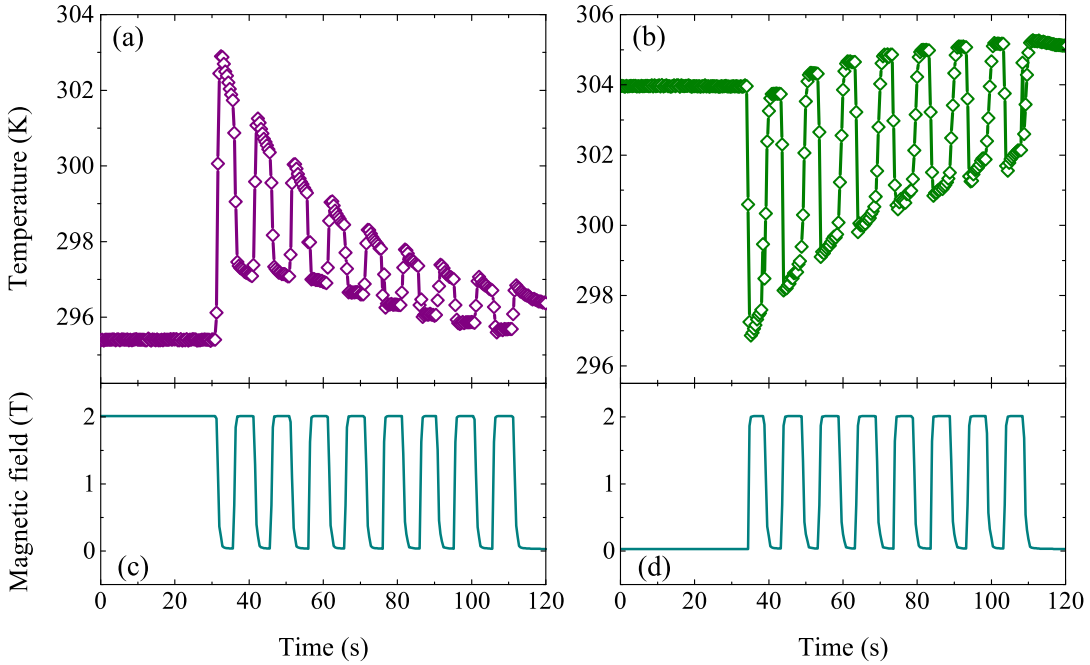


Fig. 4.11 Illustrative examples of the recorded temperature (a) and (b) and magnetic field (c) and (d) as a function of time. Left panels correspond to a cooling protocol and right panels to a heating protocol.

state which precedes a heating (heating protocol) ending at a state at isothermal equilibrium at the starting temperature of the measurement ($T_1$) or, otherwise, the sample is thermally brought to a full FM state under a constant magnetic field of 2T which precedes a cooling (cooling protocol) down to a state at isothermal equilibrium at the starting temperature of the measurement ($T_1'$).

In each case once the sample had reached the new thermal equilibrium, the magnetic field was cycled 10 times, starting with a $0 \rightarrow 2$ T magnetic field scan (heating protocol) or a 2 T $\rightarrow 0$ scan (cooling protocol). Figure 4.11 illustrates examples of the temperature and magnetic field measurements recorded during cooling (figures 4.11 (a) and 4.11 (c)) and heating (figures 4.11 (b) and 4.11 (d)) protocols. No noticeable traces of cracking were observed on the specimen after the sample was cycled through the AFM-FM transition many times (between 50 and 100 cycles).

Quasidirect determination of the adiabatic temperature change can be computed by subtraction of the entropy curves $S(T,p,H)$ at different values of hydrostatic pressure $p$ (at $H=0$) or magnetic field $H$ (at $p=0$) which are obtained from the calorimetric measurements under external field. At temperatures above and below the first order phase transition, $S(T,p,H)$ are obtained from specific heat $C$ data, while within the transition region (between

$T_1$ and $T_2$), accurate measurements come from differential scanning calorimetry (DSC) under field. The entropy curves (referenced to the value at a given temperature $T_0$) for heating runs are then computed as expressed in equation (3.19) section 3.1.1.

By using the previously presented DSC data under magnetic field and under hydrostatic pressure, and reported values of $C$ in the AFM and FM phases, [72], we have computed the entropy curves $S(T,p,H)$ at atmospheric pressure and fields for $\mu_0 H = 0$ and 2 T and, in the absence of magnetic field, for atmospheric pressure (taken as $p = 0$) and $p = 2.5$ kbar. In our calculations we have made the usual assumption that beyond the transition region $C$ does not significantly depend upon magnetic field and pressure. Furthermore, in order to account for the slight difference in the transition entropy change between present sample and the sample employed for the calorimetric measurements, DSC results have been scaled by a factor 0.9.

Figure 4.12 compiles the whole set of results. Left panels refer to the barocaloric effect and right panels refer to the magnetocaloric effect. Top panels display the entropy curves $S(T,p,H)$ where dashed lines correspond to cooling curves and solid lines, to heating curves. Subtraction of the curves provides the estimated adiabatic temperature changes, as indicated by the horizontal arrows, and left/right arrows indicate the reversible values corresponding to successive field cycling. Bottom panels display the $\Delta T$ values. Solid lines refer to the values computed from the entropy curves and the reversibility region corresponds to the shaded region. The magnetocaloric $\Delta T$ values depicted in figure 4.12 (d) also include the direct measurements. Solid symbols correspond to the first application (green circles) and removal (purple circles) of the field, while open symbols stand for the data recorded upon successive field cycling. For the sake of clarity, error bars are only displayed for the data corresponding to the first application and removal of the field, and are estimated from reproducibility of three independent measurements.

In accordance with the inverse nature of the magnetocaloric effect in Fe-Rh, application of magnetic field results in cooling while removal of the field heats the sample. The maximum values found for the first application (and first removal) of the field are very large ($|\Delta T| = 8K$), which result in a magnetocaloric strength which is among the largest values reported for giant magnetocaloric materials [1]. Upon successive cycling of the magnetic field, $|\Delta T|$ decreases but still large values ($|\Delta T| = 6$ K) are obtained. It is also worth noting that the reversibility region (indicated by the shaded area) spans over a considerable temperature interval of around 20 K. For the magnetocaloric effect, there is a good coincidence between the two sets of data although the values for the direct measurements of $\Delta T$ are systematically lower (around 10 %) than those computed from the entropy curves. Such a small difference can be attributed to a lack of perfect adiabaticity in our experimental set-up, and to a non-ideal thermal contact between the sample and the thermocouple.

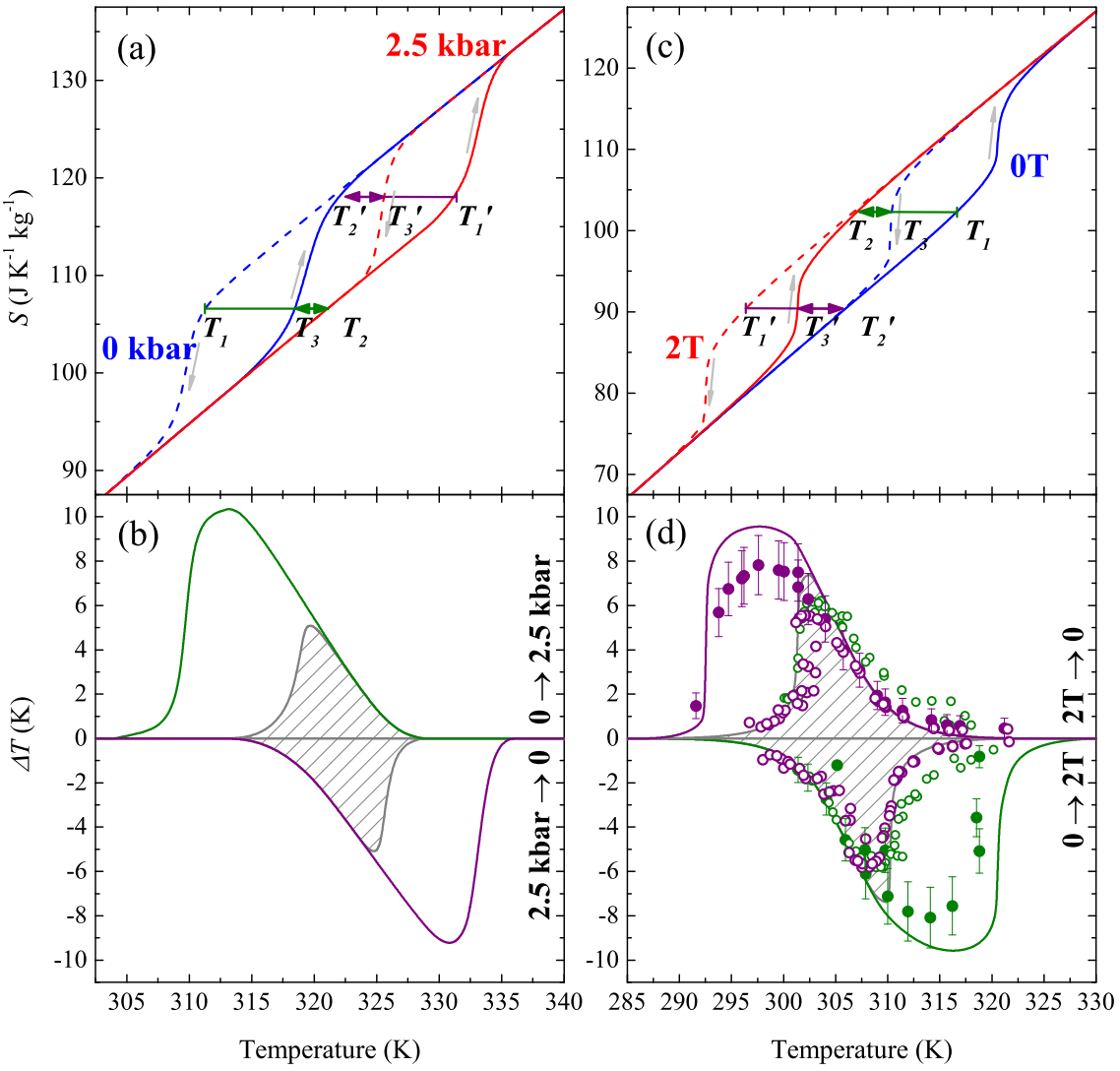


Fig. 4.12 Entropy as a function of temperature at zero field (blue colour) and 2 T (red colour) magnetic fields in (a) and at zero pressure (blue colour) and 2.5 kbar (red colour) in (c). Dashed lines in (a) and (c) correspond to cooling and solid lines, to heating runs. Horizontal arrows indicate the adiabatic temperature changes computed from these curves. Adiabatic temperature change corresponding to the application and removal of a 2.5 kbar pressure in (b) and the application and removal of a 2 T magnetic in (d). Lines in (b) and (d) refer to the $\Delta T$ values computed quasi-directly from entropy curves and symbols in (d) refer to the direct measurements. Green lines and green solid symbols correspond to the $\Delta T$ values associated with a process of a first application of the field ($T_1 \rightarrow T_2$ as illustrated in (a) and (c)) and purple lines and purple solid symbols correspond to a process of a first removal of the field ($T_1' \rightarrow T_2'$). Open symbols correspond to the subsequent field cycling for cooling (violet symbols, $T_2' \leftrightarrow T_3'$) and heating (green symbols, $T_2 \leftrightarrow T_3$) protocols. The grey shaded area indicates the reversibility region ($T_2 \leftrightarrow T_3$, $T_2' \leftrightarrow T_3'$).

In the case of the barocaloric effect, it is shown that application of pressure heats up the sample while the sample cools down when pressure is released, in concordance with the conventional nature of the barocaloric effect in Fe-Rh. The maximum values ($\Delta T \sim 10$ K) are very large for a relatively small pressure of 2.5 kbar. These values are significantly larger than those reported (or estimated) for other barocaloric materials [1, 5, 41, 89, 90]. It is also worth noting that upon pressure cycling $|\Delta T|$ remain at relative large values of $\sim 4$ K over a temperature span of $\sim 10$ K.

### 4.3.4 Summary and conclusions

By means of calorimetry under hydrostatic pressure we have shown that $Fe_{49}Rh_{51}$ exhibits a giant barocaloric effect. This functional property adds to the already reported magnetocaloric and elastocaloric effects in this alloy. The maximum pressure-induced entropy change value found for $Fe_{49}Rh_{51}$ ($|\Delta S| = 12.5$ J K$^{-1}$ kg$^{-1}$) compares well with the values reported for other giant barocaloric materials [5, 41, 89]. Interestingly, such a maximum isothermal entropy change is achieved for relatively low pressures. This establishes Fe-Rh to be a material with a large barocaloric strength ($|\Delta S|/|\Delta p|$) of $\sim 12$ J K$^{-1}$ kg$^{-1}$ kbar$^{-1}$. Indeed, the magnetocaloric strength ($|\Delta S|/|\mu_0 \Delta H|$) $\sim 12$ J K$^{-1}$ kg$^{-1}$ T$^{-1}$ is also one of the largest reported so far among giant magnetocaloric materials [46]. All these caloric effects share the same physical origin, which is the occurrence of a first-order AFM-FM phase transition which encompasses a significant entropy change. Actually, this transition entropy change ($|\Delta S_t| = 12.5 \pm 1$ J K$^{-1}$ kg$^{-1}$) represents the upper bound for the pressure-induced and magnetic-field-induced entropy changes.

The reproducibility of the magnetocaloric effect has been studied by a direct determination of the field-induced entropy change from isothermal calorimetric measurements. The comparison between direct and quasi-direct methods at the magnetocaloric effect has enabled us to assess also the reproducibility of the barocaloric effect from the quasi-direct data. With regards to the entropy changes, we have found that for a field of 2 T the magnetocaloric effect is perfectly reproducible upon field cycling. This reproducibility is restricted within the temperature range 294–306 K and is increased to 257–306 K for a field of 6 T. The barocaloric effect is estimated to be reversible upon pressure cycling in the temperature range 319–325 K for applied pressures of 2.5 kbar.

We have determined the adiabatic temperature changes associated with the magnetocaloric and barocaloric effects in Fe-Rh. Large $|\Delta T| \sim 8 - 10$ K values have been found for relatively low values of magnetic field (2 T) and hydrostatic pressure (2.5 kbar). It has been shown that both magnetocaloric and barocaloric effects are reproducible upon magnetic field and pressure cycling, over considerable temperature spans ($T_{span} \sim 10 - 15$ K). The

maximum value for the adiabatic temperature change obtained under cycling reduces to $|\Delta T| \sim 4-6$ K, which is still a significantly large value.

The energy difference between AFM and FM phases has been found to decrease with increasing magnetic field. Present results provide reproducible experimental data which we expect will encourage the development of theoretical models that include the effect of magnetic field in the computation of both energy and entropy values for the different phases involved in the transition. The combination of reliable experimental data and theoretical modeling should help in the understanding of the role played by the different contributions (electronic, magnetic, and structural) in driving the AFM-FM transition in Fe-Rh alloys.

The sharpness of the transition together with the strong sensitivity of the transition to the external fields results in barocaloric and magnetocaloric strengths which compare favorably to those reported for other giant magnetocaloric and barocaloric materials. As a consequence of such large strengths, $Fe_{49}Rh_{51}$ achieves its maximum isothermal entropy change at very low values of hydrostatic pressure and magnetic field. This fact, added to the aforementioned good reproducibility, makes this alloy particularly interesting in cooling applications where the external stimuli need to be restricted to low values.

## 4.4 The multicaloric effect driven by hydrostatic pressure and magnetic field

### 4.4.1 Sample details

The sample used for the experiments was a $Fe_{49}Rh_{51}$ long shaped polycrystalline (28.9 mg) specimen from the same batch of the sample employed for the previously described baro- and magnetocaloric studies.

### 4.4.2 Experimental details

Magnetization measurements at ambient and hydrostatic pressure (up to 5.1 kbar) were performed using a superconducting quantum interference device (Quantum Design, SQUID) magnetometer in magnetic fields up to 5 T and within the temperature range, 240 K < T < 390 K. Hydrostatic pressure was applied to the sample using the CuBe piston clamp pressure cell (Mcell10 manufactured by Almax EasyLab) as described in section 3.10. To minimize errors due to differential thermal contraction between the metallic components of the pressure cell and the pressure transmitting medium, the temperature sweep-rate during measurement was set at 1 K/min. The pressure inside the cell was calibrated in situ by measurement of the shift of the superconducting transition temperature of a Sn standard. Experiments were carried out during a research stay at the Northeastern University, Boston (US), in collaboration with the Nanomagnetism research group.

### 4.4.3 Results and discussion

Figure 4.13 shows the set of magnetization curves $M(T,p,H)$ at selected (constant) values of applied magnetic field obtained upon heating and cooling as illustrated by the arrows at each value of the applied pressure. The first order transition from the antiferromagnetic low temperature phase to the ferromagnetic high temperature phase is seen as a sharp change of magnetization as previously depicted in figure 4.4. On cooling the sample undergoes the forward transition from a saturated ferromagnetic state to an antiferromagnetic phase and the reverse transition takes place on heating with a thermal hysteresis of $\sim$ 10 K.

Since experimental magnetization values are only known for given values of magnetic field and hydrostatic pressure, it is convenient to fit an analytical function $M^*(T,p,H)$ in order to be able to determine magnetization over the whole space of thermodynamic quantities $T$, $p$ and $H$. Experimental data gather a proper framework for the parametrization of $M(T,H,p)$

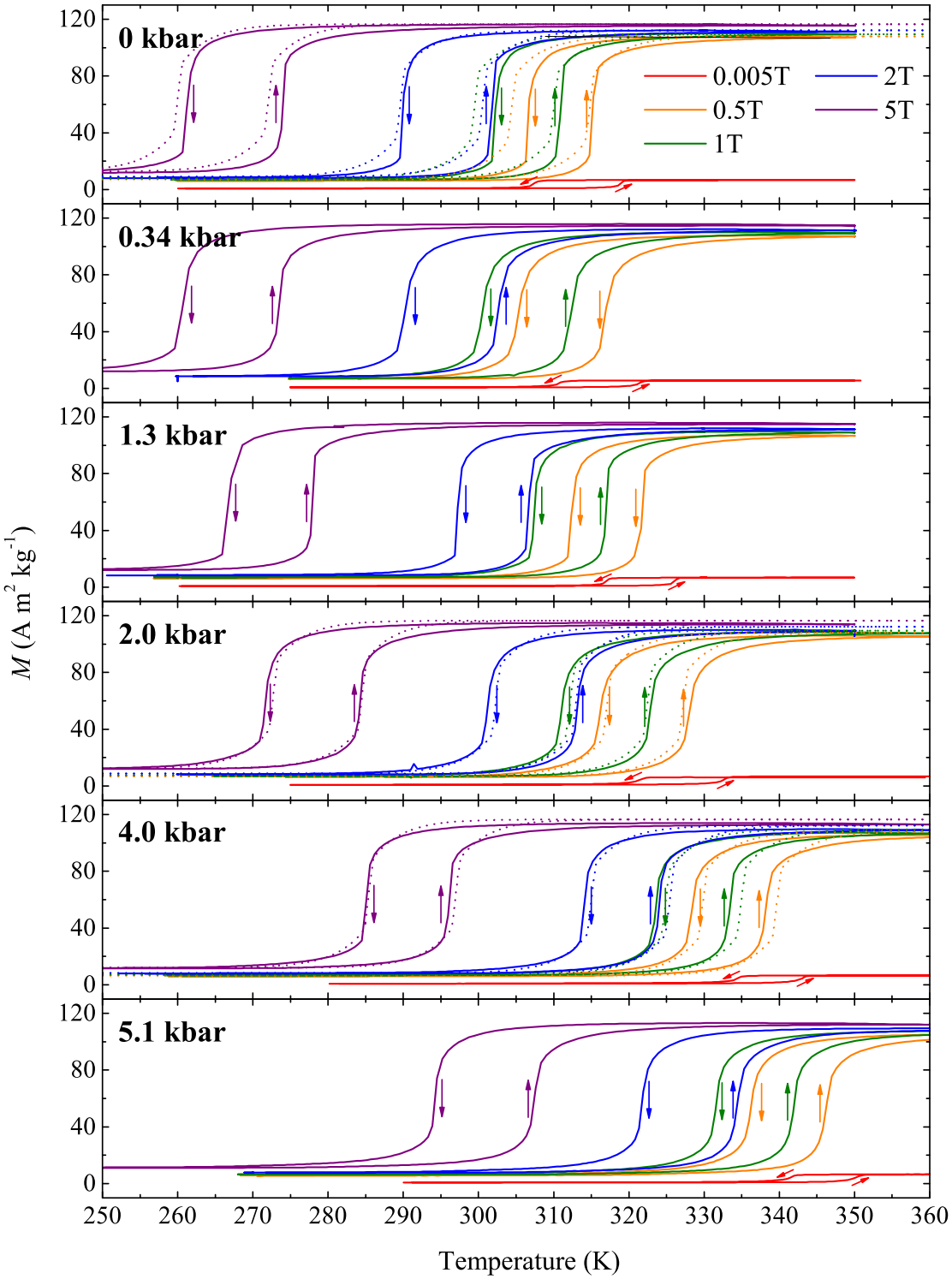


Fig. 4.13 Magnetization curves measured on cooling and heating the sample through the AFM-FM transition at selected (constant) values of magnetic field. Each panel displays a family of curves at a selected (constant) value of pressure. Solid lines correspond to experimental data and dotted lines correspond to fitted curves.

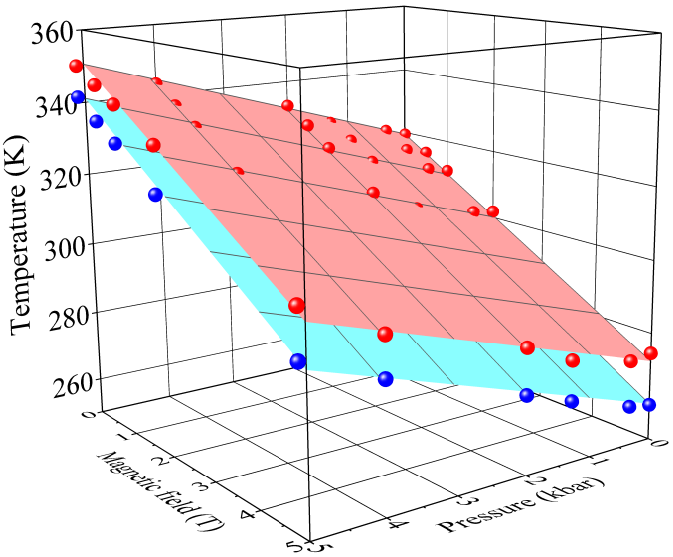


Fig. 4.14 Transition temperature as a function of magnetic field and pressure. Upper red plane corresponds to the AFM to FM transition, and lower blue plane, to the FM to AFM transition. Solid symbols stand for experimentally measured values.

and an extended analysis of these curves has been performed with the aim of selecting a proper pattern for the analytical function.

The fact of magnetic field stabilizing the high magnetization FM phase and pressure stabilizing the low-volume AFM phase is also corroborated when both pressure and magnetic fields are applied simultaneously. Hence, the FM-AFM transition shifts to lower temperatures with increasing magnetic field while it moves to higher temperatures with increasing pressure. To quantify these dependences we have taken the inflection point of the $M$ vs $T$ curves as a characteristic transition temperature $T_t$. Experimental values are plotted as blue (forward transition: $T_{t_c}(p,H)$) and red (reverse transition: $T_{t_h}(p,H)$) symbols in figure 4.14. The pressure dependence of the transition temperature in the absence of magnetic field $T_t(p,0)$, and the magnetic field dependence at atmospheric pressure $T_t(0,H)$ are in line with the equations (4.1) to (4.4). The general behaviour of $T_t(p,H)$ at these ranges of the applied pressure and magnetic field is linear and can be parameterized as two planes with equations:

$$T_{t_h}(p,H) = 319.5 - 9.5\mu_0 H + 6.2p \tag{4.6}$$

$$T_{t_c}(p,H) = 309.3 - 9.9\mu_0 H + 6.3p \tag{4.7}$$

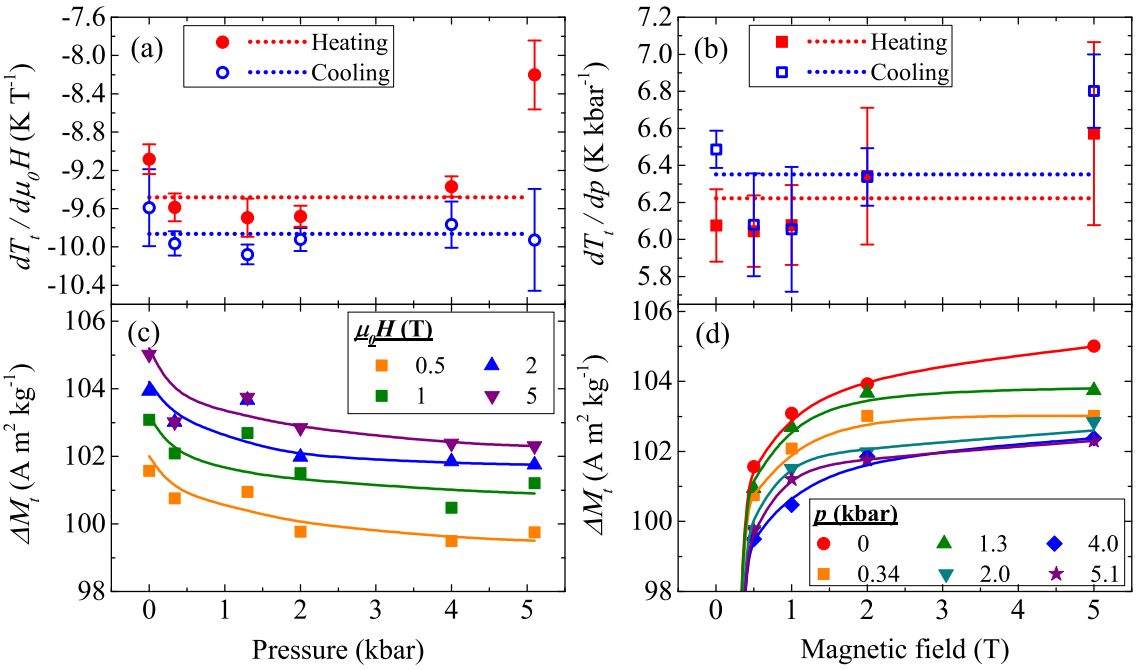


Fig. 4.15 Top panels illustrate the behaviour of $\frac{dT_{t_h}}{dp}(p,H)$ (red symbols) and $\frac{dT_{t_c}}{dp}(p,H)$ (blue symbols) as a function of hydrostatic pressure (a) and magnetic field (b). Bottom panels illustrate the $\Delta M_t$ values as a function of pressure at selected values of the applied magnetic field as depicted in the legend (c) and $\Delta M_t$ values as a function of magnetic field at selected values of the applied pressure as depicted in the legend (d).

as seen in figure 4.14. The parameters $\frac{dT_t}{dp}(p,H)$ and $\frac{dT_t}{d\mu_0 H}(p,H)$ written in equations (4.6) and (4.7) are estimated as follows:

- A set of $\left\{\frac{dT_t}{d\mu_0 H}(p_i,H)\right\}$ values is computed from the linear fits of each family of points $\{T_t(p_i,H_j)\}$ at each value of the applied pressure $p_i = 0$, 0.34, 1.3, 2.0, 4.0, and 5.1 kbar. $\left\{\frac{dT_t}{d\mu_0 H}(p_i,H)\right\}$ values are plotted as a function of the pressure values $p_i$ in figure 4.15 (a) as blue [forward transition, $\frac{dT_{t_c}}{d\mu_0 H}(p,H_i)$] and red [reverse transition, $\frac{dT_{t_h}}{d\mu_0 H}(p,H_i)$] squares.

- Analogously, a set of $\left\{\frac{dT_t}{dp}(p,H_i)\right\}$ values is computed from the linear fits of each family of points $\{T_t(p_j,H_i)\}$ at each value of the applied magnetic field $\mu_0 H_i = 0.005$, 0.5, 1, 2, and 5 T. $\left\{\frac{dT_t}{dp}(p,H_i)\right\}$ values as a function of the magnetic field values $\mu_0 H_i$

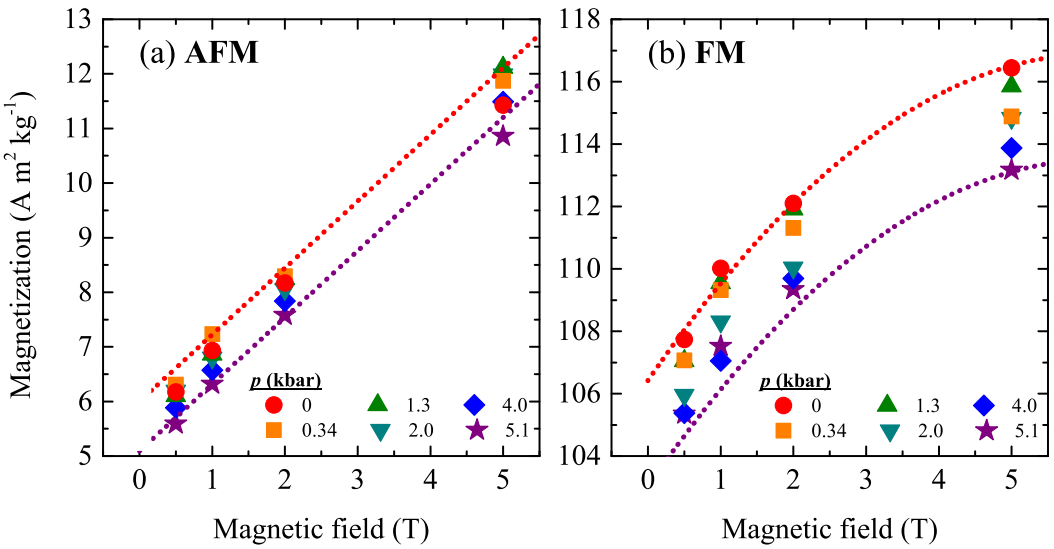


Fig. 4.16 Magnetization values at the AFM phase (a) and at the FM phase (b) as a function of magnetic field for selected values of pressure. For comparison with the experimental data, dotted lines correspond to the fitted behaviour at 0 kbar (red) and at 5.1 kbar.

are plotted in figure 4.15 (b) as blue [forward transition, $\frac{dT_{t_c}}{dp}(p,H_i)$] and red [reverse transition, $\frac{dT_{t_h}}{dp}(p,H_i)$ ] circles.

- As shown in figure 4.15 (a) and (b) average values of $\left\{\frac{dT_t}{d\mu_0 H}(p_i,H)\right\}$ and $\left\{\frac{dT_t}{dp}(p,H_i)\right\}$ (plotted as dotted horizontal lines) fall within the experimental errors and verify the assumption of linearity for $T_t(p,H)$ at this range of the applied fields.

Hence, we assume the absence of cross terms in equations (4.6) and (4.7) due to the fact that

$$\frac{\partial^2 T_t}{\partial H \partial p}(p,H) = \frac{\partial^2 T_t}{\partial p \partial H}(p,H) = 0 \tag{4.8}$$

which has physical consequences concerning the Clausius-Clapeyron equation presented in (2.21). As will be discussed below in more detail, the introduction of the expression $\frac{dT_t}{d\mu_0 H} = \frac{\Delta M_t}{\Delta S_t}$ into equation (4.8) points the fact that the fraction $\frac{\Delta M_t}{\Delta S_t}$ remains constant over the pressure and magnetic field ranges at which expressions (4.6) and (4.7) are valid.

Figure 4.15 (c) and (d) show the behaviour of the magnetization change at the transition, $\Delta M_t(p,H) = M_{FM}(p,H) - M_{AFM}(p,H)$, computed by subtracting the values of the magnetization outside the boundaries of the temperature region of the first-order transition which

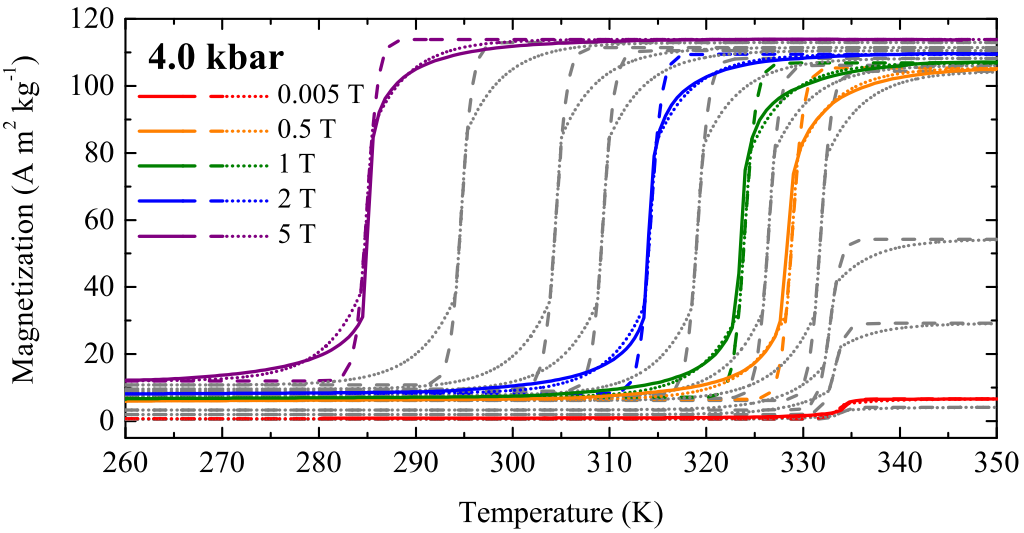


Fig. 4.17 Sets of $M(T,p,H)$ curves at $p = 4.0$ kbar at selected values of the applied magnetic field. Coloured lines correspond to the values at which the experimental curves are available (0.005, 0.5, 1, 2, 5 T) and grey lines refer to other illustrative values of the applied magnetic field (from left to right: 4, 3, 2.5, 1.5, 0.75, 0.25, 0.1, 0.05, and 0.0025 T). Solid lines refer to the experimental curves, dashed lines refer to the employed $\tanh(x)$ function for the analytical fits written in (4.11), and dotted lines refer to the full analytical fits which include the regions with the $\tanh(x)$ and $\exp(x)$ functions.

are displayed in figure 4.16 (a) and (b) for $M_{AFM}$ and $M_{FM}$, respectively. There is a small increase in the magnetization of both FM and AFM phases with increasing magnetic field, which results in a marginal increase in the magnetization change ($\Delta M_t$) at the AFM-FM phase transition. On the other hand $\Delta M_t$ slightly decreases with increasing pressure ($\sim 2\%$ decrease for 5 kbar).

With these general features in hand, we have fitted the values of $M_{AFM}(p,H)$ and $M_{FM}(p,H)$ as a function of pressure and magnetic field with the following expressions:

$$M_{AFM} = 6.61 - 0.18p + 1.22\mu_0 H \tag{4.9}$$

$$M_{FM} = 106.42 - 0.67p + 3.39\mu_0 H - 0.27(\mu_0 H)^2 \tag{4.10}$$

which are displayed in figure 4.16 (a) and (b) as dotted lines for the cases in which $p = 0$, 5.1 kbar.

It is observed that the parametrization of the $M(T,p,H)$ curves distinguishes two temperature regions. On the one hand, we have used an hyperbolic tangent function for the temperature region of the transition which fits the sharp change of the magnetization over

this range. On the other hand, an exponential function fits the magnetization behaviour at the temperature boundaries of the transition which decay to $M_{FM}(p,H)$ and $M_{AFM}$ values above and below the transition temperature region, respectively. Figure 4.17 depicts illustrative examples of the curves at 4.0 kbar at selected values of the applied magnetic field. The $\tanh(x)$ illustrated by dashed lines in this figure exhibit a proper fit at the temperatures close to the transition. The full analytical fits which include the $\exp(x)$ functions at the corresponding temperature boundaries are illustrated by dotted lines.

Hence, at the temperatures close to the transition the analytical fit is expressed as:

$$M^*(T,p,H) = \frac{1}{2}\left(M_{AFM} + M_{FM} + (M_{FM} - M_{AFM})\tanh\left(\frac{T-T_t}{\omega}\right)\right)$$
$$\forall T \in [T_t - 0.6, T_t + 0.6] \tag{4.11}$$

where $M_{AFM}$, $M_{FM}$ are the magnetization values given by equations (4.9) and (4.10) and $T_t$ is the transition temperature given by equations (4.6) and (4.7). $\omega$ is related to the spread of the transition over temperature and it is expressed as:

$$\omega = \pm\frac{T_\pm - T_t}{\cosh^{-1}\left(\sqrt{\frac{3}{2}}\right)} \tag{4.12}$$

The zeros of the temperature derivatives of the experimental curves $M(T,p,H)$ can provide information of the experimental behaviour to the functional fits. With this purpose, $T_+$ and $T_-$ in equation (4.12) are important parameters defined from the zeros of the third derivatives of the experimental data and have been used to derive the value of $\omega$. The derivatives of $M^*$, $\frac{d^iM^*(T,p,H)}{dT^i}$ (up to $i=3$), are written as:

$$\frac{dM^*}{dT} = \frac{M_{FM} - M_{AFM}}{2\omega}\text{sech}^2\left(\frac{T-T_t}{\omega}\right) \tag{4.13}$$

$$\frac{d^2M^*}{dT^2} = -\frac{M_{FM} - M_{AFM}}{\omega^2}\text{sech}^2\left(\frac{T-T_t}{\omega}\right)\tanh^2\left(\frac{T-T_t}{\omega}\right) \tag{4.14}$$

$$\frac{d^3M^*}{dT^3} = \frac{M_{FM} - M_{AFM}}{\omega^3}\text{sech}^2\left(\frac{T-T_t}{\omega}\right)\left[2 - 3\text{sech}^2\left(\frac{T-T_t}{\omega}\right)\right] \tag{4.15}$$

The equation $\frac{d^3M^*}{dT^3} = 0$ can be easily solved by finding the zeros of the second term on the right hand side of equation (4.15) and defining the corresponding solutions as the

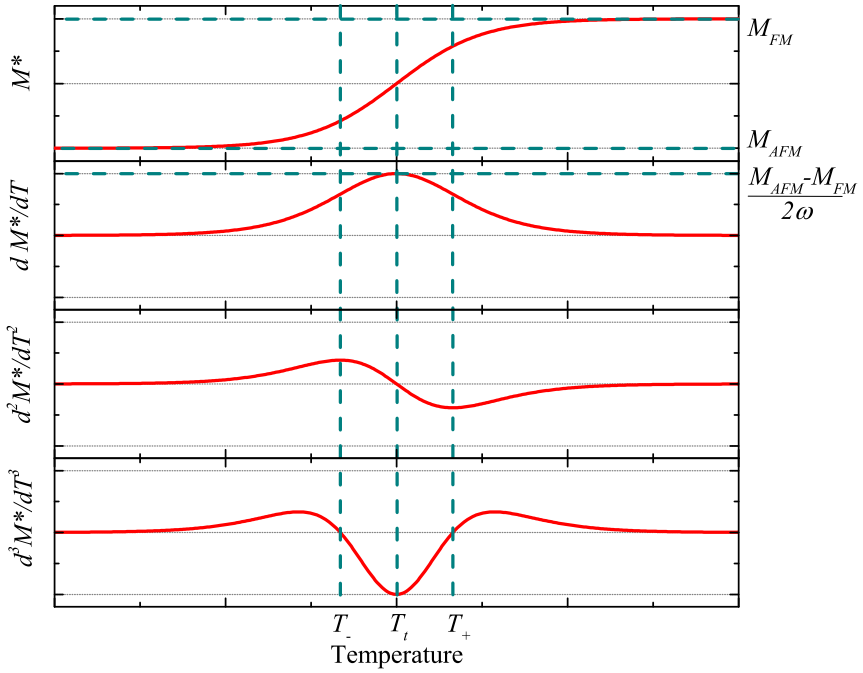


Fig. 4.18 The hyperbolic tangent fit of the magnetization curves written in equation (4.11) and the corresponding derivatives up to the third order which are written in equations (4.13) to (4.15). The plots are marked with some relevant parameters of the functions.

parameters $T_+$ and $T_-$:

$$T_\pm = \pm\omega \cosh^{-1}\sqrt{\frac{3}{2}} + T_t \tag{4.16}$$

The values of $T_\pm$ have been computed for each experimental $M(T,p,H)$ curve and the spread of the transition temperature has been taken from the corresponding average value, i. e. $\omega = 1.15$. In this regards, figure 4.18 illustrates the function $M^*$ written in (4.11) and the corresponding derivatives written in equations (4.13) to (4.15) as well as some relevant parameters related to the analytical function.

The temperature boundaries above (${M^*}_{FM}$) and below (${M^*}_{AFM}$) the transition is covered by the following exponential functions:

$${M^*}_{AFM} = M_{AFM} + (M^*(T_t - 0.6) - M_{AFM}) \exp\left[\alpha_1 (T - T_t + 0.6)\right], \quad \forall T < T_t - 0.6\text{K} \tag{4.17}$$

$${M^*}_{FM} = M_{FM} + (M^*(T_t + 0.6) - M_{FM}) \exp\left[\alpha_2 (T_t - T + 0.6)\right], \quad \forall T > T_t + 0.6\text{K} \tag{4.18}$$

where $\alpha_1$ and $\alpha_2$ are positive constants.

By the definition of the analytical function $M^*(T,p,H)$ written in equations (4.11) to (4.18) over the whole temperature range at each value of the applied magnetic field and pressure, a large matrix of $M^*$ values is generated[2] over the whole space of $(T,p,H)$ in order to map the magnetization behaviour at each point $M_i^*(T_i,p_i,H_i)$ and apply the thermodynamic expressions described in section 2.1.1 for deriving the corresponding multicaloric isothermal entropy change $\Delta S_i$. Figure 4.19 shows different projections of the $M^*(T,p,H)$ matrix and reveals that an accurate characterization of the magnetization behaviour as a function of pressure and magnetic field is also obtained which is required for the computation of the derivatives involved in the calculus of $\Delta S$ values.

**Derivation of the multicaloric entropy change**

At this point, it is worth noting the analogies between the thermodynamic processes related to the application or removal of a field at the vicinity of the first-order transition in $Fe_{49}Rh_{51}$ due to its inherent hysteresis which directly influences the magnetization behaviour. It must be taken into account that the parametrization process of the magnetization along the $(T,p,H)$ space has been done by fitting the analytical functions to experimental $M(T,p=p',H=H')$ curves obtained by scanning temperature while pressure and magnetic field were kept at constant values. Thus, temperature has been the only driving field of the transition for the experimental data. Interestingly, the full matrix of $M(T,p,H)$ data allows the exploration of the magnetization behaviour under the influence of other thermodynamic processes in which temperature can be kept constant while the other fields are modified, as shown in figure 4.19. In computing multicaloric effects in Fe-Rh from experimental data, attention has to be paid to the fact that application of magnetic field stabilizes the FM phase, whereas application of pressure stabilizes the AFM phase. Also, the noted hysteresis of the transition implies that simultaneous (or subsequent) application of both magnetic field and pressure will take the sample through a minor loop within the two-phase co-existence region (i.e. the region bounded by the two planes in figure 4.14, and between two magnetization surfaces in figure 4.19 (e)). As detailed trajectories of these minor loops are not accessible from present experimental data, study of the Fe-Rh multicaloric response will be restricted to experimental values obtained from application of the magnetic field and the removal of hydrostatic pressure (i.e. trajectories on the AFM to FM surface) and to removal of magnetic field and application of pressure (i.e. trajectories on the FM to AFM surface). In relation to this, the process of heating ($\Delta T > 0$) has analogies with a magnetizing process ($\Delta H > 0$) or a removal of

[2]For further details on the computation of $M(T,p,H)$ values and the multicaloric entropy change, the appendix C includes the Fortran code from which these values have been computed.

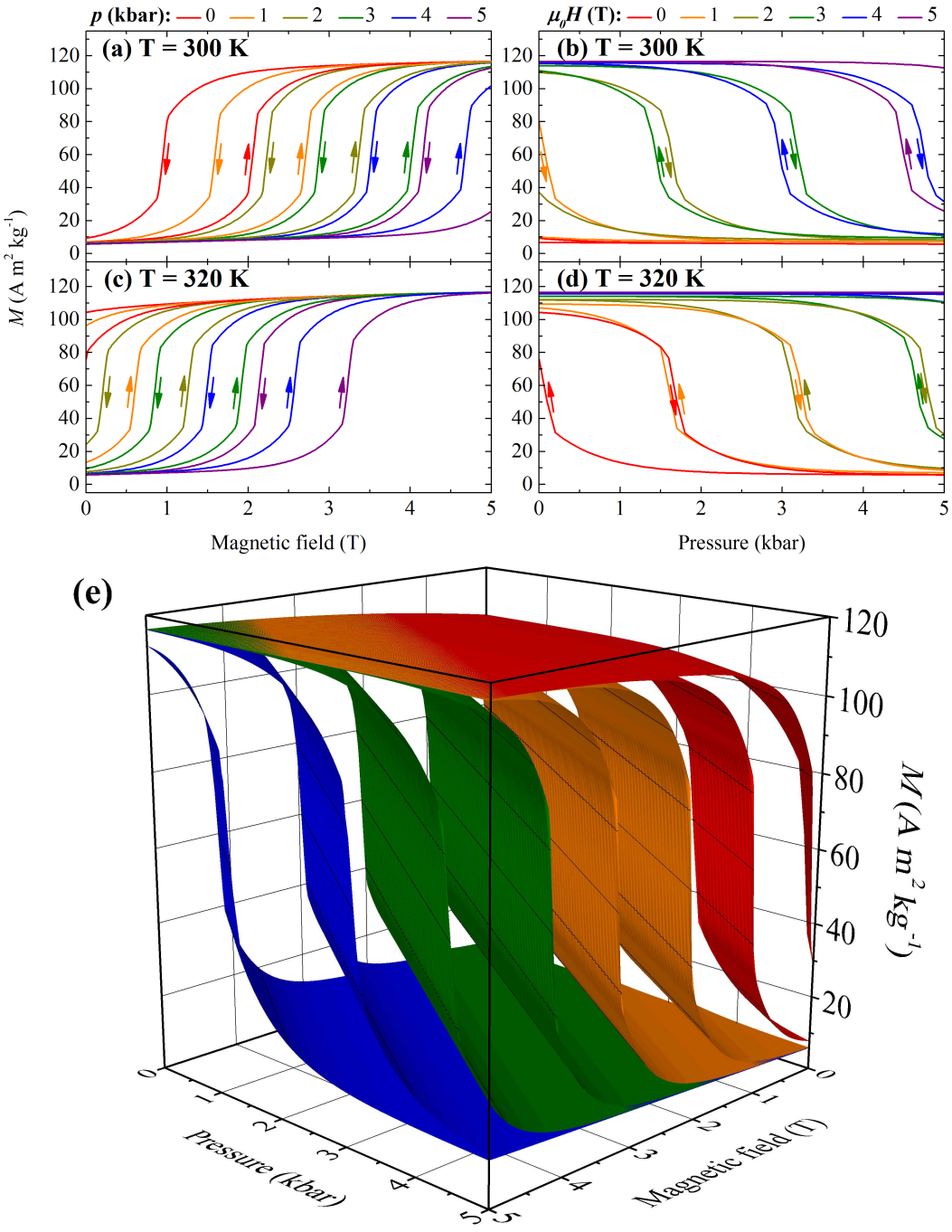


Fig. 4.19 Top left panels: Isothermal magnetization as a function of magnetic field at selected values of pressure, at 300 K (a) and 320 K (c). Top right panels: Isothermal magnetization as a function of pressure at selected values of magnetic field, at 300 K (b) and 320 K (d). Panel (e) displays the isothermal magnetization as a function of magnetic field and pressure. Data correspond to 340 K (red), 320 K (orange), 300 K (green) and 280 K (blue). For each temperature the sheets on the left correspond to application of field and removal of pressure (AFM to FM transition), while the sheets of the right correspond to removal of field and application of pressure (FM to AFM) transition.

Table 4.1 The thermodynamic processes of heating (cooling), magnetizing (demagnetizing) or decompressing (compressing) can be considered as equivalent in the vicinity of the first-order transition in $Fe_{49}Rh_{51}$.

| | | |
|---|---|---|
| Heating, $\Delta T > 0$ | Magnetizing, $\Delta H > 0$ | Decompressing, $\Delta p < 0$ |
| Cooling, $\Delta T < 0$ | Demagnetizing, $\Delta H < 0$ | Compressing, $\Delta p > 0$ |

pressure ($\Delta p < 0$) since in each case the process is endothermic ($\Delta S > 0$) and energetically favours the high temperature FM phase. In short, the analogies between heating and cooling processes are outlined in table 4.1.

Following the steps described in section 2.1.1 the expressions for the multicaloric entropy change can be written in the case of FeRh as:

$$\Delta S(T, p' \to 0, 0 \to H') =$$
$$\Delta S(T, p', 0 \to H') + \Delta S(T, p' \to 0, 0) + \int_{p'}^{0} \int_{0}^{H'} \frac{\partial}{\partial T} \left( \frac{\partial M}{\partial p} \right)_{T,H} dp dH \tag{4.19}$$

$$\Delta S(T, 0 \to p', H' \to 0) =$$
$$\Delta S(T, 0, H' \to 0) + \Delta S(T, 0 \to p', H') + \int_{0}^{p'} \int_{H'}^{0} \frac{\partial}{\partial T} \left( \frac{\partial M}{\partial p} \right)_{T,H} dp dH \tag{4.20}$$

On the one hand, equation (4.19) refers to an entropy change driven by a magnetizing and decompressing process which favours the high temperature FM phase. Thus, as previously explained this multicaloric entropy change must be computed by the matrix $M^*(T, p, H)$ originated from the experimental heating curves. On the other hand, the values of $\Delta S$ computed by equation (4.20) must correspond to experimental cooling curves because they refer to the FM $\to$ AFM transition.

The first and second terms on the right hand side in equations (4.19) and (4.20) refer to the magnetocaloric and barocaloric effects exhibited by application or removal of magnetic field and pressure, respectively, departing from the initial thermodynamic state at which the multicaloric $\Delta S$ is being computed. The third term is the cross-response term. For simplicity, in the following we will restrict our study to the process described by equation (4.19). The first two terms refer to the previously presented equations (2.8) and (2.17) and are expressed as

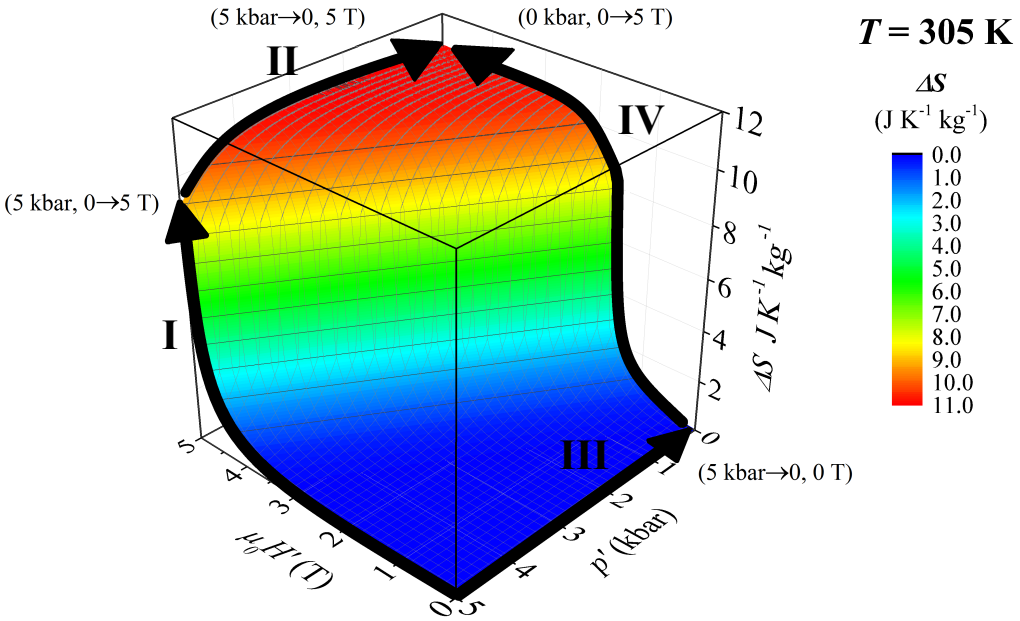


Fig. 4.20 Multicaloric entropy change $\Delta S(T, 5\text{ kbar} \rightarrow p', 0 \rightarrow \mu_0 H')$ at $T = 305$ K as a function of $p'$ and $\mu_0 H'$. The plot is aimed at illustrating that the multicaloric entropy change $\Delta S(T, 0, 5\text{T})$ can be equivalently computed with independence of the path from the initial state at $(5\text{ kbar}, 0)$ to the final state at $(0, 5\text{T})$ as marked by the black arrows (I, II, III, and IV).

$$\Delta S(T, p', 0 \rightarrow H') = \int_0^{H'} \left(\frac{\partial M}{\partial T}\right)_{p',T} dH \tag{4.21}$$

$$\Delta S\left(T, p' \rightarrow 0, 0\right) = \int_{p'}^{0} \frac{\left(\frac{\partial M}{\partial p}\right)_{T,H}}{\left(\frac{\partial M}{\partial H}\right)_{T,p}} \left(\frac{\partial M}{\partial T}\right)_{H,p} dp \tag{4.22}$$

where for this particular case the reference conjugate displacement $X_1$ from which the multicaloric entropy change is derived is the magnetization $M$ which exhibits a cross-response by applying pressure as a secondary field $y_2 = p$.

If one remembers that entropy is a state function, it can be assumed that the system is in thermodynamic equilibrium while the fields are applied or removed, and interconnected thermodynamic paths taking the system from the initial state $(5\text{kbar}, 0)$ to the final state $(0, 5\text{T})$ can be considered, as illustrated in figure 4.20. Thus, the total entropy change which accounts for the multicaloric entropy change is independent of the path and one can trace

the two alternative paths depicted in figure 4.20 with the resulting contributions to the total entropy change:

$$\Delta S(T, p' \to 0, 0 \to H') = \Delta S(T, p', 0 \to H') + \Delta S(T, p' \to 0, H') \tag{4.23}$$

$$\Delta S(T, p' \to 0, 0 \to H') = \Delta S(T, p' \to 0, 0) + \Delta S(T, 0, 0 \to H') \tag{4.24}$$

where the terms in (4.23) and (4.24) are expressed as in (4.21) and (4.22) with the appropriate integration limits. The path described by equation (4.23) is marked by the arrows in the left half of figure 4.20 (arrow I refers to the first term in equation and II, to the second) and the arrows in the right half depict the path related to (4.24) (arrow III refers to the first term in equation and IV, to the second) .

Therefore, the three expressions (4.19), (4.23), and (4.24) represent equivalent ways of computing the multicaloric entropy change $\Delta S(T, p' \to 0, 0 \to H')$. We can restrict the analysis to $p' = 5$ kbar and $\mu_0 H' = 5$ T and compute the corresponding contributions to the entropy change in each case as shown in figure 4.21. Panel (a) displays the multicaloric entropy change for the whole process and (b) shows the three terms on the right hand side in (4.19) decomposing the multicaloric response. The cross-response term has an important role in balancing the fact that the two terms describing the magneto- and the barocaloric effects are not thermodynamically connected as illustrated in figure 4.20. Panel (c) shows the two contributions arising from the path described by (4.23) and panel (d) displays the terms in (4.24). Thus, the sum of each contribution in each panel (b), (c) and (d) lead to the same multicaloric entropy change depicted in panel (a). While panels on the left hand side [(a) - (d)] illustrate the multicaloric entropy change for the field-driven AFM $\to$ FM transition which results in an endothermal process with positive values of the entropy change, panels on the right hand side [(e) - (f)] display the corresponding terms related to the field driven FM $\to$ AFM transition which lead to an exothermal process with negative values for the entropy change.

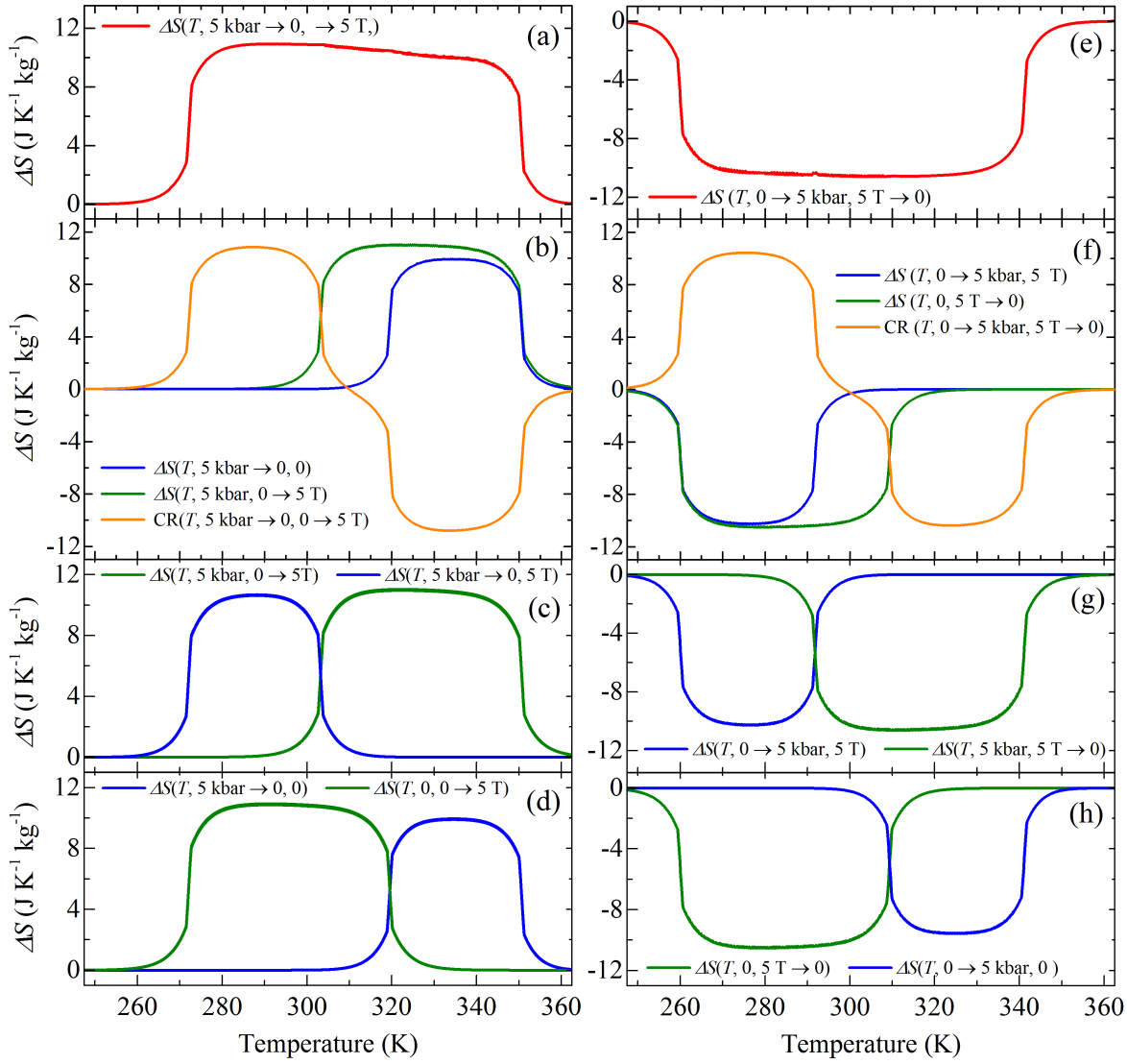


Fig. 4.21 (a) Multicaloric entropy change for a process consisting in a removal of pressure (5 kbar) and application of magnetic field (5 T). (b) Each of the three terms which decompose the multicaloric entropy change as shown in equation (4.19): the magnetocaloric effect at 5 kbar, the barocaloric effect at 0 T and the cross-response (CR) term, $\int_0^{5\mathrm{T}} \int_{5\mathrm{kbar}}^{0} \frac{\partial}{\partial T}\left(\frac{\partial M}{\partial p}\right)_{T,H} dpdH$. Panels (c) and (d) show the terms in (4.23) and (4.24), respectively. Panels on the right hand side illustrate the corresponding terms related to a process consisting in a removal of magnetic field (5 T) and application of pressure (5 kbar): the multicaloric entropy change (e), the terms written in (4.20) (f), and the entropy changes related to alternative thermodynamic paths in (g) and (h).

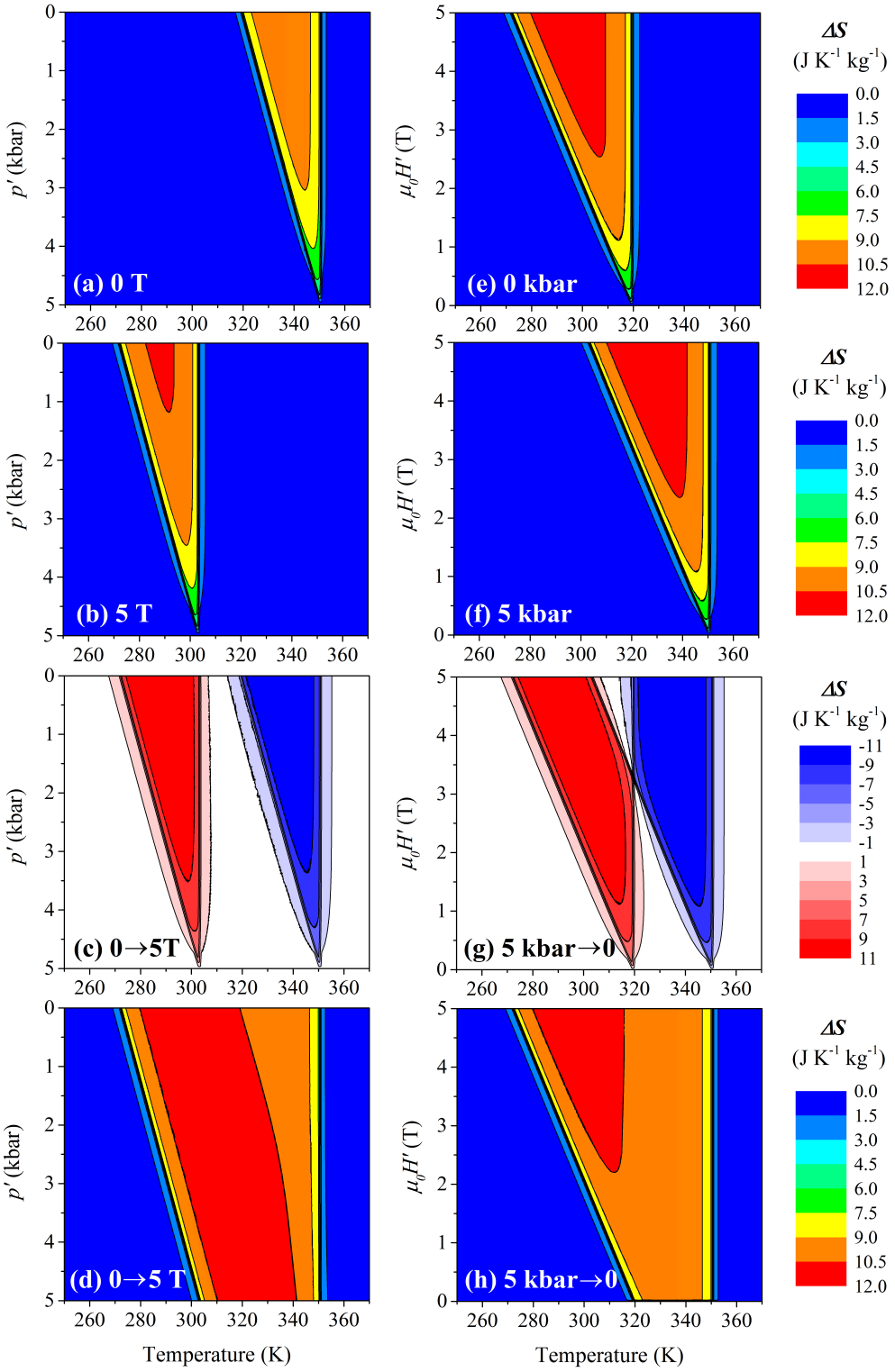


Fig. 4.22 Coloured contour maps of the barocaloric entropy change $\Delta S(T, 5\text{kbar} \rightarrow p', \mu_0 H)$ at 0 (a) and 5 T (b). The magnetocaloric entropy change $\Delta S(T, p, 0 \rightarrow \mu_0 H')$ at 0 (e) and 5 kbar (f). The cross-response term (equation 4.19) for the thermodynamic process $(5\text{kbar} \rightarrow p', 0 \rightarrow 5\text{T})$ in (c) and $(5\text{kbar} \rightarrow 0, 0 \rightarrow \mu_0 H')$ in (g). The multicaloric entropy change $\Delta S(T, 5\text{kbar} \rightarrow p', 0 \rightarrow \mu_0 H')$ as a function of $p'$ (d) and $\mu_0 H'$ (h). The corresponding colour charts are shown on the right hand side.

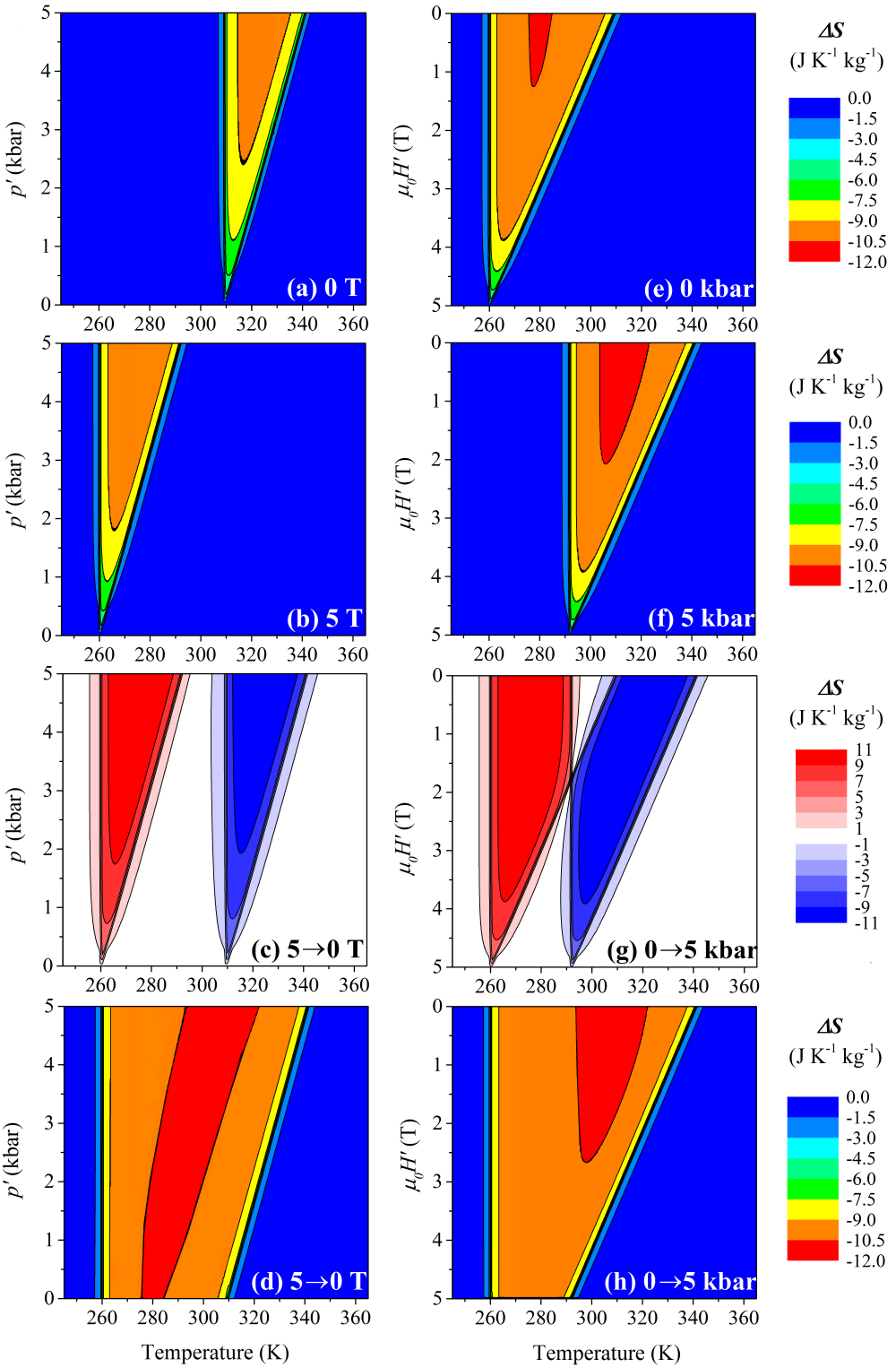


Fig. 4.23 Coloured contour maps of the barocaloric entropy change $\Delta S(T, 0 \rightarrow p', \mu_0 H)$ at 0 (a) and 5 T (b). The magnetocaloric entropy change $\Delta S(T, p, 5\text{T} \rightarrow \mu_0 H')$ at 0 (e) and 5 kbar (f). The cross-response term (equation 4.20) for the thermodynamic process $(0\text{kbar} \rightarrow p', 5\text{T} \rightarrow \mu_0 H')$ in (c) and $(0 \rightarrow 5\text{kbar}, 0 \rightarrow \mu_0 H')$ in (g). The multicaloric entropy change $\Delta S(T, 0 \rightarrow p', 5\text{T} \rightarrow \mu_0 H')$ as a function of $p'$ (d) and $\mu_0 H'$ (h). The corresponding colour charts are shown on the right hand side.

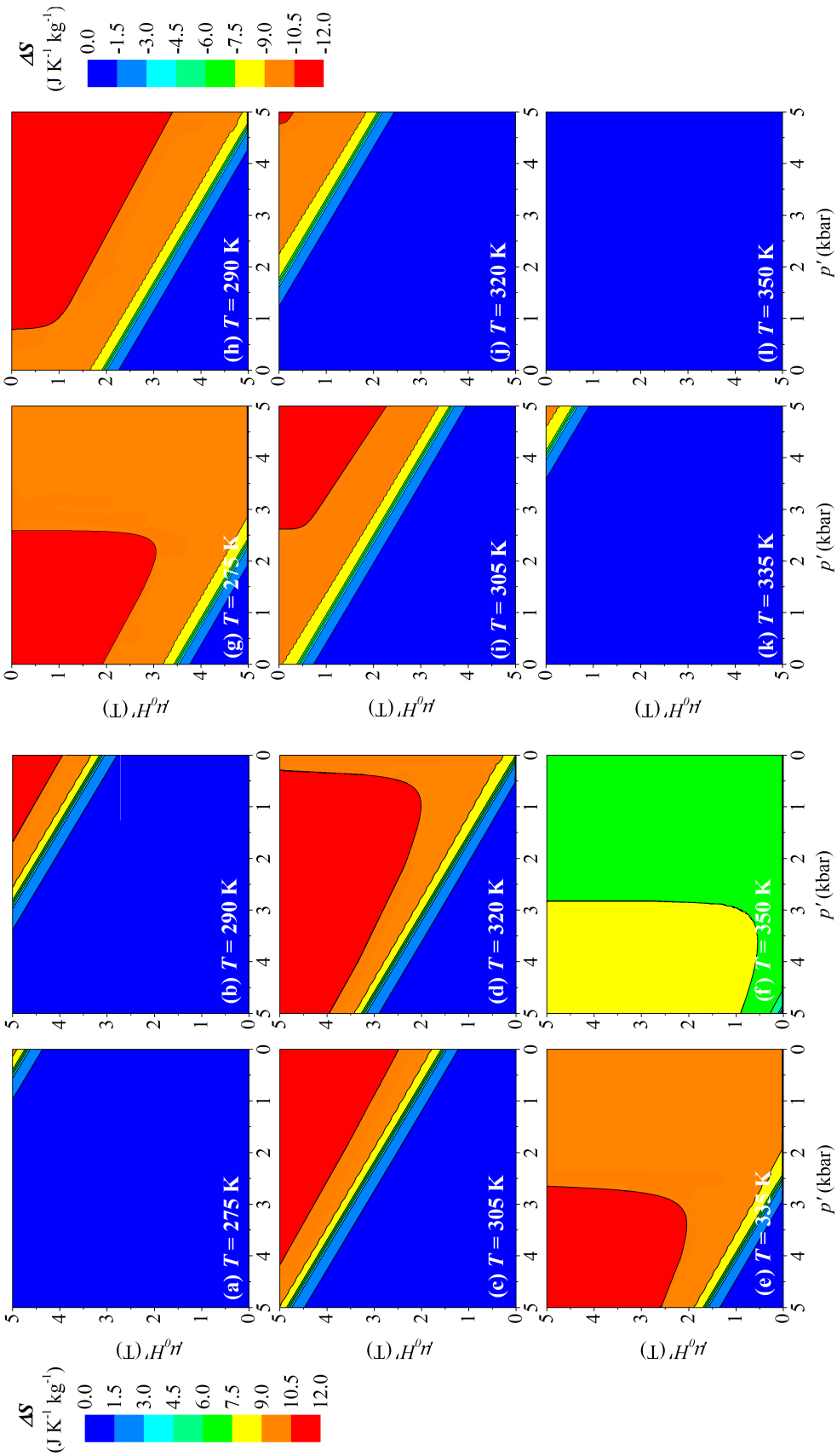


Fig. 4.24 Coloured contour maps of the multicaloric entropy change $\Delta S(T, 0 \rightarrow \mu_0 H', 5\text{kbar} \rightarrow p')$ in panels (a) - (f) and $\Delta S(T, 5\text{T} \rightarrow \mu_0 H', 0 \rightarrow p')$ in panels (g) - (l) at temperatures 275 K [(a) and (g)], 290 K [(b) and (h)], 305 K [(c) and (i)], 320 K [(d) and (j)], 335 K [(e) and (k)], and 350 K [(f) and (l)]. (a) - (f) panels display positive values of the entropy change and share the same colour chart shown on the top left hand side. (g) - (l) panels display negative of the entropy changes and share the same colour chart shown on the top right hand side.

A further step is to consider an arbitrary value of the pressure within the range $p' \in [0,5]$ kbar and any value of the magnetic field within $\mu_0 H' \in [0,5]$ T for a more general description. Results for the computed entropy change are shown in the coloured contour plots in figure 4.22 which display the abovementioned entropy terms as a function of temperature and pressure (left panels), and magnetic field (right panels). The barocaloric effect at 0 T and at 5 T is shown in panels (a) and (b) and the magnetocaloric effect at 0 kbar and at 5 kbar in panels (e) and (f), respectively. The cross-response term as a function of pressure 5kbar $\rightarrow p'$ once magnetic field has been applied $0 \rightarrow 5$ T is shown in panel (c) and as a function of the magnetic field $0 \rightarrow \mu_0 H'$ once pressure has been removed 5kbar $\rightarrow 0$ is shown in panel (g). The sum of panels (a) and (c) leads to the results shown in panel (d) which refer to the multicaloric entropy change as a function of $p'$ once the magnetic field has been applied. The sum of panels (f) and (g) leads to the results shown in panel (d) which refer to the multicaloric entropy change as a function of $\mu_0 H'$ once pressure has been removed. Figure (4.23) display the analogous panels to figure 4.22 related to the process of application of 5 kbar and the removal of 5 T which drive the FM-AFM transition and give rise to an exothermal process with negative values of the entropy change.

The multicaloric response is depicted by the isothermal contour plots for selected values of the temperature ($T$ = 275, 290, 305, 320, 335, and 350 K) as a function of the pressure drop and the applied magnetic field presented in figure 4.24 (a), (b), (c), (d), (e), and (f), respectively, and as a function of the magnetic field drop and the applied pressure in (g), (h), (i), (j), (k), and (l), respectively. In comparison to the pure BCE or the pure MCE, the illustration of the results concerning the multicaloric entropy change is more complex due to the fact that its magnitude depends on temperature and the two fields. For a better understanding of the interconnection of the contents presented in figures 4.21, 4.22, 4.23 and 4.24, it can be useful to note that the values of the entropy change at the top right corners with coordinates $(5\text{kbar} \rightarrow 0, 0 \rightarrow 5\text{T})$ for panels (a) - (f) in figure 4.24 or the values with coordinates $(0 \rightarrow 5\text{kbar}, 5\text{T} \rightarrow \mu_0 H')$ for panels (g) - (l) coincide with the values depicted in figure 4.21 (a) and (e) at the corresponding temperatures, respectively. The slices of the contour plots in figure 4.22 and 4.23 at the top position where $p' = 0$ kbar or $\mu_0 H' = 5$ T or $p' = 5$ kbar or $\mu_0 H' = 0$ T coincide with the plots of the corresponding terms in figure 4.21.

In all cases $\Delta S$ increases with increasing magnetic field and increasing pressure drop, up to a saturation value around 11 J kg$^{-1}$K$^{-1}$ which coincides with the reported transition entropy change for the magnetostructural transition in Fe-Rh previously presented in figure 4.8 (c). It is noted that the material exhibits a large multicaloric entropy change over a broad range of magnetic field and pressure values. The larger the pressure drop, the smaller the magnetic field required to achieve the saturation value; conversely, the larger the magnetic

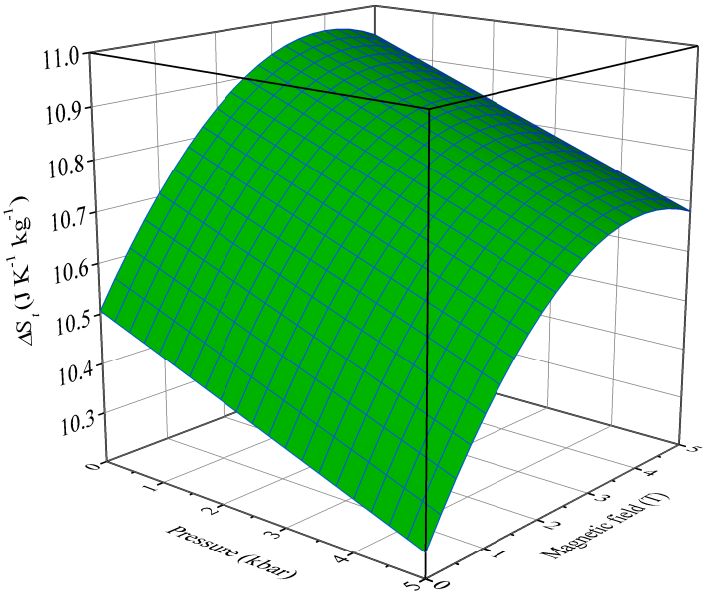


Fig. 4.25 Transition entropy change $\Delta S_t = (99.81 - 0.49p + 2.17\mu_0 H - 0.27(\mu_0 H)^2)/9.5$ as a function of pressure and magnetic field. The plot has been computed by use of the expression (4.25) and the heating magnetization curves parameters which are applicable to thermodynamic processes consisting in an application of magnetic field and/or a removal of pressure.

field applied, the smaller the pressure drop required. As shown in figures 4.22, 4.23 and 4.24, it is also remarkable that the region where $\Delta S$ increases from zero to the maximum value (the multi-coloured bands) is rather narrow, indicative of a very large multicaloric strength.

As previously explained, the ratio $\dfrac{\Delta M_t}{\Delta S_t}$ remains constant as a consequence of the validity of equation (4.8). Therefore, the transition entropy change $\Delta S_t$ at which the multicaloric saturates is forced to follow the pressure and magnetic field dependence of $\Delta M_t(T,p,H)$ presented in figures 4.15 (c) and (d). Consequently, the values of the $\Delta S_t$ must exhibit a relative reduction as the values of the applied pressure increase in parallel with the small relative reduction of the $\Delta M_t$ illustrated in figure 4.15 (c) and (d). $\Delta S_t$ values are derived by applying the Clausius-Clapeyron equation,

$$\Delta S_t(T,p,H) = \frac{\Delta M_t(T,p,H)}{\dfrac{dT_t}{dH}} \tag{4.25}$$

where the expression for $\Delta M_t$ is computed by subtracting $M_{FM} - M_{AFM}$ in equations (4.10) and (4.9) and $\dfrac{dT_t}{d\mu_0 H}$ values are found in equations (4.6) and (4.7). Results computed from

heating data are presented in figure 4.25. The barocaloric effect is then expected to saturate at lower values as seen in figure 4.22 (a) ($\sim 10\text{JK}^{-1}\text{kg}^{-1}$). In comparison with this plot, the magnetocaloric effect shown in panel (e) saturates at slightly larger values ($10.7\text{JK}^{-1}\text{kg}^{-1}$ as well as the barocaloric effect at a constant field of 5 T shown in panel (b) ($10.7\text{JK}^{-1}\text{kg}^{-1}$) because the applied magnetic field forces a larger magnetization change at the transition. In this sense, this marginal decrease of the saturation entropy change is clearly evidenced in figure 4.22 (d) and (h) and at $T$ = 320, 335 K in figure 4.24 (d) and (e) as the caloric effect is induced by a pressure change rather than a magnetic field change. In short words, the magnitude of the multicaloric entropy change depends on the competition between the magnetocaloric and the barocaloric character which originate the thermal response. The predominance of the barocaloric character leads to a slight reduction of the values at which $\Delta S$ saturates.

From figures 4.21, 4.22 and 4.23 it is seen that a suitable combination of magnetic field and pressure significantly expands the temperature range where large (giant) values of the entropy change are obtained in comparison with the narrower temperature windows restricted to the pure magnetocaloric and barocaloric effects. It is worth noting that a large temperature window for the entropy change not only results in a larger operational range in potential refrigeration devices, but also increases the reproducibility of these large entropy values upon pressure and magnetic field cycling. Furthermore, as shown in panels (a), (b), (e) and (f) in figures 4.22 and 4.23 the application of a constant secondary field tunes the temperature window at which the primary field drives the caloric effect. Accordingly, the temperatures at which the barocaloric effect (magnetocaloric effect) is exhibited are shifted towards lower (higher) values under the influence of magnetic field (hydrostatic pressure).

The inverse nature of the magnetocaloric effect combined with the conventional barocaloric effect results in a peculiar multicaloric response in Fe-Rh. As outlined in table 4.1 and explained along this section, if the changes on the applied pressure and magnetic field have different sign, the multicaloric effect is strengthened, whereas changes of the same sign lead to a competition between fields favouring either the AFM or the FM phase. Figure 4.26 (a) displays the computation of $\Delta S(T, 0 \rightarrow H', 0 \rightarrow p') = \Delta S(T, p', H') - S(T, p = 0, H = 0)$ derived from the mean field model described in the appendix B which do not include hysteresis so that we can gain insight on the multicaloric behaviour obtained upon application (or removal) of the two fields. At low values of magnetic field [top panels in the figure 4.26 (a)], the barocaloric effect dominates and application of pressure reduces the compound's entropy. As the magnetic field magnitude is increased, the inverse effect gains significance as evidenced by the expanded temperature window where the entropy change is positive. Interestingly, the multicaloric entropy change reverses sign for a particular combination of

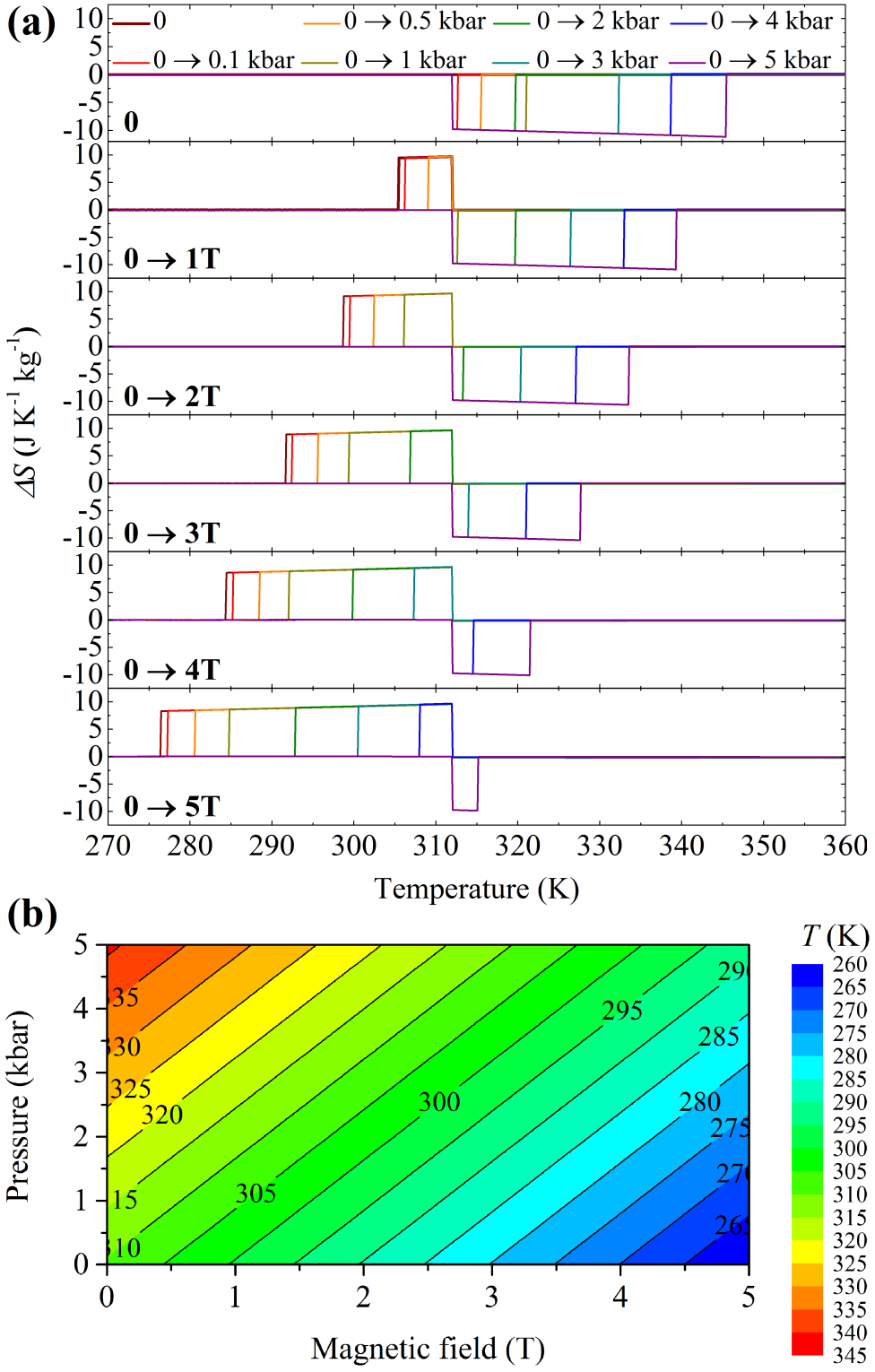


Fig. 4.26 (a) Temperature dependence of the multicaloric isothermal entropy change, $\Delta S(T, 0 \rightarrow H, 0 \rightarrow p)$ for selected values of applied magnetic field and applied hydrostatic pressure following the results derived from the model described in the appendix B. (b) Isothermal contour lines where multicaloric entropy reverses its sign.

pressure and magnetic field. This effect is described in more detail in figure 4.26 (b) which depicts the isothermal lines on a $(p,H)$ plane where the multicaloric entropy change reverses its sign. These lines are projections of the phase diagram (see the AFM $\rightarrow$ FM plane in figure 4.14) onto the $(p,H)$ (horizontal) plane. For $p$ and $H$ values to the right of each isothermal line, the multicaloric entropy change $\Delta S(T,0 \rightarrow p',0 \rightarrow H') > 0$, while for values on the left hand side, $\Delta S(T,0 \rightarrow p',0 \rightarrow H') < 0$. It is therefore demonstrated that very fine tuning of the caloric and multicaloric response can be achieved by simultaneous (or sequential) application of magnetic field and pressure to this Fe-Rh system.

The hysteresis inherent to the first-order transition represents a drawback with regards to the magnitude and the reproducibility of the thermal response upon field cycling. The width along each of the three axis of the region bounded by the two planes in figure 4.14 depicts the additional temperature $\Delta T_H$, pressure $\Delta p_H$ and magnetic field $\Delta H_H$ cost to be paid for the attainment of the reversibility of the caloric effect. Following (4.6) and (4.7), the hysteretic region has a slight field dependence:

$$\Delta T_H = T_{AFM\rightarrow FM} - T_{FM\rightarrow AFM} = 10.2 + 0.4\mu_0 H + 0.1p \tag{4.26}$$

$$\mu_0 \Delta H_H = \mu_0 (H_{AFM\rightarrow FM} - H_{FM\rightarrow AFM}) = 2.4 - 4.3 \cdot 10^{-4} T + 1.6 \cdot 10^{-2} p \tag{4.27}$$

$$\Delta p_H = p_{AFM\rightarrow FM} - p_{FM\rightarrow AFM} = -2.5 + 2.6 \cdot 10^{-3} T - 3.9 \cdot 10^{-2} \mu_0 H \tag{4.28}$$

In this regard, it has recently been reported that in a metamagnetic shape memory alloy, magnetization of the sample at atmospheric pressure and demagnetization under an applied hydrostatic pressure of 1.3 kbar resulted in a significant reduction of hysteresis [91]. This phenomenon is attributed to the shift of the first-order transition to lower temperatures with magnetic field, and the shift towards higher temperatures with hydrostatic pressure. In our $Fe_{49}Rh_{51}$ specimen magnetic field and pressure also shift the magnetostructural transition in a similar way, as discussed in previous sections and therefore a reduction of hysteresis is also expected from the combined effect of $H$ and $p$. This phenomenon is illustrated in figure 4.27 (a) which shows isothermal magnetization loops at atmospheric pressure and under an applied pressure of 1.7 kbar. It is seen that the hysteresis is almost suppressed by magnetizing the sample at atmospheric pressure and demagnetizing it under 1.7 kbar. However, such a reduction in hysteresis is only apparent because the reduction of hysteresis in magnetic field occurs at the expense of hysteresis in pressure. This fact is illustrated in figure 4.27 (b) which indicates the actual thermodynamic path followed by the sample in such a combined magnetic field/pressure cycle.

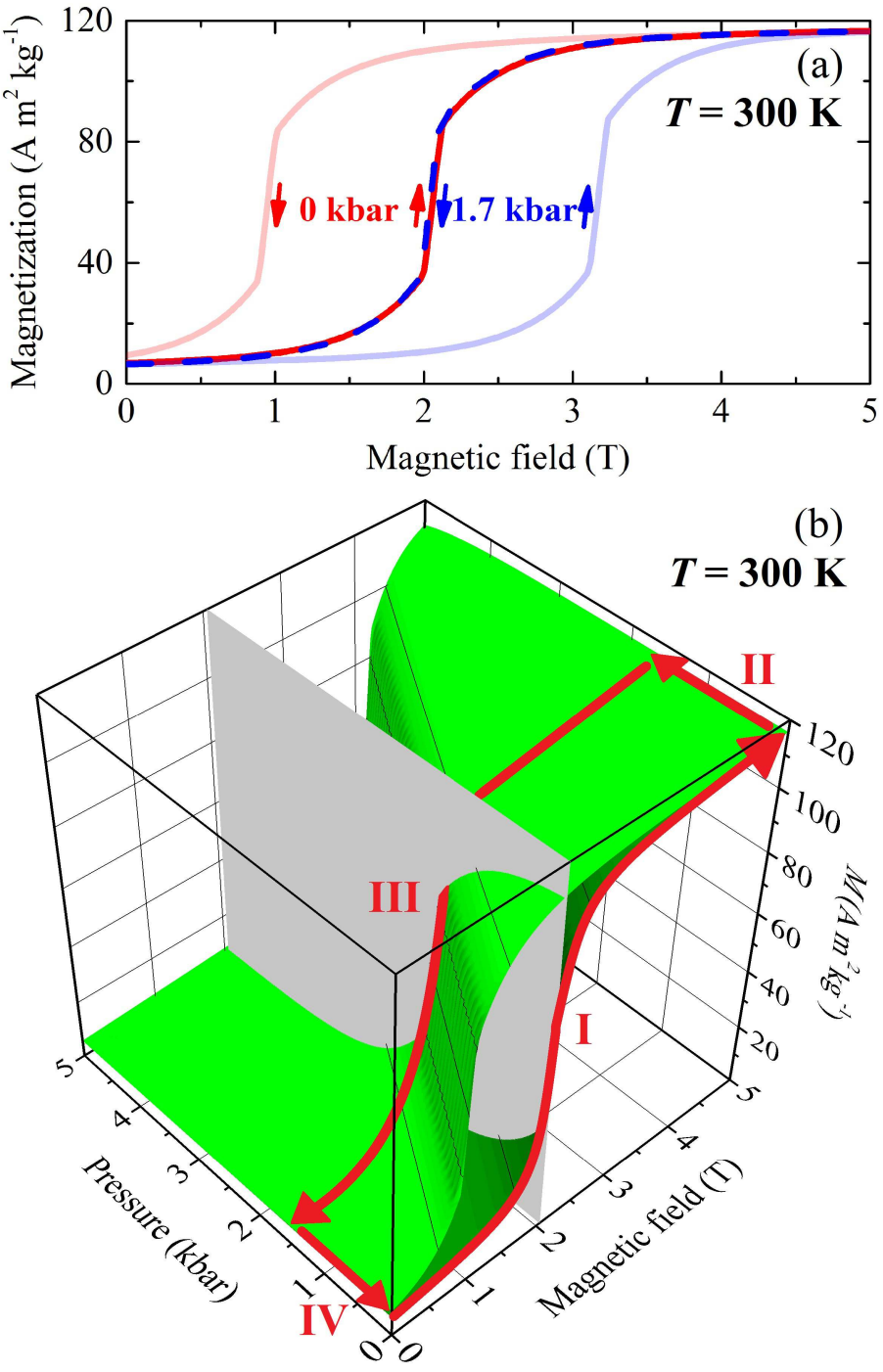


Fig. 4.27 (a) Isothermal magnetization obtained on increasing and decreasing magnetic field at selected (constant) values of hydrostatic pressure. (b) Isothermal magnetization surface as a function of pressure and of magnetic field. The red arrows indicate a complete loop corresponding to increase of magnetic field at atmospheric pressure (path I), application of a 1.7 kbar pressure in the FM phase (path II), removal of the magnetic field under 1.7 kbar (path III), and removal of hydrostatic pressure in the AFM phase (path IV).

It is instructive to compare the energy dissipated in a magnetic field loop (at atmospheric pressure) $E_H$, to that dissipated in the combined cycle $E_{H,p}$. These quantities are computed as:

$$E_H = \mu_0 \int H dM(T,H,0) \tag{4.29}$$

and

$$E_{H,p} = E_I + E_{II} + E_{III} + E_{IV} \tag{4.30}$$

where $E_I$, $E_{II}$, $E_{III}$ and $E_{IV}$ correspond respectively to the work associated with trajectories I, II, III and IV indicated in figure 4.27 (b). Under the assumption that volume compressibilities of AFM and FM phases are similar ($\kappa_{AFM} \simeq \kappa_{FM}$), and

$$\int_I H dM(T,H,0) \simeq \int_{III} H dM(T,H,p) \tag{4.31}$$

this expression reduces to

$$E_{H,p} \simeq \Delta p \Delta v \tag{4.32}$$

where $\Delta v$ is the difference in the atomic volume of the two phases.

For our $Fe_{49}Rh_{51}$ sample we obtain $E_H \simeq 115$ J kg$^{-1}$ and $E_{H,p} \simeq 170$ J kg$^{-1}$. While the energy corresponding to the multicaloric loop is marginally larger than that corresponding to the magnetic field loop (at constant pressure) it is worth noticing that both quantities are much smaller than the latent heat of the transition ($\sim 3300$ J kg$^{-1}$).

For the sake of completeness, figure 4.28 presents an example of a converse cycle at the same temperature (300 K) in which the transition is pressure-driven, instead of being driven by magnetic field, and illustrates that alternative thermodynamic cycles can also yield to the apparent hysteresis reduction.

### 4.4.4 Summary and conclusions

Materials with cross-response to more than one external field are particularly interesting [1]. In Fe-Rh application of hydrostatic pressure enhances the stability of the AFM phase and shifts the $H-T$ transition line to higher temperature values, and application of magnetic field enhances the stability of the FM phase and shifts the $p-T$ transition line to lower temperature values.

We have presented a thorough study of the multicaloric behaviour of Fe-Rh where the mechanical and magnetic contributions have been determined, as well as the contributions due to the cross-response of the alloy arising from the interplay between magnetism and

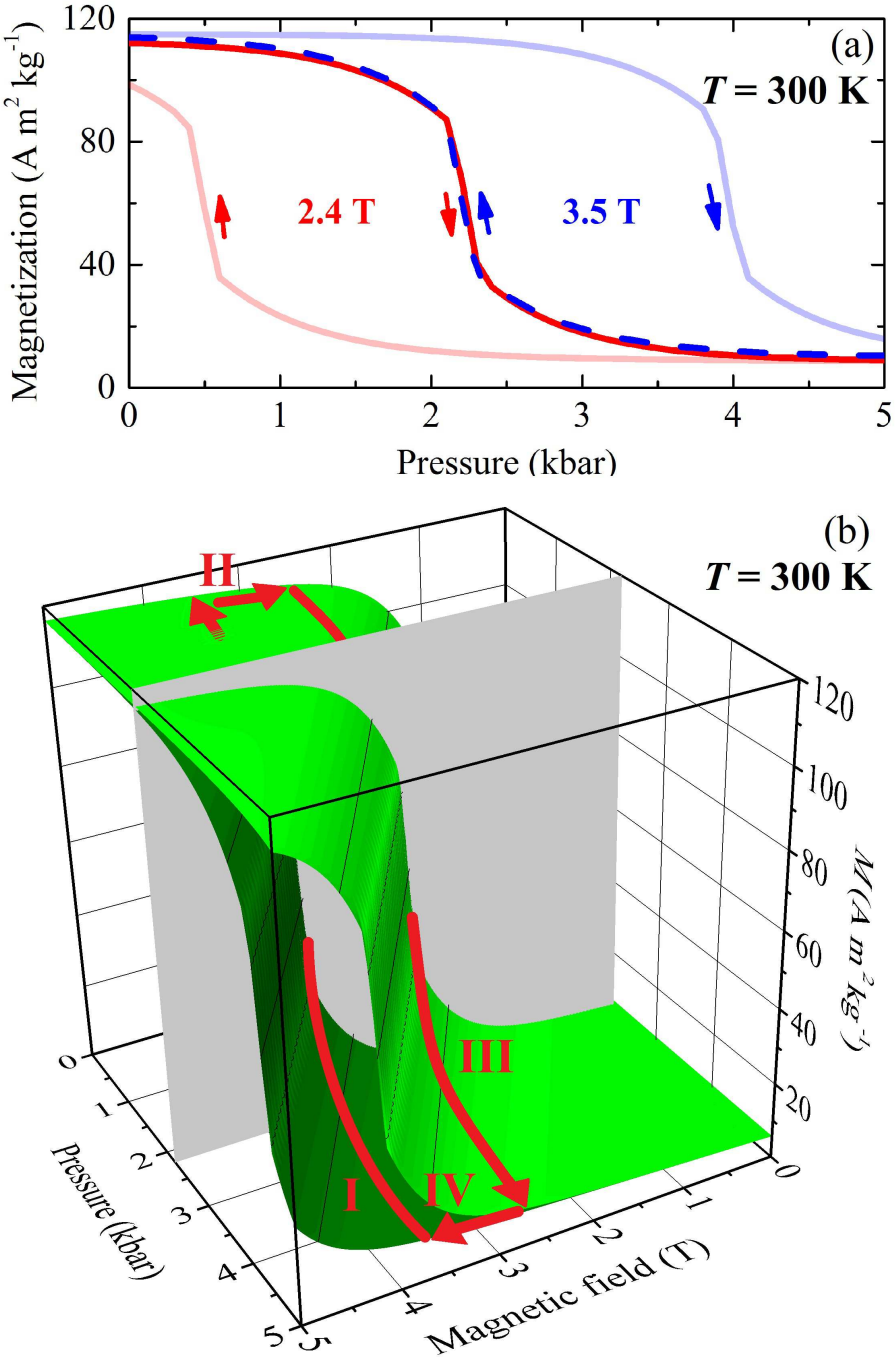


Fig. 4.28 (a) Isothermal magnetization obtained on increasing and decreasing pressure at selected (constant) values of magnetic field. (b) Isothermal magnetization surface as a function of pressure and of magnetic field. The red arrows indicate a complete loop corresponding to increase of pressure at 3.5 T (path I), removal of a magnetic field of 1.1 T in the FM phase (path II), removal of the pressure under 2.4 T (path III), and application of magnetic field of 1.1 T in the AFM phase (path IV).

structure. It has been shown that the combined effect of two external stimuli lead to interesting multicaloric properties: it is possible to enlarge the temperature window where giant effects are observed, and also, the material can be shifted from heating to cooling by a fine tuning of pressure and magnetic field. Interestingly, the reproducibility of the barocaloric and magnetocaloric effects can be ensured if magnetic field and pressure are conveniently applied as a secondary field, respectively. In this sense, a thermodynamic cycle including the application and removal of $\sim$ 1 T magnetic field is indicated to ensure the full reproducibility of the barocaloric effect, whereas the application and removal of $\sim$ 1.7 kbar hydrostatic pressure might yield to a reproducible magnetocaloric effect. In $Fe_{49}Rh_{51}$ application of magnetic field results in just a small increase of the pressure-induced entropy change because the magnetostructural transition occurs well below the Curie point, but for materials with a magnetostructural transition close to the Curie point it is expected that the combined effect of pressure and magnetic field can result in a significant enhancement of the entropy change corresponding to pure barocaloric and magnetocaloric effects.

## 4.5 Magnetocaloric effect under uniaxial compression

### 4.5.1 Sample details

The sample used for the experiments was a long shaped parallelepiped $Fe_{49}Rh_{51}$ polycrystalline specimen which was cut from a different batch of the studies presented in the previous sections. The sample mass was 468.715 mg and the dimensions were $3.3 \times 3.1 \times 6.6$ mm$^3$.

### 4.5.2 Experimental details

- A previous calorimetric characterization of the AFM-FM transition at zero fields has been performed with a DSC Q2000 from TA instruments at rate 15 K min$^{-1}$.
- Calorimetric measurements under uniaxial stress and magnetic field were performed using the setup described in section 3.3 for stress values $\sigma =$ -2.9, -54.7, -100.6, -111.7, and -147.4 MPa, and magnetic field values $\mu_0 H = 0$, 1, 2, 3, 4, 5, and 6 T, while temperature is scanned at a rate 0.4 K/min; and isothermal measurements at selected values of the compressive stress ($\sigma =$ -2.9, -54.7, -100.6, -111.7, and -147.4 MPa) while magnetic field is scanned at a rate 0.33 T/min.

### 4.5.3 Results and discussion

The first-order magnetostructural transition at zero magnetic field and in the absence of uniaxial stress in the present sample exhibits similar features as in the previous cases. The enthalpy and entropy changes are computed from the thermogram shown in 4.29 and display slightly lower values ($\sim -10\%$) in comparison to the sample batch used for the previous sections, i. e. $\Delta H_t = 3500$ J kg$^{-1}$ and 11 J K$^{-1}$ kg$^{-1}$. The temperatures at the peaks identify the transition temperature values upon cooling and heating and correspond to $T_{t_c}$ = 311.9 K and $T_{t_h}$ = 321.5 K, respectively.

Figures 4.30 and 4.31 show representative calorimetric runs collected at constant values of magnetic field $H$ and stress $\sigma$ upon heating and cooling, respectively. As explained in section 3.3.1, the current experimental system displays a lower sensitivity in comparison with the other calorimetric setups employed for the previous sections which hinders a net calorimetric characterization of the first-order transition. Despite of that, transition temperatures $T(\sigma, H)$ can be clearly tracked as a function of the applied magnetic field and uniaxial compressive stress because there is still evidence of the peak temperature as indicated by the arrows in figures 4.30 (heating runs) and 4.31 (cooling runs).

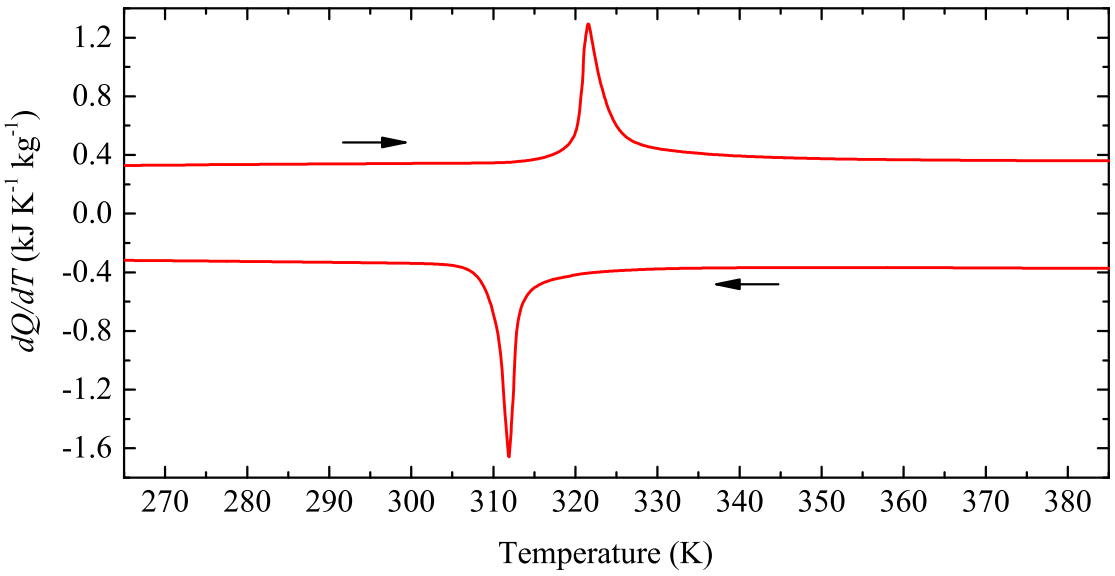


Fig. 4.29 Differential scanning calorimetry heating and cooling runs at 15 K/min performed with a TA Q2000 setup.

Figure 4.32 shows the isothermal measurements in which the magnetic field has been scanned under constant stress $\sigma$ and temperature $T$. Each isothermal measurement has been performed after a previous thermal excursion as described in section 3.1.1 and includes a set of magnetic field scans so that the reproducibility of the magnetocaloric effect at each value of the temperature and uniaxial stress can be analysed. The peak of the thermogram identifies the critical magnetic field which drives the transition at each temperature.

Figure 4.33 illustrates the behaviour of the transition temperature as a function of $H$ (a) and $\sigma$ (b) and the corresponding parameters $\frac{dT_t}{d\sigma}$ (c) and $\frac{dT_t}{d\mu_0 H}$ (d) obtained from the linear fits from both the isofield and the isothermal measurements. Experimental data exhibit excellent linearity and we can assume a linear behaviour of the transition temperature expressed as:

$$T(\sigma,H) = T_0 + \frac{dT}{d\sigma}\sigma + \frac{dT}{dH}H \tag{4.33}$$

The linear fits from both the isofield and isothermal measurements depicted in (a) and (b) display good agreement and can provide $\frac{dT_t}{d\sigma}$ and $\frac{dT_t}{d\mu_0 H}$ values if each parameter is properly identified from equation (4.33). Average values of experimental data allow the parametrization of the transition temperature as a function of magnetic field and uniaxial stress:

$$T(\sigma,H) = (-10.1 \pm 0.2)\mu_0 H + (-0.030 \pm 0.007)\sigma + (329.5 \pm 0.7) \tag{4.34}$$

$$T(\sigma,H) = (-10.0 \pm 0.4)\mu_0 H + (-0.026 \pm 0.003)\sigma + (316.1 \pm 1.4) \tag{4.35}$$

where (4.34) refers to heating or a process of application of magnetic field and (4.35) refers to cooling or a process of a field removal. Figure 4.34 illustrates the $T(\sigma,H)$ planes given by the previous equations together with the experimental points. At this point, these results can be compared with the previously given equations (4.6) and (4.7) and the corresponding plot shown in figure 4.14[3]. The isotropic $\omega \sim 1\%$ volume expansion associated with the $AFM \rightarrow FM$ first-order transition involves a deformation matrix expressed as [92]:

$$\boldsymbol{\varepsilon} = \begin{pmatrix} \omega/3 & 0 & 0 \\ 0 & \omega/3 & 0 \\ 0 & 0 & \omega/3 \end{pmatrix} \tag{4.36}$$

where the diagonal values related to a pure dilation are given by $\varepsilon_{ii} = \dfrac{\omega}{3}$. Thus, the Clausius-Clapeyron equation is written for the uniaxial stress along the $i$ direction case and for the hydrostatic pressure case as:

$$\text{eCE}: \quad \frac{dT_t}{d\sigma} = \frac{\omega}{3\Delta S_t} \qquad\qquad \text{BCE}: \quad \frac{dT_t}{dp} = \frac{\omega}{\Delta S_t} \tag{4.37}$$

Accordingly, $Fe_{49}Rh_{51}$ is expected to exhibit a much higher sensitivity to the applied hydrostatic pressure in comparison with the uniaxial stress with a ratio

$$\frac{dT_t}{dp}\left(\frac{dT_t}{d\sigma}\right)^{-1} = 3 \tag{4.38}$$

With respect to the experimental data shown in this section, the shift of the transition temperature by application of each type of mechanical stress are given by:

$$\text{Heating:} \quad \frac{dT_t}{d\sigma} = -0.030 \pm 0.007 \text{K MPa}^{-1} \quad \frac{dT_t}{dp} = 0.062 \pm 0.01 \text{K MPa}^{-1} \tag{4.39}$$

$$\text{Cooling:} \quad \frac{dT_t}{d\sigma} = -0.026 \pm 0.003 \text{K MPa}^{-1} \quad \frac{dT_t}{dp} = 0.063 \pm 0.01 \text{K MPa}^{-1} \tag{4.40}$$

[3]For a proper comparison, it is worth noting that by convention a compressive mechanical force is described by negative values of the applied stress $\sigma$ and positive values of the hydrostatic pressure $p$, as explained in section A. Results related to the BCE are given in units of kbar (100 MPa).

The experimental values of the ratio $\frac{dT_t}{dp}\left(\frac{dT_t}{d\sigma}\right)^{-1}$ are 2.1 (heating) and 2.4 (cooling), which are slightly lower than their expected value given by 4.38. In this regard, the fact that the present sample batch features lower $\Delta S_t$ values together with the larger experimental error associated with the employed experimental technique might explain the slight overestimation of the $\frac{dT_t}{d\sigma}$ values. Indeed, the fact that the values of $\frac{dT_t}{d\mu_0 H}$ are also slightly overestimated in comparison with the results obtained from the other sample batch and the other experimental techniques would reinforce these suggestions. In this sense, reference [32] reported a shift of $\frac{dT_t}{d\sigma} \sim -0.020\text{K MPa}^{-1}$, which would be closer to the relation given by (4.38). In this case, the transition temperature shifted towards lower values due to the tensile character of the applied uniaxial stress ($\sigma > 0$).

Taking into account the sensitivity functions provided in section 3.3.1, the calorimetric peaks are integrated by following the expression given in section 3.1.1 which lead to the magnetocaloric entropy change $\Delta S$ at selected values of the applied compressive stress. The corresponding results are shown in figure 4.35. Due to the larger error associated with the sensitivity functions $S(T,\sigma)$ for the reasons explained in section 3.3.1, the integrated $\Delta S$ values carry larger relative error ($\sim \pm 7.5\%$). In parallel to the results shown in figure 4.9 (b), the magnetocaloric effect upon cyclic application of a 6 T magnetic field saturates at values $\sim 12 \pm 1$ J K$^{-1}$ kg$^{-1}$ and display excellent reproducibility over a temperature window of $\sim 45$ K. The application of the compressive uniaxial stress yields to a shift of the overall caloric effect towards higher temperature values in analogy with the application of hydrostatic pressure.

### 4.5.4 Summary and Conclusions

In summary, the influence of both magnetic field and compressive uniaxial stress on the $Fe_{49}Rh_{51}$ first-order magnetostructural transition has been evaluated. Both fields yield to an opposite behaviour at the phase diagram. On the one hand, application of compressive uniaxial stress energetically favours the low-temperature low-volume phase. On the other hand, application of magnetic field energetically favours the high-temperature phase FM phase. In comparison with the case in which hydrostatic pressure is applied, the uniaxial compression yields to a lower field sensitivity of the transition temperature ($\sim 2.4$ times lower) due to the fact that hydrostatic pressure is the field which best couples the dilational strain associated with the first-order transition. The magnetocaloric effect exhibits an overall shift to higher temperatures with increasing values of the applied compressive stress.

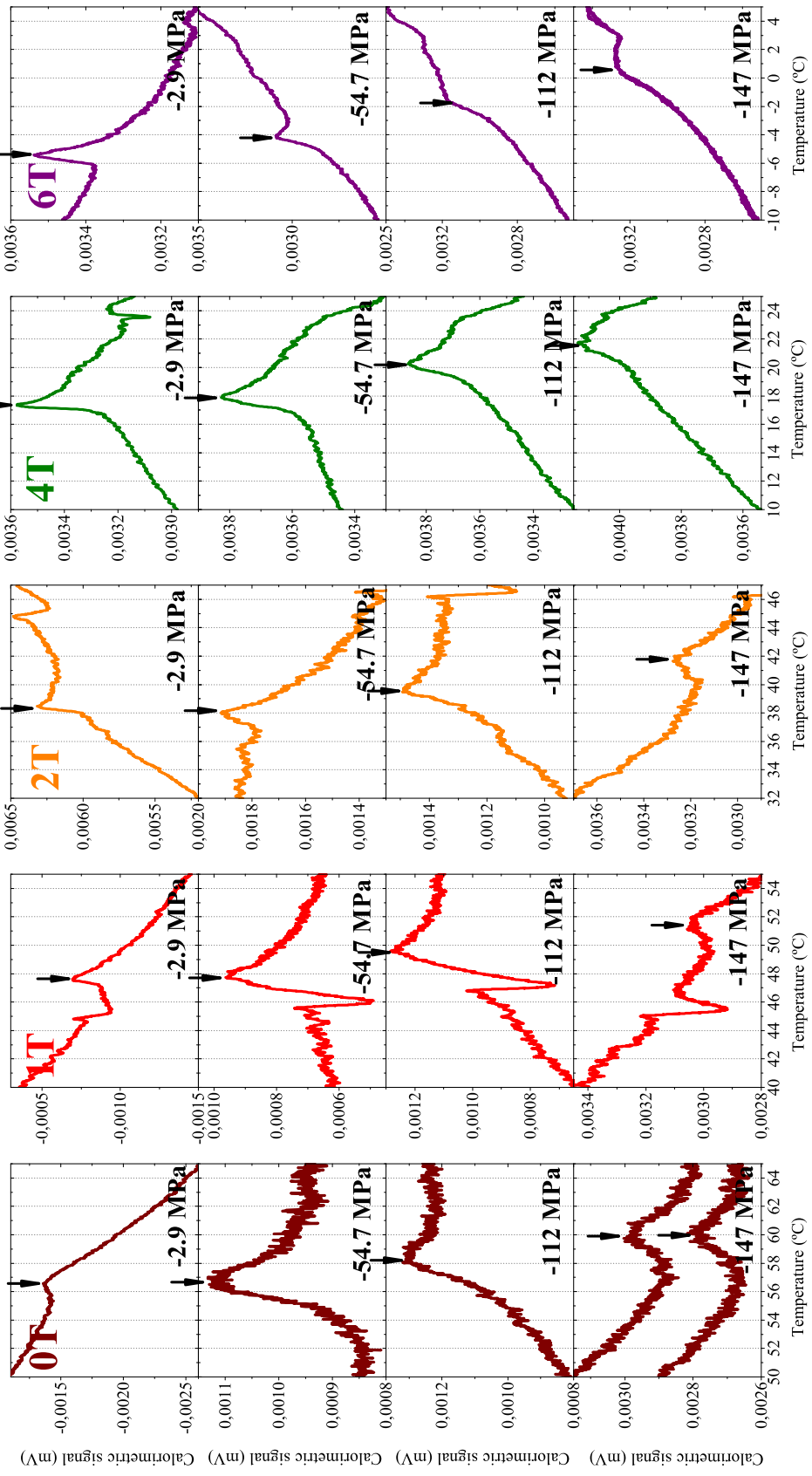


Fig. 4.30 Compendium of representative calorimetric heating runs at selected values of applied uniaxial stress (rows) and magnetic field (columns). The arrows identify the peak associated with the first-order transition.

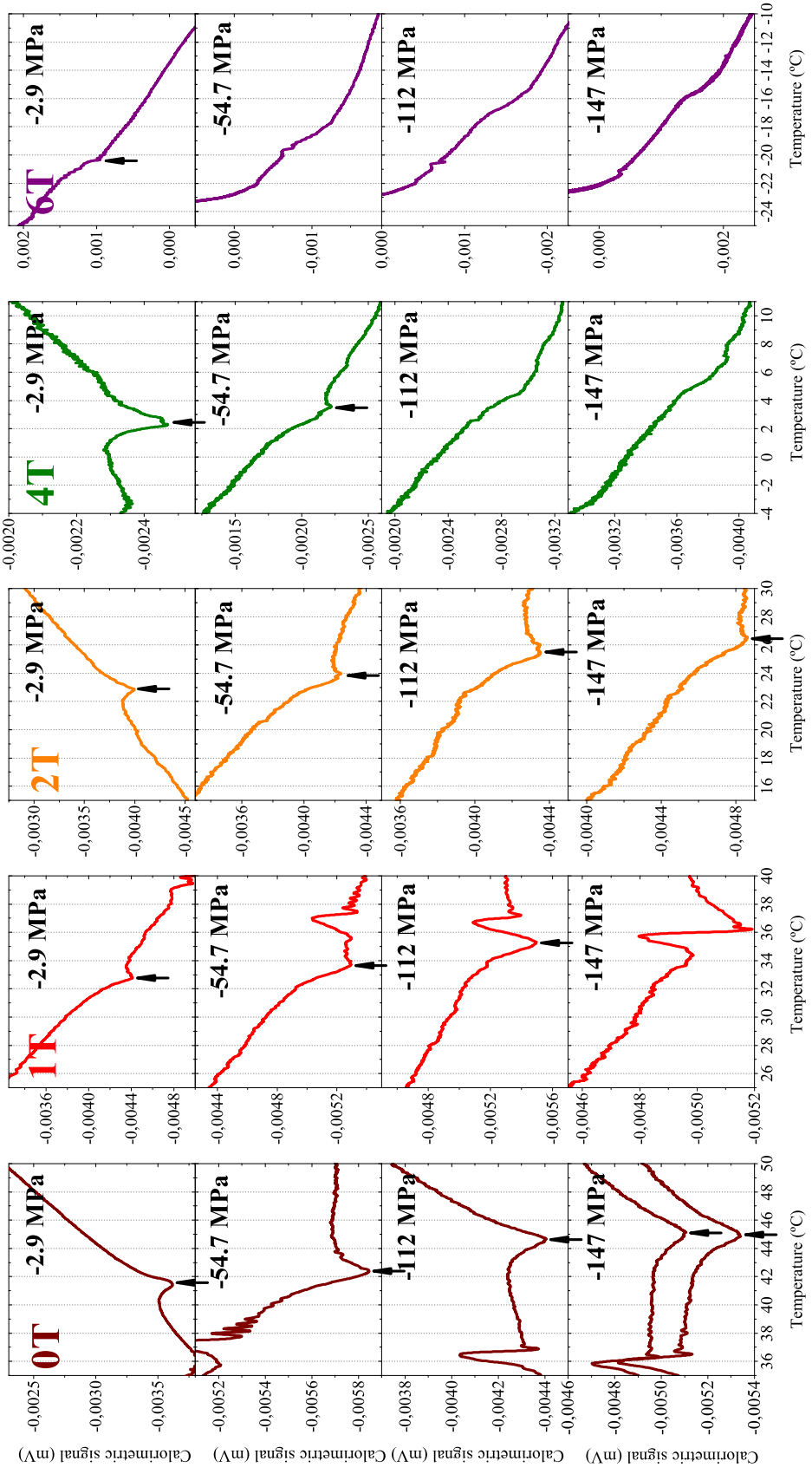


Fig. 4.31 Compendium of representative calorimetric cooling runs at selected values of applied uniaxial stress (rows) and magnetic field (columns). The arrows identify the peak associated with the first-order transition.

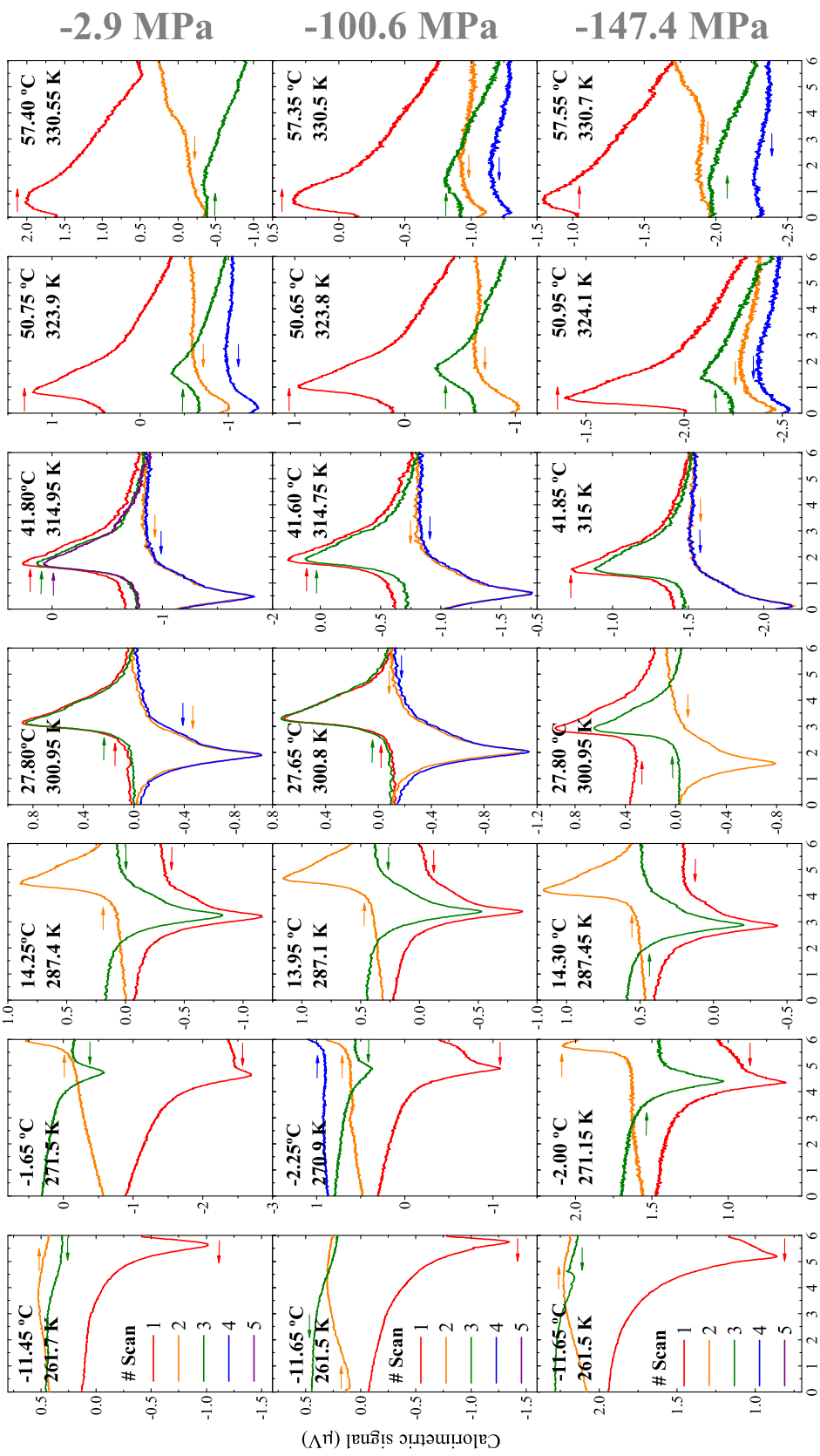


Fig. 4.32 Isothermal calorimetric curves recorded at selected values of uniaxial stress by scanning magnetic field. For a better comparison, each row of thermograms are recorded at -2.9, -100.6, and -147.4 MPa, and each column displays thermograms at approximately the same temperature. Arrows in each thermogram indicate whether the magnetic field is applied or removed. A previous thermal excursion towards either the high temperature phase or the low temperature phase has been performed before each isothermal measurement and each magnetic field scan is associated with a different colour as illustrated in the scale.

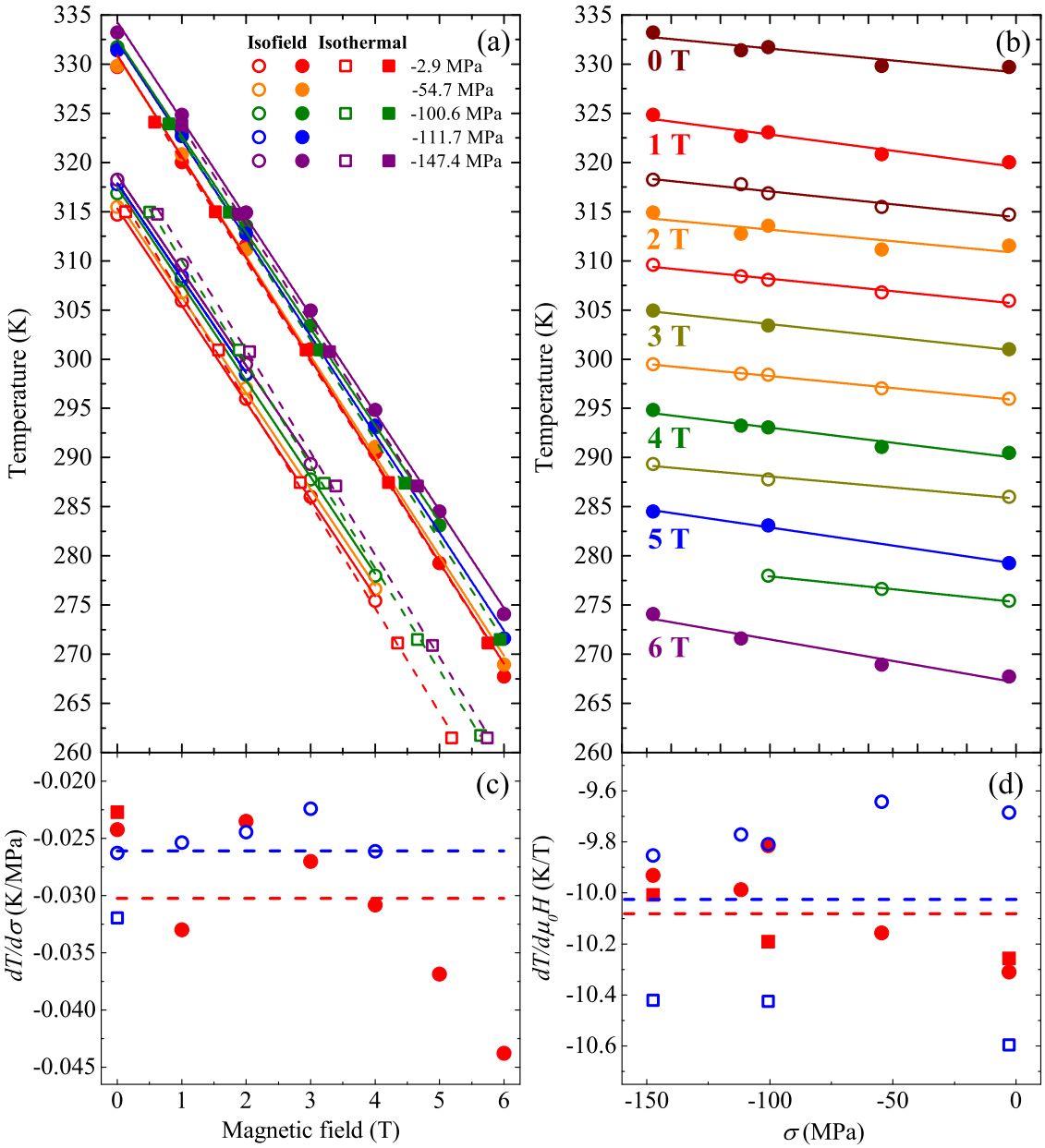


Fig. 4.33 Transition temperature as a function of magnetic field at selected values of uniaxial stress (a), and as a function of uniaxial stress at selected values of magnetic field (b). Lines correspond to linear fits. Circles refer to isofield measurements and squares to isothermal measurements. Solid symbols correspond to a process of heating or application of magnetic field and open symbols to a process of cooling or removal of magnetic field. Panels (c) and (d) illustrate the values of the shift of the transition temperature, $\frac{dT}{d\sigma}$ and $\frac{dT}{d\mu_0 H}$ as a function of the applied magnetic field and stress, respectively. Dashed red (heating/application of $H$) and blue (cooling/removal of $H$) lines represent the average values and are employed for parametrization of $T(\sigma, H)$.

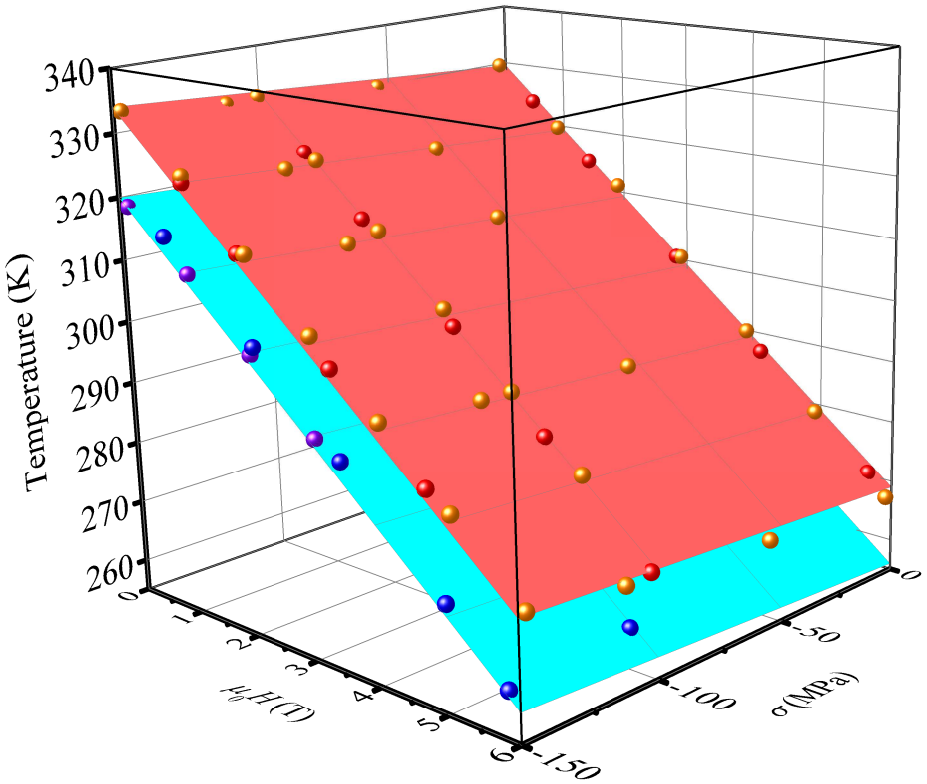


Fig. 4.34 Transition temperature as a function of magnetic field and uniaxial stress. Upper red plane corresponds to the AFM to FM transition, and lower blue plane, to the FM to AFM transition. Solid symbols stand for experimentally measured values. Red and blue symbols are obtained from isothermal calorimetric measurements at selected values of applied stress and correspond to a process of an application of magnetic field and a process of a removal of the field, respectively. Values obtained from calorimetric measurements at constant magnetic field and uniaxial stress are displayed by orange (heating runs) and purple (cooling runs) symbols.

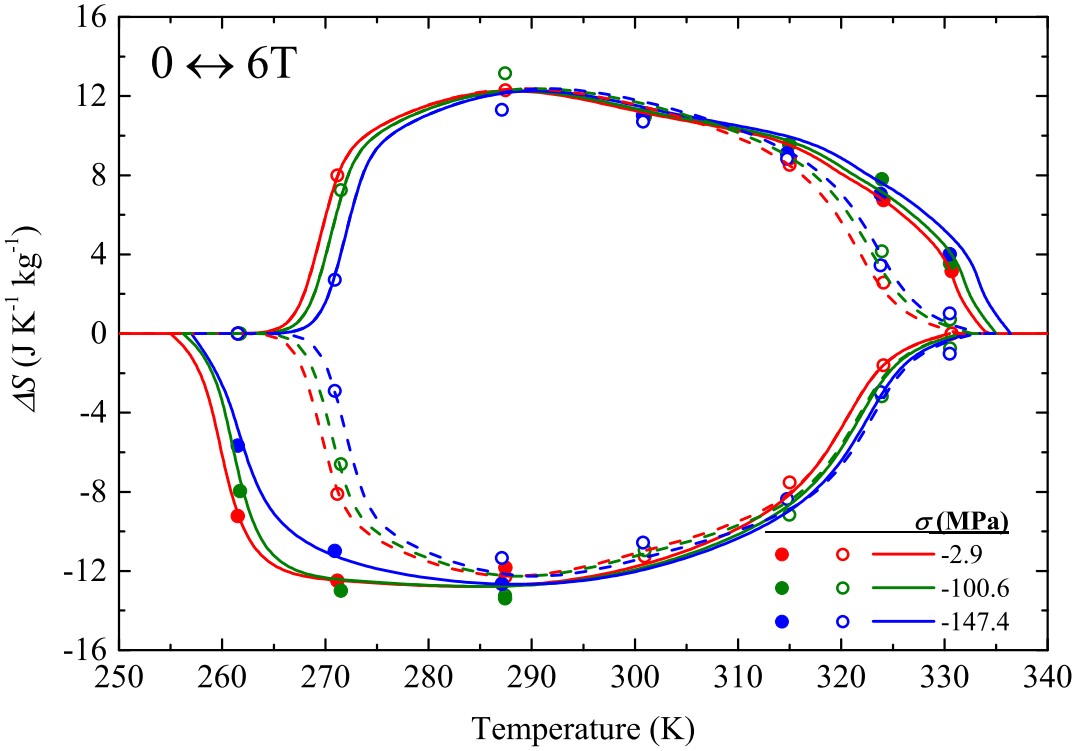


Fig. 4.35 Magnetocaloric entropy change at selected values of the applied compressive uniaxial stress $\sigma$ = -2.9 (red), -100.6 (green), and -147.4 (blue) MPa. Symbols specify the results computed from the isothermal calorimetric runs and lines are guides to the eye. Solid circles and solid lines stand for the first magnetic field scan and open circles and dashed lines refer to the subsequent scans.

# Chapter 5

# Giant caloric effects in Ni-Mn based Heusler alloys

In 1903 the German chemist and mining engineer Friedrich Heusler discovered that $Cu_2MnAl$ is ferromagnetic even though that each one of the three constituents is not magnetic by itself [93, 94]. Since then, little research effort was devoted to their synthesis and the understanding of their properties until their *rediscovery* in the last years. Nowadays, the family of Heusler compounds refer to an extensive list of more than 1000 materials [11] and their interest has remarkably increased due to their striking magnetic, structural and electronic features which can lead to great functional and multifunctional properties like magnetic shape memory properties [13], giant magneto- and mechanocaloric effects [5, 42, 92], magneto-optical properties [95], polarization of the conduction electrons [96], tunability of the band gaps [97], superconductivity [98], topological insulator behaviour [97], and thermoelectricity [99].

The present chapter is organized as follows. A first section is devoted to providing a background description of the structural and magnetic properties in the Ni-Mn based shape memory Heusler alloys. These materials are very appealing because the coupling between structure and magnetism and their characteristic martensitic first-order transition confers to these alloys a multicaloric character. For instance, it has recently been shown that the magnetocaloric effect can be suitably tuned by the combined application of magnetic field and hydrostatic pressure [91]. In shape memory alloys, their associated martensitic transition usually takes place with a negligible volume change. However in magnetic alloys, the balance between magnetic and structural free energies can lead to differences in the volume of the unit cell of the high and low temperature phases [100, 101]. In that case, the first-order transition will be sensitive to applied hydrostatic pressure. Giant magnetocaloric [13, 102], barocaloric [5] and elastocaloric [103] effects have already been reported for these alloys and the present work is aimed at contributing to the characterization of these phenomena.

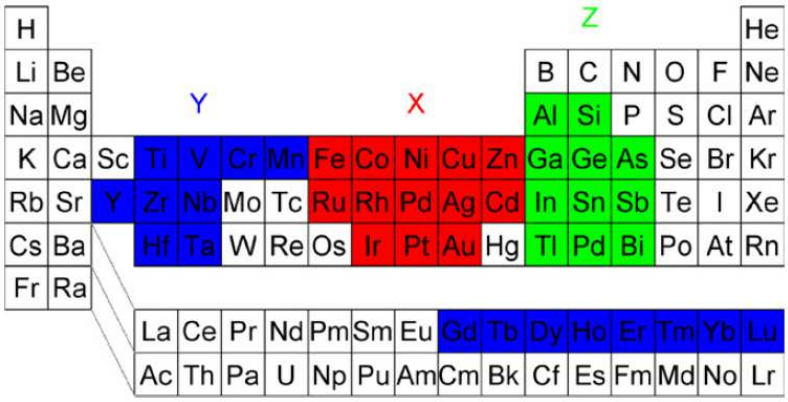


Fig. 5.1 Periodic table of the elements in which the coloured regions are indicative of the typical X-Y-Z elements which constitute a Heusler alloy, after [104].

An analysis of the magneto- and mechanocaloric effects has been performed on an extensive list of materials which have been tailored by considering their structural and magnetic properties. As will be shown, we have tuned a number of key parameters such as the transition temperatures $T_t$ and their distance to the Curie temperature $T_C$, the hysteresis, the transition entropy change $\Delta S_t$, or the sensitivity of the transition temperatures with the applied fields. For a better comparison of the their caloric performance, table 5.1 compiles important caloric parameters of the materials under study. The second section of this chapter describes the giant MCE in $Ni_{51}Mn_{33.4}In_{15.6}$, with tailored composition such that it exhibits a remarkably low thermal hysteresis of 4 K. The third section is devoted to a systematic analysis of the MCE and BCE on a number of low hysteresis Ni-Mn-In samples which allows determining a series of general trends for the performances associated with both effects. The magneto- and barocaloric effects on a series of Ni-Co-Mn-Ga-In alloys are presented in the fourth section. The fifth section presents the MCE exhibited by a composite of Cu-doped Ni-Mn-In components as an strategy for enlarging the caloric operation range. The sixth section reports a thermodynamic study which contributes to the understanding of the intermartensitic transition phenomena, since it is still not well established if these changes occur through a phase transition or not. Finally, the last section outlines the corresponding general conclusions.

Table 5.1 Sample composition, Curie temperature ($T_C$), forward ($T_M$) and reverse ($T_A$) martensitic temperatures, thermal hysteresis ($T_A - T_M$), transition entropy change ($\Delta S_t$), magnetic field dependence of the martensitic transition temperature $\frac{dT_t}{\mu_0 dH}$, pressure dependence of the martensitic transition temperature $\frac{dT_t}{dp}$, and effective magnetic moment per formula unit (four atoms per unit cell) $\mu$. $^c$ and $^h$ superscripts refer to cooling and heating processes, respectively.

| Label | Composition | $T_C$ (K) | $T_M$ (K) | $T_A$ (K) | $T_A - T_M$ (K) | $\Delta S_t$ (J / K kg) | $\frac{dT_t}{\mu_0 dH}$ (K / T) | $\frac{dT_t}{dp}$ (K / kbar) | $\mu$ ($\mu_B$) |
|---|---|---|---|---|---|---|---|---|---|
| A | $Ni_{2.02}Mn_{1.36}In_{0.62}$ | 304 | 346 | 350 | 4 | 39.9 | -0.12 | 1.83 | 4.79 |
| B | $Ni_{2.05}Mn_{1.30}In_{0.65}$ | 298 | 330 | 336 | 6 | 40.8 | -0.26 | 1.65 | 4.25 |
| C | $Ni_{1.99}Mn_{1.37}In_{0.64}$ | 307 | 329 | 333 | 4 | 40.3 | -0.42 | 1.95 | 5.93 |
| D | $Ni_{1.99}Mn_{1.34}In_{0.67}$ | 302 | 305 | 309 | 4 | 32.0 | -1.37 | 1.37 | 5.13 |
| E | $Ni_{2.00}Mn_{1.32}In_{0.68}$ | 307 | 275 | 280 | 5 | 24.0 | -2.64 | 1.88 | 4.80 |
| $In_0$ | $Ni_{43.3}Co_{7.4}Mn_{30.8}Ga_{18.5}$ | 440 | 396 | 413 | 17 | 16.4 | | $3.2^c$, $2.0^h$ | |
| $In_{20}$ | $Ni_{42.47}Co_{8.87}Mn_{31.67}Ga_{14.98}In_{2.01}$ | 435 | 407 | 422 | 15 | 22.8 | $-2.0^c$, $-1.8^h$ | $3.2^c$, $2.1^h$ | |
| $In_{21}$ | $Ni_{42.2}Co_{8.4}Mn_{32.3}Ga_{15}In_{2.1}$ | 430 | 373 | 391 | 18 | 21.2 | | $2.7^c$, $2.7^h$ | |
| $In_{30}$ | $Ni_{41.5}Co_{9.2}Mn_{32}Ga_{14}In_{3.3}$ | 440 | 341 | 355 | 14 | 18.0 | $-5.0^c$, $-6.9^h$ | | |
| $Cu_0$ | $Ni_{50.1}Mn_{35.3}In_{14.6}$ | 311 | 301 | 305 | 4 | 25.2 | -2.2 | | |
| $Cu_{1.9}$ | $Ni_{49.4}Mn_{33.9}In_{14.8}Cu_{1.9}$ | 307 | 289 | 293 | 4 | 26.7 | -2.6 | | |
| $Cu_{2.2}$ | $Ni_{49.0}Mn_{33.8}In_{15.0}Cu_{2.2}$ | 306 | 284 | 289 | 5 | 25.3 | -2.7 | | |
| $Cu_{2.7}$ | $Ni_{48.5}Mn_{34.3}In_{14.5}Cu_{2.7}$ | 304 | 272 | 278 | 6 | 23.3 | -3.5 | | |

## 5.1 Physical properties of Ni-Mn based Heusler alloys

Heusler materials are intermetallics ternary compounds displaying the characteristic *Heusler* cubic phase in which the X, Y and Z atoms are arranged on four interpenetrated fcc lattices. In general, we can divide the Heusler compounds into two families: (i) the *full-Heuslers* family which respond to the $X_2YZ$ stoichiometry and their characteristic phase is the cubic $L2_1$ crystallographic structure which belongs to the $Fm\bar{3}m$ space group, and (ii) the *half-Heuslers* family which respond to the XYZ stoichiometry and have a cubic $C1_b$ structure ($F\bar{4}3m$ space group). As illustrated by the coloured regions of the periodic table shown in figure 5.1, the Heusler phase usually crystallizes when the X and Y are transition metals (sometimes the Y element can be a rare earth) and Z is a main group element, even though these conditions do not involve stability of this phase. The magnetic and electronic properties of these materials have strong correlations with their structural features, the atomic arrangement in the crystallographic structure and the particular interatomic distances. There exists a particularly rich diversity of Heusler materials with non-stoichiometric composition, as well as other groups of Heusler materials like the *quaternary Heuslers* which have two different elements X and X' and a resulting composition (XX')YZ [11]. Thus, tailoring their physical properties of Heusler compounds, such as the prevalence of ferromagnetic order or the existence of first-order transitions to other energetically favorable phases, is possible by tuning their structural features by procedures like adjusting the composition, doping the material with other elements, or tuning the annealing temperature.

### 5.1.1 Structural properties and phase transitions

In the present thesis, the interest is focused on the Ni-Mn based full-Heusler (X = Ni, Y = Mn) alloys and the corresponding vast family of materials which depart from the strict $Ni_2MnZ$ stoichiometry and display a strong composition dependence of the physical properties. In this case, the Z element can be either Ga, Al, In, Sn, or Sb. With regards to the study of the giant caloric effects, the interest on Ni-Mn based Heusler materials relies on their particular magnetic properties and the first-order martensitic transition with magnetostructural coupling from the austenitic $L2_1$ phase to the martensitic phase with tetragonal $L1_0$ structure. In general, the $L2_1$ phase is created after the $A2 \rightarrow B2 \rightarrow L2_1$ order-disorder transitions when the material is cooled after its solidification [105, 106]. The A2 phase is the fully disordered bcc cubic crystallographic structure and the B2 phase is the partially ordered phase which consists on the bcc CsCl-type structure in which the Ni atoms occupy the corner positions and the Mn and Z atoms randomly occupy the central positions. Typically, the degree of atomic order in Heusler structures can be tuned by specific heat treatments and sometimes

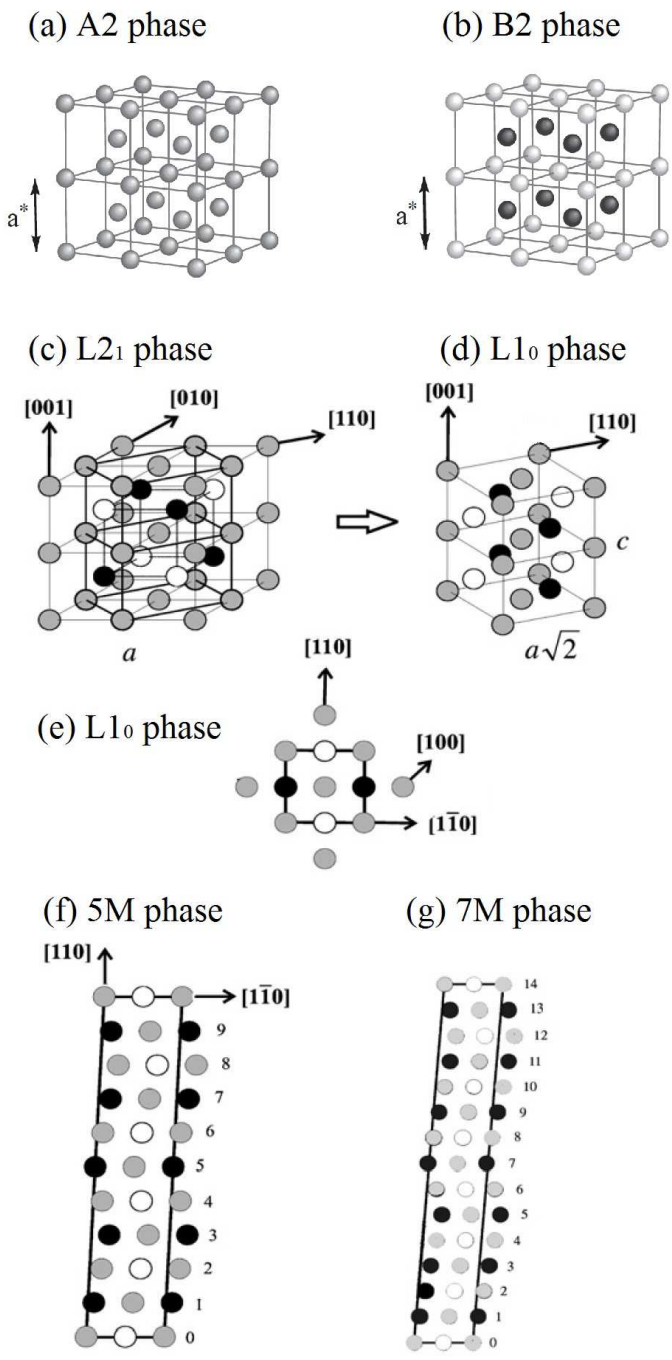


Fig. 5.2 Representation of the A2 (a), B2 (b), $L2_1$ (c), $L1_0$ (d, e) and the modulated 5M (or 10M) (f) and 7M (or 14M) (g) phases. For the case of A2 phase in (a), all atoms randomly occupy the positions indicated by the grey balls, whereas for the B2 case shown in (b) the black ball positions are occupied by either Mn or Z atoms and the white balls for Ni atoms. The representation in (e) depicts a top view of the $L1_0$ structure. (a) and (b) panels have been obtained from [105] and (c-g) from [13].

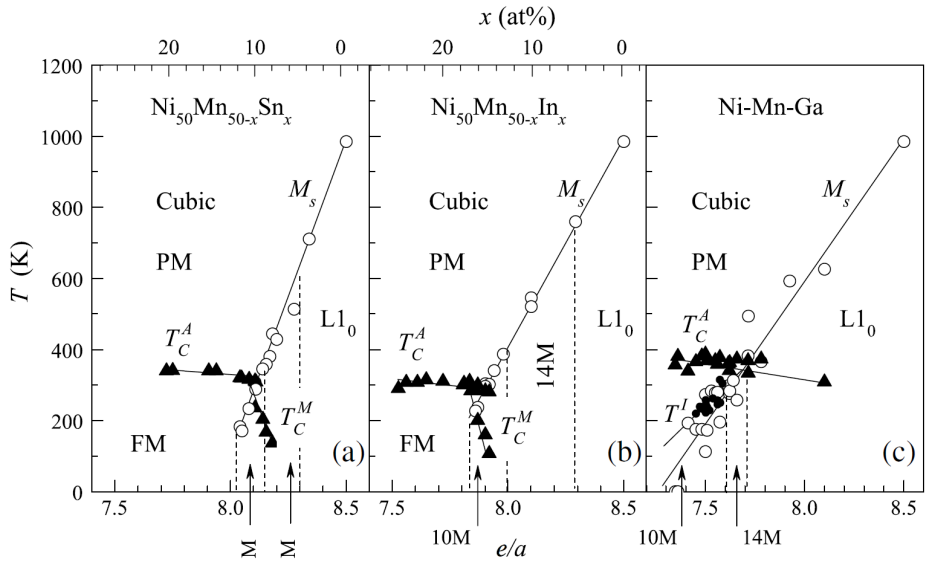


Fig. 5.3 The magnetic and structural phase diagrams of Ni–Mn–Z Heusler alloys with Z as (a) Sn, (b) In and (c) Ga, after [13]. The triangles and the circles correspond to the magnetic and martensitic transformation temperatures respectively. The regions corresponding to the different structures are separated by discontinuous lines. Small solid circles in (c) correspond to the premartensitic transition temperature.

the full atomic arrangement of the $L2_1$ is not achieved and the materials display traces of retained B2 phases. Both A2 and B2 crystallographic structures are drawn in figures 5.2 (a) and (b), respectively. In figure 5.2 (c) the $L2_1$ austenite phase is shown for the case of $Ni_2MnGa$ which is the only stoichiometric Ni-Mn based Heusler material exhibiting a martensitic transition, whereas in the other cases in which Z $\neq$ Ga the transition takes place for compositions out of the stoichiometry as shown in figure 5.3, which depicts the phase diagrams for the Z = Sn (a), In (b), and Ga (c) cases. The $L2_1$ phase can be described as a bcc structure which results from the superposition of four interpenetrated fcc lattices, being two of them equally occupied by Ni atoms. The Ni atoms occupy the Wyckoff position 8c (1/4, 1/4, 1/4), the Mn atoms occupy the 4a (0, 0, 0) position and the Z atoms, 4b (1/2, 1/2, 1/2) [93].

As previously mentioned, in many Ni-Mn based Heusler alloys the $L2_1$ Heusler phase becomes unstable upon cooling and transform to the more energetically favorable low symmetry $L1_0$ tetragonal phase (space group $P4/mmm$). Typically, this is the case for alloys with low concentractions of the Z element, since the $L1_0$ is the ground-state structure of the parent NiMn compound [13]. However, in addition to the $L2_1 \rightarrow L1_0$ first-order transition, the austenite phases can also exhibit transitions to monoclinic structures which

can be described as modulated variations of the martensite phase originated by shearing the tetragonal $L1_0$ phase, as seen by comparing the top views of these structures in figure 5.2 (e), (f), and (g). Figures (f) and (g) show top views of the low temperature modulated five-layered (5M) martensite structure and the modulated seven-layered (7M) martensite monoclinic structures, which are named as a function of the periodicity of the modulation.[1] These two kinds of modulations are the most frequent monoclinic structures in martensitic Ni-Mn based Heusler alloys. Alternatively, the orthorhombic 4O phase can also be present. Recently, these modulated structures have been interpreted as adaptive phases constituted of twin-related nano-variants of the non modulated phase stacked with the appropriate periodicity which enables minimizing the strain energy in the nucleation process [107]. In some cases, the system exhibits a sequence of first-order transitions before it reaches the $L1_0$ ground state structure which involve the presence of *intermartensitic* or *premartensitic* phases [14, 108], such as the sequence $L2_1 \rightarrow 10M \rightarrow 14M \rightarrow L1_0$. In relation to this, the first-order character of the intermartensitic structural changes is discussed in section 5.7.

As corroborated by figure 5.3, many properties of the Ni-Mn based Heusler compounds can be predicted by counting the average valence electron per atom $e/a$ [109] determined by the particular composition of the compound. Each phase diagram departs from the value $e/a = 8.5$ given by the reference composition $Ni_{50}Mn_{50}$. At regions where the martensitic transition takes place, it can be observed that the transition temperature $T_t$ values increase by increasing the value of $e/a$ with great linearity. In families of materials with compositions $Ni_2Mn_{1+x}Z_x$ as the Heusler alloys studied in the present dissertation, an increment in the value of $x$ results in a decrease of $e/a$ and, thus, a decrease of the martensitic transition temperature. In addition, it can be seen that changing the Z element results in a variation of the slope of the $T_t$ vs. $e/a$ regressions [13, 106]. With regards to the experimental values of $T_C$, it can be seen that they generally have comparable values within the temperature range of $T \in [300, 400]$ K, even though the magnetic interactions originating the ferromagnetic behaviour can significantly differ from compositions with one Z element to the other [110].

Martensitic transitions refer to the solid-to-solid diffusionless first-order transitions in which the change in crystallographic structure is induced by the nucleation and growth of the variants of the new phase by a shear-like behaviour of displacive nature. In the occurrence of a martensitic transition, the new martensite phase nuclei experience a growth due to the mobility of the *habit phase* (phase boundary) along the region with the Heusler $L2_1$ phase. As will be discussed in the following paragraphs, the creation of this habit plane signifies and energetic cost which contributes to the hysteresis. The tetragonal geometry of the $L1_0$

[1] In the literature, these phases are indistinctly labeled by either 5M and 7M or 10M and 14M, depending on how the periodicity is defined. *M* refers to the *monoclinicity* to which the phase structure evolves as a consequence of the modulation.

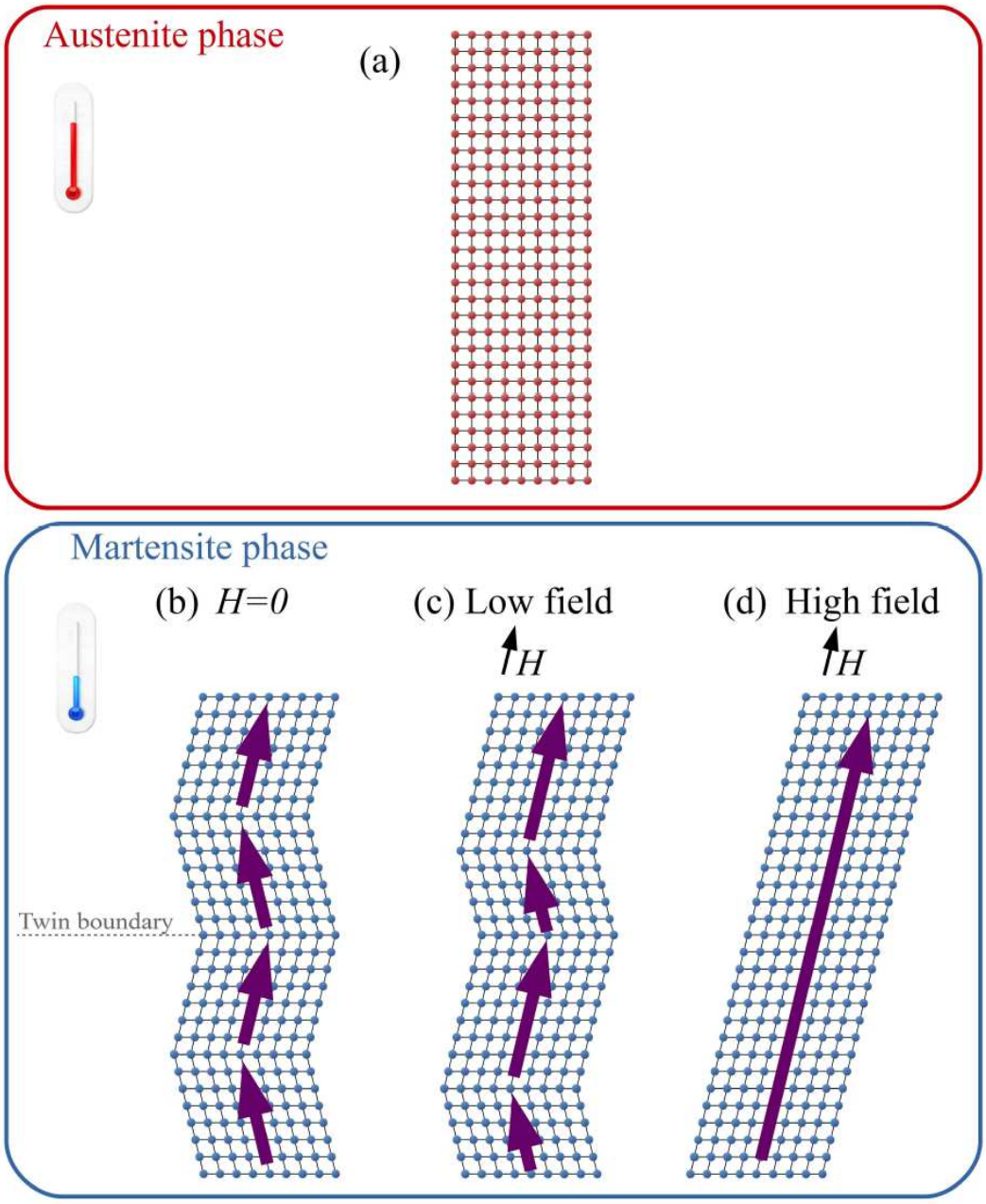


Fig. 5.4 Sketches of the microstructure of the high temperature austenite phase (a) and the low temperature martensite phase (b, c, d). In case of ferromagnetic order at the martensite phase, each twin variant is associated with a particular magnetic domain. In absence of magnetic field (b), the twin variants are distributed so that they minimize the magnetostatic energy [13]. As shown in (c), as the magnetic field is applied, certain magnetic domains are energetically favoured and they expand due to the motion of the corresponding twin boundaries. At sufficiently high magnetic fields (d), the magnetic domains are already aligned with the magnetic field. The microstructure rearrangement prompts the superelastic and magnetic shape memory properties.

structure allows the formation of three different *twin variants* as a function of their orientation. The martensite phase consists in a complex microstructure of twin variants which, in turn, are separated by hierarchically distributed twin boundaries on many length scales [111]. If none of the variants is energetically favoured by application of external fields, the absence of a preferred orientation prompts the distribution of the twin variants on the three possible orientations. In view of the superelastic behaviour exhibited by these materials with strain values up to 10% [112], a high mobility of the twin boundaries favours a proper alignment of the variants along the preferred orientation given by the applied stress [111]. Sometimes, by virtue of the magnetostructural interplay the twin-variant reorientation can be induced by means of applied magnetic fields. Figure 5.4 sketches the microstructure at the austenite and martensite phases and the mobility of the magnetic martensite variants by application of magnetic field which promotes the growth of certain variants. Hence, the re-accommodation of variants and the field-induced deformations are explained by the deformation processes (*twinning*) mediated by a proper shear. An analysis of the crystallographic conditions of these processes yields to the definition of two types of twins (type I and type II). Each type of twin stands for a particular configuration of variants with specific orientations on each side of the twin plane [113]. In relation to this, the reorientation of magneto-elastically coupled domains on application of magnetic field gives rise to the magnetic shape memory effect and the superelastic properties. If the reverse transition to the austenite phase is driven by either a heating process or by application or removal of a certain thermodynamic field (stress or magnetic field), the twinned structure disappears and, thus, the undeformed structure is recovered.

The magnetic anisotropy energy density $K$, i. e. the energy cost of rotating the magnetic moment of a single crystal from the easy to the hard direction, plays an important role on the magnetic properties of these materials. While the $L2_1$ cubic phase has low magnetocrystalline anisotropy, the martensite phase can display significant values of magnetic anisotropy in the special case in which the Z component is Ga. Low values of magnetic anisotropy $K$ facilitate the local rotation of the magnetic moments within the twin variants structure. As the value of $K$ increases, the rotation and mobility of the structural domains and the alignment of the corresponding easy axis with the applied magnetic field becomes more energetically convenient than deflecting the local magnetic moments. Thus, the magnetoelastic coupling of the twinned structure with the magnetic domains results from a competition between magnetic anisotropy $K$ and the elastic energy associated with the mobility of the twin bowndaries.

The nucleation and growth procedures associated with the martensitic transition lead to a hysteresis and, thus, an energy cost for the first-order transition to be completely field-driven. As explained in section 2.2.3, these energy losses inherent to first-order transitions must

be reduced in view of a better energetic efficiency for cooling applications. A number of strategies and procedures have been suggested for the minimization of the hysteresis effects in Heusler compounds, as avoiding the additional energetic cost associated with the nucleation process by cycling the materials through minor loops [114, 115] or introducing artificial defects by nanoindentation which act as nucleation sites [116].

From the structural point of view, the hysteresis is associated with the geometrical compatibility between the martensite and the austenite phases [117–119]. When the first-order transition takes place, millions of austenite/martensite interfaces are created. The volume change associated with the phase transition generates stress in each island of martensite growing in the austenite matrix and vice versa. This hinders the energetical favority of the phase transition and represents a contribution to enhance the hysteresis loops. In addition, this concentration of stresses at the transition layer generates a gradual degradation of the material upon field cycling due to the promotion of dislocations and microcracks growth [119] at the microstructure. We can define $\mathbf{U}$ as the matrix in the cubic basis related to the linear transformation which maps the austenite to the martensite lattice [120]. It is only a function of the lattice paramaters and it also measures the volume ratio of martensite to austenite phases so that $\det\mathbf{U} = 1$ when there is no volume change upon the transition. Hence, a first condition for better reversibility in the martensitic transition is $\det\mathbf{U} = 1$. We can now define $\lambda_1$, $\lambda_2$, and $\lambda_3$ as the ordered ( $\lambda_1 \leq \lambda_2 \leq \lambda_3$) eigenvalues of the distortion matrix $\mathbf{U}$. In general, a low-elastic-energy transition layer can exist in particular arrangements of the martensite variants (type I and type II) in which a specific rotation of the variants allows a proper accommodation of the microstructure due to their fine twinning. This situation is depicted in figure 5.5. In general, these conditions are only satisfied for certain volume fractions of each of the two variants: $f$ and $1-f$. Furthermore, it can be demonstrated that $\lambda_2 = 1$ is a necessary and sufficient condition for the compatibility between austenite and martensite phases, so that the fine twinning configuration of the martensite phase disappears because in this especial case $f = 0$ or $f = 1$ [121]. Accordingly, it has been reported that a successful strategy for reducing the hysteresis is tailoring materials with $\lambda_2 \to 1$ [118, 120].

At this point, a further step is to consider a third set of conditions on the lattice parameters and the twin system. These conditions are named as the *cofactor conditions* and imply the existence of a low elastic energy interface for any value of the volume fraction of the twin variants, $0 \leq f \leq 1$ [122]. Following the description given in [119], these conditions can be given in a simplified form as:

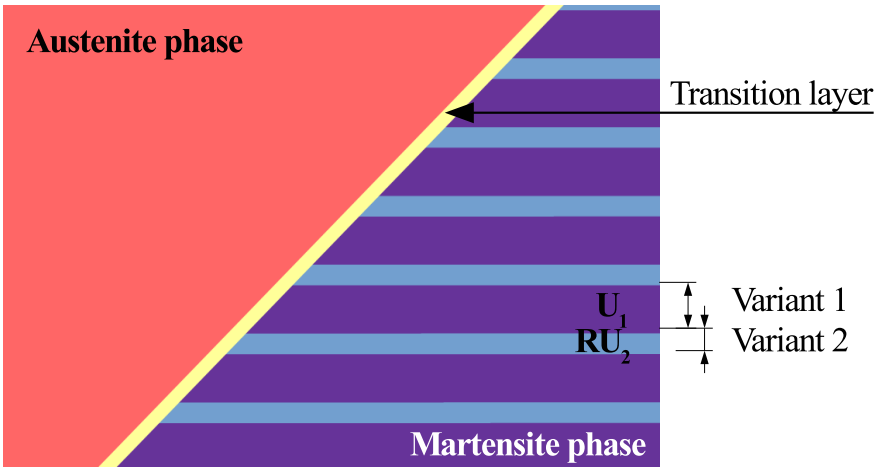


Fig. 5.5 Sketch of the interface region between austenite and martensite phases. Martensite configuration corresponds to a *twin system* which meets compatibility with the austenite phase and minimizes the elastic energy at the transition layer. $\mathbf{U_1}$ and $\mathbf{U_2}$ are the distortion matrices of variants 1 and 2, respectively. The twin system configuration relies on a particular rotation of the variant 2 ($\mathbf{RU_2}$), and its periodic arrangement with the variant 1. In general, this is satisfied for certain volume fractions $f$ of variant 1, and $1-f$ of variant 2.

$$\bullet\ \lambda_2 = 1 \qquad \bullet \begin{cases} X_I := |\mathbf{U}^{-1}\hat{\mathbf{e}}| = 1 & \text{for type I twins.} \\ X_{II} := |\mathbf{U}\hat{\mathbf{e}}| = 1 & \text{for type II twins} \end{cases} \tag{5.1}$$

where $\hat{\mathbf{e}}$ is the *twinning axis* and is given as a function of the eigenvalues and the eigenvectors of $\mathbf{U}$ [119]. When these conditions are satisfied, it has been show that the martensitic transition exhibits high reversibility and weak degradation during cycling [117, 120].

### 5.1.2 Magnetic properties

It is well known that the elementary Mn atom orders antiferromagnetically, but ferromagnetic order can appear in structures which increase the distance between manganese atoms $r_{Mn-Mn}$ and, thus, increase the value of the fraction $\frac{r_{Mn-Mn}}{r_d}$ as follows from the Bethe-Slater curve [123] illustrated in 5.6 (a), where $r_d$ is the radius of the $3d$ orbital. This yields to a change in sign of the exchange integral $J$ in the Heisenberg hamiltonian $H_{ij} = -2JS_iS_j$ from a negative (antiferromagnetic order) to a positive value (ferromagnetic order).

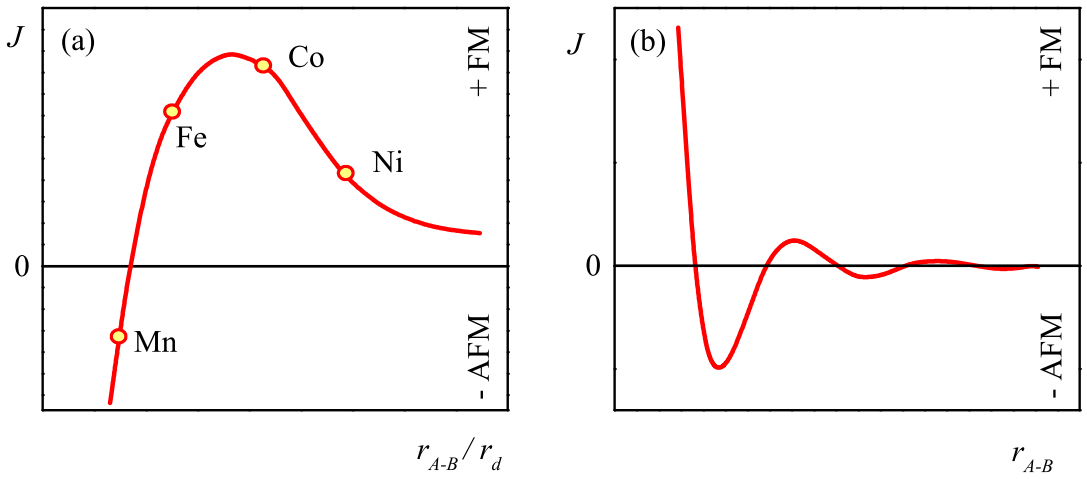


Fig. 5.6 Diagrams of the exchange interaction parameter $J$ between magnetic moments. (a) The Bethe-Slater curve illustrating the value of $J$ as a function of the $\frac{r_{A-B}}{r_d}$, where $r_{A-B}$ is the interatomic distance and $r_d$ is the radius of the $3d$ orbital. (b) Sketch of the indirect exchange coupling constant $J$ calculated by the RKKY interaction as a function of the interatomic distance.

The origin of the magnetic behaviour of Ni-Mn based Heusler materials is a complex question. The magnetic properties in this family of materials are strongly linked to the role of Mn atoms and the structure. In the $L2_1$ phase, the interatomic $r_{Mn-Mn}$ distance is too big for a simple description restricted to the direct exchange interaction between their magnetic moments. Since the study of Kübler et al. in 1983 [12] based on the first free density functional theory calculations of the exchange interactions on a series of full Heusler alloys with composition $X_2MnY$, it is established that Mn atoms mainly confine the magnetic moment as a result of the exclusion of the minority-spin electrons. The interaction can be described in terms of the RKKY (Ruderman-Kittel-Kasuya-Yosida) interaction which describes the indirect coupling mechanism of the localized magnetic moments at site $i$ and $j$ in a metal by means of conduction electrons, which belong to the $s$ and $p$ energy levels. Thus, the magnetic moment in $i$ polarizes the electron gas which, in turn, is able to polarize the magnetic moment in $j$. The resulting exchange energy which describes the indirect exchange interaction is plotted in figure 5.6 and takes over a few interatomic distances. As shown in figure 5.6, this energy has an oscillatory pattern and, consequently, a variety of magnetic behaviours can arise.

In the $L2_1$ structure, one can consider that the two nickel sublattices form a bcc cubic lattice in which the Mn or the Z atoms settle in the central position. Each Mn and Z atoms

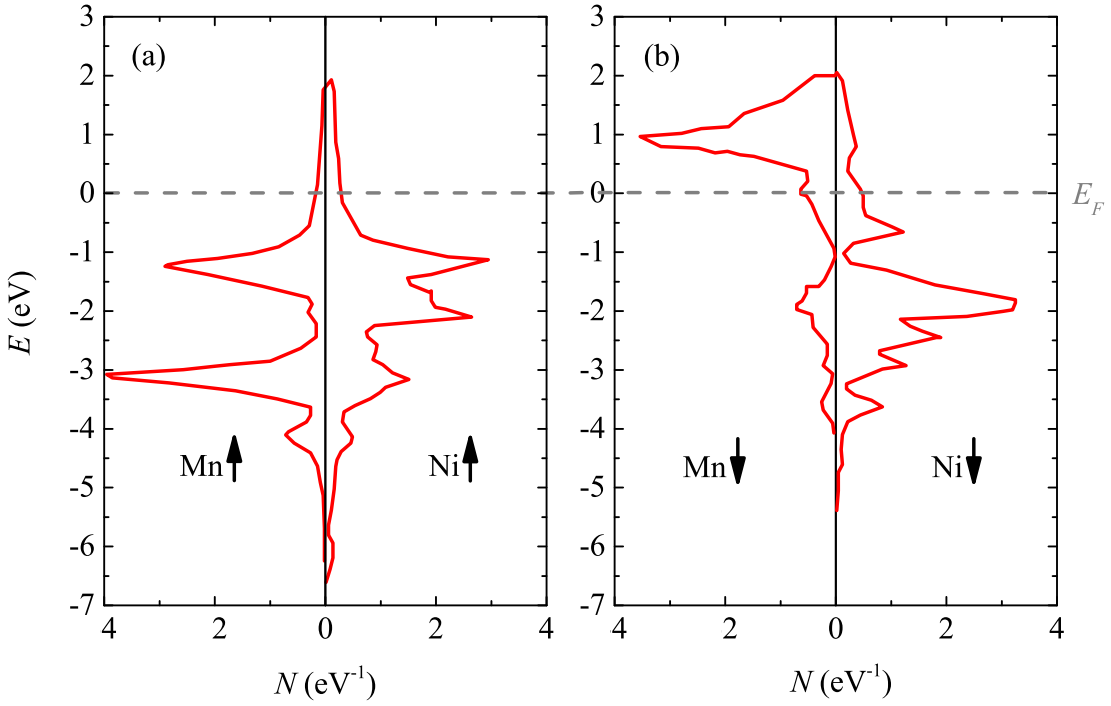


Fig. 5.7 Density of states of the spin-up (a) and spin-down (b) *d* electrons of the Mn and Ni atoms in $Ni_2MnSb$ Heusler alloy. This figure has been adapted from [12].

have eight Ni atoms as first neighbors, while the first neighbors of each Ni atom are four Mn atoms and four Y atoms. Theoretical studies reveal that hybridization occurs between the 3*d* orbitals of the Ni and Mn atoms [12, 110, 124–126]. As a consequence of that, the minority spin-down density of states is excluded and pushed up to energy levels which are higher than the Fermi energy $E_F$. This difference between spin-up and spin-down occupied states results in a net magnetization which is localized at the manganese atoms and composed of itinerant electrons moving in a common *d* band [124]. This is illustrated in figure 5.7, which displays the majority-spin (a) and the minority-spin (b) density of states of the *d* Mn and Ni electrons in $Ni_2MnSn$ calculated in [12].

The exchange parameters related to the Mn-Mn and Ni-Mn interactions is not identical in each kind of Ni-Mn full-Heusler alloy, even though the corresponding macroscopic magnetic behaviour can indeed be similar. These parameters are tuned by the particular number of *sp*-electrons given by the Z atoms and their spin polarization which mediate the interatomic covalent interaction between Mn atoms [12, 110, 127].

All these factors favour the magnetic behaviour to exhibit a strong dependence on the interatomic distances between Mn atoms and the lattice parameters of the structure, as well

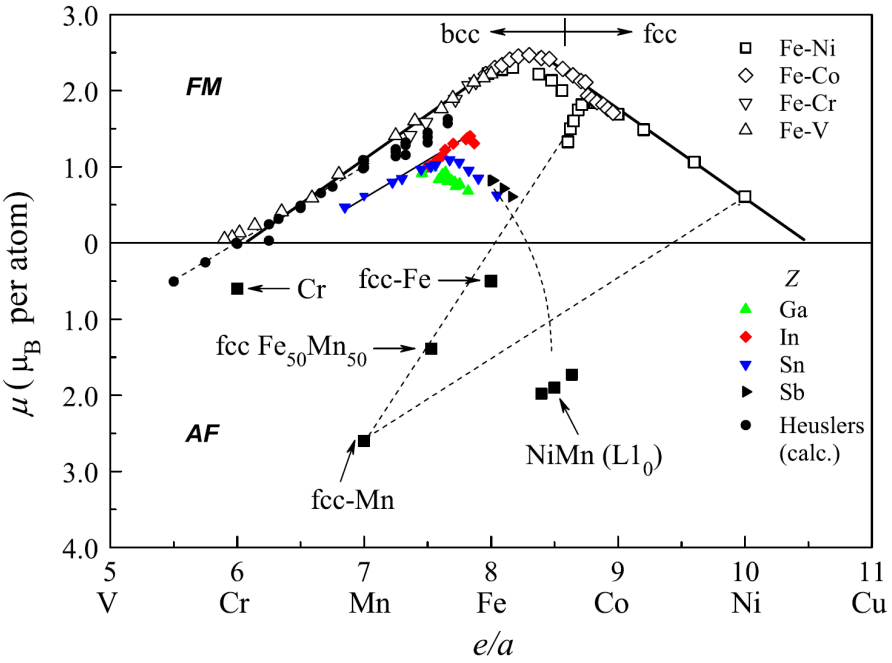


Fig. 5.8 Values of the magnetic moment $\mu$ as a function of the $e/a$ for a broad list of $3d$ metals and alloys (open symbols), Ni-Mn-Z Heuslers (filled small symbols) and antiferromagnets (filled squares), after [13].

as the number of excess Mn atoms when the composition falls out of the stoichiometry [13, 128].

The Slater-Pauling curve provides a general overview of the ferromagnetic and antiferromagnetic behaviour of the Heusler compounds as a function of the average number of the valence electrons per atom $e/a$ which fill the electronic bands [129, 130], as shown in figure 5.8. The value of $e/a$ is composed by a number of majority spin-up $N_\uparrow$ and minority spin-down $N_\downarrow$ electrons, $e/a = N_\uparrow + N_\downarrow$. The average magnetic moment per atom $\mu$ (in units of $\mu_B$) is given by the difference between both populations $\mu = N_\uparrow - N_\downarrow$, which can be expressed as $\mu = e/a - 2N_\downarrow$. Thus, for a fixed number of $N_\downarrow$ electrons the magnetic moment $\mu$ of the materials can be aligned as a function of the $e/a$ value given by the particular composition [131]. Materials on the left hand side of the Slater-Pauling curve ($e/a < 8.5$) shown in figure 5.8 typically display bcc structures, whereas the cubic close packed fcc structure is the typical structure of the materials on the right. The negative values of the magnetic moment refer to the AF order. It can be seen that the calculated values of the magnetic moment for stoichiometric full-Heusler and half-Heuslers lie on the Slater-Pauling bcc branch in which $3d$ metals and alloys are found. The experimental data for Ni-Mn-Z are plotted with the coloured symbols. The average magnetic moment of these materials is paral-

lel to the Slater-Pauling curve in which the other materials are gathered and it exhibits the same slope. However, off-stoichiometric Ni-Mn based materials with an excess of Mn atoms clearly deviate from the Slater-Pauling curve and approach the value of the antiferromagnetic $Ni_{50}Mn_{50}$ in which they approach in composition [13].

At this point, it is useful to remind the Curie-Weiss law which describes reasonably well the susceptibility behaviour in the paramagnetic region above the Curie point. Interestingly, the applicability of this law allows the extraction from magnetization measurements of important information related to the magnetic properties of the particular Heusler alloy under study. The magnetic susceptibility is written as [28, 130]:

$$\chi = \lim_{H \to 0} \left( \frac{M}{H} \right) = \frac{C}{T - T_C} \tag{5.2}$$

where the Curie constant and the Curie temperature of the system, i.e. $C$ and $T_C$, are expressed as:

$$\bullet \quad T_C = \lambda C \qquad\qquad \bullet \quad C = \frac{\mu_0 N J(J+1) {g_J}^2 {\mu_B}^2}{3k_B} = \frac{\mu_0 N \mu_{eff}^2}{3k_B} \tag{5.3}$$

where $g_J = \frac{3}{2} + \frac{S(S+1) - L(L+1)}{2J(J+1)}$ is the Landé g-factor, $\mu_{eff} = g_J \sqrt{J(J+1)} \mu_B$ is the effective magnetic moment, and $\lambda$ is the parameter related to the strength of the molecular field.

## 5.2 Sample preparation

The polycrystalline samples presented in table 5.1 and the Ni-Mn-Ga sample presented in section 5.7 were prepared by arc-melting the pure metals under an argon atmosphere in a water-cooled Cu crucible. For homogeneity, the samples were remelted several times and, subsequently, the ingots were vacuum sealed in a quartz tube and annealed at high temperature for a specific time followed by quenching in ice water. The temperature and time in which the samples were annealed was 900 °C and 48 hours for Ni-Mn-In and Ni-Mn-Ga samples, 800 °C and 72 hours for Ni-Co-Mn-Ga-In samples described in section 5.5, and 900ºC and 24h for Ni-Cu-Mn-In presented in section 5.6. In each case, the specimens were cut with a diamond saw in order to obtain the shape and mass properly adapted for each experimental system. The corresponding compositions (in at%) were measured by EDX.

The Ni-Mn-In samples were prepared in collaboration with the Indian Association for the Cultivation of Science (IACS) settled in Kolkata (India). In particular, the series of Ni-Mn-In samples analysed in section 5.4 were prepared during a stay in february 2014 at the IACS. The Ni-Co-Mn-Ga-In samples analysed in section 5.5 were prepared in collaboration with the Magnetic Materials Group at the Istituto Materiali per Elettronica e Magnetismo (IMEM-CNR) settled in Parma (Italy). The set of Cu-doped Ni-Mn-In samples studied in section 5.6 and the Ni-Mn-Ga sample studied in section 5.7 were prepared in collaboration with the Instituto Potosino de Investigación Científica y Tecnológica (IPICyT) settled in San Luis Potosí (Mexico).

## 5.3 Magnetocaloric effect in the low hysteresis Ni-Mn-In metamagnetic shape memory Heusler alloy

The relatively large hysteresis associated with the martensitic transition strongly hampers the available cooling capacity in these alloys and therefore their performance in cooling devices. This section presents the magnetocaloric properties of a $Ni_{51}Mn_{33.4}In_{15.6}$ alloy. This alloy has been especially designed to display large enough entropy changes together with a low-temperature width of hysteresis and reasonably large temperature-shift of the whole hysteresis loop due to application of a magnetic field. The studied material has been grown with an appropriate composition for which optimal geometrical compatibility between low and high symmetry phases is expected.

Section 5.3.1 describes the experimental procedures and sample characteristics. The obtained magnetization and calorimetric results are presented in section 5.3.2. In section 5.3.2, the magnetocaloric properties of the studied material are discussed. Finally, the main conclusions are summarized in section 5.3.2.

### 5.3.1 Experimental details and alloy design

A 105.7 mg sample with the shape of an eighth of an ellipsoid with 3.7, 2.7, 2 mm semi-axis was used for neutron diffraction and magnetic measurements and a 372.5 mg sample with quarter ellipsoid shape with 5.4, 4.3, 3.6 mm semi-axis was used for calorimetric measurements. In all measurements the magnetic field was applied along the direction of the long semi-axis.

An enlarged view of the phase diagram of Ni-Mn-In alloys is shown in figure 5.9. Transition temperatures are plotted as a function of the valence electron concentration ($e/a$). Continuous lines are the fits to experimental data for quasi-stoichiometric $Ni_{50}Mn_{50-x}In_x$ alloys published in reference [13] and shown in figure 5.3. Symbols correspond to published data for alloys of the Ni-rich, $Ni_{51}Mn_{49-x}In_x$, family. Open symbols are from reference [132] and solid symbols correspond to the alloy studied in the present section. While the martensitic transition line for Ni-rich alloys is very close to quasi-stoichiometric alloys, the Curie temperatures of the parent phase are located at slightly higher temperatures.

Neutron diffraction measurements were carried out by using the D1B high resolution neutron two-axis diffractometer at ILL under a flux at $\lambda$ =2.52Å. The polycrystalline sample was placed into an irradiated cylinder in permanent rotation with the use of a rotator device in order to prevent prevalent contributions to the diffraction spectra. One hour exposure time measurements were performed under isothermal conditions.

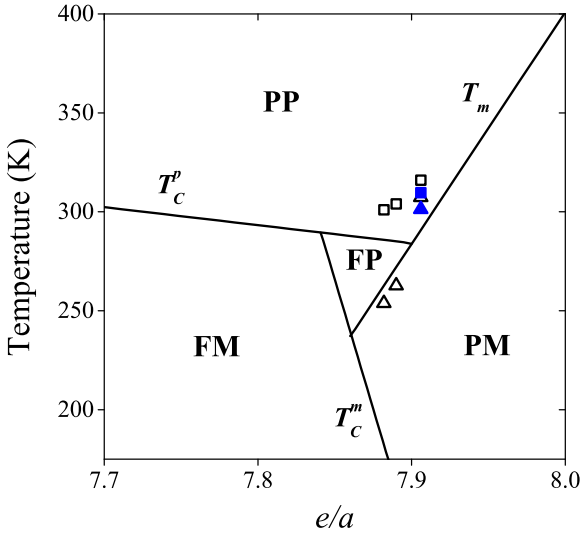


Fig. 5.9 Phase diagram of $Ni_{50}Mn_{50-x}In_x$ (continuous lines). Symbols correspond to $Ni_{51}Mn_{49-x}In_x$ alloys (squares: $T_m$, triangles: $T_c^p$). PP: paramagnetic parent phase, FP ferromagnetic parent phase, PM: paramagnetic martensite, FM: ferromagnetic martensite. $T_m$: martensitic transition, $T_c^p$: Curie temperature of the parent phase, $T_c^m$: Curie temperature of the martensitic phase.

Analysis of neutron diffraction patterns collected at 325 and 280 K (shown in figure 5.10) evidences the existence of a structural phase transition. The pattern collected at 325 K can be indexed with a cubic cell (space group $Fm3m$ no. 225) with $a = 6.008(2)$ Å. This structure corresponds to the parent phase. At 280 K the neutron diffraction pattern can be indexed with a monoclinic cell (average structure) with $a = 4.394(1)$ Å, $b = 5.640(2)$ Å, $c = 4.340(1)$ Å, and $\beta = 86.88(3)^{\circ}$. This is the martensitic phase.

As previosly mentioned, hysteresis is to a large extent determined by a geometric compatibility condition between parent and martensitic phases in martensitic materials. When this condition is satisfied the martensitic transition occurs with very low hysteresis [117]. From the obtained cell parameters above and below the martensitic transition we have determined the cofactor conditions by using the procedures explained in reference [119]. From the analysis, we have obtained quite a good compatibility of parent/twinned martensite interfaces. Specifically, we have found that the middle eigenvalue of the stretch tensor **U**, $\lambda_2 = 0.9981(15)$ and the norms $X_{\mathrm{I}}$ and $X_{\mathrm{II}}$ for type I and II twins are 0.9985 and 1.0084 (for $\hat{e} = [110]/[1\bar{1}0]$) respectively. As expressed in equation (5.1), ideal compatibility requires that $\lambda_2 = 1$ and $X_{\mathrm{I}}$ or $X_{\mathrm{II}}$ = 1. Our values deviate from ideal compatibility by less than 0.2% which anticipates that thermal hysteresis should be very small in the studied material.

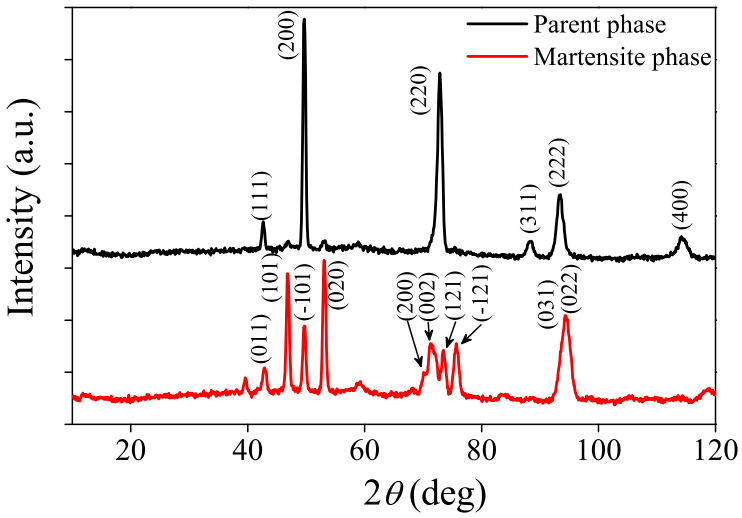


Fig. 5.10 Neutron diffraction patterns of the sample in the parent (325K) and martensitic (280K) phases.

Magnetization was measured by using a superconducting quantum interferometer device (SQUID, Quantum Design) in collaboration with Institut de Ciència de Materials de Barcelona (ICMAB-CSIC). Measurements were done under applied fields ranging from 0.005 to 5 T in cooling-heating cycles between 280-320 K at a rate of 0.4 K/min.

Isothermal and isofield calorimetric measurements were performed by using the calorimeter capable of operating under external magnetic fields described in section 3.2.

### 5.3.2 Results: magnetometry and calorimetry

#### Magnetometry

Figure 5.11 shows magnetization versus temperature measurements $M_{p(m)}(T,H)$ during heating and cooling runs across the martensitic and ferromagnetic transitions for selected values of the applied magnetic field (isofield measurements). Hereafter, the sub-indices $p$ and $m$ will indicate measurements performed during reverse and forward martensitic transitions. Results show that the paramagnetic martensite phase structurally transforms on heating to a ferromagnetic parent phase. The Curie point of the parent phase is located from measurements at low applied magnetic field at $T_C \simeq 302K$ as indicated in the inset of figure 5.11. The existence of a martensitic transition is revealed by the sharp change of magnetization as temperature is increased or decreased. This behaviour is in agreement with the significant first-order character of the martensitic transition. The corresponding change of

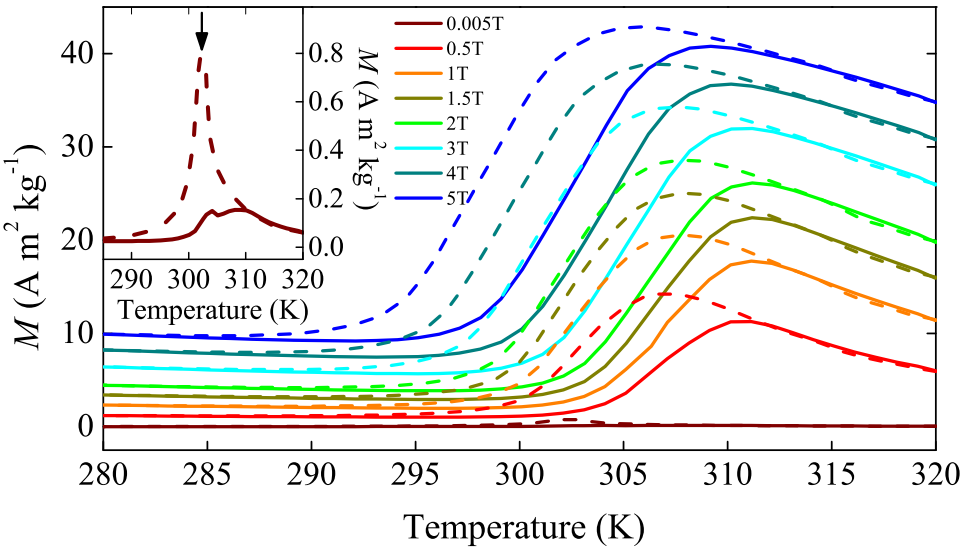


Fig. 5.11 Magnetization versus temperature curves at selected applied magnetic fields [indicated in the legend] obtained upon heating (continuous lines) and cooling (dashed lines). The inset shows a low-field measurement from which the Curie temperature has been identified. $T_C$ is indicated with the arrow.

magnetization, $\Delta M_{t_{p(m)}}$, can be estimated for each applied magnetic field as the magnetization difference at the transition temperature between extrapolations of the linear behaviour of $M_{p(m)}$ vs. $T$ curves well above and well below the transition. Transition temperatures have been identified with inflection points in the magnetization curves. We will denote $T_p$ and $T_m$ as the corresponding transition temperatures of the reverse (heating) and forward (cooling) transitions. Note that the difference $T_p - T_m$ ($\sim 4$ K) provides a measure of the thermal hysteresis of the transition. It is found that to within error hysteresis remains independent of the applied magnetic field. Note that the value of the hysteresis is quite small, and is comparable to that of low-hysteresis martensitic materials [119].

$\Delta M_{t_{p(m)}}$ and transition temperatures are plotted as a function of the applied magnetic field for heating and cooling runs in Figs. 5.12 (a) and (b) respectively. It is interesting to note that as magnetic field is increased, the martensitic transition temperatures shift towards lower temperatures. From the rates $dT_p/dH$ and $dT_m/dH$ corresponding to the reverse and forward transitions respectively and the changes of magnetization at the transition, transition entropy changes $\Delta S_{t_{p(m)}}$ can be estimated from the Clausius-Clapeyron equation. That is,

$$\Delta S_{t_{p(m)}} = -\mu_0 \Delta M_{t_{p(m)}}(T,H) \left( \frac{dT_{p(m)}}{dH} \right)^{-1} \tag{5.4}$$

The obtained results are shown in figure 5.12 (c). It is obtained that the transition entropy change (absolute value) slightly decreases with increasing magnetic field.

### Calorimetry

#### Isofield calorimetry

Thermal curves obtained from temperature scans performed at a rate 0.4 K/min and selected values of magnetic field (isofield measurements) are shown in Figs. 5.13 (a) and (b). Positive peaks (endothermal) correspond to reverse martensitic transitions, while negative peaks (exothermal) correspond to forward transitions. The figures clearly show that as the applied field is increased the peaks shift to lower temperatures. No anomaly associated with the occurrence of the paramagnetic-ferromagnetic transition at $T_C$ is detected in the thermal curves due to the overlap of both first- and second-order structural and magnetic transitions and the prevalence of the peak associated with the structural transition which involves a large latent heat. The maxima of the thermal curves are identified with the temperatures $T_p$ and $T_m$. These temperatures are plotted in figure 5.12 (b). Note that the obtained values slightly deviate from those determined from the inflection point of magnetization curves. This is likely to be due to the fact that calorimetric and magnetization measurements have been performed on different specimens. Nevertheless, hysteresis is very similar in both cases.

As described in section 3.1.1, the partial integration of the thermal curves given in figures 5.13 (a) and (b) from a temperature $T_0^m$ below the finish temperature of the forward transition to a temperature $T$ enables entropy curves at each applied magnetic field to be obtained. These curves describe the variation of the entropy with temperature for reverse and forward transformation processes from a reference entropy $S_0^m$ associated with the martensitic phase. The total integration up to a temperature above the finish temperature of the reverse transition or the start temperature of the forward transition provide the martensitic transition entropy change $\Delta S_{t_{p(m)}} = S_{p(m)}(T,H) - S_0^m$ for the reverse and forward transitions respectively. The obtained values for heating and cooling runs are plotted in figure 5.12 (c) and can be compared to the estimates derived from the Clausius-Clapeyron equation. Reasonably good agreement is obtained for all values to within errors.

At each temperature in the interval between the reverse or forward transformation regions, the fraction of parent phase $\chi_{p(m)}(T,H)$ can be computed from normalization of entropy curves with respect to transition entropy as expressed in 3.13.

The dissipated energy, $E_{diss}$, associated with transformation hysteresis can be estimated as the area of the hysteresis loop in entropy-temperature space. Therefore, it can be expressed

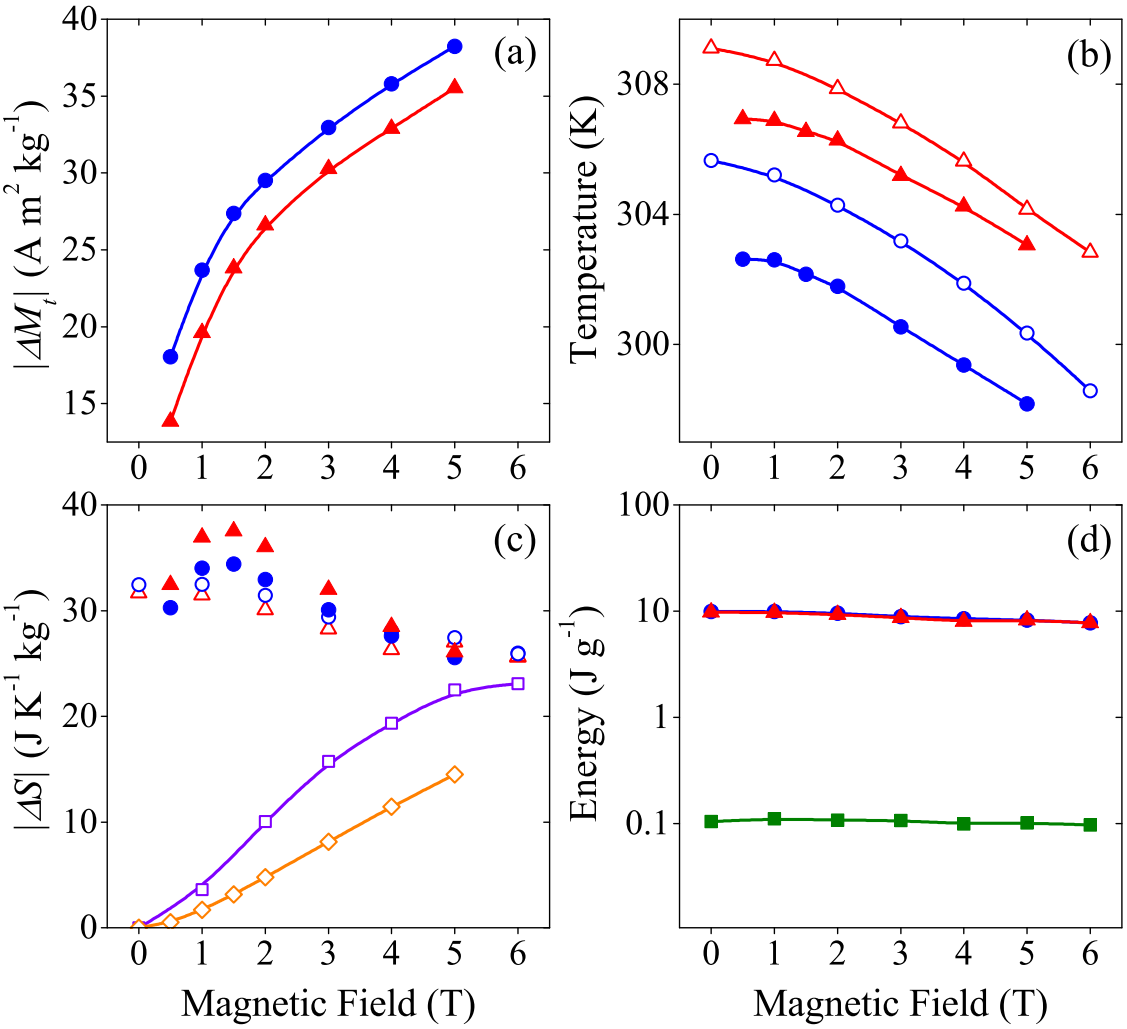


Fig. 5.12 Magnetization changes $\Delta M_{t_{p(m)}}$ for the martensitic transition as a function of the applied magnetic field, $\mu_0 H$, are plotted in (a). Panel (b) shows transition temperatures as a function of the applied magnetic field from both magnetometry (solid symbols) and calorimetry (open symbols) measurements. Red triangles refer to heating runs and blue circles refer to cooling. With the same symbols, panel (c) shows the transition entropy changes obtained either from the isofield calorimetric curves and from the Clausius-Clapeyron equation. For the sake of comparison, violet squares indicate the quasi-direct maximum field-induced entropy change obtained at each applied field change $\mu_0 \Delta H$. Orange squares correspond to the maximum value of the field-induced entropy change obtained from magnetization curves. Panel (d) shows the latent heat (enthalpy changes $L$ of the martensitic transition) computed from the isofield calorimetric curves (red and blue solid symbols) and the dissipated energy $E_{diss}$ (green solid squares) on a logarithmic scale.

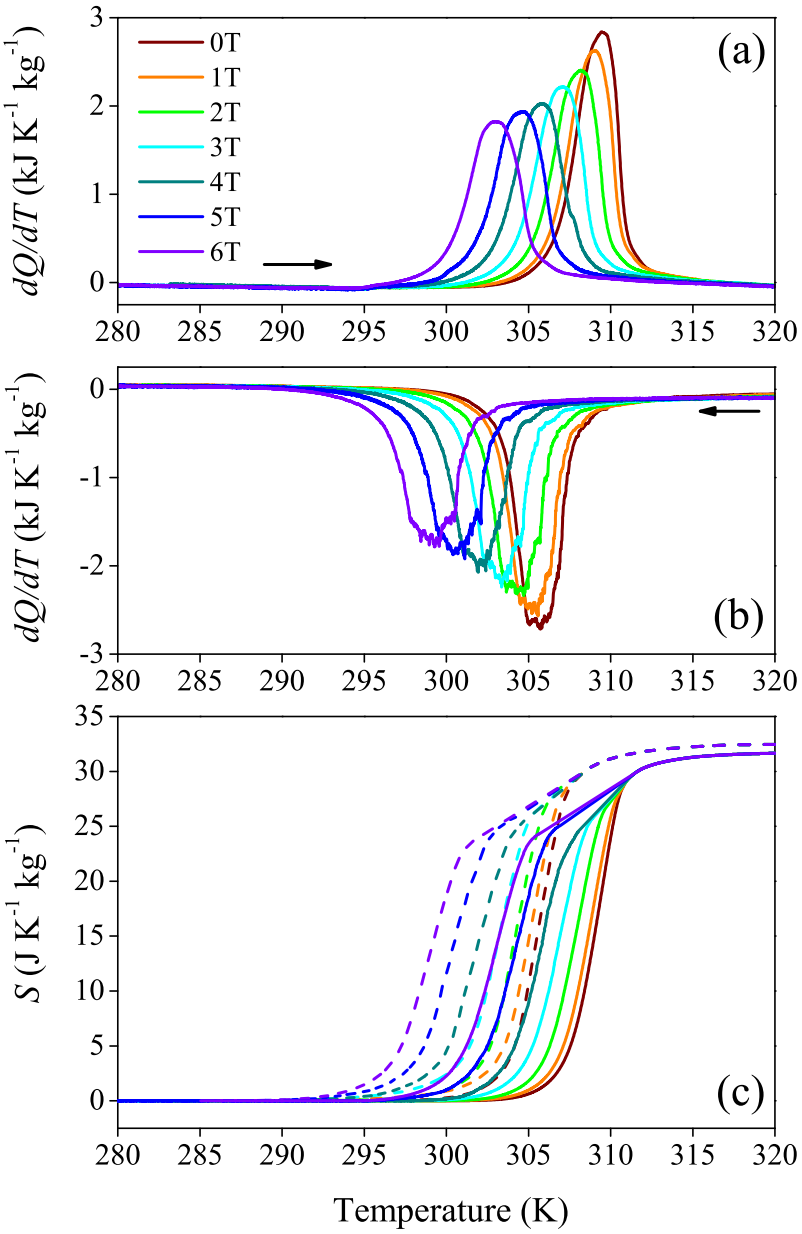


Fig. 5.13 Isofield calorimetric curves at selected values of the applied magnetic field. (a) heating runs, (b) cooling runs, and (c) entropy curves for cooling (dashed lines) and heating (continuous lines) runs.

as,

$$E_{diss} = \Delta S_t \left[ \int_{T_0^m}^{T_0^p} \chi_p dT + \int_{T_0^p}^{T_0^m} \chi_m dT \right], \tag{5.5}$$

where $T_0^p$ is a temperature above the finish temperature of the reverse transition, and $\Delta S_t$ is the transition entropy change computed as an average value between heating and cooling runs, $\Delta S_t = (\Delta S_p + \Delta S_m)/2$. It is interesting to compare this dissipated energy with the transition latent heat that can be estimated as $L \simeq T_t \Delta S_t$, where $T_t = (T_p + T_m)/2$. The latent heat and the dissipated energy are plotted (on a logarithmic scale) as a function of the applied magnetic field in figure 5.12 (d). Both energies remain independent of the applied field to a good approximation. Results show that the dissipated energy is very small, two orders of magnitude lower than the latent heat ($E_{diss}/L \simeq (T_p - T_m)/T_t \sim 10^{-2}$).

### Isothermal calorimetry

Taking into account the fact that in the studied materials the transition shifts to a lower temperature under an applied magnetic field, isothermal calorimetric measurements have been performed according to the protocol for materials displaying inverse caloric effects in the vicinity of first-order transitions described in 3.1.1. Examples of calorimetric curves (represented as heat released/absorbed per unit of magnetic field change vs. magnetic field) corresponding to the first isothermal magnetic field scans obtained at selected temperatures are shown in figure 5.14 (a). Panels (b) and (c) show the results corresponding to magnetic field cycling at selected temperatures. Calorimetric curves are represented here as released/absorbed heat flow versus time. Examples shown in panel (b) start in the martensitic phase by application of the field [as indicated in the upper plot of figure 5.14 (b)], while in (c) the system is initially in the parent phase and the field is first removed [as seen in the upper plot of figure 5.14 (c)]. It is worth pointing out that measurement protocol prevents the influence of hysteresis in the first application/removal of the magnetic field. In subsequent cycles, only the reversible contribution is detected.

### Magnetocaloric effect

The magnetocaloric effect in the vicinity of the magnetostructural martensitic transition can be quantified from the entropy change induced from the isothermal application or removal of a given magnetic field. This entropy change can be obtained from both magnetization (indirect method) and calorimetric measurements (quasi-direct and direct methods). From

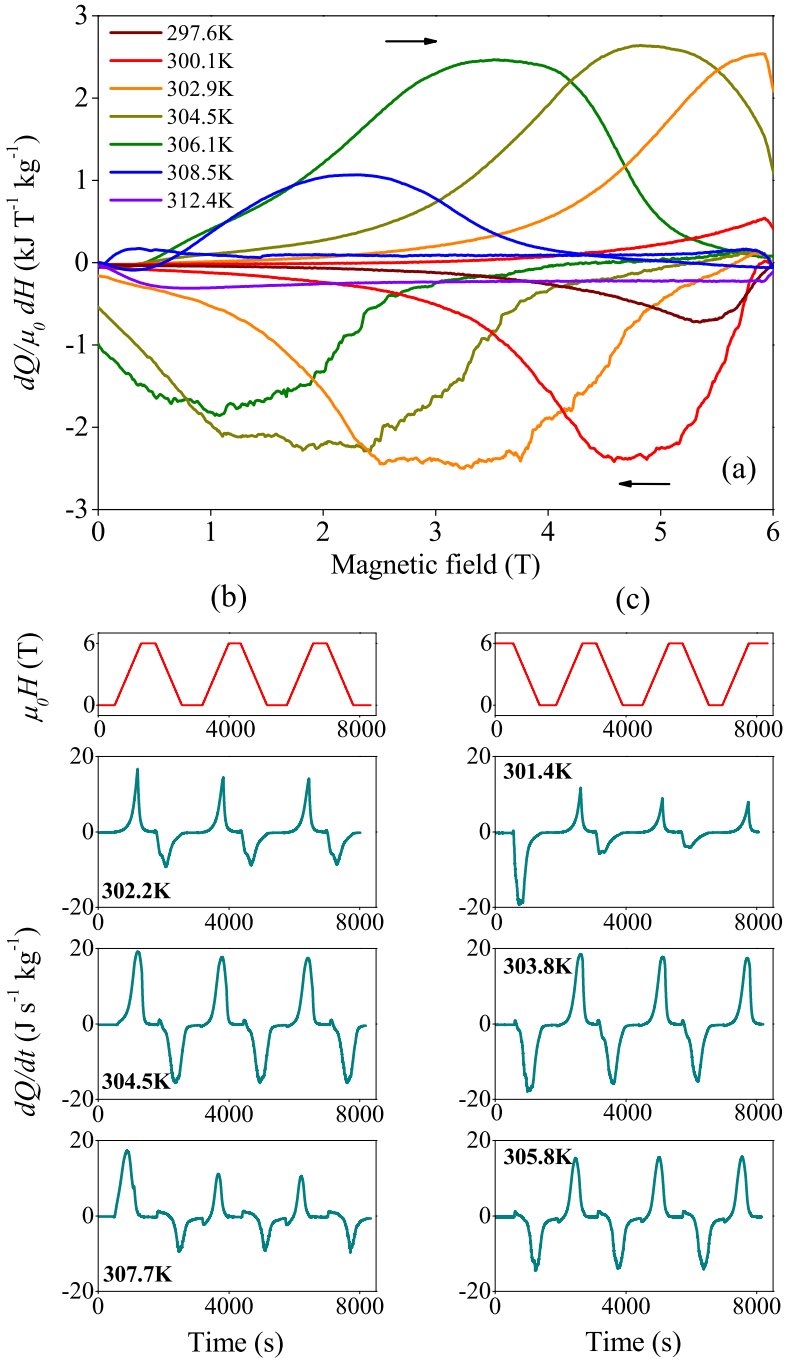


Fig. 5.14 (a): Calorimetric curves obtained upon first application of the magnetic field (positive peaks) and first removal of magnetic field (negative peaks) at several representative temperatures. Panels (b) and (c) show calorimetric curves obtained upon consecutive magnetic field scans at selected temperatures. Calorimetric curves in panel (b) correspond to cycles that begin with an application of the magnetic field ($0 \rightarrow 6$ T), whereas calorimetric curves shown in panel (c) are those where the magnetic field is first removed ($6$ T$\rightarrow 0$). The upper figures in panels (b) and (c) show the time variation of the applied magnetic field.

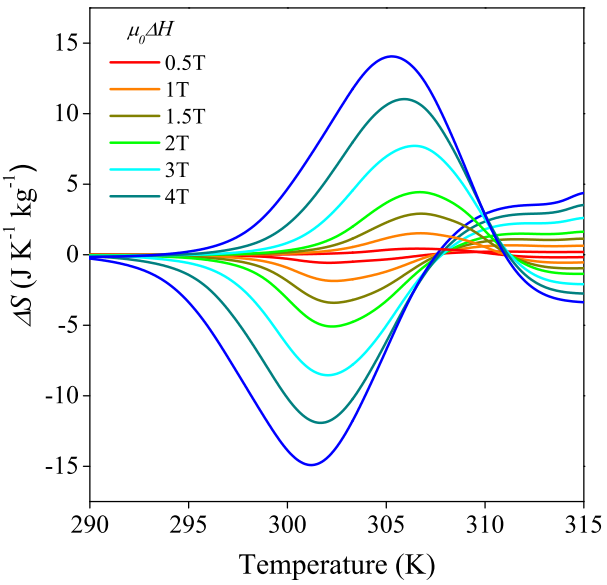


Fig. 5.15 Field-induced entropy changes at selected values of the applied/removed magnetic field (indicated in the figure) from magnetization measurements.

magnetization curves it can be determined as:

$$\Delta S_{p(m)}[T, 0(H) \rightarrow H(0)] = \mu_0 \int_{0(H)}^{H(0)} \left( \frac{\partial M_{p(m)}}{\partial T} \right)_H dH \tag{5.6}$$

which is obtained from integration of the Maxwell relation expressed in equation (2.8). Results giving $\Delta S$ computed from this indirect method as a function of $T$ for heating ($p$) and cooling ($m$) runs at given values of the magnetic field, are shown in figure 5.15 for fields (applied/removed) up to 5 T. Clearly, the magnetocaloric effect is inverse and increases in magnitude by increasing the applied magnetic field. For a field of 5 T, a maximum value of about 15 J/K kg is obtained.

Isothermal field-induced entropy changes can also be obtained from isofield calorimetric data. From this quasi-direct method, entropy changes are computed from subtraction, at each temperature, of the calorimetric entropy curves shown in figure 5.13 (c). As previously indicated, integration of calorimetric curves is performed with respect to a base line by following the expression (4.5.3), which excludes any background entropy contribution related to a difference of heat capacity, $\Delta C$, between both martensitic and parent phases. This effect can be taken into account from the temperature dependence of the entropy change since

$$\frac{\Delta C}{T} = \frac{\partial \Delta S_t}{\partial T}. \tag{5.7}$$

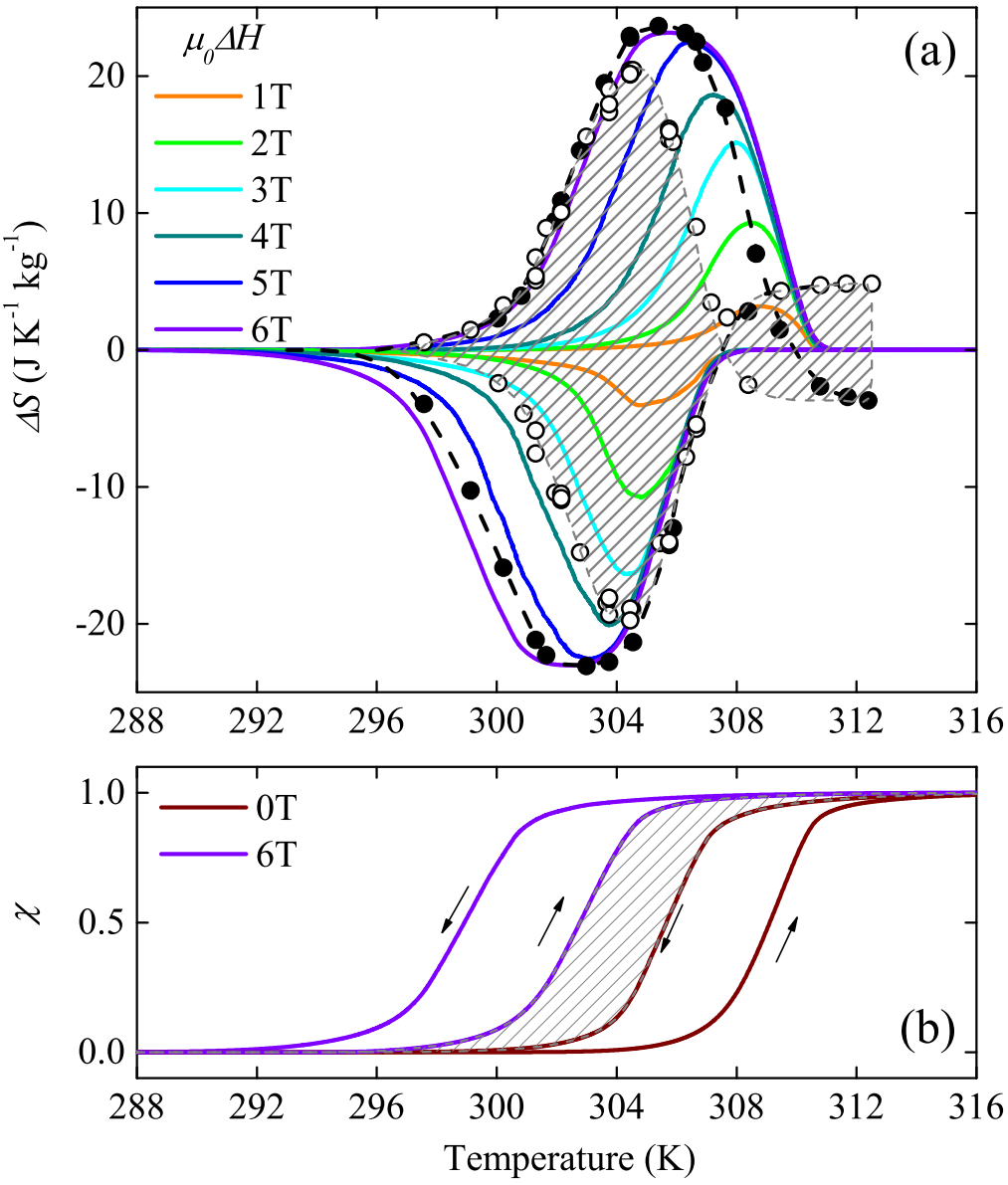


Fig. 5.16 (a): Magnetic entropy change $\Delta S(\mu_0 \Delta H)$ obtained from quasi-direct computation are plotted with colored lines. Each color refers to the field change $\mu_0 \Delta H$. Black solid circles refer to entropy changes from the first magnetic field ramps from isothermal calorimetry. Open circles refer to entropy changes from subsequent field cycling. Dashed lines are a guide for the eye. The reversibility region is dashed with grey lines. (b): Transformed fraction curves upon heating and cooling at zero field and high field ($\mu_0 H = 6T$). The reversible region that separates the loops at zero and 6 T is dashed with grey lines.

This slope is plotted in figure 5.13 (c) and is taken into account when subtracting the calorimetric entropy curves in order to obtain field-induced entropy changes. The results obtained from this method are depicted as solid lines in figure 5.16 for fields (applied/removed) up to 6 T. The magnetocaloric effect increases in magnitude by increasing the applied magnetic field and tends to reach a saturation value for fields above 5 T. The maximum value of the field-induced entropy change has been plotted in figure 5.12 (c), which shows that the saturation value coincides, as expected, with the total transition entropy change. It is worth noting that at each field, the field-induced entropy change obtained from calorimetric measurements is slightly larger than the entropy change obtained from magnetization measurements [see figure 5.12 (c)]. While the difference could be ascribed to the fact that different specimens are used in calorimetric and magnetization measurements, it must also be considered that the quasi-direct calorimetric method only takes into account the contribution to the entropy change arising from the transition itself. Since the contribution from outside the transition has the opposite sign ($\partial M/\partial T < 0$) to the contribution from the transition ($\partial M/\partial T > 0$), indirect estimations based on magnetization measurements should (in absolute values) be lower than the quasi-direct estimations. In any case, note that only the high temperature contribution from outside the transition is relevant since in the martensitic phase $\partial M/\partial T \simeq 0$ to a good approximation.

From the isothermal calorimetric curves obtained at $T$ by sweeping the magnetic field, entropy changes can be computed as,

$$\Delta S_{p(m)}[T, 0(H) \rightarrow H(0)] = \frac{1}{T} \int_{0(H)}^{H(0)} \frac{\dot{q}_{p(m)}(T,H)}{\dot{H}} dH, \tag{5.8}$$

where $\dot{H}$ is the rate at which the field has been swept. The integration baseline must be chosen in such a way that in addition to the contribution from the transition, the effect of a difference of heat capacities between both parent and martensitic phase is taken into account. Therefore, this method should provide estimations comparable to those obtained from the calorimetric quasi-direct method. Results obtained in the first cycle by application and removal of a magnetic field of 6 T are shown as solid symbols in figure 5.16 (a). The agreement with quasi-direct measurements is very good. Only the right-hand side of the curves corresponding to temperatures close to the ferromagnetic-paramagnetic transition show some discrepancies. These differences arise from the conventional magnetocaloric effect associated with this ferromagnetic-paramagnetic transition which is taken into account in direct calorimetric measurements, but not in quasi-direct measurements. The same conventional contribution at high temperatures is in fact observed in magnetocaloric curves obtained from magnetization measurements (see figure 5.15).

Results obtained upon further magnetic field cycling (up to 6 T) are shown in figure 5.16 (a) as open symbols. Compared with the first cycle, a lower field-induced entropy change is obtained. Interestingly, these values are reproducible from cycle to cycle and thus define a reversible region which is shown as a shadowed area in figure 5.16. For an applied field $\mu_0\Delta H$ = 6T, the maximum value of the reversible entropy change is 20 J $K^{-1}$ $kg^{-1}$ which represents more than 80% of the total MCE entropy change obtained at the first magnetic field ramp.

The reversibility of the magnetocaloric effect depends crucially on the competition between the width of thermal hysteresis and the sensitivity of transition temperatures upon an applied magnetic field. A narrow hysteresis and a large shift of transition temperatures with the applied field favors reversibility. For a given hysteresis, substantial reversibility occurs when the shift of forward and reverse transition temperatures is larger than hysteresis. That is, the magnetic field-induced shift of the whole hysteresis loop must be larger than thermal hysteresis. This is illustrated in figure 5.16 (b) which shows hysteresis loops (represented as the fraction of parent phase vs. temperature) for applied magnetic fields of zero and 6 T. From the comparison of panels (a) and (b) it is clear that the reversible region of the magnetocaloric effect corresponds to the temperature interval that separates these two loops [shadowed area in panel (b)]. In other words, reversible values for the magnetocaloric effect are found within a temperature interval bounded by the start of the forward martensitic transition at zero field and the start of the reverse transition under an applied field. Actually, in this temperature region, the magnetic field carries the state of the material through a minor hysteresis loop [133], and the reversibility in the magnetocaloric effect is directly related to the reversibility in the fraction of material that undergoes the forward and reverse transition in the cycle. Of course, when the size of the shift in martensitic transition temperatures due to the magnetic field is large enough, the minor loops approach the full transformation loop and a maximum reversible magnetocaloric effect is obtained.

Magnetocaloric properties of Ni-Mn-In alloys with composition similar to the material studied in the present section have been reported in [132] and [134]. In the first of these papers, the authors studied the influence of composition on magnetocaloric properties in $Ni_{51}Mn_{49-x}In_x$ alloys. The martensitic transition was found to show minimum hysteresis close to $x = 15.6$ which corresponds to the composition studied in the present section. From our results, this minimum value is explained due to the optimal compatibility between parent and martensitic structures. Interestingly, a maximum isothermal magnetic field-induced entropy change associated with the martensitic transition was also observed close to the same composition, $x = 15.6$. Actually, this is the result that we would expect taking into account the fact that for $x = 15.6$ martensitic and magnetic transitions are almost coincident

and the transition entropy change in Ni-Mn-In alloys is known to decrease when increasing the separation between magnetic and martensitic transitions [135, 136]. This behaviour is a consequence of the competition between structural and magnetic contributions to the entropy change which have opposite signs [137] and will be discussed in more detail in section 5.4.

In reference [134] adiabatic field-induced temperature changes for an alloy with $x = 15.6$ have been reported. For the studied alloy, the hysteresis was much larger than in our case. During adiabatic heating temperature changes of 1 K/T were measured while changes of 0.5 K/T were found during cooling. These values are slightly lower than our estimations of the shift of martensitic transition under an applied field obtained in the present section.

### 5.3.3 Summary and conclusions

We have studied MCE at room temperature in a low hysteresis $Ni_{51}Mn_{33.4}In_{15.6}$ metamagnetic shape memory alloy by means of magnetometry and differential scanning calorimetry measurements. Good coincidence has been found between both experimental methods and the derivation of the MCE features using direct, quasi-direct and indirect methods.

The alloy composition has been designed so that high and low symmetry phases satisfy optimal geometric compatibility conditions. Compatibility has been quantified by cofactor conditions. From the lattice parameters determined by means of neutron diffraction experiments we have shown that in our alloy these conditions deviate less than 0.2% from the expected ideal situation. This ensures that the martensitic transition in our alloy occurs with a high degree of reversibility measured by a thermal hysteresis as low as 4 K.

Despite the fact that transition temperatures show only moderate sensitivity to an applied magnetic field, the small hysteresis of the transformation enables to obtain large reversible entropy changes up to 20 J $K^{-1}$ $kg^{-1}$ with successive application and removal of a magnetic field of 6 T. Overall, for a given magnetic field, in the vicinity of a magnetostructural first-order transition, the magnetocaloric reversible region extends from the start temperature of the forward transition at zero field to the start temperature of the reverse transition under applied field. The rule indeed applies to direct, quasi-direct and indirect kind of measurement used to quantify the magnetocaloric effect.

It is worth mentioning that a similar strategy to the one followed in the present section was already proposed by Srivastava et al. [118] in order to design Heusler alloys with low hysteresis. A $Ni_{45}Co_5Mn_{20}Sn_{10}$ alloy with $\lambda_2$ only slightly greater than 1 was shown to display a relatively low thermal hysteresis of about 6 K. Similar to our case, the compatibility condition was found to occur in an alloy with martensitic and Curie temperatures very close each other. Whether or not this is a general condition related to the interplay between

magnetism and structure in this class of Heusler alloy or simply a mere coincidence is a point that warrants further investigation in the future.

## 5.4 Tailoring barocaloric and magnetocaloric properties in low-hysteresis magnetic shape memory alloys

It has been shown that the caloric performance of a given material is strongly affected by the hysteretic effects and the sensitivity of the transition temperature to the external field. The former critically compromise the reproducibility of the thermal response, the latter results in large values for $\Delta S$ and $\Delta T$ and a broadening of the temperature window where giant (reversible) caloric effects occur. According to Clausius–Clapeyron equation, the field dependence of the transition temperature weakens as the entropy change increases (provided that the change of the property conjugated to the applied field remains constant). Therefore, the optimal caloric performances of a given material will result from the best balanced tuning of all these parameters. In the present section these issues are addressed for the case study of magnetic shape memory alloys.

In magnetic shape memory alloys there are two major contributions to the transition entropy change $\Delta S_t$: structural and magnetic. The structural contribution is mainly due to lattice vibrations (phonons) and stabilizes the high temperature cubic phase while the magnetic contribution stabilizes the magnetically more disordered phase which, depending on the alloy family can be either the austenite or the martensite [138]. While the structural contribution is almost constant within a broad temperature range, the magnetic contribution does depend on how far the martensitic transition temperature is from the Curie point of the austenitic phase. Actually, for certain magnetic shape memory alloy families (such as Ni–Mn–In) it has been found that the value of $\Delta S_t$ can be tailored by tuning the relative distance between the Curie point and the martensitic transition [135, 136, 139].

We have investigated the Ni–Mn–In system which has been shown to exhibit the strongest sensitivity of the transition temperatures to both magnetic field and hydrostatic pressure [140]. The relative distance between the martensitic transition and the Curie point of the cubic phase has been tailored by tuning the composition of the samples. Furthermore, the compositions have been selected in such a way that the crystal structures of both phases meet the geometric compatibilities so that the martensitic transition takes place with a very narrow hysteresis, in analogy with the alloy described in section 5.3. Calorimetry under magnetic field and under hydrostatic pressure have been used to study the barocaloric and magnetocaloric response of these samples.

### 5.4.1 Experimental details

Specimens for magnetization (typically $\sim$ 50 mg), for calorimetry under magnetic field (typically $\sim$ 150 mg) and for calorimetry under hydrostatic pressure (typically $\sim$ 1 g) were cut with a diamond saw.

Magnetization was measured by using a superconducting quantum interferometer device (SQUID, Quantum Desing Inc.) at ICMAB-CSIC (Barcelona). Measurements were done under an applied field of 5 mT, in cooling–heating cycles between 240 and 400 K at a rate of 2 K/min.

Isofield calorimetric runs at constant magnetic field and pressure were carried out on the setups described in sections 3.2 and 3.4, respectively. Isothermal calorimetric runs were also performed while the magnetic field was cyclically swept between 0 and 6 T at a rate 0.16 T/min. The calorimeter under magnetic field features a better accuracy than the one under hydrostatic pressure and therefore it is used to determine the thermal properties (transition temperatures and entropy changes) associated with the martensitic transition at atmospheric pressure and in the absence of magnetic field.

### 5.4.2 Experimental results

For each of the studied samples, EDX analysis were performed on three separate locations of the sample surface, and sample compositions listed in table 5.1 correspond to averaged values over these three measurements[2]. The samples are close to the composition line $Ni_2Mn_{1+x}In_{1-x}$ with the exception of sample B which is slightly Ni rich and Mn deficient. This sample has also been included into the study to reinforce the finding that the relevant parameter which controls many caloric performances is the reduced distance between martensitic and Curie temperatures, as will be shown later.

Figure 5.17 (a) shows low field magnetization as a function of temperature for the studied samples. The inset shows a magnified view which illustrates the magnetization change at the martensitic transition for samples A, B and C, for which the austenite is paramagnetic. By contrast, for sample E, the martensitic transition occurs well below the Curie point of the austenite. For sample D both martensitic and magnetic transitions are almost coincident. For all samples the low field magnetization in martensite is lower than in austenite. Figure 5.17 (b) shows the inverse of the magnetic susceptibility ($\chi^{-1}$) as a function of temperature. Data exhibit a good linear behaviour within the temperature range corresponding to the paramagnetic state of austenite. Linear fit to the data enabled us to determine the paramagnetic Curie point ($T_C$) and the effective magnetic moment $\mu$ which are

[2]Sample D is the same sample under study in section 5.3.

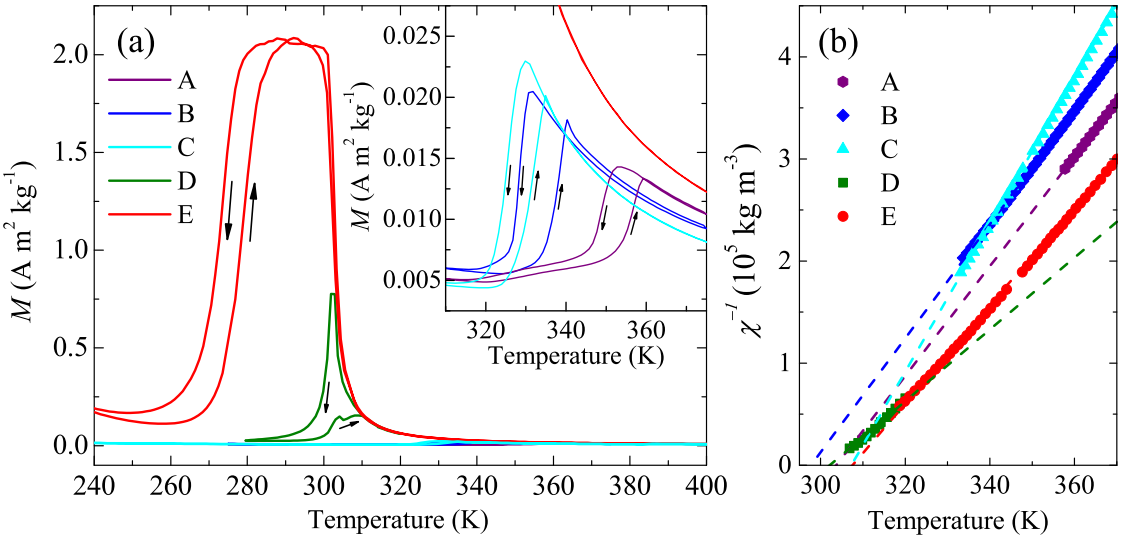


Fig. 5.17 (a) Temperature dependence of the magnetization measured under a magnetic field of 5 mT. The inset shows an enlarged view over a restricted temperature domain that illustrates the changes taking place at the martensitic transition in the paramagnetic state. The arrows indicate cooling and heating runs. (b) Inverse of the magnetic susceptibility as a function of temperature. Dashed lines are linear fits to the data.

listed in table 5.1 for all samples. Within experimental errors no systematic dependence upon sample composition has been found for these quantities. The values found for $\mu$ are consistent with those reported for magnetic shape memory alloys with compositions close to those of the samples studied here [121] but they are slightly lower than the magnetic moments obtained from high field magnetization measurements [141] and from first principle calculations [142] and [143]. Such a difference may be due to the presence of antiferromagnetic correlations [144]. On the other hand, the paramagnetic Curie temperatures determined for our samples are in good agreement with the Curie points reported for Ni–Mn–In alloys with compositions similar to those studied here [141].

Illustrative examples of the calorimetric curves obtained under constant hydrostatic pressure and under constant applied magnetic field are presented in figure 5.18. From the calorimetric curves we have computed forward ($T_M$) and reverse ($T_A$) transition temperatures which correspond, respectively, to the temperatures where 50% of the sample has transformed to martensite on cooling, and to austenite on heating. The thermal hysteresis is computed as the difference between these two temperatures and the data are compiled in table 5.1. It is noticeable that for all samples hysteresis is in the range 3-6 K, which is a significantly low value for martensitic transformations [119]. Interestingly, the lowest value is found for the sample with the martensitic transition closest to the Curie point (sample D), in

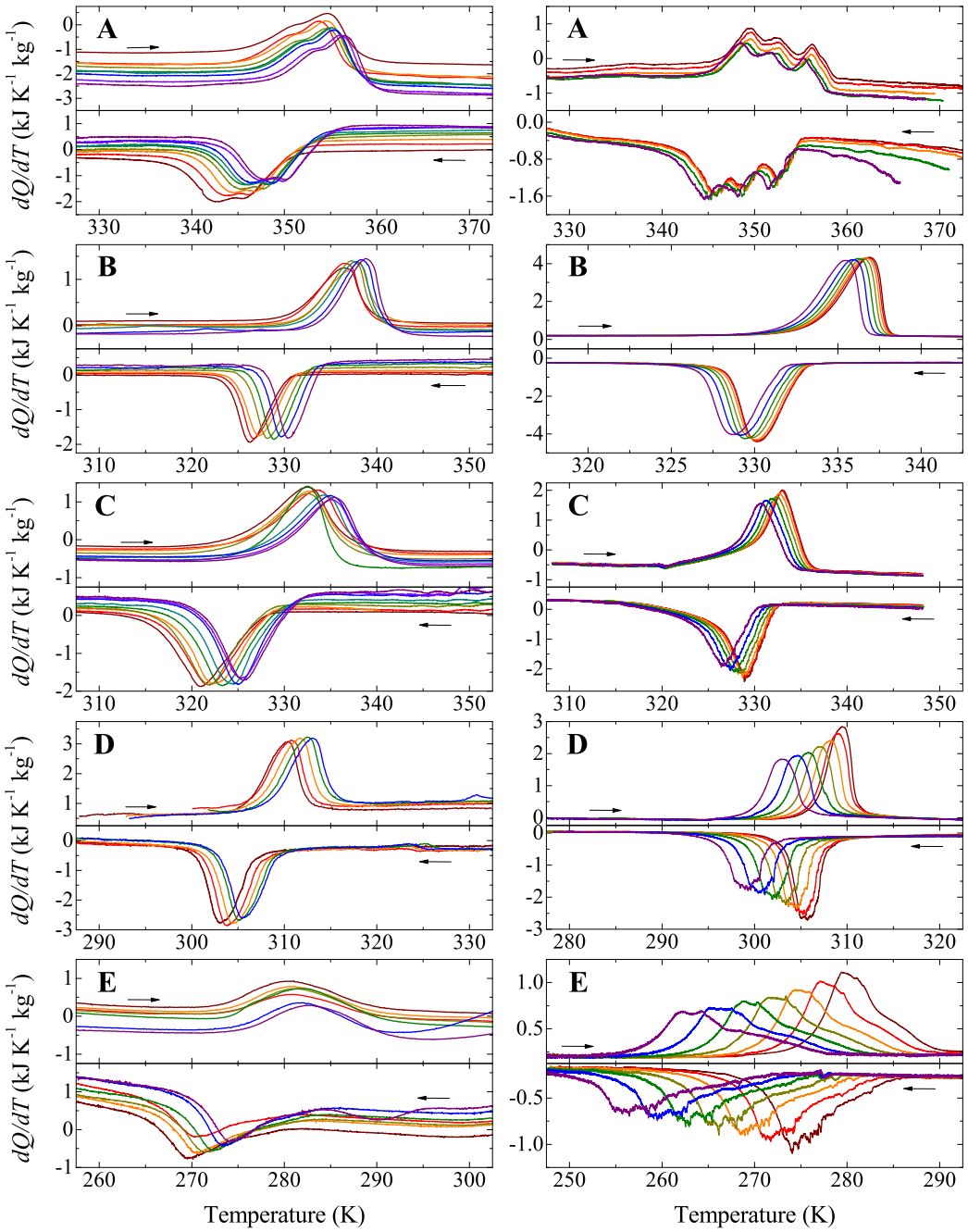


Fig. 5.18 Left panels: Calorimetric curves recorded under hydrostatic pressure. From left to the right the curves correspond to the following applied pressures: sample A, 0.3, 0.5, 0.8, 1.0, 1.2, 1.5, 1.7, 2.2 and 2.5 kbar. Sample B, 0, 0.3, 0.6, 1.1, 1.6, 2.0 and 2.6 kbar. Sample C, 0, 0.3, 0.5, 0.8, 1.0, 1.6, 2.1, 2.3 and 2.5 kbar. Sample D, 0, 0.6, 1.1, 1.6 and 2.0 kbar. Sample E, 0, 0.3, 0.5, 0.8, 1.0, 1.4, 2.0 and 2.5 kbar. Right panels: Calorimetric curves recorded under magnetic field. From right to the left the curves correspond to magnetic fields of 0, 1, 2, 4 and 6 T (sample A) and 0–6 T (samples B, C, D and E). In each panel, upper curves (endothermal process) correspond to heating runs while bottom curves (exothermal process) correspond to cooling runs.

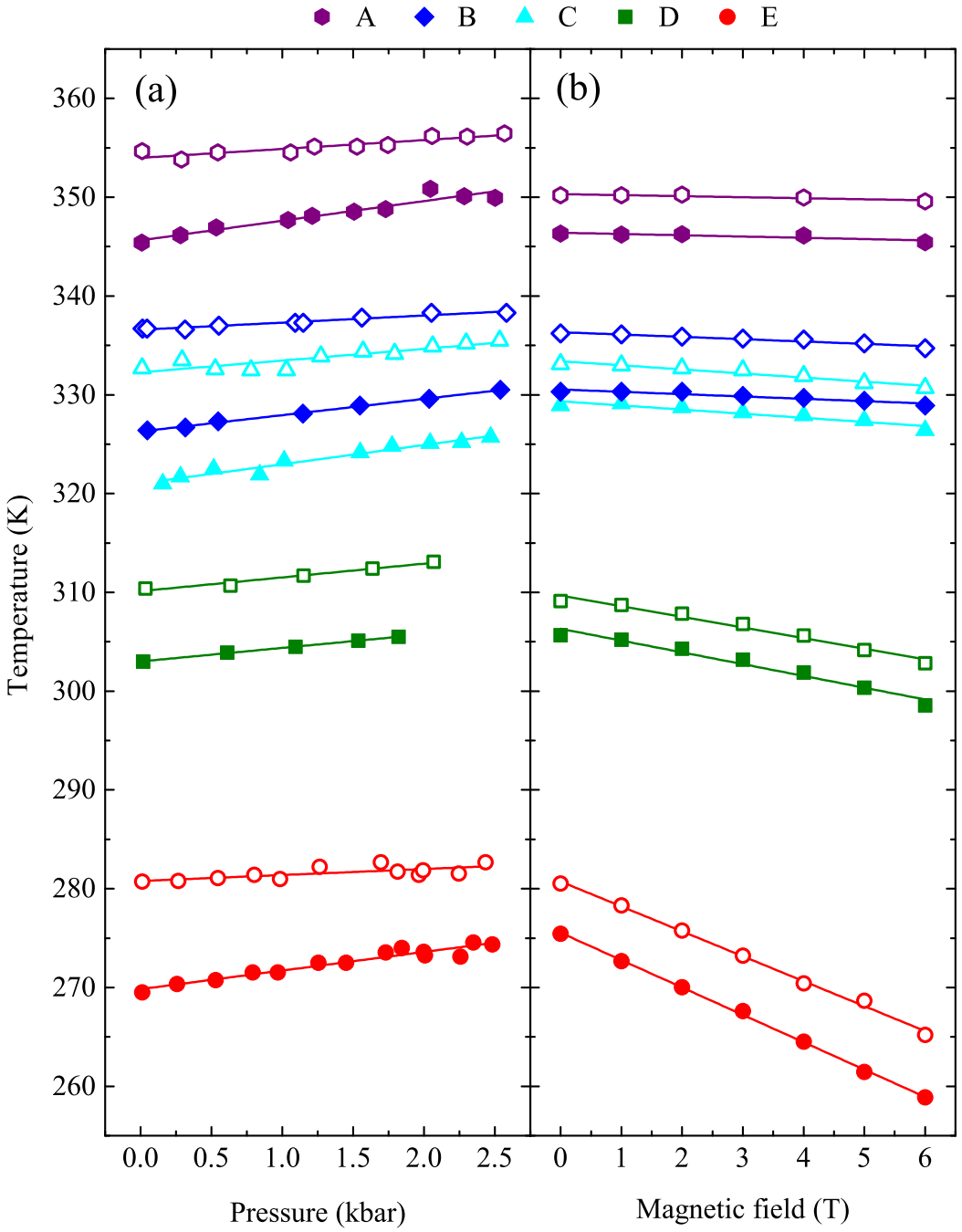


Fig. 5.19 Transition temperatures of the forward (solid symbols) and reverse (open symbols) martensitic transitions, as a function of hydrostatic pressure (a) and magnetic field (b). Lines are linear fit to the data.

accordance with the reference [118] and the previously presented $Ni_{51}Mn_{33.4}In_{15.6}$ alloy which points to the fact that the maximal lattice compatibility is achieved in those alloys with martensitic and Curie transitions very close to each other. From numerical integration of the calorimetric curves we have obtained the transition entropy change $\Delta S_t$. Values listed in table 5.1 correspond to the data obtained at atmospheric pressure and at zero magnetic field, and are an average over cooling and heating values. Application of hydrostatic pressure shifts the transition towards higher temperatures (figure 5.18, left panels) which indicates an enhancement in the stability of the martensite which has a lower unit cell volume while application of a magnetic field, shifts the martensitic transition towards lower temperatures (figure 5.18, right panels), which is consistent with magnetic field stabilizing the austenite phase which displays a larger magnetization than martensite. The hydrostatic pressure and magnetic field dependences of the temperatures $T_M$ and $T_A$ are plotted in figure 5.19 (a) and (b). Within experimental errors the increase of $T_M$ and $T_A$ with pressure and the decrease with magnetic field are found to be linear. We have quantified the shift in the martensitic transition with hydrostatic pressure and magnetic field by averaging the values of the slopes of the lines in figure 5.19 obtained on cooling and heating runs for each sample. The corresponding data are listed in table 5.1.

### 5.4.3 Discussion

#### Isothermal entropy changes

The quasi-direct estimations of the BCE and MCE are shown in figure 5.20 for each sample. Since pressure stabilizes the martensitic phase (as cooling does), the pressure induced entropy change in 5.20 has been computed from calorimetric curves on cooling. On the other hand, as magnetic field stabilises the austenitic phase (as heating does), entropy values have been computed from calorimetric curves on heating.

For all the samples, BCE is found to be conventional (entropy decreases when the sample is isothermally compressed) and MCE is found to be inverse (entropy increases upon isothermal application of magnetic field). The absolute values of $\Delta S$ increase upon increasing hydrostatic pressure and magnetic field as shown in figure 5.21. It is worth remarking that present data for the pressure induced entropy change are the highest $\Delta S$ values reported for any magnetic alloy until now [5, 41, 89, 90].

A good estimation of the reversibility of a caloric effect can be gained from the quasi-direct method by analysing the overlap of the $|\Delta S|$ vs. $T$ curves obtained during heating and cooling runs. In the left panels of figure 5.22 we have plotted the BCE for 2.5 kbar (except for sample D for which the maximum pressure was 2.0 kbar) and in the right panels of figure

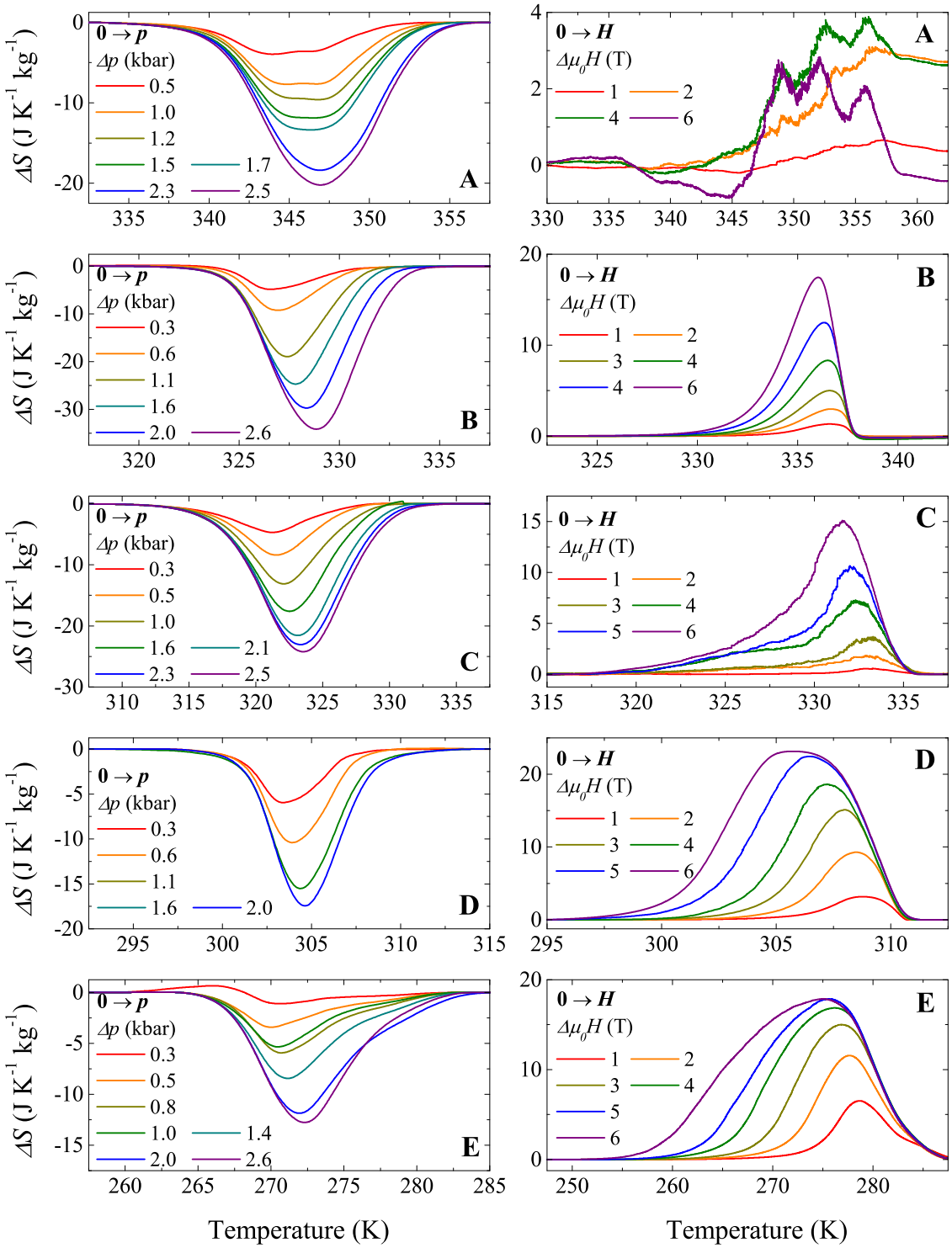


Fig. 5.20 Isothermal entropy changes associated with the barocaloric (left panels) and magnetocaloric (right panels) effects. Barocaloric data are computed from calorimetric curves under hydrostatic pressure for cooling runs and magnetocaloric data, from calorimetric curves under magnetic field for heating runs.

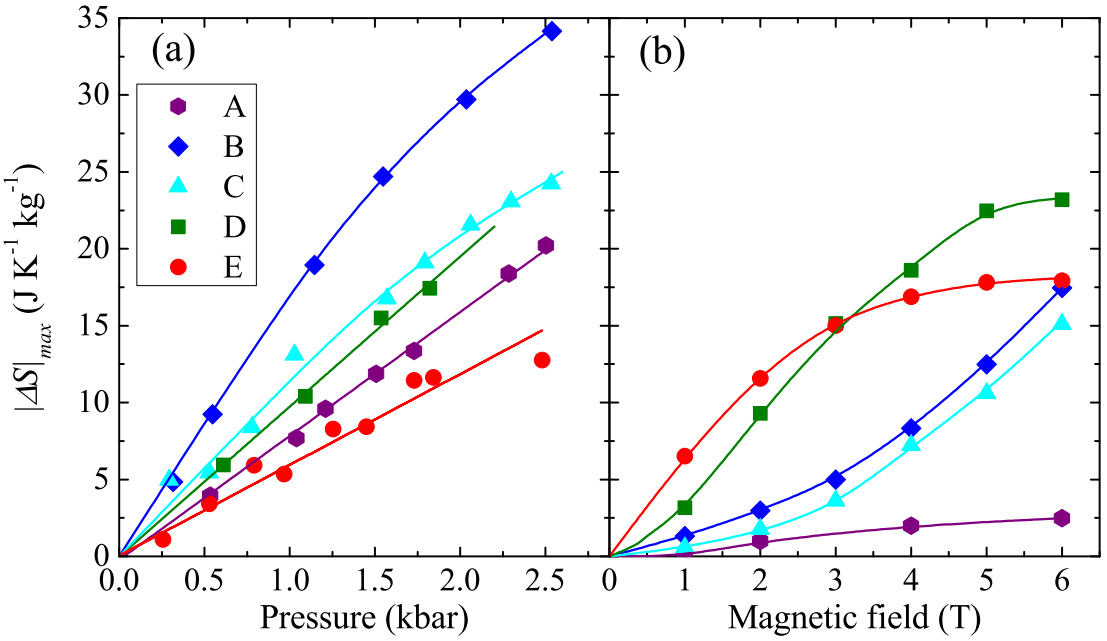


Fig. 5.21 Maximum isothermal entropy change as a function of hydrostatic pressure (a, barocaloric effect) and as a function of magnetic field (b, magnetocaloric effect). The estimated relative error in $\Delta S$ is $\pm 10\%$.

5.22 we have plotted the MCE for a magnetic field of 6 T. The expected entropy values for cyclic variation of hydrostatic pressure and magnetic field are depicted as light grey lines, and the temperature region where reversibility is expected corresponds to the shaded region. To confirm the reliability of the method in determining the repeatability of BCE and MCE we have performed isothermal calorimetric measurements for samples D and E while magnetic field was cyclically varied between 0 and 6 T. The obtained entropy values are plotted as symbols in figure 5.22, where solid symbols stand for the first application (or removal) of the magnetic field and open symbols stand for the successive application (or removal) of the field. As shown in the figure there is a good coincidence between data derived from the quasi-direct method and those obtained for the direct method. While for the studied range of pressures the reproducibility of the BCE is small for all samples, significant repeatable values for $\Delta S$ are obtained at the MCE of samples D and E over a temperature span of several degrees.

### Adiabatic temperature changes

For magnetic shape memory alloys, the specific heat in both martensite and austenite does not significantly depend on composition [138, 145, 146]. We have measured $C$ for one of

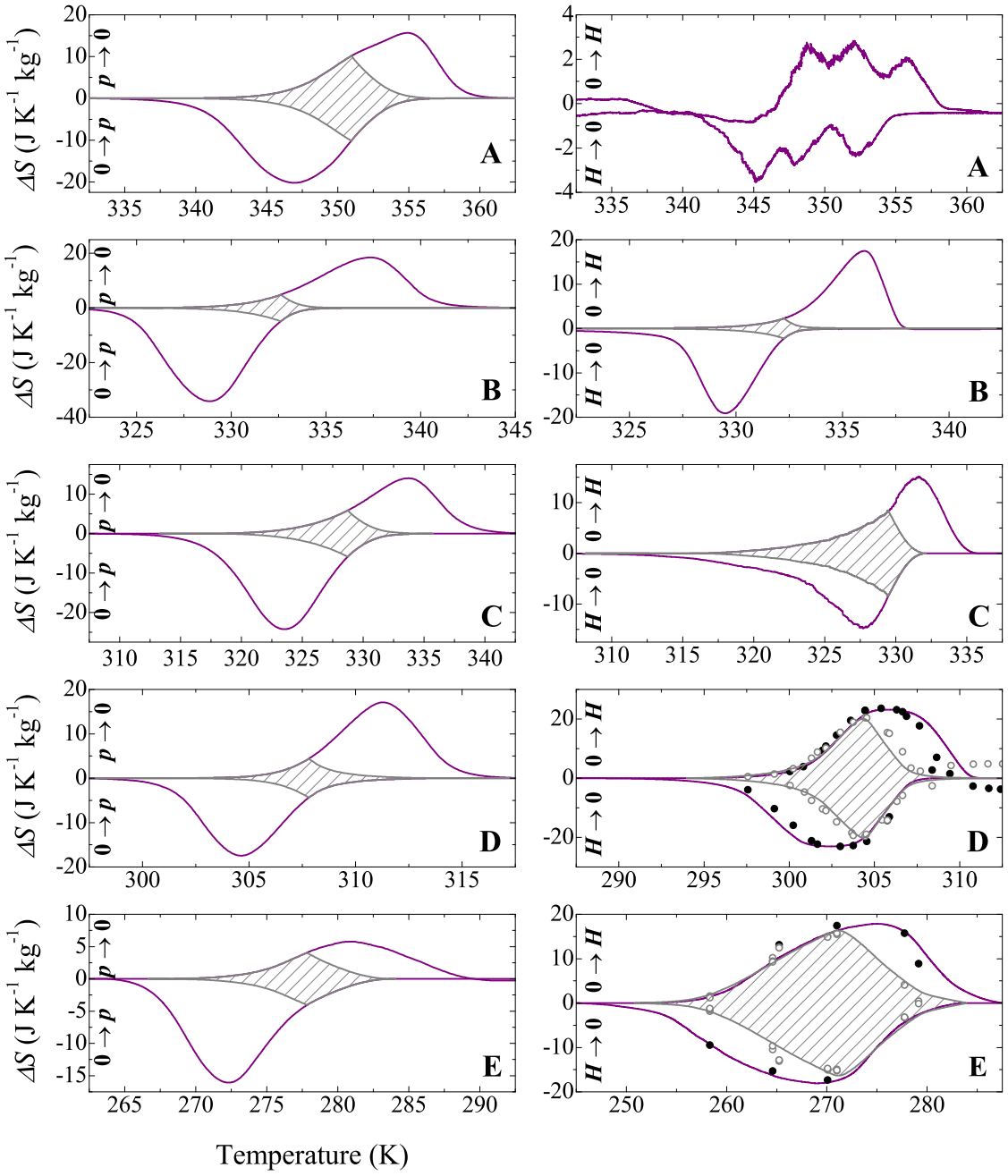


Fig. 5.22 Left panels: Isothermal entropy changes associated with the barocaloric effect for a hydrostatic pressure of 2.5 kbar (except for sample D which corresponds to 2.0 kbar). Right panels: Isothermal entropy values associated with the magnetocaloric effect for a magnetic field of 6 T. Purple lines correspond to the values obtained by the quasi-direct method. Symbols correspond to direct isothermal measurements (sweeping magnetic field) where solid circles stand for the first application (and removal) of the magnetic field and open circles, for successive field cycling. The reversibility region is indicated by the shaded area.

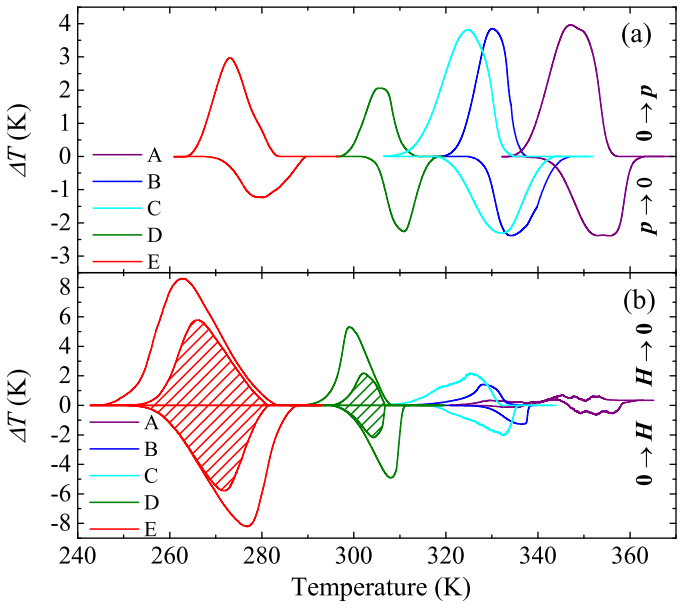


Fig. 5.23 (a) Adiabatic temperature changes corresponding to the application (upper curves) and removal (lower curves) of a hydrostatic pressure of 2.5 kbar (except for sample D that corresponds to 2.0 kbar). (b) Adiabatic temperature changes corresponding to the application (lower curves) and removal (upper curves) of a magnetic field of 6 T. Shaded areas indicate the reversibility region.

the studied Ni–Mn–In samples (sample D) by using the modulated differential scanning calorimeter (Q2000) from TA Instruments. Results are in good agreement with those reported for other magnetic shape memory alloys [121, 138, 145, 146]. We have combined these data with the entropy vs. temperature curves obtained at different values of hydrostatic pressure and magnetic field to compute the pressure induced and magnetic field induced adiabatic temperature changes $\Delta T$ as explained in section 3.1.1. The $\Delta T$ values are shown in figure 5.23

The adiabatic application of hydrostatic pressure increases the temperature of the sample (in concordance with the conventional nature of the BCE) while application of magnetic field decreases the temperature of the sample (in agreement with the inverse nature of the MCE). Regarding MCE, $\Delta T$ exhibits very tiny values for those samples with the martensitic transition temperature above the Curie point, but for samples transforming below the Curie point $\Delta T$ reaches values significantly large (6–8 K at 6 T), which are slightly above those reported (7 K) for a Ni–Mn–In alloy of close composition at 6 T [145]. On the other hand, the BCE exhibits larger $\Delta T$ values for those samples with the martensitic transition in the paramagnetic state, with values around 3–4 K (at 2.5 kbar).

### Tuning caloric performances

The large changes in entropy in giant caloric materials are associated with the latent heat (and thereby with the transition entropy change $\Delta S_t$) of a first-order phase transition, which scales with the relative distance between the martensitic transition and the Curie point of the austenite $(T_C - T_M)/T_C$ [136, 135]. In figure 5.24 (a) we have plotted $\Delta S_t$ (at atmospheric pressure and zero magnetic field) for the studied samples as a function of $(T_C - T_M)/T_C$ (solid green squares). It is shown that for $T_M > T_C$, $\Delta S_t$ tends towards a constant value, while it begins to decrease as $T_M$ approaches $T_C$. This behaviour is a consequence of the opposite contributions from the magnetic and vibrational degrees of freedom to the transition entropy change: the vibrational entropy in martensite is lower than in austenite, with a value which does not depend on composition. Hence, for those samples transforming martensitically from a paramagnetic austenite, the magnetic contribution is very small and $\Delta S_t$ is dominated by the vibrational contribution which is constant. However, for $T_M \leq T_C$, the magnetic contribution becomes relevant, with the magnetic entropy of martensite being larger than that of austenite. Hence, as $T_M$ gets lower than $T_C$ the magnetic entropy increases in magnitude thereby leading to a decrease in $\Delta S_t$. Eventually for low enough $T_M$ the magnetic term balances the vibrational one resulting in a vanishing transition entropy change and the martensitic transition no longer occurs [147, 148].

The scaling of $\Delta S_t$ points to the fact that the relative distance between martensitic and Curie temperatures can also be a good parameter to rationalise the several quantities accounting for the caloric effects in magnetic shape memory alloys. In that case, the shift in the martensitic transition with hydrostatic pressure and with magnetic field must be taken into account, and the actual $T_M$ values that have to be used in computing $(T_C - T_M)/T_C$, are those measured at the corresponding values of $p$ and $H$. Isothermal entropy changes for the BCE (red triangles) and MCE (blue circles) are plotted in figure 5.24 (a) as a function of $(T_C - T_M)/T_C$. For BCE, $\Delta S$ data correspond to an applied pressure of 2.5 kbar, and for MCE, $\Delta S$ data correspond to a magnetic field of 6 T. The entropy change corresponding to the BCE parallels the behaviour of $\Delta S_t$, showing larger and constant values for $T_M > T_C$ and decreasing for $T_M \leq T_C$. The fact that the entropy values for BCE are lower than $\Delta S_t$ reflects that the applied pressures are not large enough to accomplish transformation of the full sample. Interestingly, the entropy values for the MCE exhibit a behaviour different from that of $\Delta S_t$. For $T_M > T_C$, MCE exhibits low entropy values, as expected from the weak magnetism in this region (see figure 5.17). A maximum field-induced entropy change is attained when the martensitic transition occurs close to the Curie point of the austenite ($T_M \sim T_C$), and for $T_C > T_M$ it decreases again because of the decrease in $\Delta S_t$.

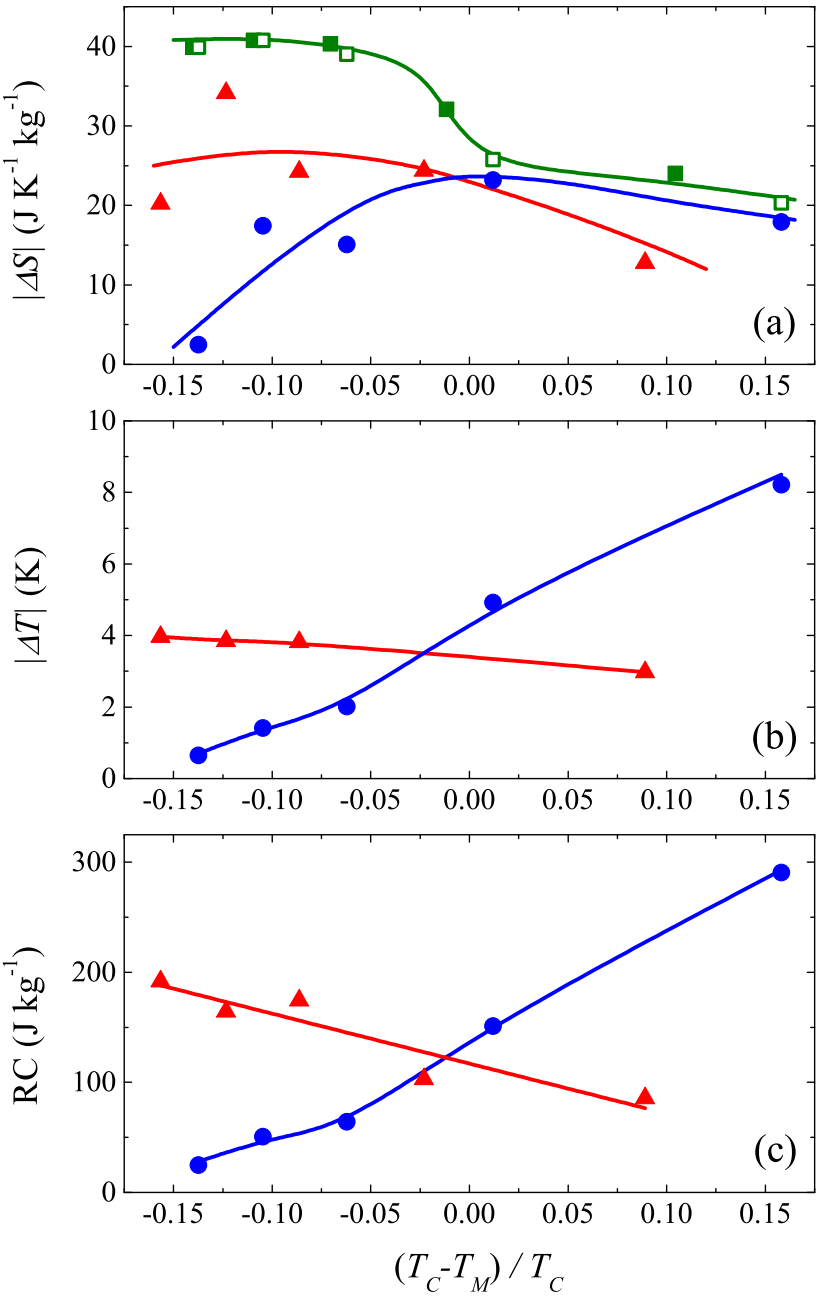


Fig. 5.24 (a) Transition entropy change at zero field and atmospheric pressure (solid green squares) and at 6 T and atmospheric pressure (open green squares); pressure induced entropy change (red triangles, barocaloric effect) and magnetic field induced entropy change (blue circles, magnetocaloric effect) as a function of the reduced temperature. (b) Adiabatic temperature change for the barocaloric (red triangles) and magnetocaloric (blue circles) effects as a function of the reduced temperature. (c) Refrigerant capacity for the barocaloric (red triangles) and magnetocaloric (blue circles) effects as a function of the reduced temperature. For all samples $p$ = 2.5 kbar and $\mu_0 H$ = 6 T. The entropy and RC values at 2.5 kbar for sample D have been estimated from extrapolation of the data at lower pressures. Lines are guides to the eye.

We have also plotted the maximum adiabatic temperature change for BCE (red triangles) and MCE (blue circles) as a function of $(T_C - T_M)/T_C$ in figure 5.24 (b). Data correspond to a hydrostatic pressure of 2.5 kbar and to a magnetic field of 6 T. Again, the behaviour of $\Delta T$ for BCE is similar to the behaviour of $\Delta S_t$. However, for the MCE, $\Delta T$ does not follow the trends of the magnetic-field induced entropy change: as expected it shows low values for weak magnetic samples, but it raises steadily as $T_M$ becomes lower than $T_C$. Actually, it has to be taken into account that for a given caloric effect, the adiabatic temperature change does not only depend on the entropy change but also on how sensitive the transition temperature is to the applied external field. As shown in table 5.1, $dT_t/dp$ can be considered to be constant within the studied range. On the other hand, a significant increase is observed in $dT_t/dH$. Such an increase is understood in terms of the Clausius–Clapeyron equation and is a consequence of the larger values of the magnetization change across the martensitic transition arising from the larger ferromagnetic order of the austenite as $T_M$ becomes lower and lower than $T_C$ (see figure 5.17). Inspection of figure 5.24 (a) and (b) shows that for the MCE although the entropy change decreases at large $T_C - T_M$ values, the adiabatic temperature change is large due to the strong sensitivity of the transition temperature to the magnetic field (see table 5.1).

It is finally worth analysing the behaviour of the Refrigerant Capacity (RC) which we have computed as

$$\mathrm{RC} = |\Delta S|_{max} \times \delta T, \tag{5.9}$$

where $\delta T$ is the full width at half maximum for the $\Delta S$ vs $T$ curves (figure 5.20). Data for a hydrostatic pressure of 2.5 kbar (red triangles) and a magnetic field of 6 T (blue circles) are shown in figure 5.24 (c). For the BCE, weakly magnetic samples exhibit the largest RC, in concordance with the trends exhibited by both $\Delta S$ and $\Delta T$. On the other hand, for MCE, although samples with martensitic and Curie points close each other have the largest entropy change, the RC is significantly larger for samples with the martensitic transition well below the Curie point, due to the strongest sensitivity of the transition temperature to magnetic field which results in a broader temperature span.

### 5.4.4 Summary and conclusions

We have studied the barocaloric and magnetocaloric effects in a series of composition related Ni–Mn–In magnetic shape memory alloys by means of calorimetry under hydrostatic pressure and magnetic field. We have tailored the composition of the alloys in such a way that all samples exhibit a martensitic transition with a very narrow hysteresis of 3–6 K. We have shown that the relative distance between the martensitic transition and the Curie point of the

austenite is a good parameter to rationalise the behaviour exhibited by the different quantities that characterise a giant caloric effect i.e. isothermal entropy change, adiabatic temperature change and RC.

It is found that the BCE is larger for samples transforming martensitically above the Curie point of the austenite. As the martensitic transition occurs below the Curie point, all quantities start to decrease. Such a decrease is due to the lowering of the transition entropy change, arising from the magnetic contribution to the entropy. With regards to the MCE, the entropy change attains a maximum for those samples with martensitic and magnetic transitions close to each other. However, the adiabatic temperature change and RC are larger for samples transforming martensitically slightly below the Curie point, as a consequence of the stronger sensitivity of the martensitic transition to the magnetic field, resulting from a larger change in magnetization at the transition.

We expect that present findings can provide useful guidelines in the selection of magnetic shape memory alloys for possible refrigerating devices. While it is commonly accepted that a large entropy change is required, for certain specific applications using the MCE it can be more interesting to use materials with slightly lower entropy values but with larger temperature changes and with a broader temperature span of applicability. On the other hand, for BCE applications, weakly magnetic samples exhibit the best performances. The opposite trends exhibited by BCE and MCE effects point to a delicate balance between the two effects in order to attain an optimal multicaloric response.

## 5.5 Barocaloric and magnetocaloric effects in Ni-Co-Mn-Ga-In shape memory alloys

In the present section, the magnetocaloric and barocaloric effects in a series of composition-related metamagnetic shape memory alloys (Co and In-doped Ni–Mn–Ga) are reported. The compositions of the alloys were chosen so that the Curie temperature of martensite is below the structural transformation [149, 150] and they were tailored in such a way that the martensitic transition takes place at different distances below the Curie point of the austenite. Furthermore, by doping with Co, the martensitic transition occurs well above room temperature so that no kinetic arrest is expected for these samples [147, 149]. Interestingly, a maximization of the volume change at the transition is expected for samples of these particular compositions [151].

### 5.5.1 Experimental details

The compositions (in at%) of the prepared samples measured by EDX are listed in table 5.1 with the corresponding labels as a function of the indium content: $In_0$, $In_{2.0}$, $In_{2.1}$, and $In_{3.0}$.

From the ingots, samples for magnetic measurements and conventional DSC (typical mass $\sim$ 0.14 to 0.16 g), and for calorimetry under magnetic field (typical mass $\sim$ 0.1 g) and pressure (typical mass $\sim$ 1.7 to 1.8 g) were cut using a low-speed diamond saw. Crushed powders prepared for X-ray measurements were annealed before the measurements to improve crystallinity.

X-ray diffraction patterns were collected using a Thermo ARL X-FTRA diffractometer equipped with a solid-state Si(Li) Peltier detector and an environmental chamber, which allows to perform measurements in the range 100-600 K. Thermomagnetic analysis (TMA), was used to determine the temperature dependence of the ac susceptibility in an applied field of a few Oe at IMEM-CNR (Parma, Italy). Conventional differential scanning calorimetry (DSC) was conducted using a Q2000 calorimeter from TA Instruments. Hydrostatic pressure and magnetic field calorimetry was carried out in the calorimeters described in sections 3.2 and 3.4.

### 5.5.2 Results and discussion

Examples for the X-ray diffraction patterns collected at selected temperatures are shown in figure 5.25 for samples $In_{2.0}$, $In_{2.1}$, and $In_{3.0}$. For the sake of clarity, data collected during cooling runs are not displayed in the figure. The selected range displayed in figure 5.25 highlights the onset of the austenitic phase and the concurrent fading of the martensitic

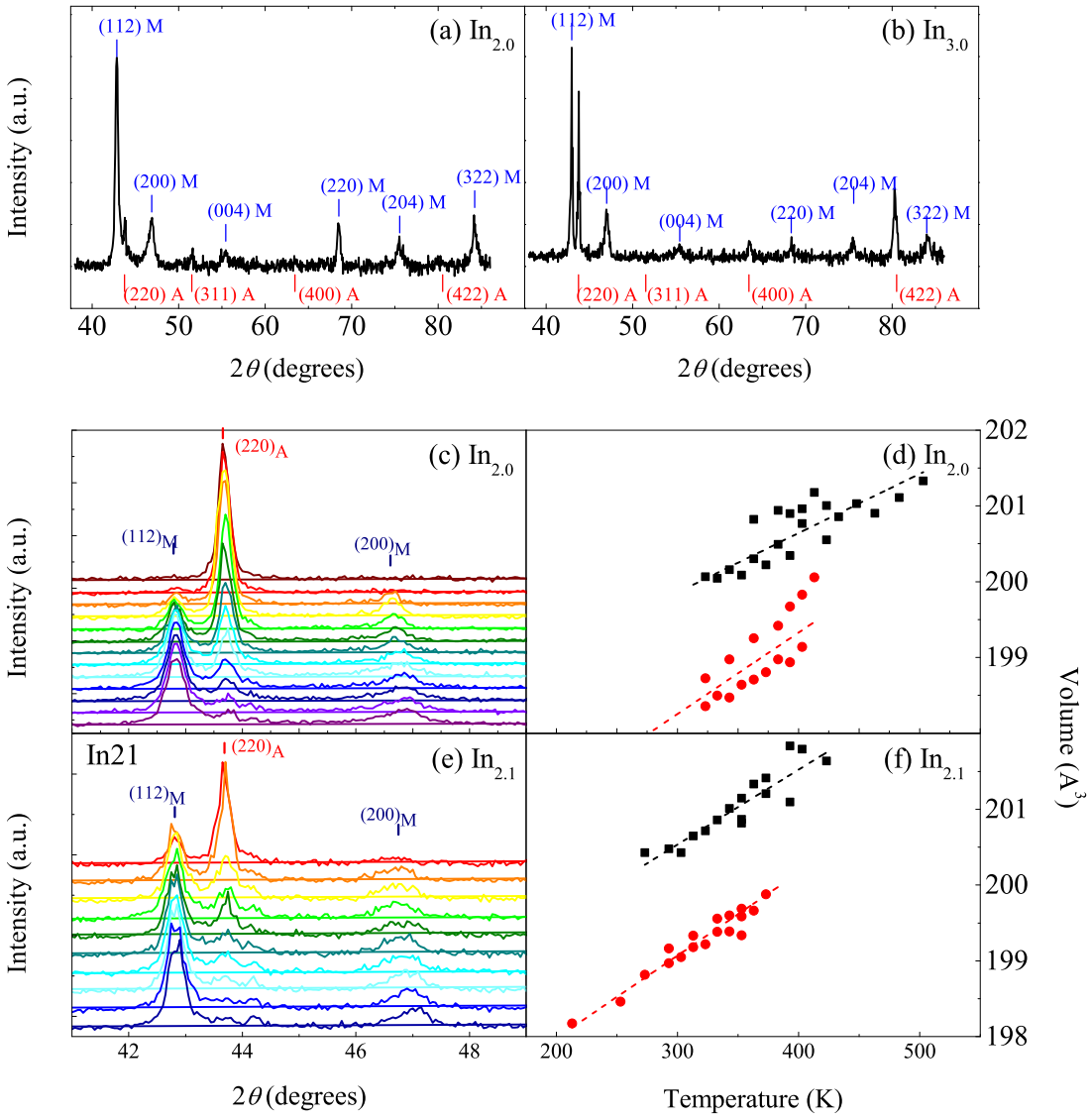


Fig. 5.25 X-ray diffraction patterns taken in the martensitic phase for (a) sample $In_{2.0}$ and (b) sample $In_{3.0}$. The peaks labelled with a subscript M correspond to the tetragonal martensite and those labelled with a subscript A correspond to the residual cubic phase. (c) and (e) panels display X-ray diffraction patterns at selected values of temperature. For sample $In_{2.0}$ (top panel), temperatures from top to bottom are: 448, 423, 413, 403, 393, 383, 373, 363, 353, 343,333, 323, and 313 K. For sample $In_{2.1}$ (bottom panel), temperatures from top to bottom are: 353, 343, 333, 323, 313, 303, 293, 273, 253,and 213 K. Panels (d) and (f): Temperature dependence of the unit cell volume in the austenitic (squares) and martensitic (circles) phases. Lines are linear fit to the data.

Table 5.2 Lattice parameters of the austenite and martensite phases and relative volume change at the martensitic transition for samples $In_{2.0}$ and $In_{2.1}$.

| | $In_{2.0}$ | $In_{2.1}$ |
|---|---|---|
| **Austenite phase** | $a_A$=5.855 ± 0.003 | $a_A$ = 5.859 ± 0.005 |
| **Martensite phase** | $a_M$= 3.893 ± 0.005 | $a_M$ = 3.900 ± 0.005 |
| | $c_M$= 6.57 ± 0.01 | $c_M$= 6.56 ± 0.01 |
| $\Delta v_t/v$ | 0.7 ± 0.2% | 0.7 ± 0.3% |

reflections while the austenitic peak steadily grows on heating. The austenitic phase has been found to be cubic, and the martensitic phase, tetragonal non modulated for the two samples. Lattice parameters for the different structures have been refined for each temperature. The values obtained at the transition and the corresponding relative volume change $\Delta v_t/v$ for samples $In_{2.0}$ and $In_{2.1}$ are listed in table 5.2. From the refined lattice parameters, the crystal volume of the two phases is obtained as a function of temperature. Results are shown in figure 5.25 (right panels) for samples $In_{2.0}$ and $In_{2.1}$. The thermal expansion of the two phases is different, and the relative volume change shows a non-negligible drift with temperature.

Figure 5.26 (left panels) shows heating and cooling DSC curves for the four studied alloys. A tiny feature at high temperatures (illustrated in the insets) corresponds to the Curie point of the cubic phase, and large and broad exothermal and endothermal peaks correspond, respectively, to the forward and reverse martensitic transitions. The jerky character of the curves reflects the avalanche behaviour kinetics of the martensitic transition [152]. The values for the Curie point ($T_C$) and the transition entropy change $\Delta S_t$ calculated from these curves are shown in table 5.1.

Representative examples of the isofield thermal curves obtained during heating and cooling at selected values of magnetic field and hydrostatic pressure are shown in figure 5.27. The MCE is studied for samples $In_{2.0}$ (a) and $In_{3.0}$ (b), and the BCE for $In_0$ (c) and $In_{2.0}$ (d), and $In_{2.1}$ (e). The corresponding transition temperature values as a function of the applied magnetic field and pressure are plotted in (f) and (g), respectively, and are in accordance with the results presented in the previous section. The lower magnetization of the martensitic phase gives rise to the inverse magnetocaloric effect, in agreement with the shift of the transition temperatures to lower values as magnetic field is increased. By contrast, the barocaloric effect has been found to be conventional, reflecting the lower volume of the martensitic unit cell. Accordingly, the transition shifts to higher temperatures with increasing pressure.

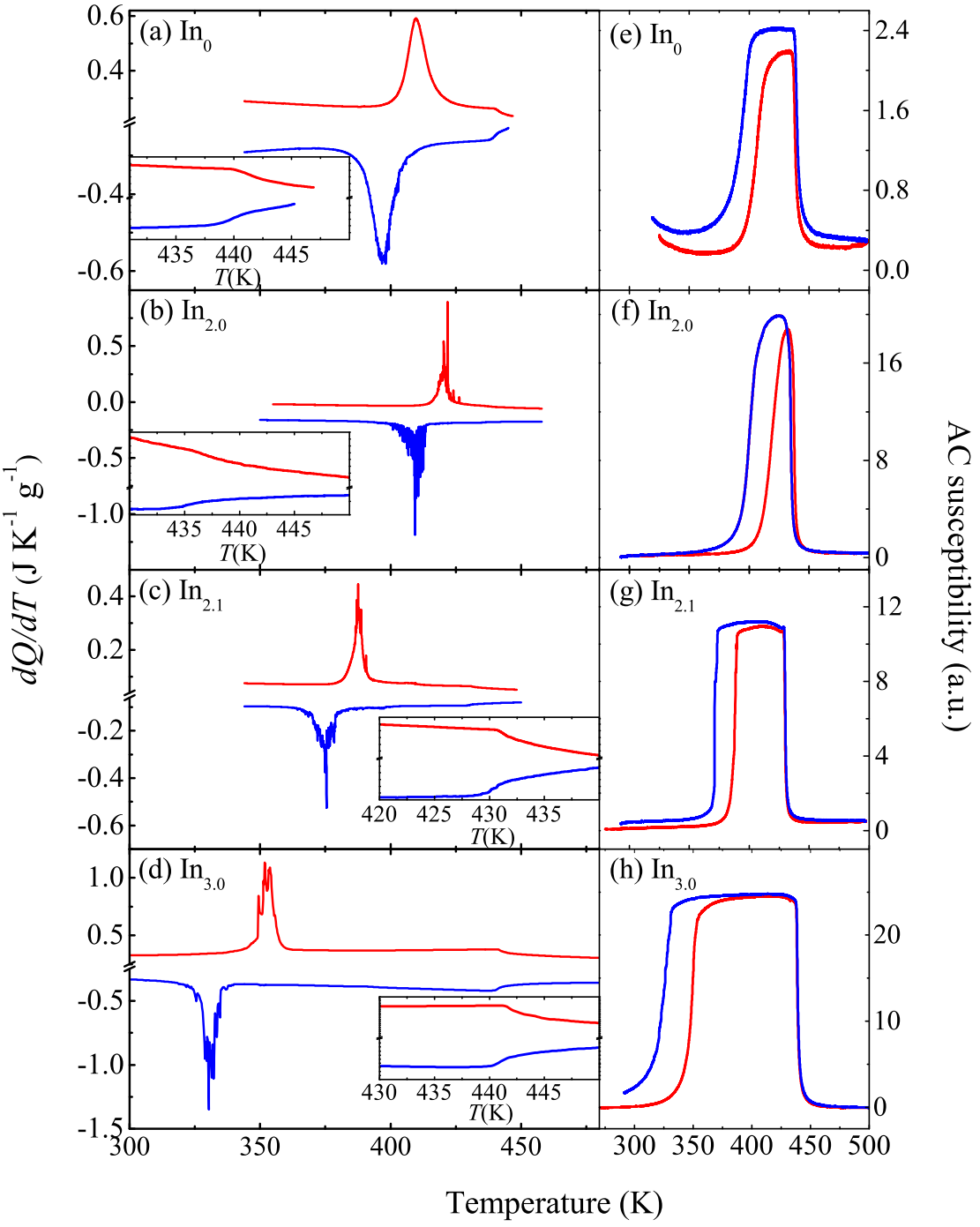


Fig. 5.26 Left panels: Differential scanning calorimetry curves for the four studied samples. On each panel, bottom curves correspond to cooling runs and upper curves, to heating runs. The insets show enlarged views of the calorimetric curves to illustrate the feature associated with the Curie point. Right panels: Temperature dependence of the AC magnetic susceptibility.

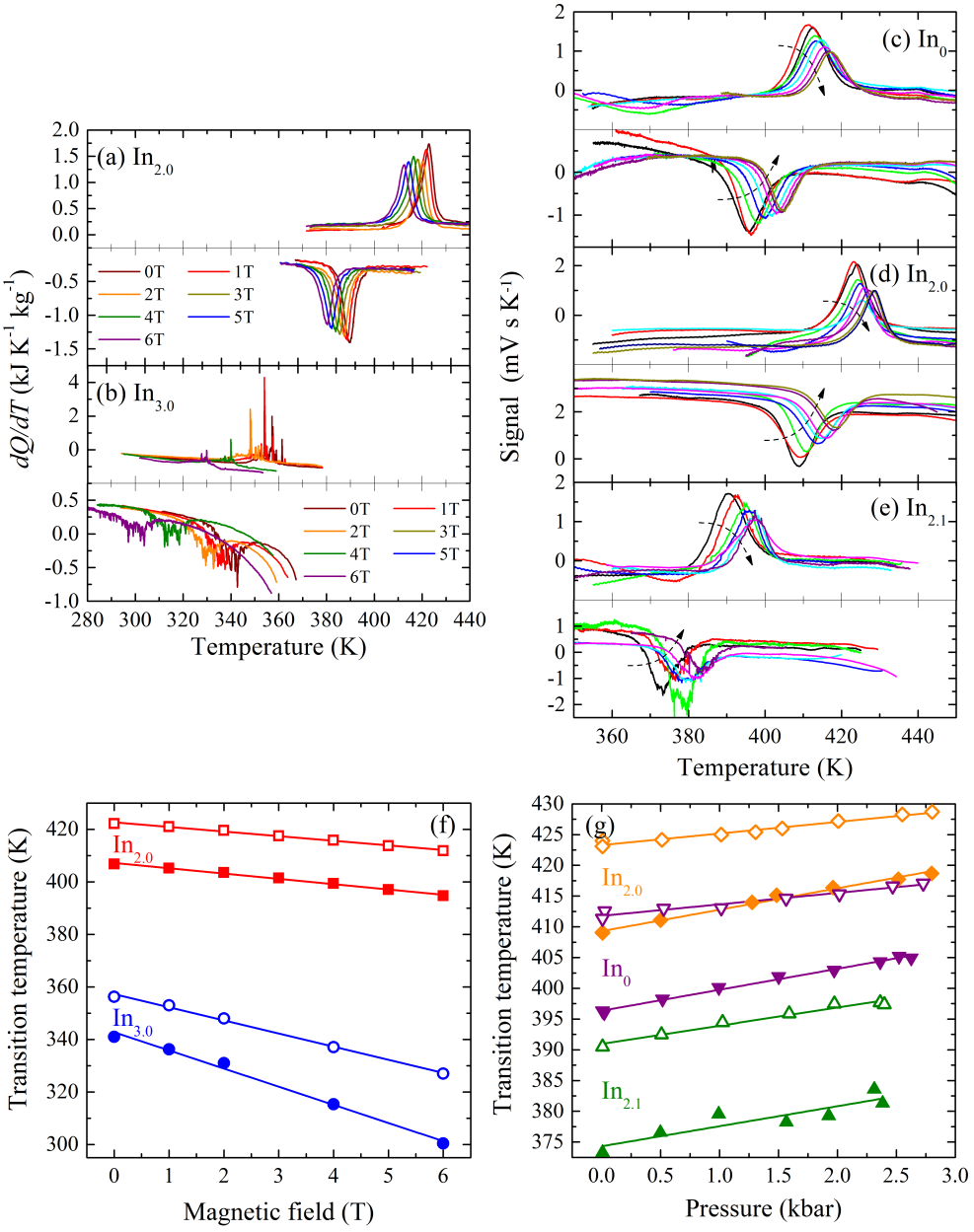


Fig. 5.27 Top panels: Calorimetric curves at selected values of the magnetic field (a, b) and hydrostatic pressure (c, d, and e). On each panel, bottom curves correspond to cooling runs and upper curves, to heating runs. Dashed arrows indicate increasing pressure. Curves correspond to pressures as follows. For $In_0$: 0 (black and red), 0.5 (green), 1.0 (blue), 1.5 (cyan), 2.0 (magneta),2.5 (purple) and 2.8 kbar (dark yellow). For $In_{2.0}$: 0 (black and red),0.5 (green), 1.0 (blue), 1.2 (cyan), 1.5 (magneta), 2.0 (purple), 2.5(dark yellow) and 2.7 kbar (navy). For $In_{2.1}$: 0 (black), 0.5 (red), 1 (green), 1.5 (blue), 2.0 (cyan), and 2.5 kbar (magneta and purple).
Bottom panels: Transition temperatures as a function of magnetic field (f) and pressure (g) for the forward (solid symbols) and reverse (open symbols) transitions.

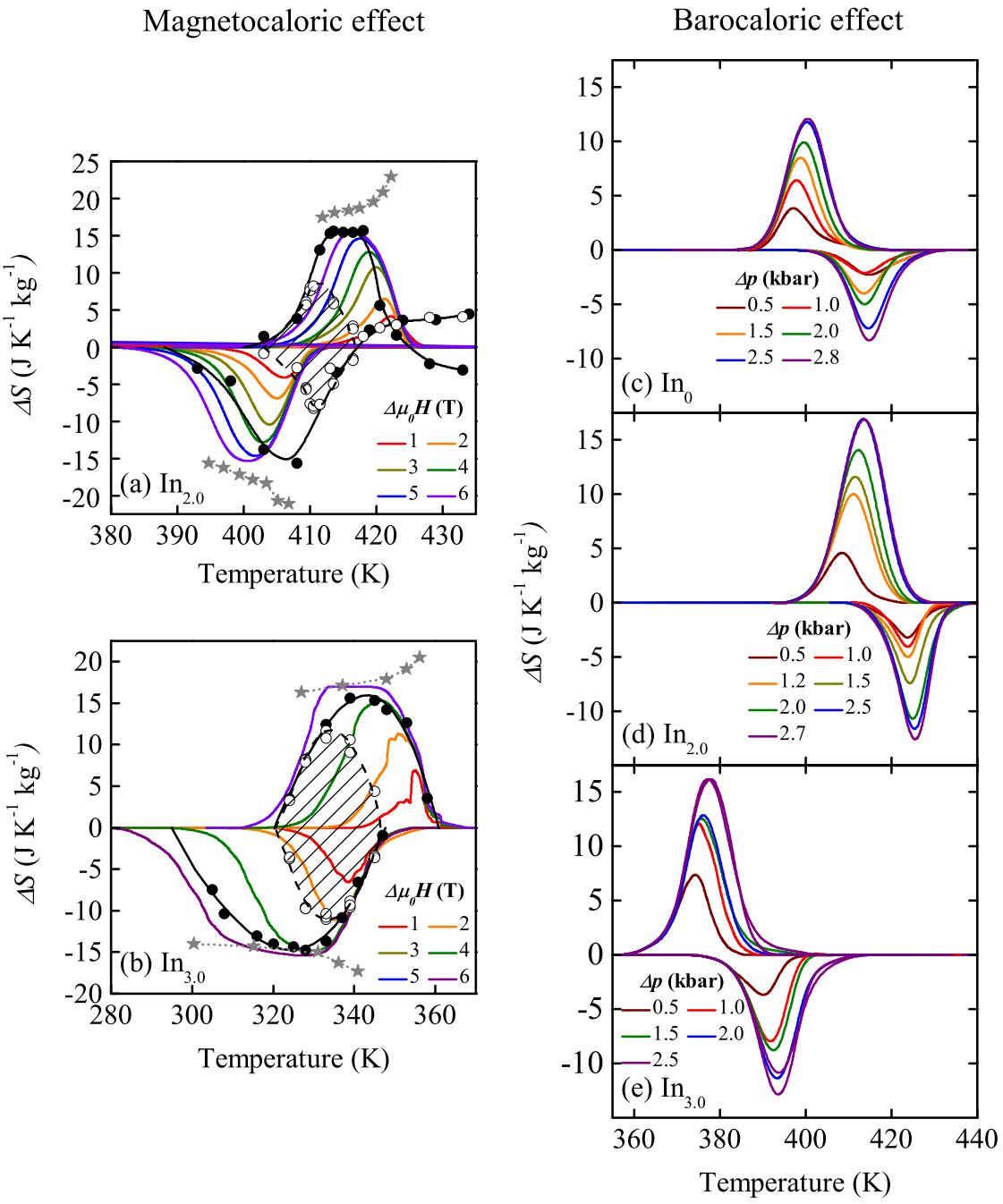


Fig. 5.28 Magnetocaloric (left panels) and barocaloric (right panels) entropy change. Coloured lines refer to the quasi-direct derivation and their corresponding values of the field change, i.e. $\Delta\mu_0 H$ and $\Delta p$, are indicated in the legends. Left panels include the values obtained by the direct isothermal measurements (black circles). Solid circles stand for the first magnetic field field scan and open circles refer to the subsequent scans. The dashed area includes the reversible entropy change. Stars correspond to the values of $\Delta S_t[T_t(H), H]$.

The values of the quasi-direct derivation of the entropy change are shown in figure 5.28. Values for the magnetocaloric effect in panels (a) and (b) also include the direct estimates obtained by isothermal calorimetry which also enables a direct characterization of the reversible entropy change obtained upon field cycling, as shown by the dashed regions. The isothermal calorimetric measurements have been perfomed by following the protocols described in section 3.1.1. Overall, there is a good coincidence for the entropy values obtained from both isofield and isothermal measurements. Samples exhibit an inverse magnetocaloric effect and a conventional barocaloric effect, i.e. application of a magnetic field, $0 \rightarrow H$, increases the entropy of the sample and application of a hydrostatic pressure, $0 \rightarrow p$ decreases the entropy.

In absolute terms, the pressure induced entropy change values increase with increasing the magnitude of the applied field as illustrated in figure 5.29 (left panel), which shows the maximum values entropy $|\Delta S|_{max}$ as a function of the hydrostatic pressure. In general, the values are slightly lower than those for Ni–Mn–In alloys presented in the previous section. However, it is worth mentioning that the barocaloric $|\Delta S|_{max}$ values are comparable to those reported for Gd–Si–Ge [89] and larger than the values reported for La–Fe–Si magnetocaloric materials [41]. The upper bound of the $|\Delta S|_{max}$ values is given by the transition entropy change $\Delta S_t$. From figure 5.27, it can be seen that the coincidence between the magnetic field induced entropy value and the $\Delta S_t$ value at 6 T reflects the fact that within such an interval a field of 6 T is enough for driving the whole of the sample through its martensitic transition. In contrast, for the three alloys in which the BCE has been studied they do not reach the upper bound value for the range of studied pressures. Thus, the pressure is not large enough to promote the transformation of the full sample.

The refrigerant capacity (RC) values have been computed as indicated in equation 5.9. Results for cooling and heating runs are shown in figure 5.29 (right panel) as a function of pressure. The increase in RC with increasing pressure (magnetic field) is a consequence of the increase in $\Delta S_{max}$ and the broadening of the $\Delta S$ versus $T$ peak (figure 5.27) resulting from the shift in the martensitic transition to higher (lower) temperatures with increasing pressure. The RC values found for the barocaloric effect in metamagnetic alloys compare well to those reported for magnetocaloric materials at moderate magnetic fields [153].

The volume change at the martensitic transition can be obtained by using the Clausius-Clapeyron equation: $\Delta v_t = \Delta S_t \dfrac{dT_t}{dp}$. Within experimental errors, $\Delta S_t$ has been found to be independent of pressure for the studied range of pressures. Hence, the good linearity exhibited by the transition temperature versus pressure [see figure 5.27 (g)] indicates that the volume change at the transition does not depend on pressure. The computed values of $\Delta v_t$ are $(4 \pm 1)$ $10^{-7}\mathrm{m}^3\mathrm{kg}^{-1}$ for sample $\mathrm{In}_0$, and $(6 \pm 1)$ $10^{-7}\mathrm{m}^3\mathrm{kg}^{-1}$ for samples $\mathrm{In}_{2.0}$ and $\mathrm{In}_{2.1}$. In the case

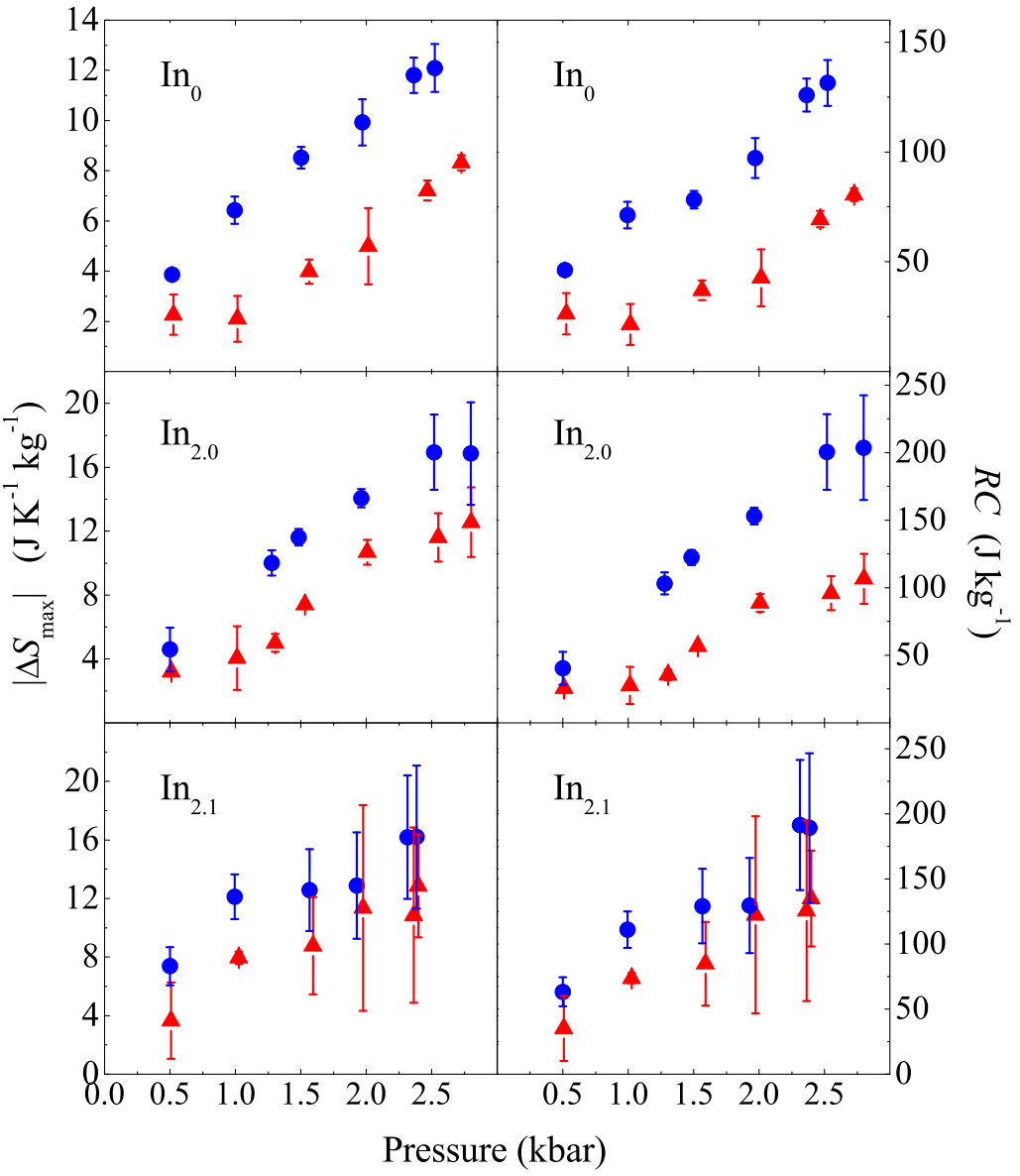


Fig. 5.29 Left panels: Absolute value for the maximum pressure induced entropy change as a function of pressure. Right panels: Refrigerating Cooling Power as a function of pressure. Blue circles correspond to data from cooling runs and red triangles, to data from heating runs.

of the latter samples, they correspond to relative changes of $\Delta v_t/v = 0.5 \pm 0.1\%$ (for the two samples), where the unit cell volume for the two samples is taken as $v = 1.2510^{-4}\mathrm{m}^3\mathrm{kg}^{-1}$, computed from X-ray data. Although these values are slightly lower than those from X-ray (see table 5.2), there is a quite good agreement between the two set of data taking into account the uncertainties associated with the two methods.

For a conventional caloric effect(as the barocaloric effect found here), the temperature region where the effect is expected to be reproducible is bounded by the martensitic start transition under applied pressure and the austenite start transition at atmospheric pressure, according to the description given in the previous sections 5.3 and 5.4. A graphical approach is provided by the temperature region where the $|\Delta S|$ versus $T$ curves recorded on heating and cooling overlap. Inspection of figure 5.28 (c, d, and e) suggests a poor reproducibility for the barocaloric effect in the studied metamagnetic alloys. Such a lack of reproducibility must be ascribed to a relatively large hysteresis of the transition $\sim$ 15 K and a moderate pressure dependence of the transition temperatures. Taking into account the pressure dependence of the transition temperatures and the values for the thermal hysteresis we can estimate that pressures of $\sim$ 8 kbar would be necessary to obtain a reversible barocaloric effect.

Both transition enthalpy and entropy changes slightly decrease with increasing magnetic field and give an upper bound of the caloric effects, as explained in the previous sections. This is seen for the case of the MCE by the stars plotted on the left panels in figure 5.28. With regard to the energy dissipated in a complete transformation loop, the values in each case are calculated by following the expression given by 5.5 in section 5.3.2. Even though these materials display a larger hysteresis if compared to the samples presented in sections 5.3 and 5.4, it is seen that they still display low values of the dissipated energy in comparison to the transition enthalpy change (3%–8%). The lowest values correspond to the samples with the lowest hysteresis.

### 5.5.3 Summary and conclusions

In Ni-Co-Mn-Ga-In metamagnetic alloys the entropy changes at the barocaloric and magnetocaloric effect at moderate pressures up to 2.8 kbar and magnetic fields up to 6T are in the range of the values reported for materials exhibiting giant caloric effects [154].

Although the relatively large thermal hysteresis compromises the reproducibility of the barocaloric effect, a good reproducibility for the magnetocaloric effect is found. The maximum reversible entropy values for fields of 6 T are 8 J/kg K and 11 J/kg K for the samples with the weakest and strongest field dependence of the martensitic transition, respectively. These values represent, respectively, 60 % and 70% of the total magnetocaloric effect (corresponding to application of the field for the first time) in these materials.

As previously explained, the reversibility in the magnetocaloric effect depends, primarily, upon two factors: the width in the hysteresis loop and the shift in the transition temperatures with field. Indeed, the materials studied in this section display larger hysteresis in comparison with the previously presented Ni-Mn-In alloys in sections 5.3 and 5.4, but this drawback can be compensated with the larger sensitivity of the transition to the applied magnetic field. In addition, it has been calculated that the energy losses associated with the hysteresis is less than an order of magnitude lower than the latent heat of the transition which bounds the magnitude of the caloric effect. It is therefore expected that hysteresis will not severely reduce the energetic efficiency of a potential refrigerating cycle using these materials.

Tailoring materials with low hysteresis and strong field dependences will result in larger temperature regions where the magnetocaloric effect is reversible. Within this temperature range, large values for the reversible entropy (approaching the total entropy change) will be found for those samples with a sharp martensitic transition. Moreover, the opposite behaviour of the transition temperatures with magnetic field and pressure suggests that the reproducibility could be enhanced (increased temperature region and entropy values) either by tuning the magnetocaloric effect by hydrostatic pressure or by tuning the barocaloric effect by a magnetic field.

## 5.6 Expanding the magnetocaloric operation range in Ni–Mn–In Heusler alloys by Cu-doping

A number of strategies have been proposed in order to extend the operation range of the giant MCE [91, 155, 156]. For a given material, it is known that the range over which a first-order transition occurs depends on the amount of disorder in the form of chemical disorder, lattice defects, etc, which gives rise to a spatial distribution of local transition temperatures [157, 158]. This suggests that the transition range can be increased by tailoring the amount and distribution of disorder. Nevertheless, controlling disorder in an appropriate way to engineer materials showing large caloric response in an extended temperature span is in general difficult.

An effective strategy consists in building composite materials made of components with slightly shifted operation ranges [91, 159–163]. In the present section we take advantage of the high sensitivity of the transition temperature on composition in Ni-Mn based magnetic martensitic materials and we show that a magnetocaloric composite material can be designed by assembling (stacking) pieces of Ni–Mn–In with fine tuned amounts of Cu-doping.

In Ni-Mn based Heusler alloys hybridization between the Ni 3*d* states and the 3*d* states of excess of Mn-atoms located at Z sites have been shown to play a crucial role in controlling the relative stability between parent and martensitic phases [128, 164]. Therefore, in Ni–Mn–In small substitution of Mn atoms located at In sites by Cu atoms should give rise to a decrease of the range of stability of the martensitic phase due to a weakening of the hybridization. Nevertheless, doping should have little effect on the magnetic properties of the material. Therefore, it is expected that both the reduced thermal hysteresis and the large magnetization jump associated with the martensitic transition that control the excellent reversible magnetocaloric properties of Ni–Mn–In materials remain essentially unaffected by Cu-doping. Consequently, doping with selected amounts of Cu should provide a very convenient procedure to design composite materials with broad magnetocaloric operation range.

### 5.6.1 Experimental details and alloy design

Sample compositions are listed on table 5.1 and are labelled as a function of the Cu-fraction: $Cu_0$, $Cu_{1.9}$, $Cu_{2.2}$, and $Cu_{2.7}$. Compositions have been determined by averaging the EDX results on three different surfaces of each studied sample. XRD measurements have confirmed that Cu-doping prompts minor effects on the structural nature of Ni-Mn-In alloys and have

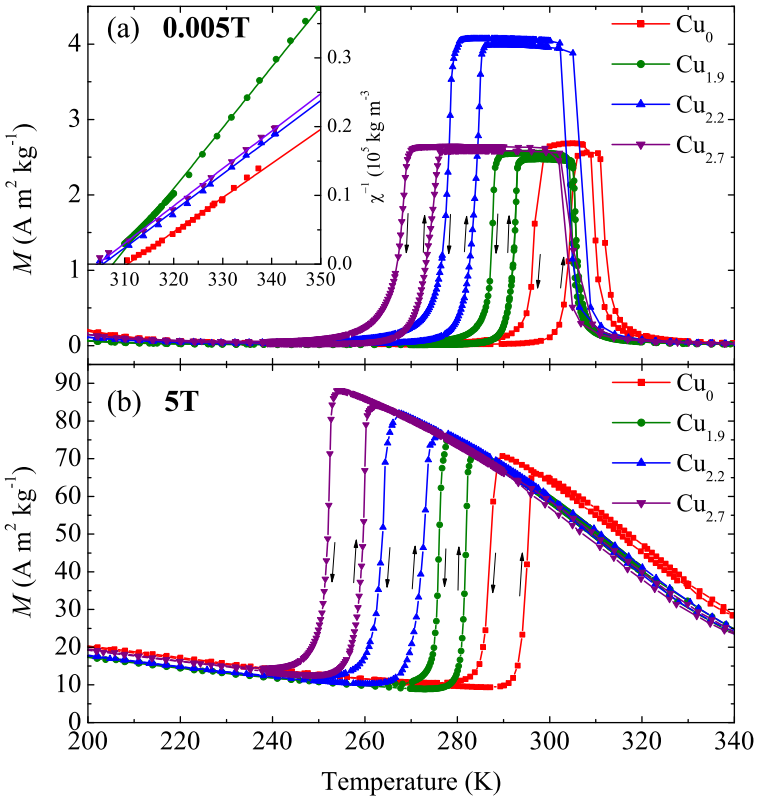


Fig. 5.30 Magnetization versus temperature curves at a low applied magnetic field of 0.005T (a) and at high field 5T (b) for heating and cooling runs. Inset: Inverse of the magnetic susceptibility as a function of temperature in the high temperature paramagnetic regime.

verified the presence of a cubic $L2_1$ austenite phase and a modulated martensite structure on each sample, in accordance with previous studies [13, 84, 107, 165].

Magnetization measurements were carried out with a vibrating sample magnetometer in a Physical Property Measuring System (PPMS, Quantum Design) at Instituto Potosino de Investigación Científica y Tecnológica (IPICyT, San Luis Potosí, Mexico) from which isothermal scans of magnetic field and isofield temperature scans have been performed on samples with a typical mass $\sim$ 15 mg.

Calorimetric measurements under magnetic fields were performed by using the calorimeters described in section 3.2 by scanning the temperature at a rate 0.6 K min$^{-1}$ (isofield measurements), and magnetic field at a rate 0.2 T min$^{-1}$ (isothermal measurements). The mass of specimens for calorimetry measurements was $\sim$ 200 mg.

### 5.6.2 Results

Magnetization versus temperature curves are shown in figure 5.30. Panel (a) shows the low field (5 mT) magnetization measurements. On cooling the magnetization first increases at the Curie temperature and it decreases at a lower temperature where the martensitic transition occurs. The inset displays the behaviour of the inverse of the susceptibility $\chi^{-1}$ (obtained from cooling runs) in the high temperature region where samples are in the paramagnetic state. $\chi^{-1}$ exhibits, as expected, a linear behaviour and values of the paramagnetic Curie temperature, $T_C$, are obtained from the corresponding linear fits taking into account the Curie-Weiss law $\chi = \dfrac{C}{T - T_C}$, where $C$ is the material's specific Curie constant. The obtained paramagnetic Curie temperatures slightly decrease by increasing the amount of Cu (see table 5.1). Panel (b) shows magnetization vs. temperature curves obtained during cooling and heating runs at 5 T. The sharp decrease in magnetization is associated with the first-order martensitic transition from a high temperature ferromagnetic phase to a low temperature paramagnetic martensitic phase. At temperatures above the forward and reverse martensitic transition temperatures ($T_M$ and $T_A$, respectively) the magnetization drops due to the occurrence of the second-order Curie transition to a paramagnetic state. It is worth noting that both high and low magnetic field magnetization curves show very similar behaviour except for the significant shift of the martensitic transition. The slightly higher low magnetic field magnetization in the region between the Curie and martensitic transition temperatures displayed by sample $Cu_{2.2}$ is indeed not relevant.

Calorimetric measurements under constant applied field are presented in figure 5.31 (left panels). The first-order magnetostructural transition and its associated latent heat and entropy change is identified by positive peaks on heating runs (endothermal process) and negative peaks on cooling runs (exothermal process). The change in heat capacity associated with the ferromagnetic-paramagnetic transition at $T_C$ is detected as a small feature in the thermograms, which is two orders of magnitude lower than the magnitude of the peaks corresponding to the magnetostructural transition. Peak temperatures define transition temperatures $T_M$ and $T_A$, which are plotted as a function of the applied magnetic field in figure 5.32. As shown in table 5.1, for all samples significantly low hysteresis, $T_A - T_M$, ranging between 4 and 6 K has been found.

Calorimetric measurements allow the computation of entropy curves $S(T) - S(T_0)$ in the temperature range at which the first-order transition takes place. They are computed by integration (with appropriate baseline) of the calorimetric curves as indicated in the expression (4.5.3).

As shown in figure 5.32 and table 5.1, the first-order martensitic transition temperatures decrease when the Cu-content increases. Application of a magnetic field shifts the martensitic

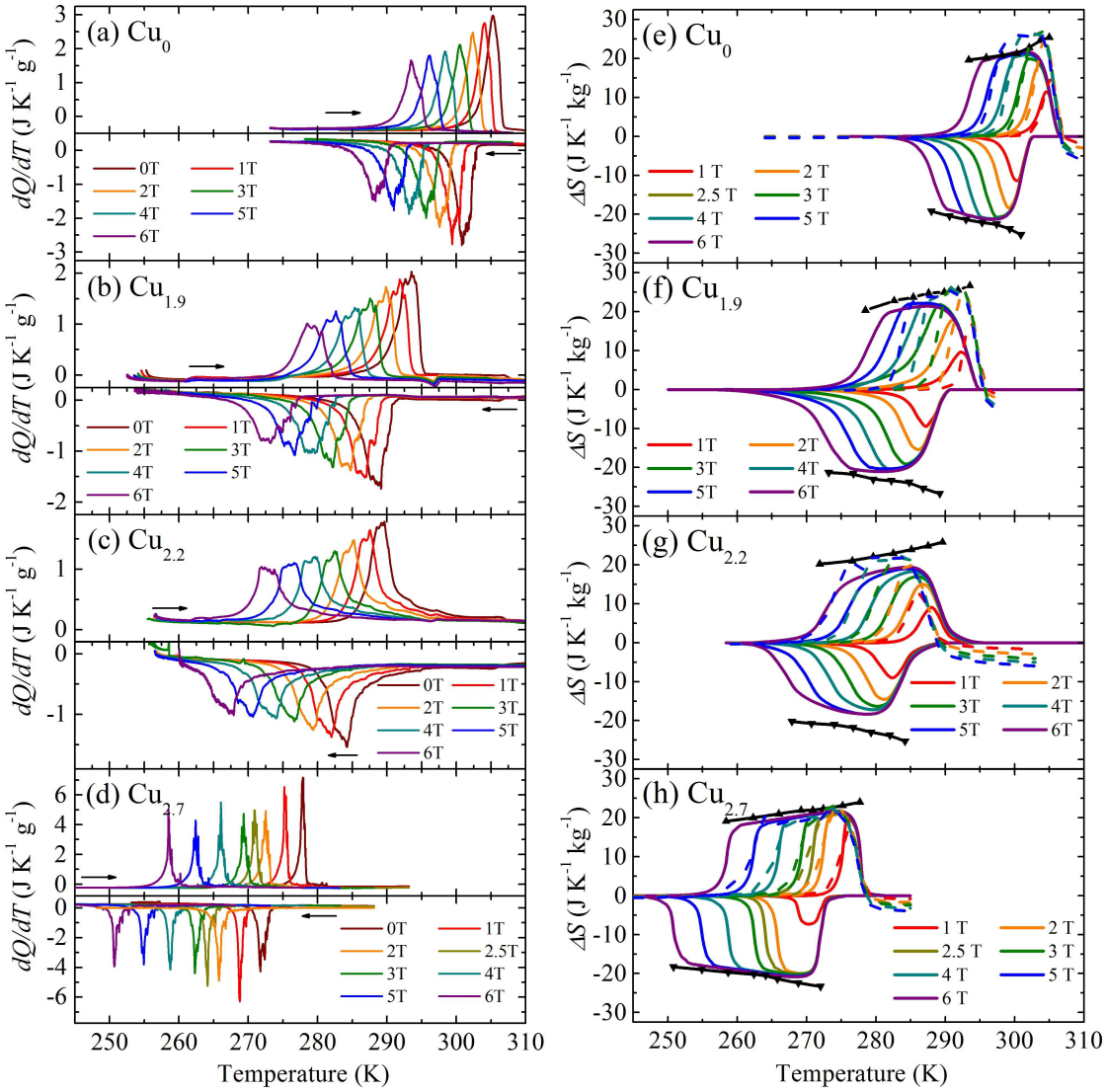


Fig. 5.31 *Left panels:* Isofield thermal curves corresponding to samples $Cu_0$ (a), $Cu_{1.9}$ (b), $Cu_{2.2}$ (c), $Cu_{2.7}$ (d). Values of the applied magnetic field are shown in the legends. Positive curves correspond to heating runs and negative curves to cooling runs. *Right panels:* Magnetic field-induced entropy change as a function of temperature for: (e) $Cu_0$, (f) $Cu_{1.9}$, (g) $Cu_{2.2}$, (h) $Cu_{2.7}$, at selected values of the applied magnetic field. Solid lines refer to the quasi-direct method of computation of the magnetocaloric effect and dashed lines refer to the indirect method. Up black triangles refer to $\Delta S_t$ on heating at each applied magnetic field whereas down black triangles refer to $\Delta S_t$ on cooling. $\Delta S_t$ values are plotted at the corresponding $T_A(\mu_0 H)$ or $T_M(\mu_0 H)$ values. Black lines are guides to the eyes.

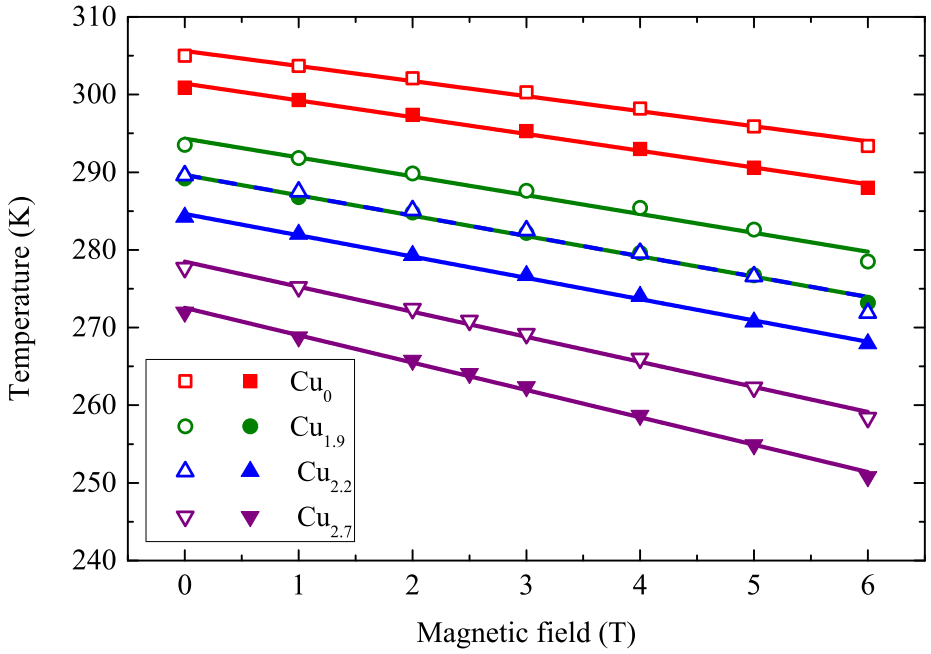


Fig. 5.32 Transition temperatures $T_M$ (solid symbols) and $T_A$ (open symbols) as a function of magnetic field. Linear fits to the data provide the values of $\frac{dT_M}{d\mu_0 H}$ given in table 5.1.

transition towards lower temperatures owing to the fact that the martensite has lower magnetization than the parent phase. The sensitivity values $\frac{dT_M}{d\mu_0 H}$ follow the behaviour described in section 5.4.3 and are enhanced (in absolute terms) as the distance between martensitic and Curie transition temperatures increases, as shown in table 5.1.

Figure 5.31 (right panels) shows quasi-direct and indirect estimations of the magnetocaloric entropy change for the studied samples. Indirect estimations were obtained from isofield magnetization curves (not shown here) as $\Delta S(0 \rightarrow H) = \mu_0 \int_0^H \left(\frac{\partial M}{\partial T}\right)_H dH$. Both quasi-direct and indirect methods display an inverse character of the magnetocaloric effect and give almost coincident results. The small discrepancies may be attributed to small inhomogeneity gradients in each sample and the fact that different specimens have been used for calorimetric and magnetization measurements. The indirect method display a tail with sign opposite to the sign of the main peak, which is not observed on quasi-direct results. This tail is reminiscent of the conventional magnetocaloric effect associated with the ferromagnetic order that develops below the Curie temperature and is not detected by the quasi-direct method since it only takes into account the contribution associated with the first-order magnetostructural transition.

As shown in the right panels of figure 5.31, the transition entropy change provides the limit of the maximum available absolute value of the magnetocaloric entropy change, which is achieved for large enough applied magnetic fields enabling to fully induce the transition. The corresponding magnetic field threshold is minimum at temperatures close to $T_M$ (0T) and $T_A$(0T) ($\sim$ 2.5T for samples $Cu_0$, $Cu_{1.9}$, $Cu_{2.2}$, and $\sim$ 2T for $Cu_{2.7}$). As mentioned previously, $\Delta S_t$ and the maxima of $\Delta S$ are slightly reduced as the transition is shifted towards low temperatures when the maximum applied magnetic field increases.

It is noticeable that the magnetocaloric effect exhibited by the studied samples may cover a large temperature interval about room temperature if the caloric contributions of each sample were combined. With this result in mind, a composite specimen of total mass $m = 262$ mg has been prepared by stacking 19.9% $Cu_{1.9}$, 42.4% $Cu_{2.2}$, 37.8% $Cu_{2.7}$ components for calorimetric measurements. The aim was to obtain a direct determination of the magnetocaloric response of the composite. Results corresponding to isothermal magnetic field cycles up to 5 and 6T are shown in figure 5.33. Examples of the obtained thermal curves are given in figures 5.33 (b) and (c). Integration of the calorimetric curves provide the magnetocaloric entropy change values (direct method) displayed as symbols in panel (d). In this panel, dashed lines and their enclosed dashed area indicate the region of full reproducibility of the entropy change upon cyclic application and removal of a magnetic field of 6T. Solid lines are estimates from the quasi-direct measurements and have been computed as

$$\Delta S = \sum_i x_i \Delta S_i, \tag{5.10}$$

where $x_i$ stands for the fraction of each specimen of the composite and $\Delta S_i$ is the corresponding entropy change of each specimen (shown in figure 5.33). The overlap of two peaks in panel (b) is associated with the latent heat inherent to the first-order transition taking place in $Cu_{1.9}$ and $Cu_{2.2}$ samples whereas in (c) there is the only contribution of sample $Cu_{2.7}$ and one peak occurs at each magnetic field scan. Each set of magnetic field cycles has been preceded by an isofield thermal excursion towards a temperature at which the components of the composite were fully at the low (high) temperature phase as described in section 3.1.1. The low hysteresis of the samples ensures the occurrence of a large reversibility region as indicated by the shaded area in figure 5.33 (d). Reversible entropy changes of $\sim 7.5$ J kg$^{-1}$ K$^{-1}$ are obtained upon cyclic application of 6T. It is worth mentioning that the conventional magnetocaloric effect exhibited by components of the composite in the austenite phase can compete with the inverse contribution of opposite sign arising from the first-order transition. In any case, the conventional contribution is one order of magnitude lower than the inverse contribution and has little relevance to the overall magnitude of the magnetocaloric effect.

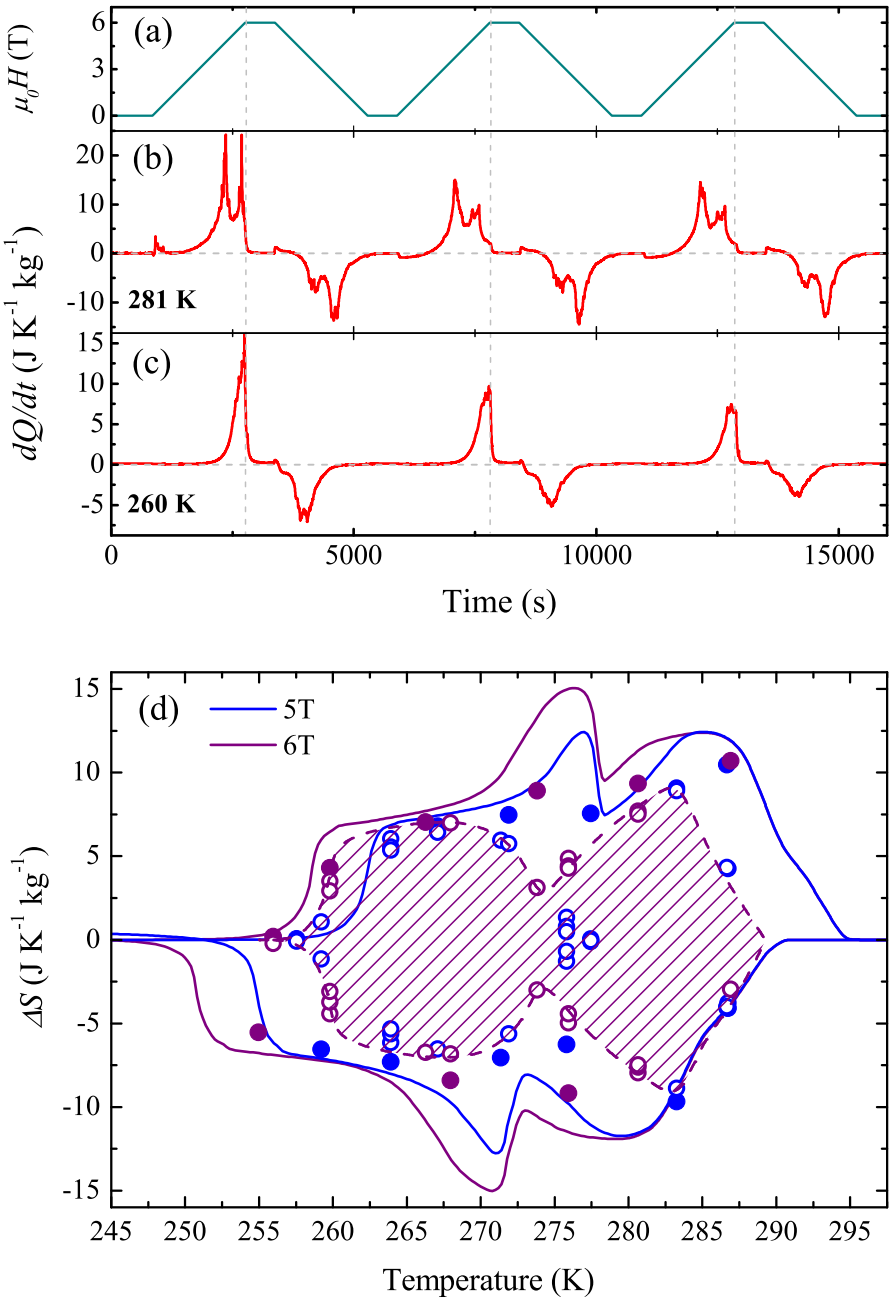


Fig. 5.33 Isothermal calorimetry under magnetic field scans: applied magnetic field versus time (a) and the corresponding thermal curves at 281 K (b) and 260 K (c). Panel (d) shows the magnetocaloric entropy change exhibited by the composite specimen upon magnetic field cycles up to 5 T (blue) and up to 6 T (purple). Purple and blue lines give the entropy change obtained by the quasi-direct method. Symbols stand for results obtained by isothermal calorimetry. Solid circles correspond to the first application or removal of the magnetic field whereas open circles correspond to successive field cycles. The purple dashed region indicates the interval of reproducibility of the entropy change upon magnetic field cycles of 6 T.

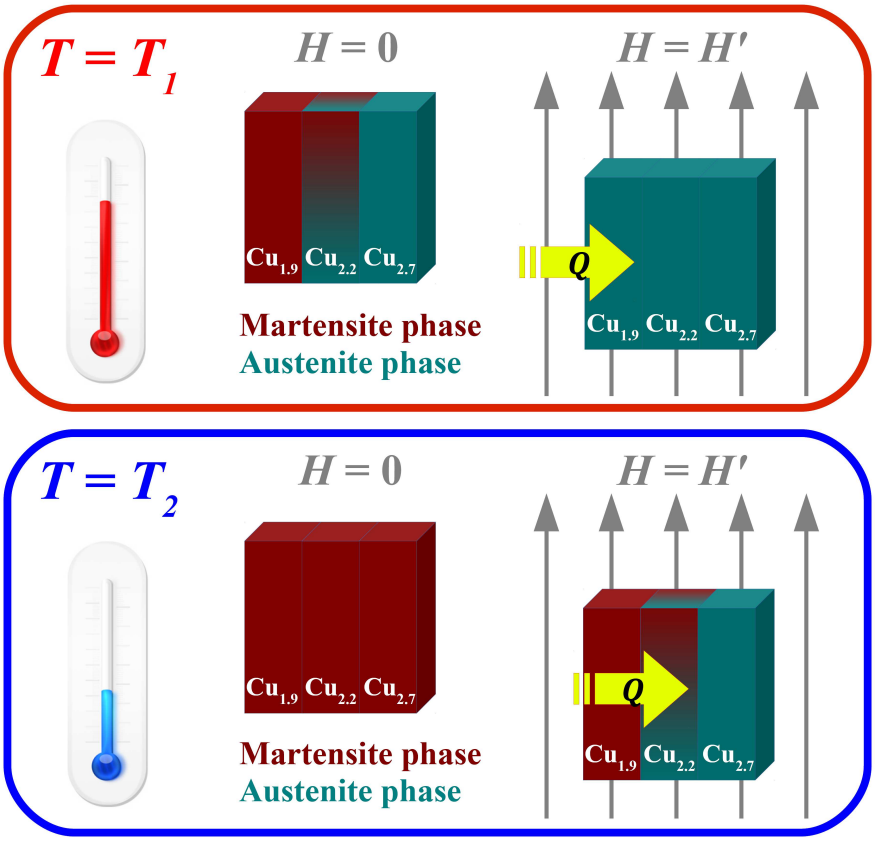


Fig. 5.34 Sketch of the composite thermal response when magnetic field is isothermally scanned at $T = T_1$ (top figure) and at $T = T_2$ (bottom figure), where $T_1 > T_2$. The yellow arrows indicate the absorption of heat at the composite fragment which transforms to the austenite phase by application of magnetic field.

### 5.6.3 Summary and conclusions

The giant magnetocaloric effect in Cu-doped Ni-Mn-In Heusler alloys has been studied by means of indirect and quasi-direct methods with the use of magnetometry and calorimetry under applied magnetic field measurements. The samples exhibit a large entropy change of $\sim$21 J K$^{-1}$ kg$^{-1}$ upon application of 6T in the vicinity of their first-order magnetostructural transition. In the studied composition range, increasing the Cu-fraction tunes the transition temperature towards lower values whereas the Curie temperature of the high temperature phase remains at values about $\sim$ 307 K. Consequently, the overall magnetocaloric effect in each specimen can be tuned as a function of temperature with the addition of copper. This has enabled the design of a composite constituted of three Cu-doped Ni-Mn-In components which show a large magnetocaloric response over a broad temperature range.

Direct isothermal calorimetric measurements under applied magnetic field have provided a characterization of the magnetocaloric response of the composite. Accordingly, figure 5.34 sketches the behaviour of the composite when the magnetic field is isothermally scanned at two different temperatures $T_1 > T_2$. The consequent heat absorption at different fragments of the composite is indicated by the yellow arrow. Results show large reproducible entropy changes of $\sim 7.5$ J K$^{-1}$ kg$^{-1}$ upon application of 6T over a temperature span of $\sim 30$ K. It is also shown that there is a clear competition between enlarging the composite operation range and lowering the magnitude of the entropy change since the thermal response at each temperature interval is exhibited by a particular segment of the composite. This ensures a proper design for a purpose-built composite as a function of applicational requirements since favouring the magnetocaloric performance in a certain temperature interval becomes feasible by tailoring a particular composition range of the material. We claim that from a technological point of view the development of composites constituted of components with gradual changes of composition can be highly advantageous for the enlargement of the magnetocaloric operation range and the optimization of the magnetocaloric performance at a desired temperature interval.

## 5.7 Thermodynamic study of the intermartensitic transition in a Ni-Mn-Ga Heusler shape memory alloy

Ni-Mn-Ga alloys display an interesting composition region at the interval with valence electron concentration close to $e/a = 7.5$, which corresponds to the 2-1-1 stoichiometry. As sketched in the phase diagram shown in figure 5.3, in this region, on cooling, the cubic $L2_1$ high temperature phase first becomes ferromagnetic and further transforms martensitically. By increasing $e/a$ from 7.5, the martensitic structure changes from modulated 5M and 7M structures to a non modulated (NM) $L1_0$ structure. In some cases, the non modulated $L1_0$ ground state structure is reached through a multistage transformation process. In particular, for $e/a \leq 7.6$, the martensitic transition is preceded by a premartensitic transition to a 3R modulated phase. For slightly larger $e/a$ values, the parent phase directly transforms to martensite. Different sequences which involve intermartensitic changes have been reported [14], including 5M $\rightarrow$ 7M $\rightarrow$ NM, and 7M $\rightarrow$ NM depending on compositions.

Nevertheless, the physical origin of intermartensitic changes is not yet well established. While the existence of an intermartensitic line in the phase diagram could be understood as a continuation of the premartensitic line, the fact that in some cases on heating the NM structure reverts to the cubic high temperature phase in a single step could indicate that modulated and non-modulated phases have very similar free energies and consequently the selection of one of these phases at nucleation may be strongly influenced by small differences of the corresponding energy barrier to be overcome in each case [15]. Interestingly, the fact that the NM structure corresponds to the ground state (lowest energy phase) suggests that intermartensitic changes may simply be understood as detwinning processes of nano-twinned structures at which dissipation of the excess of surface energy associated with twin boundaries should occur. Therefore, it is not yet well established whether or not intermartensitic changes occur through a phase transition. In spite of that, hereafter we will denote these changes as intermartensitic transitions. The present section is aimed at trying to elucidate the mechanism driving the intermartensitic transition in Ni-Mn-Ga alloys.

### 5.7.1 Experimental details

A polycrystalline $Ni_{47.7}Mn_{31.2}Ga_{21.1}$ alloy was selected in order to carry out the present study. For this alloy $e/a \sim 7.6$ and the martensitic and intermartensitic transitions are expected to occur rather close to each other. This is the situation in which the reverse transformation is expected to occur as a single step.

Neutron diffraction, calorimetric and magnetization measurements are performed in order to study the effect of an applied magnetic field on the relative stability of the parent, martensitic and intermartensitic phases. Magnetization vs. temperature measurements during cooling and heating runs were carried out in a physical property measurement system (PPMS, Quantum Design) under applied fields up to 5 T. Experiments were conducted on a specimen of approximate dimensions 1 mm $\times$ 1 mm $\times$ 5 mm (mass, $m \simeq 0.019$ g). Calorimetric measurements under applied magnetic fields up to 6 T have been performed using the calorimetric set-up described in section 3.2.

### 5.7.2 Results and discussion

Transition temperatures were estimated from conventional DSC (TA Q2000, TA-Instruments) measurements. On cooling, the martensitic transformation takes place in the temperature range between $M_S \simeq 307$ K and $M_F \simeq 298$ K. During further cooling a second process is detected which confirms the two-step martensitic transformation. It corresponds to the intermartensitic transition which occurs below $M_{IS} \simeq 295$ K. The observed two-step transformation process has previously been reported for alloys of similar composition [166–168]. On heating a single peak is only detected which confirms that the reverse transition happens as a single step. It is observed in the range between $A_S \simeq 305$ K and $A_F \simeq 315$ K.

Diffraction patterns obtained during cooling/heating sequences are shown in figure 5.35. On cooling an intermediate structure is obtained at 296 K, however it does not reappear on heating where a direct change from the low temperature martensitic phase to the high temperature parent phase takes place. Therefore, the patterns clearly indicate the formation of an intermediate structure crystallographically different from both the high and low temperature phases during cooling. The high temperature phase has been found to be cubic. The intermediate pattern is consistent with a 7M commensurate structure, while the low temperature phase is a monoclinic phase with an incommensurate modulation that approaches a 5M structure. These structural changes involve both lattice parameter and volume changes. The coexistence of 7M and 5M modulated structures has already been reported in alloys of similar composition [14]. In our case, the resolution of neutron diffraction data does not allow the observation of such a coexistence.

The magnetization behaviour in the vicinity of the martensitic transition (below the Curie point) measured during cooling and heating runs at selected values of the applied field are shown in figure 5.36 (a) and (b), respectively. A sharp change of magnetization is observed when the martensitic transition takes place. For low applied magnetic fields, the magnetization is observed to decrease while it slightly increases for large enough magnetic fields. This is the expected behaviour of the magnetization in the vicinity of the martensitic transition

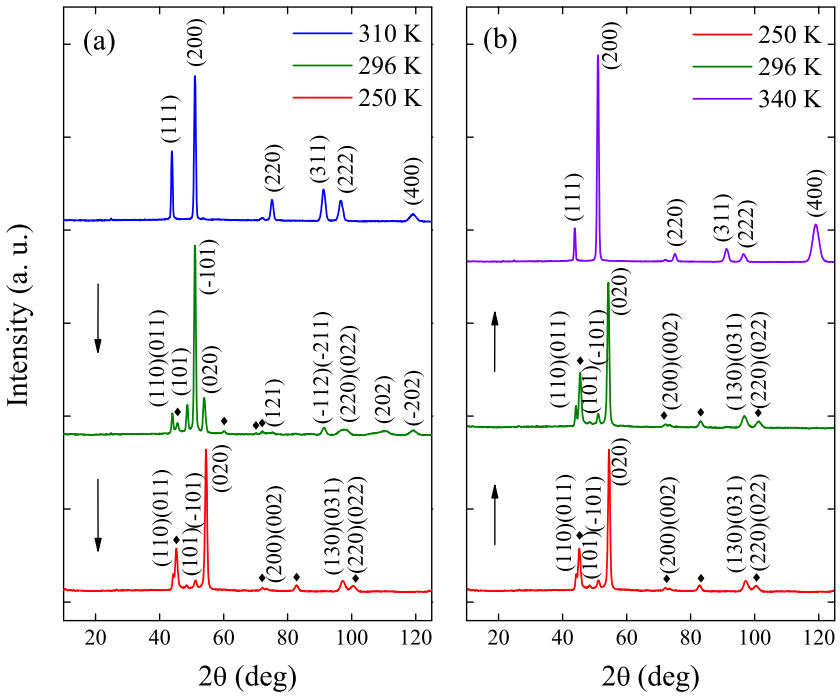


Fig. 5.35 Neutron difracction patterns. (a) During cooling at 340 K, 296 K and 250 K. (b) During heating at 250 K, 296 K and 310 K. Diamonds indicate superstructure peaks.

in nearly stoichiometric Heusler shape memory alloys [13]. Actually, the decrease of the magnetization at low fields is a consequence of the strong increase of the magnetocrystalline anisotropy in the martensitic phase (the parent phase is a very soft magnetic phase while the martensite shows a strong uniaxial magnetocrystalline anisotropy). The small increase of the magnetization observed at high fields simply indicates that the magnetic moment of the martensitic phase is larger than the magnetic moment of the parent phase. On further cooling, at the temperature region of the intermartensitic transition, the magnetization displays small kinks. For each field, magnetization changes at the intermartensitic transition are of opposite sign to magnetization changes at the martensitic transition. During heating, the magnetization changes in a single step associated with the reverse martensitic transition.

Calorimetric curves at selected values of the applied magnetic field for cooling and heating runs are shown in figure 5.37 (a). It is worth pointing out that while the peak associated with the martensitic transition is rather smooth on cooling, the intermartensitic transition shows a significant jerky character. This behaviour is in fact in agreement with the existence of kinks in the magnetization curves in the same temperature region. In magnetometry, only big changes of magnetization are detected while calorimetry is able to detect a larger number of jerks due to its high sensitivity to small magnetostructural changes. Note that the jerky character of the intermartensitic transition remains irrespective of the applied magnetic

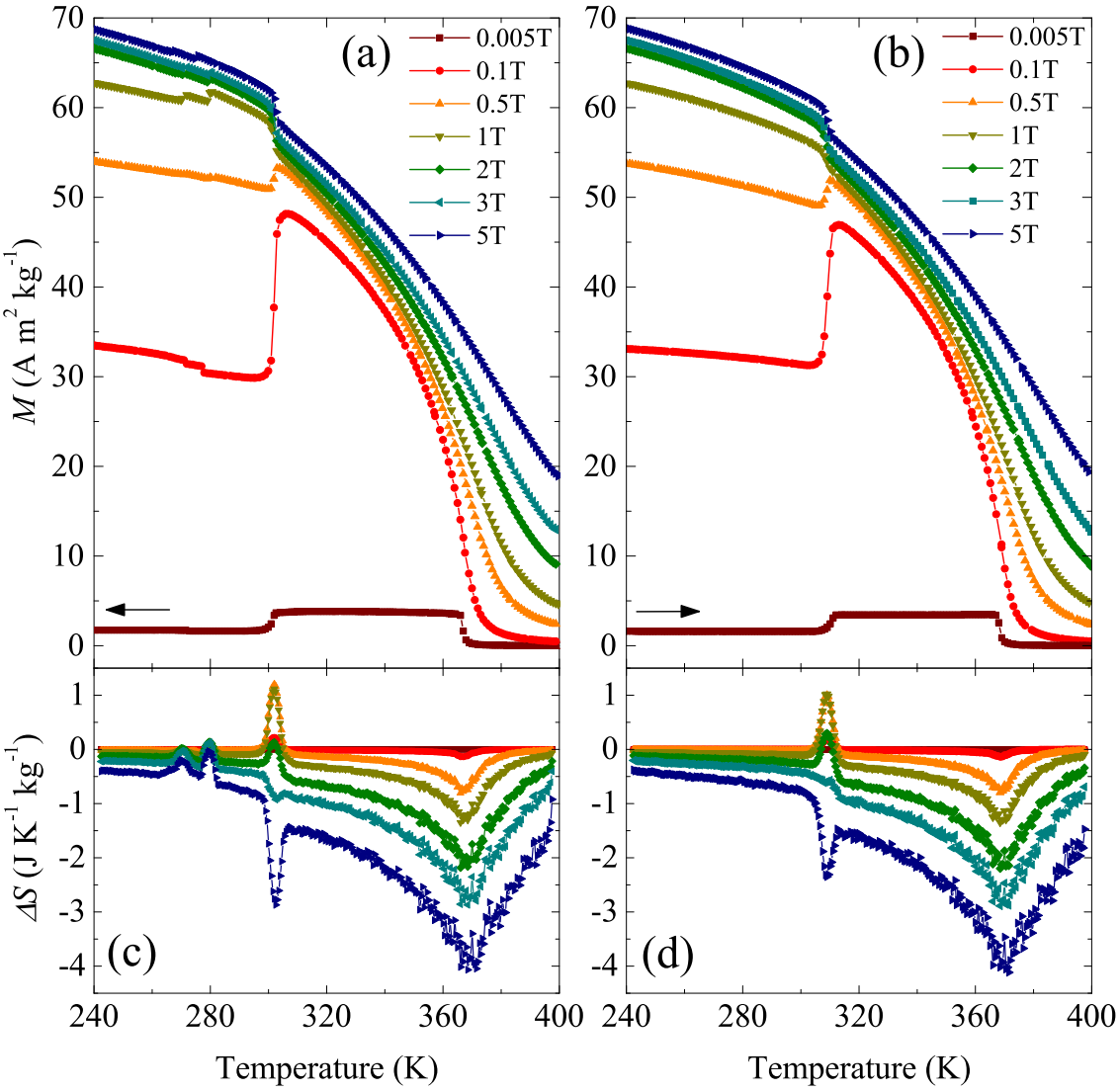


Fig. 5.36 Magnetization vs. temperature curves at selected values of the applied magnetic field measured during cooling (a) and heating runs (b). Field-induced entropy changes on cooling (c) and heating (d).

field. The calorimetric peak associated with the reverse transition also shows jerks which are superimposed to a large and smooth background. These jerks might occur due to the overlapping of both reverse martensitic and intermartensitic transitions.

Calorimetric and magnetization results reflect a weak dependence of both martensitic and intermartensitic transitions on the applied magnetic field. For low fields, the martensitic transition slightly shifts to lower temperatures while the intermartensitic transition has tendency to shift to higher temperatures. By increasing the field above 0.5 T, both transitions show a change of tendency; the martensitic transition shifts to higher temperatures while the intermartensitic moves in opposite sense. Actually, for the martensitic transition this is expected from the behaviour of the magnetization at the transition. For the intermartensitic transition it is also consistent with the corresponding behaviour of the magnetization. This last result is different from that reported in reference [169] where an increase of the intermartensitic transition temperature was reported in spite that no change of magnetization was detected at the intermartensitic transition. On heating, by increasing the field reverse martensitic and intermartensitic transitions tend to split as revealed by the small peak that grows at the end of the large calorimetric peak.

Integration of the calorimetric peaks yields to the entropy and enthalpy changes corresponding to the martensitic and intermartensitic transitions on cooling and to the reverse martensitic transition on heating. Results as a function of the applied magnetic field are shown in figure 5.37 (b) and (c). Within the errors, both enthalpy and entropy changes of martensitic and intermartensitic transitions are independent of the applied magnetic field. Figure 5.37 (b) and (c) also compares the sum of the martensitic and intermantensitic enthalpy and entropy changes with the corresponding changes of the reverse transition, in absolute values. Results show to a very good approximation that the entropy and enthalpy changes of the reverse transition which occurs, essentially, as a single step is the sum of the corresponding quantities associated with the martensitic and intermartensitic transitions.

In order to analyse in more detail the effect of an applied magnetic field on the relative phase stability of the parent and martensitic phases, we have determined the change of entropy as a function of temperature resulting from the isothermal application of a given magnetic field. This magnetic field induced entropy change is indirectly estimated from magnetization measurements shown in figure 5.36 (a) and (b) by means of the expression (5.6). Entropy changes as a function of temperature for selected values of the applied magnetic fields are shown in figures 5.36 (c) (cooling runs) and (d) (heating runs). Results show that isothermal application of a magnetic field leads to a large decrease of entropy in the region of the paramagnetic-ferromagnetic transition ($\sim$ 370 K). The peak is considerably broad as expected for a continuous transition. In the vicinity of the martensitic transition, the

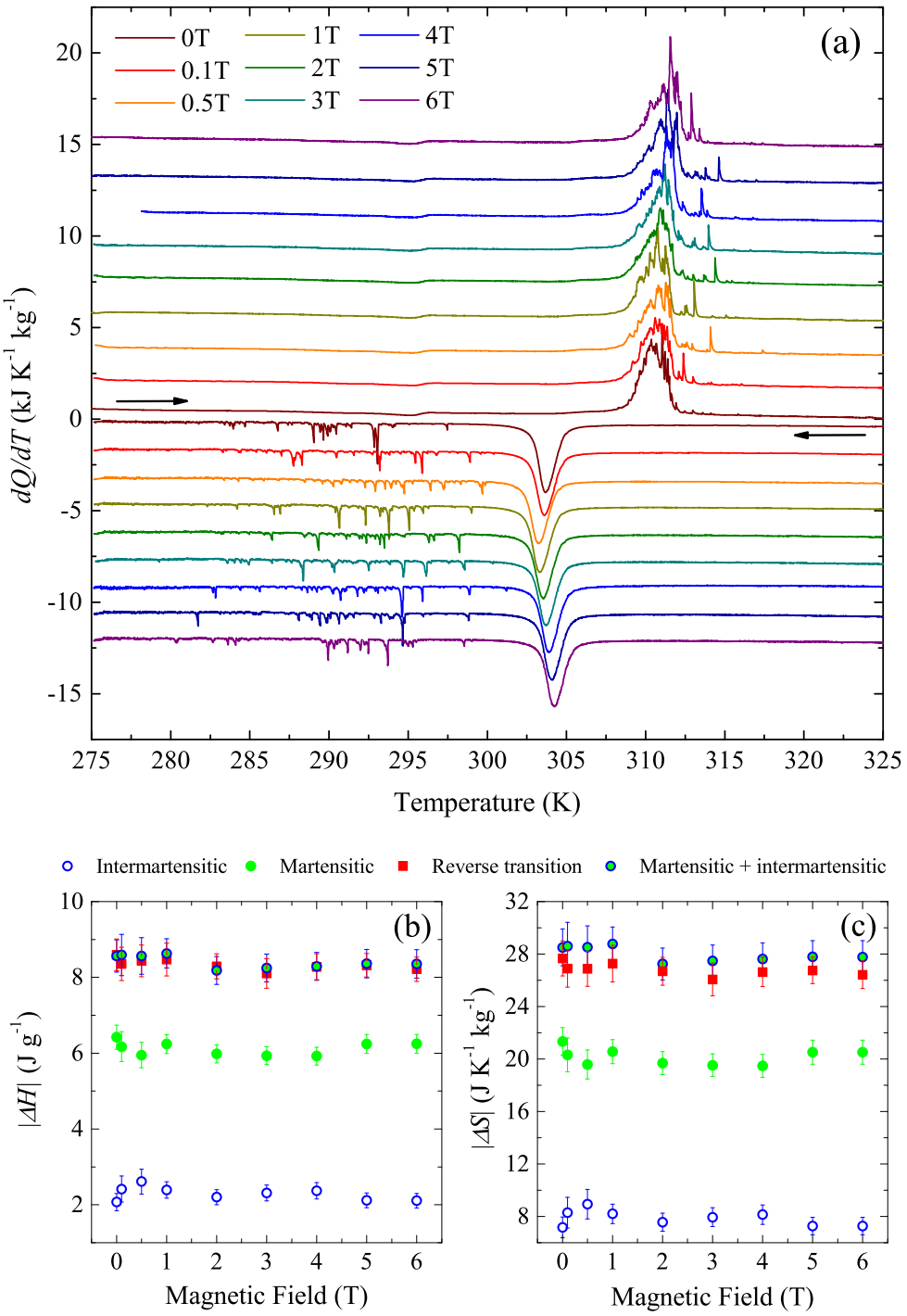


Fig. 5.37 (a) Calorimetric curves at selected values of the applied magnetic field (indicated in the figure). Enthalpy (b) and entropy changes (c) of the reverse, martensitic and intermartensitic transitions as a function of the applied magnetic field and sum of enthalpy (b) and entropy changes (c) of the intermartensitic and martensitic transitions.

entropy increases for low applied fields while it decreases for larger fields. The change from positive to negative values of the entropy change indicates that by increasing the field, the martensite first loses stability with respect to the parent phase but at larger fields it becomes more and more stable. The obtained behaviour is in agreement with the observed change of the transition temperature with an applied magnetic field. Therefore, the loss of stability at low fields must be caused by the larger magnetocrystalline anisotropy of the martensite that hinder the magnetization to reach its more favourable ferromagnetic order.

At the intermartensitic transition, the field induced entropy change has an opposite behaviour; it shows a tendency to decrease at low applied fields while it increases for larger fields. This means that application of a magnetic field reduces the relative stability of the lower temperature martensitic phase with respect to the intermediate martensite. We anticipate that this could be due to a reduction of the magnetocrystalline anisotropy and an increase of the magnetic moment taking place at the intermartensitic transition. It is worth to note that during heating this low temperature effect is not detected consistently with the fact that the reverse transition process occurs as a single step.

The significant jerky character of the intermartensitic transition together with the fact that reversion towards the parent phase occurs as a single step process might suggest that the mechanism behind the intermartensitic crossover is a detwinning process. There are however a number of features that indicate that the intermartensitic transition is an actual phase transition. First of all, the existence of a significant change of cell parameters (and cell volume) at the intermartensitic crossover between the intermediate and low temperature martensitic phases as confirmed from neutron diffraction patterns. Second, the fact that entropy and enthalpy changes of the reverse transition coincide with the sum of the absolute values of the corresponding quantities for martensitic and intermartensitic changes during the two-step forward process. Third, the fact that our measurements suggest a change of magnetocrystalline anisotropy and magnetic moment at the intermartensitic transition. These results, together with the detection of a partial jerky character of the reverse transition, confirm that both martensites revert simultaneouly towards the parent phase in a single step. This is a consequence of the fact that the hysteresis associated with the intermartensitic transition is larger than the hysteresis associated with the parent martensitic transition. Finally, the fact that, in spite of being weak, both martensitic and intermartensitic transitions shift non monotonously under an applied magnetic field is consistent with the behaviour of magnetization and entropy changes at both martensitic and intermartensitic transitions. Actually, this behaviour is in agreement with Clausius-Clapeyron equation for first-order phase transitions.

In summary, the results presented in this section confirm that in Ni-Mn-Ga a single intermartensitic transition occurs for the range of compositions with $e/a$ close to the value ($e/a \simeq 7.6$) where martensitic and premartensitic lines meet one each other. The intermartensitic transition takes place from a commensurate 7M phase to an incommensurate 5M structure. From a kinetic point of view, it is interesting to point out that the intermartensitic transition extends over a relatively large temperature range and shows a significant jerky character which could be a consequence of the need of overcoming high energy barriers in order to reach the lowest energy ground state structure.

## 5.8 Summary & conclusions

In the present chapter we have presented the study on the giant MCE and BCE arising in the vicinity of the first-order martensitic transition in Ni-Mn based alloys. The temperature at which this transition takes place and the magnetostructural properties of the martensite and austenite phases are highly dependent on the valence electron concentration $e/a$ and can be modified by slight variations in the alloy composition. Accordingly, these caloric phenomena have been analysed in a series of Ni-Mn based Heusler alloys with tailored magnetostructural properties by tuning the composition of the alloys. In the studied samples, the austenite phase has larger volume in comparison to the martensite phase, and typically shows ferromagnetic order. Consequently, the MCE and BCE are found to be inverse and conventional, respectively.

It has been shown that direct calorimetric measurements of the MCE are a great tool for the characterization of its reproducibility upon field cycling. The reported results indicate that the reproducible region arises for fields that are strong enough to shift the transition temperature so that the thermal hysteresis loop at zero field and the loop at applied field do not overlap. Hence, for an inverse effect the reversible region is bounded by the temperatures $M_s(H=0)$ and $A_s(H)$, and for a conventional effect it is bounded by $A_s(0)$ and $M_s(H)$. In relation to this, a good estimation of the reversibility of the caloric effect can also be obtained from the quasi-direct method by analysing the overlap of the $|\Delta S|$ vs. $T$ curves obtained upon heating and cooling. Therefore, the reproducibility of the MCE and the BCE has been accurately characterized by either direct or quasi-direct methods.

In view of a better reproducibility of the caloric effect, the minimization of the hysteresis associated with the martensitic transition is highly convenient. As demonstrated in section 5.3, this is achieved when the martensite and the austenite phases display geometrical compatibility and the cofactor conditions described in section 5.1.1 are met. Nonetheless, good reproducibility can also be found in materials displaying particularly large sensitivity of the transition temperature to the applied field and the effect of an unfavourable hysteresis can be overcome, as shown in the study of Ni-Co-Mn-Ga-In samples in section 5.5.

The caloric performance can be parametrized as a function of the relative distance between the martensitic transition and the Curie point of the austenite $\frac{T_C - T_M}{T_C}$. As far as this parameter increases in positive values ($T_M < T_C$), the austenite phase becomes more magnetic and the value of $\Delta M_t$ increases. Consequently, the magnetic contribution which takes part to the total transition entropy change $\Delta S_t$ significantly increases. In comparison to the other entropic contributions, this contribution has opposite sign and its enlargement yields to a reduction of the overall $\Delta S_t$ value. These conditions prompt a larger magnetic

field sensitivity of the transition temperature and lower upper bounds of the MCE entropy change due to the reduction in $\Delta S_t$ (see figure 5.12). In contrast, the materials have been reported to display a better BCE performance as $T_M > T_C$.

It is worth noticing that the opposite trends of the MCE and the BCE might lead to a poor multicaloric performance under the influence of hydrostatic pressure and magnetic field. However, the situation might change by choosing the mechanical force which best tailors the symmetries of the shear distortion associated with the martensitic transition. In this sense, this family of materials have been reported to perform large elastocaloric responses and strong sensitivity of the transition temperature with respect to uniaxial stresses [92, 103, 170]. Therefore, it is expected that these materials display an optimized multicaloric performance under the influence of uniaxial stress and magnetic field. In this regard, figure 5.38 displays preliminary calorimetric results on a $Ni_{49.0}Mn_{33.8}In_{15.0}Cu_{2.2}$ sample, with sensitivity values $\frac{dT}{d\mu_0 H}$ = -3 K $T^{-1}$ and $\frac{dT}{d\sigma}$ = -0.08 K $MPa^{-1}$ [as evidenced by the slopes in each direction of each plane illustrated in the phase diagram of panel (a)], $\Delta S_t = 26$ J $K^{-1}$ $kg^{-1}$, and thermal hysteresis of $\sim$ 7 K. The peaks of the thermograms at constant compressive stress $\sigma$ = -2 MPa shown in panel (b) are indicative of the magnetocaloric response. In this connection, panel (c) illustrates the large magnetic field driven strain ($\Delta\varepsilon \sim 1$ %) which is associated with the caloric effect and confirms the strong cross-response at the magnetostructural transition.

In section 5.6, a successful strategy for the expansion of the magnetocaloric operation range is described. In particular, a composite material consisting of fragments with gradual changes in composition has been built. In this regard, the martensitic transition temperature has been conveniently shifted towards different values in each fragment so that the magnetocaloric response is exhibited at different portions of the composite as a function of the temperature interval at which the field is applied. This results in large reproducible entropy changes of $\sim$ 7.5 J $K^{-1}$ $kg^{-1}$ upon cycling a 6 T magnetic field over an expanded temperature span of $\sim$ 30 K.

Finally, it has been shown that the developed calorimetric techniques together with magnetometric measurements have been useful for the thermodynamic study on the nature of the intermartensitic transition in Ni-Mn-Ga given in section 5.7. Our results point to the fact that these phenomena occur through first-order martensitic transitions instead of detwinning processes of nano-twinned structures.

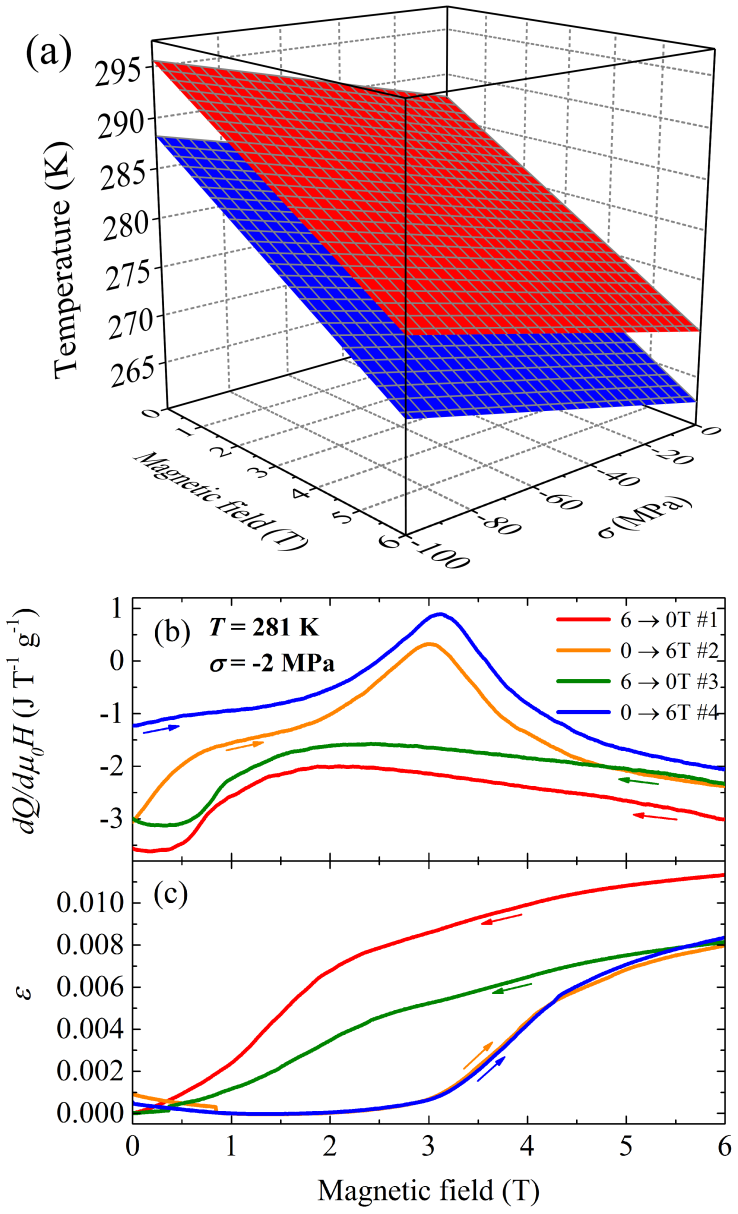


Fig. 5.38 Features of the magnetostructural first-order transition at $Ni_{49.0}Mn_{33.8}In_{15.0}Cu_{2.2}$ magnetic shape memory alloy analysed by the setup described in 3.3 which allows simultaneous calorimetric and dilatometric measurements. (a) Transition temperature upon heating (red plane) and cooling (blue plane) as a function of the applied compressive uniaxial stress and magnetic field. (b) Isothermal calorimetric curves at $\sigma$ = - 2 MPa obtained upon magnetic field cycling. (c) The corresponding behaviour of the field-induced strain at each magnetic field scan. The red, orange, green, and blue lines in (c) and (d) panels refer to data obtained at the first (6 T→ 0), second (0→ 6 T), third (6 T→ 0), and fourth (0→ 6 T) magnetic field scans, respectively.

# Chapter 6

# Giant caloric effects in $BaTiO_3$

## 6.1 Overview on perovskites and $BaTiO_3$

By virtue of its ferroelectric order at room temperature and the simplicity of its perovskite structure, $BaTiO_3$ has been widely investigated over the last decades and is employed for a large list of applications of multiple kinds. The ferroelectric properties of $BaTiO_3$ and other perovskite oxides were first reported in the 40s, in a decade in which the discovery of ferroelectricity and piezoelectricity in ceramic materials was strongly influeced by the World War II and the associated interest in exploring new functional materials [171]. This discovery signified a deep boost on the research and the physical understanding of ferroelectricity, which had been studied since then in hydrogen-bonded materials, Rochelle salt, and KDP [172]. After that, the family of perovskite oxides from which $BaTiO_3$ takes part became of particular interest. Nowadays, it has found a broad list of applications including capacitors and multilayer capacitors, sensors, ferroelectric substrates, transducers, actuators, energy storage devices, and memories [173–175].

The general formula of perovskite-type structures is $ABO_3$ and its representative compound is $CaTiO_3$ which is the material that gives the name to the whole family. In general, A and B are two cations of very different size (A is bigger than B) and O is the anion, usually oxygen, that bonds the structure. The ideal face-centered cubic structure with space group $Pm3m$ of perovskite oxides is illustrated in figure 6.1 (left image), which refers to the high temperature paraelectric phase of $BaTiO_3$. *A* atoms (Ba) are at the corners, a *B* atom (Ti) is at the center position and oxygen atoms lie on each face center. B cations ($Ti^{2-}$) are coordinated with 6 anions ($O^{2-}$) and form an octahedra in which *B* cations are settled at the center of the body and each anion at each corner.

Goldschmidt (1926) analysed the stability of the perovskite-type structures, which depends on the nature of the octahedra formed by the B cations and the oxygen anions. It is

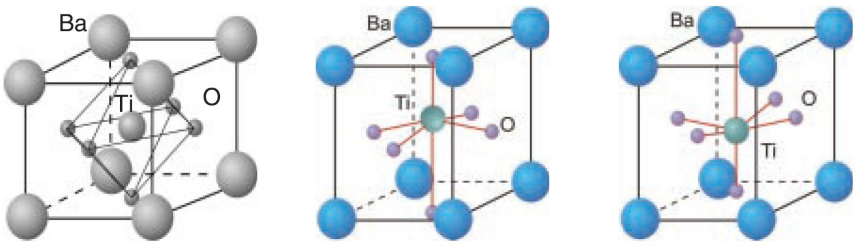


Fig. 6.1 Illustration of the $BaTiO_3$ crystallographic structures at the high temperature paraelectric phase (left figure) and at the room temperature ferroelectric phase (middle and right figures) with its too variants of polarization, from [176]. A $Ti^{4+}$ ion is settled in the body center of the cubic cell, $Ba^{2+}$ ions are at the corners and $O^{2-}$ at the face centers. The spontaneous polarization points upwards at the middle figure and downward at the right figure.

stated that each cation is surrounded by the maximum number of anions which can touch it and all the anions must be in contact with the cations. The distance between them is directly the sum of their ionic radii. The A atoms must fit the holes between the octahedra. With this in hand, ideally [172]:

$$r_A + r_O = \sqrt{2}(r_B + r_O) \tag{6.1}$$

where $r_A$, $r_B$, $r_O$ are the atomic radii of the A, B cations and the oxygen atom.

A tolerance factor $t$ is defined as the ratio between these distances:

$$t = \frac{r_A + r_O}{\sqrt{2}(r_B + r_O)} \tag{6.2}$$

The value of $t$ can slightly vary from $t = 1$. We can distinguish the following situations as a function of the value of $t$:

- $t = 1$. The ideal cubic perovskite structure is formed.
- $t > 1$. The B cation is too small to fit at the center of the octahedra. A displacement of this atom can be favoured and, thus, giving rise to a net polarization per unit cell.
- $t < 1$. The A cation is too small and each atom cannot properly bond its 12 neighbouring oxygen anions. For values slightly lower than 1, the octahedra can present rotations and tilting. For smaller values, the compound presents a strongly distorted structure.

One of the key points of perovskite oxides is the versatility of their properties due to the strong sensitivity in displaying slight structural deviations from the cubic structure, the

adaptability of this structure with a broad list of atoms and its accommodation to atomic substitutions. For instance, the density of electronic configurations at similar energies presented by the perovskite structure can favour the emergence of Jahn-Teller distortions at the octahedra [177]. Hence, this family of materials have a strong trend to exhibit a list of phases which are variations of the cubic structure (tetragonal, orthorhombic or rhombohedral). The structural richness of this family of materials and the corresponding phase transitions among them favours a multiplicity of electric and magnetic properties with the corresponding functional and multifunctional potentialities.

As previously mentioned, $BaTiO_3$ displays a high temperature paraelectric phase of cubic (C) structure ($Pm3m$) Upon cooling, the system exhibits a first-order displacive transition at $\sim 400$ K in which $Ba^{2+}$ and $Ti^{4+}$ ions experience a relative displacement in reference to the $O^{2-}$ ions due to their freedom of mobility ($t > 1$) and a tetragonal (T) structure ($P4mm$) is formed with spontaneous polarization ($P_S$) along the $c$ axis $< 100 >$ [16, 18], as sketched in figure 6.1. This phase is stable at room temperature and transforms to the orthorhombic (O) ferroelectric phase ($Amm2$) at $\sim 280$ K. In this case, the spontaneous polarization is aligned along the $< 110 >$ direction. Finally, a transition occurs at $\sim 200$ K to a ferroelectric rhombohedral phase ($R3m$) in which $P_S$ points along the $< 111 >$ direction. Each transition can be illustrated in terms of the small relative displacement of the Ti ions with respect to the oxygen octahedra which determines the polar axis direction when compared with the paraelectric cubic reference structure [172]. In addition to the dielectric changes, each transition is accompanied by a macroscopic strain and volume change. Figure 6.2 plots representative parameters of the structural features and phase transitions in $BaTiO_3$. Panels (a) and (b) display the lattice parameters and the unit cell volume of the $BaTiO_3$ ceramic sample under study in section 6.4. Panels (c) and (d) display the dielectric constant and the spontaneous polarization reported for the single domain crystal studied in [17].

## 6.2 Motivation

In view of the caloric effects, especial interest must be paid to the ferroelectric and structural changes at the first-order phase transitions in $BaTiO_3$ which prompt this perovskite oxide to exhibit a remarkable sensitivity of the transitions to applied electric fields and hydrostatic pressures [178, 179]. This sensitivity together with the latent heat are proper ingredients for a large electrocaloric and barocaloric response.

The magnetocaloric effect usually requires large changes in magnetic field for driving the giant changes in $\Delta T$ and $\Delta S$, which are challenging to generate economically. In contrast, it is straightforward to generate changes in electric field $\Delta E$ in order to drive electrocaloric

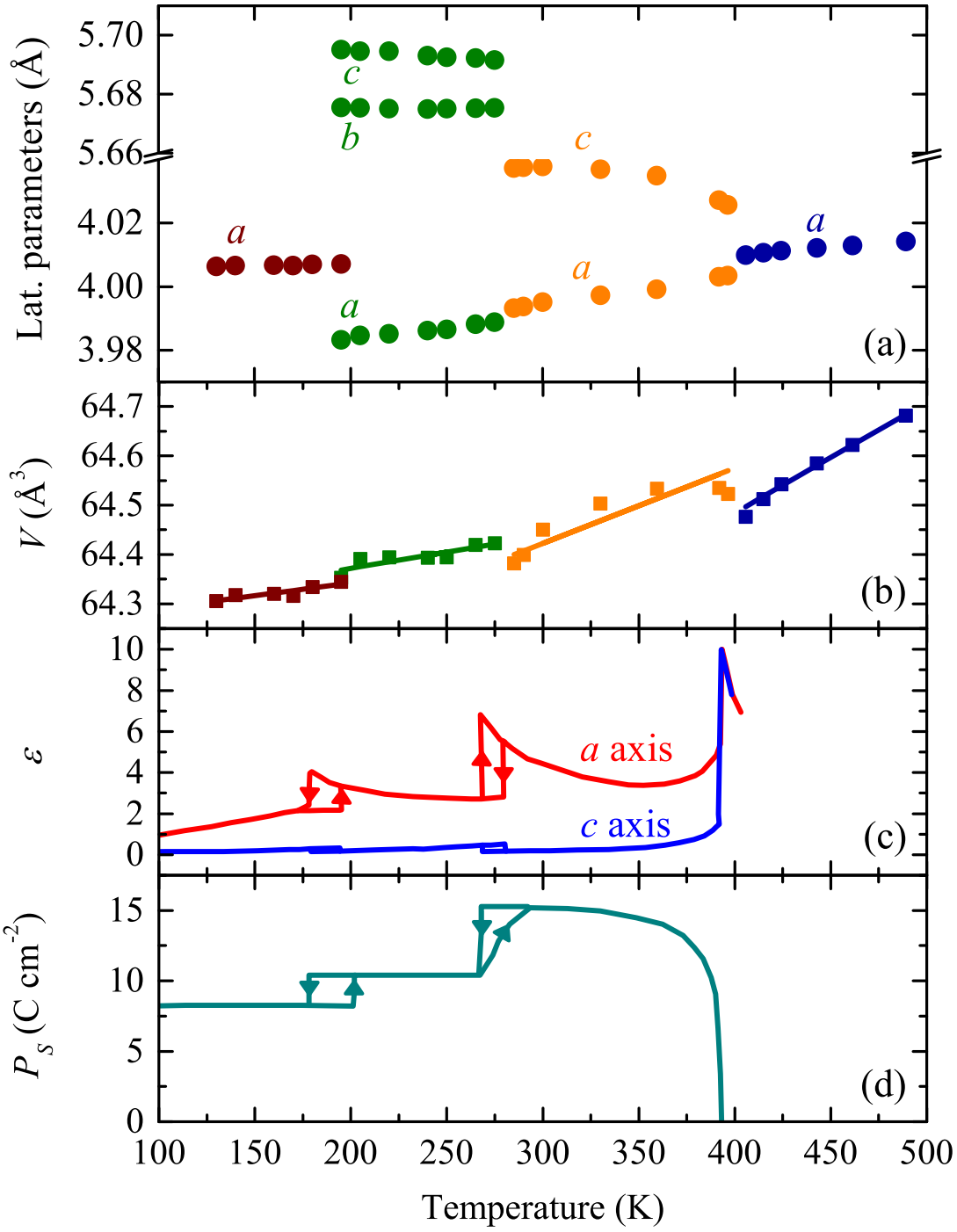


Fig. 6.2 Temperature dependence of lattice parameters (a) and unit cell volume (b) across the structural phase transitions in the $BaTiO_3$ ceramic sample from which the BCE has been studied in section 6.4. Data have been obtained from x-ray diffraction on heating at atmospheric pressure. Wine, green, orange, and dark blue symbols correspond, from left to right with respect to the temperature axis, to the rombohedral, orthorombic, tetragonal, and cubic, respectively. (c) and (d) panels display the dielectric constant ($\varepsilon$) and the spontaneous polarization ($P_S$) values, after [17].

effects near ferroelectric phase transitions. Recently, giant EC effects near nominally second-order transitions have been reported in ferroelectric thin films [3, 180], as thin films can support large driving. However, two issues arise as follows. Firstly, measurements of heat $Q$ and temperature change $\Delta T$ are typically indirect [3, 180] as the direct measurement of films is challenging. There is thus scope for error (e.g., because the possible role of thermal and electrical hysteresis is typically ignored). Secondly, the EC effects in films are disproportionately small with respect to the large driving fields, and so EC strengths $\frac{|Q|}{|\Delta E|}$ and $\frac{|\Delta T|}{|\Delta E|}$ tend to be relatively small. In section 6.3 we address both of these issues by presenting direct measurements of both Q and $\Delta T$ in single-crystal $BaTiO_3$ near the paraelectric-ferroelectric phase transition at Curie temperature $T_C$. We find EC strengths $\frac{|Q|}{|\Delta E|}$ and $\frac{|\Delta T|}{|\Delta E|}$ that are giant because the first-order ferroelectric phase transition is very sharp. The observed EC effects are reversible at any temperature above the hysteretic transition regime. Giant EC strengths near sharp first-order phase transitions with a large latent heat could therefore contribute to the future development of cooling devices with a high frequency of operation.

EC materials are good candidates for solid-state barocaloric (BC) [1, 181, 182] cooling because ferroelectric phase transitions exploited in EC effects are typically accompanied by significant changes in volume [183–185]. In fact, these are the particular conditions depicted in figure 6.2, which show that each phase transition in $BaTiO_3$ is accompanied by a unit cell volume change, in addition to the change in dielectric properties. In ferroelectric materials large BC effects in $BaTiO_3$ and $PbTiO_3$ have recently been predicted [186, 187] and experimentally demonstrated in ferrielectric ammonium sulphate [182]. Moreover, it is easier to exploit ferroelectric materials for BC cooling than EC cooling, as there is no need to fabricate multilayer capacitor devices for electrical access to films and the range of operating temperatures is not compromised by the need to avoid breakdown [1, 181, 188].

In the following sections the ECE and BCE in $BaTiO_3$ are presented. A comparison between direct, quasi-direct and indirect methods account for a complete caloric description in each case. The work presented in this chapter has been carried out in collaboration with the Department of Materials Science & Metallurgy of the University of Cambridge (Device Materials group), and with the Department of Physics and Nuclear Engineering of the Universitat Politècnica de Catalunya (UPC).

## 6.3 The electrocaloric effect in $BaTiO_3$

### 6.3.1 Experimental details

Platinum electrodes were sputtered on opposite sides of two $BaTiO_3$ single crystals (4 mm $\times$ 4 mm $\times$ 0.5 mm) purchased from Crystal GmbH. The relative permittivity $\varepsilon_r$ was measured at 100 Hz using an Agilent 4294A Precision Impedance Analyzer. The ferroelectric polarization $P$ was measured at 1 Hz using a Precision Premier II Radiant tester, equipped with a 4 kV amplifier.

In zero electric field, measurements of heat flow were performed using a commercial TA Q2000 differential scanning calorimeter (DSC). Calorimetric measurements under applied electric were performed by means of the calorimeter described in section 3.2, which allows both isothermal and isofield measurements. Electric field and temperature scans where performed at rates 0.024 kV cm$^{-1}$ s$^{-1}$ and 0.5 K min$^{-1}$, respectively. For the isothermal procedure at which electric field is swept, the sample was previously heated up to a temperature well above the first-order transition regime (420 K) and then cooled down to the desired measurement temperature, as indicated by the protocol described in section 3.1.1. In each case, the enthalpy and entropy change values, as well as the quasi-direct and direct computation of the electrocaloric effect have been performed by following the procedures described in section 3.1.1.

Zero field heat capacity, obtained using the TA Q2000 DSC, was measured on cooling using the modulated differential scanning calorimetry mode (see section 3.8 for further details) with the constant-temperature method. The temperature modulation was 0.3 K. The temperature decrement was 1 K away from the transition, and 0.7 K near the transition.

Direct measurements of EC temperature change $\Delta T$ were made, as described in reference [189], using a thin 0.1 mm-diameter Ni-Cr/Ni-Al K-type thermocouple that was connected to one of the sample electrodes using silver dag. The procedure was to cool from 440 K to each measurement temperature, stabilize for 15 min, apply the electric field, wait $\sim$ 60 s for the initial temperature to be recovered, and remove the electric field.

### 6.3.2 Results and discussion

Measurements of electrocaloric heat and temperature change were performed on two different samples of $BaTiO_3$, as extensive thermal and electrical cycling eventually led to electrical and mechanical breakdown. We measured the zero-field transition in sample 1 (figure 6.3), $Q$ in sample 2 (figure 6.5), and $\Delta T$ in sample 1 (figure 6.6). Measurements of relative permittivity $\varepsilon_r$ in sample 1 [figure 6.3 (a)] show that the paraelectric(PE)–ferroelectric(FE) transition

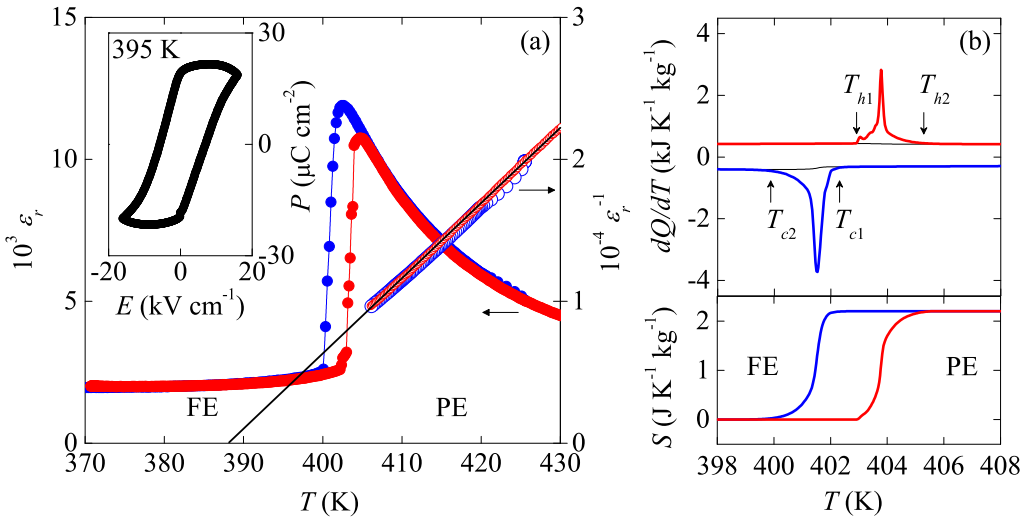


Fig. 6.3 Ferroelectric transition in $BaTiO_3$ near $T_C$ . Data for sample 1. a) Relative permittivity $\varepsilon_r$ versus temperature $T$ on cooling (blue) and heating (red). A linear fit to the inverse permittivity data above $T_C \sim 402$ K is also shown (black line). Inset, $P(E)$ measured just below $T_C$. The small high field reduction is attributed to electrical conductivity at the high measurement temperature. b) Top panel, heat flow $dQ/dT$ on cooling (blue) and heating (red) across the transition. Baselines are black, $dQ/dT > 0$ is endothermic. Bottom panel, the resulting entropy change $\Delta S$ versus $T$.

centred at $T_C \sim 402$ K is sharp, with a small thermal hysteresis of $\sim 2$ K. Measurements of heat flow $\dfrac{dQ}{dT}$ in sample 1 (figure 6.3 (b), top panel) confirm these features, and permit accurate determination of transition start and finish temperatures on cooling ( $T_{c1} = 402.3$ K, $T_{c2} = 399.9$ K) and heating ( $T_{h1} = 402.9$ K, $T_{h2} = 405.3$ K). The bottom panel in figure 6.3 (b) illustrates the entropy curves $S(T)$ obtained from integration of the thermograms, with $|\Delta S_t| = 2.2 \pm 0.2$ J K$^{-1}$ kg$^{-1}$ for the full transition. We also integrated $\dfrac{dQ}{dT}$ to calculate the latent heat $|\Delta H_t| = 890 \pm 90$ J kg$^{-1}$. These values are in good agreement with experimental literature values [190] of $|\Delta H_t| \sim 900$ J kg$^{-1}$ and $|\Delta S_t| \sim 2.4$ J K$^{-1}$ kg$^{-1}$, and values estimated from a Landau-Devonshire approach [191] of $|\Delta H_t| = T_C a \dfrac{{P_0}^2}{2\rho} \sim 880$ J kg$^{-1}$ and $|\Delta S_t| = \dfrac{|\Delta H_t|}{T_C} \sim |\Delta S_t| = 2.2$ J K$^{-1}$ kg$^{-1}$ (where density [183] $\rho = 6008$ kg m$^{-3}$, saturation polarization $P_0 \sim 21\ \mu$ C cm$^{-2}$ [figure 6.3 (a), inset] and $a = \dfrac{d(\varepsilon_r^{-1})}{\varepsilon_0 dT} = 0.6$ MV mC$^{-1}$ K$^{-1}$ [figure 6.3 (a)] agree with literature values [192, 193]).

Sample 2 was held isothermally near $T_C$, and measurements of heat flow $dQ/dE$ on sweeping $E$ from 0 to 4 kV cm$^{-1}$ (figure 6.5 (a), inset) were integrated to yield peak values of $|Q| \sim 835$ J kg$^{-1}$ and $|\Delta S| \sim 2.1$ J K$^{-1}$ kg$^{-1}$ (figure 6.5 (a)). We confirmed that these

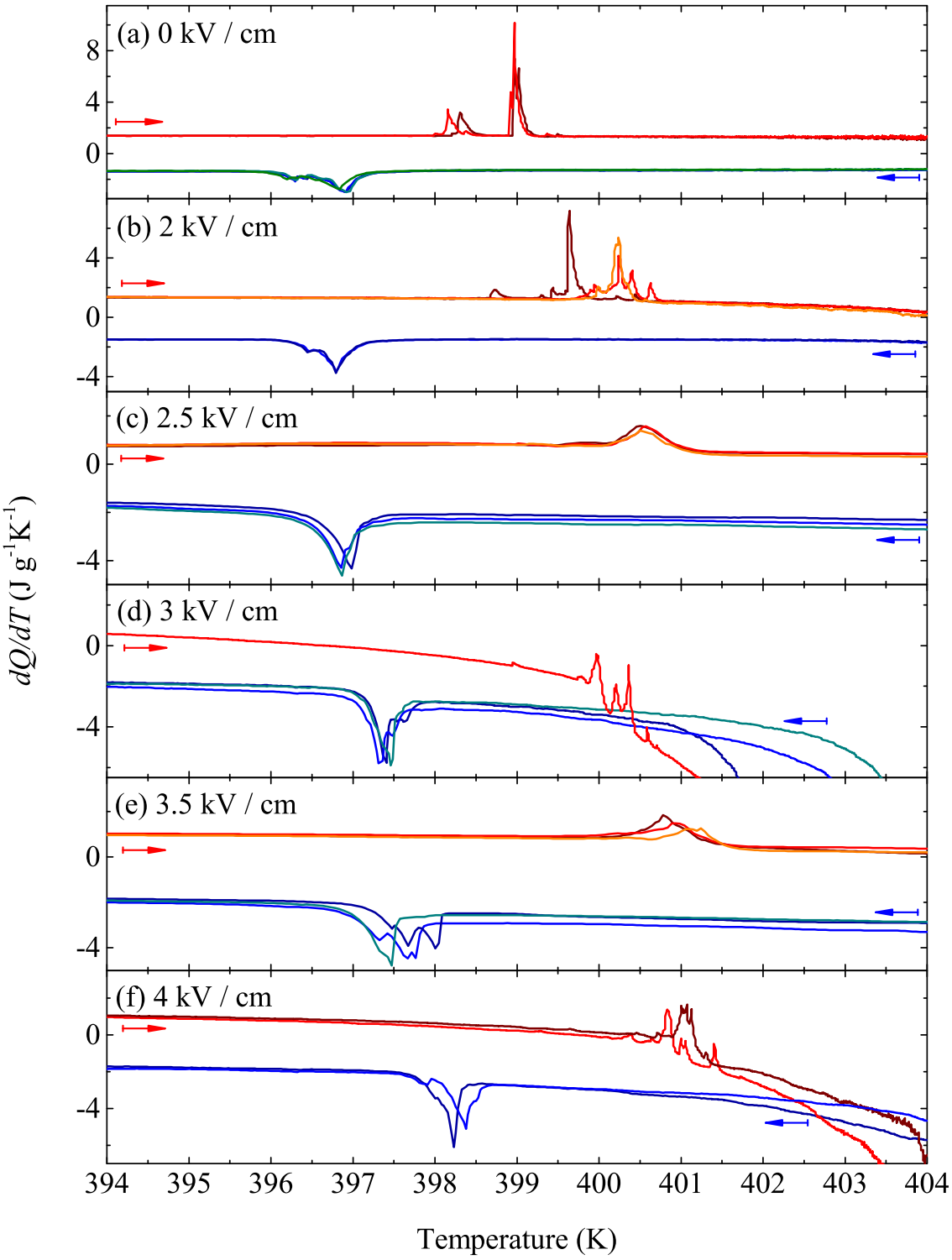


Fig. 6.4 Set of DSC runs obtained upon heating (red lines) and cooling (blue lines) at each value of the applied electric field: 0 kV/cm (a), 2 kV/cm (b), 2.5 kV/cm (c), 3 kV/cm (d), 3.5 kV/cm (e), 4 kV/cm (f).

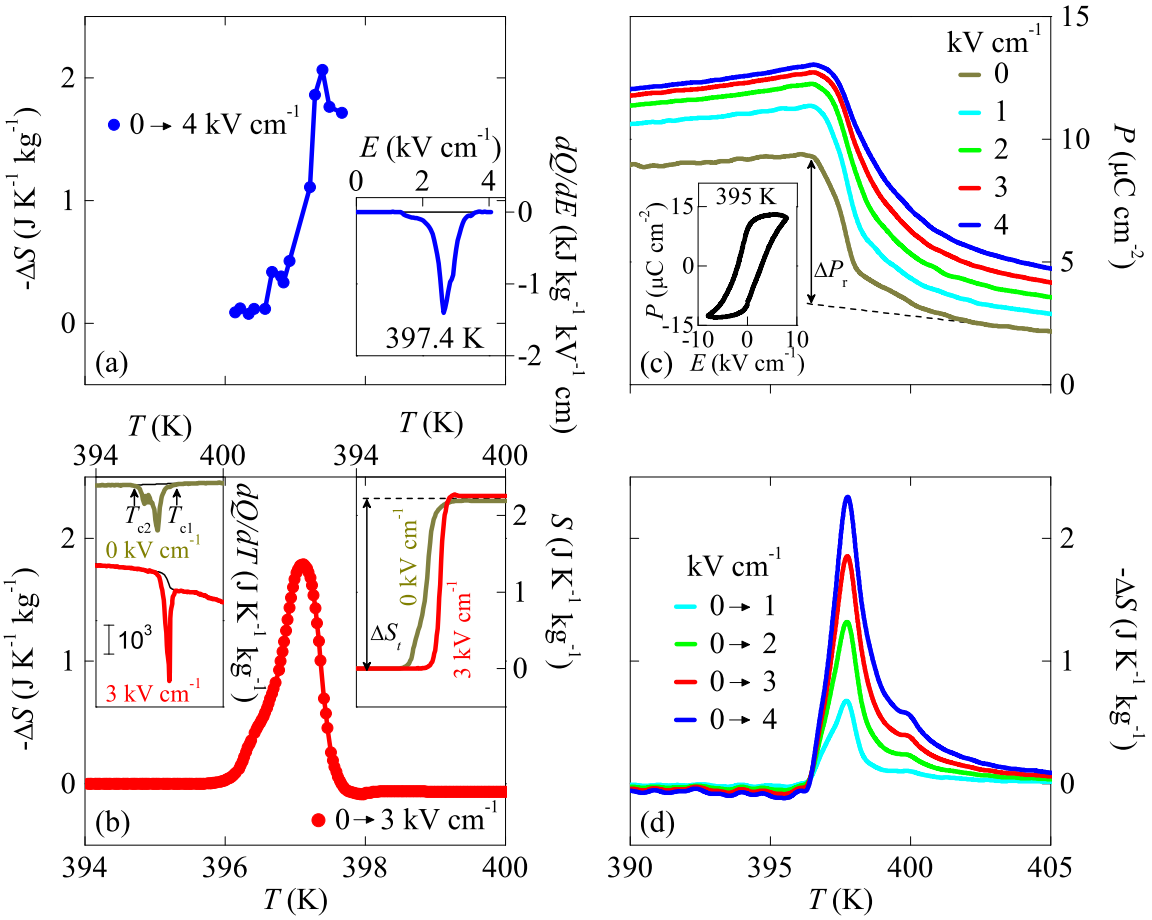


Fig. 6.5 Electrically driven heat and electrically driven entropy changes near $T_C$. Data for sample 2. (a) Direct measurements. EC entropy change $\Delta S$ on applying electric field $E = 4$ kV cm$^{-1}$ at successively lower temperatures, determined via direct measurements of heat flow $dQ/dE$. Inset: one such measurement yielding peak entropy change (baseline is black). (b) Quasi-direct measurements. EC entropy change $\Delta S$ on applying electric field $E = 3$ kV cm$^{-1}$ at selected temperatures, determined via measurements of heat flow $\frac{dQ}{dT}$ with and without an electric field. Left inset: data measured on cooling in 0 and 3 kV cm$^{-1}$ (data displaced vertically for clarity, baselines are black, $T_{c1} = 397.8$ K, $T_{c2} = 395.8$ K). Right inset: the resulting plots of $S(T)$ on cooling in each field, whose difference yields the plot in the main panel. (c) Polarization $P$ versus $T$ at selected $E$, as determined from measurements of $P(E)$ every $\sim 0.2$ K on cooling. Inset: one such $P(E)$ measurement. The change in remanent polarization $\Delta P_r \sim 6\mu$ C cm$^{-2}$ was evaluated after correcting for the background slope at $E = 0$ (dashed line). (d) The resulting EC entropy change $\Delta S$ on applying selected electric fields, as a function of temperature, determined via the indirect method.

values correspond roughly to the full transition in sample 2, as we obtained similar values of $|\Delta H_t| = 870 \pm 80$ J kg$^{-1}$ and $|\Delta S_t| = 2.2 \pm 0.2$ J K$^{-1}$ kg$^{-1}$ by integrating the zero-field calorimetry data (figure 6.5 (b), left inset).

By holding sample 2 at first 0 kV cm$^{-1}$ and then 3 kV cm$^{-1}$ , measurements of heat flow $\frac{dQ}{dT}$ on cooling (figure 6.5 (b), left inset) are integrated to yield $S(T)$ at 0 and 3 kV cm$^{-1}$ (figure 6.5 (b), right inset). The difference $|\Delta S(T, 3\text{kV cm}^{-1}) - \Delta S(T, 0\text{kV cm}^{-1})|$ peaks at $\sim 1.8$ J K$^{-1}$ kg$^{-1}$ [figure 6.5 (b)], and is similar to the data obtained by sweeping the field to 4 kV cm$^{-1}$ [figure 6.5 (a)]. (Note that 3 kV cm$^{-1}$ and 4 kV cm$^{-1}$ are comparable here, as 3 kV cm$^{-1}$ almost fully drives the transition (figure 6.5 (a), inset), and shifts the peak to a similar temperature [figure 6.5 (a,b)]. The two $\Delta S(T)$ plots (figure 6.5 (b), right inset) show an irregular field-driven shift in the transition $\frac{dT_t}{dE} \leq 0.33$K cm$^{-1}$, which is in order-of-magnitude agreement with the Clausius–Clapeyron value of $\frac{dT_t}{dE} = -\frac{\Delta P_t}{\rho \Delta S_t} \sim 0.45 \pm 0.4$ K cm kV$^{-1}$ (where $\Delta S_t = 2.2 \pm 0.2$ J K$^{-1}$ kg$^{-1}$ from above, and $\Delta P_t \sim \Delta P_r \sim 6\mu$ C cm$^{-2}$ [figure 6.5 (c)]).

The plots of $\Delta S(T)$, obtained via direct measurements [figure 6.5 (a)] and quasi-direct measurements (figure 6.5 (b)], were consistent with results obtained using the well-known indirect method [3, 180] to analyse ferroelectric polarization $P$ measurements of sample 2. By transforming the upper branches ($E > 0$) of isothermal $P(E)$ loops [e.g., figure 6.5 (c), inset] to yield plots of $P(T)$ [figure 6.5 (c)], we obtained, using the Maxwell relation $\left(\frac{\partial S}{\partial E}\right)_T = \left(\frac{\partial P}{\partial T}\right)_E$, a plot of $\Delta S(T) = \rho^{-1} \int_0^E \left(\frac{\partial P}{\partial T}\right)_{E'} dE'$ [figure 6.5 (d)]. The observed equivalence between direct [Figure 6.5 (a,b)] and indirect [figure 6.5 (d)] measurements demonstrates that the indirect method is reliable despite the significant field hysteresis [figure 6.5 (c), inset]. However, the indirect method is only reliable because we selected the correct $P(E)$ branches for analysis (i.e. the branches in which the ferroelectric-domain configurations are not dramatically modified). By contrast, using the lower branches ($E > 0$) results in the erroneous prediction of entropy changes that are $\sim 50$ % smaller.

Direct measurements of adiabatic EC temperature change in sample 1 were irreversible below $T_{h2} = 405.3$ K (figure 6.6 (a)], and reversible above $T_{h2}$ (Figure 3 b). Joule heating was negligible up to a maximum field of 12 kV cm$^{-1}$, as the initial temperature could be recovered with the field on [figure 6.6 (a,b)]. Measurements of $|\Delta T|$ as a function of starting temperature show a peak [figure 6.6 (c)] that shifts to higher temperatures when fields of increasing magnitude are applied, but there is no corresponding shift when these fields are subsequently removed, due to the observed hysteresis. These irreversible and reversible scenarios are indicated on a schematic $T - E$ phase diagram [figure 6.6 (d)], where all four

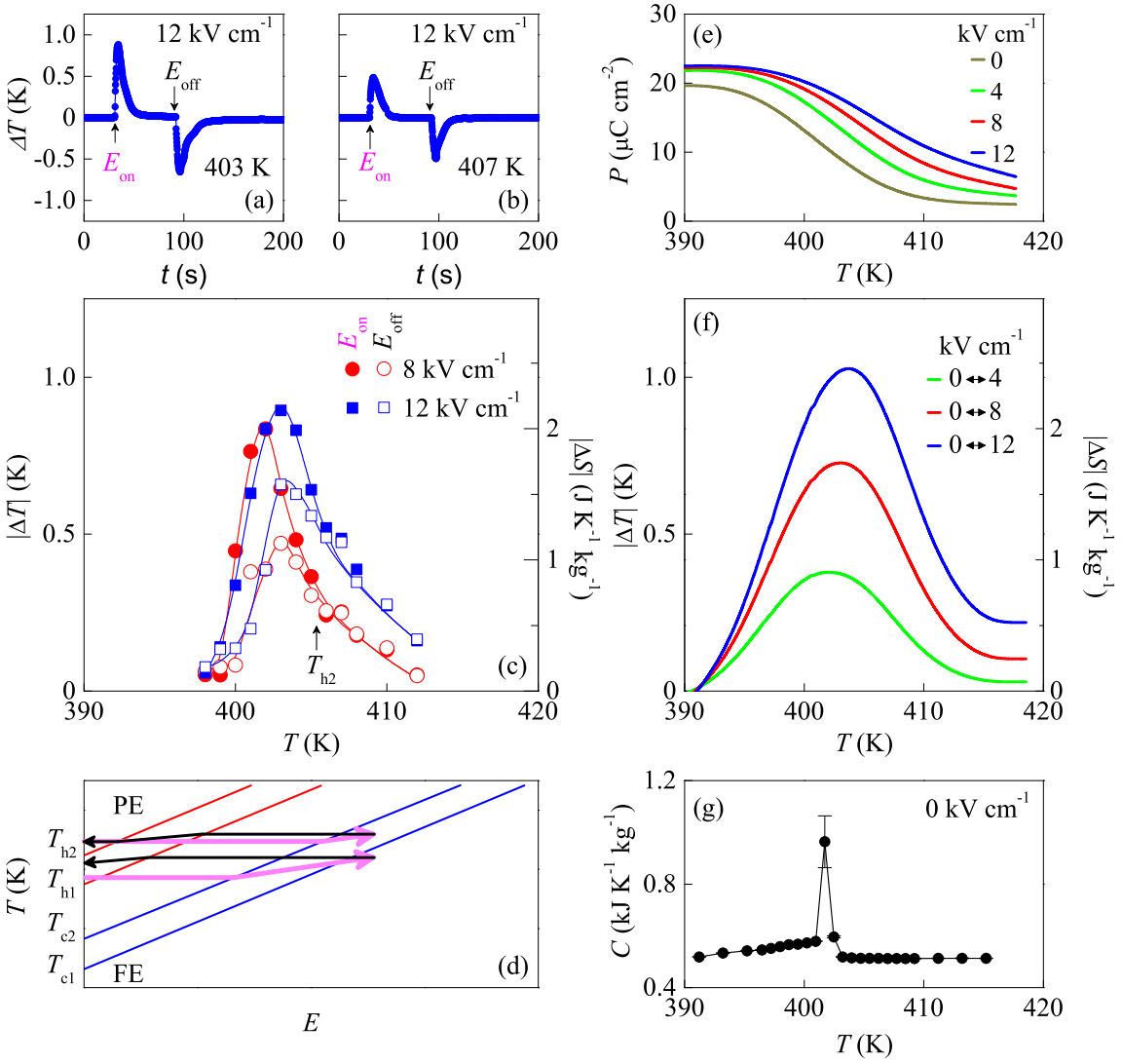


Fig. 6.6 Electrically driven changes of temperature near $T_C$. Data for sample 1. We present direct EC measurements of temperature change $\Delta T$ versus time $t$, arising due to the application ($E_{\rm on}$ ) and subsequent removal ($E_{\rm off}$) of 12 kV cm$^{-1}$ (a,b) at starting temperatures below (a) and above (b) $T_{h2}$ = 405.3 K. (c) Directly measured values of $|\Delta T|$, as a function of starting temperature, due to the application ($E_{\rm on}$) and subsequent removal ($E_{\rm off}$) of 8 and 12 kV cm$^{-1}$. (d) Schematic $T-E$ phase diagram indicating that EC temperature change near the hysteretic transition is only reversible above $T_{h2}$. (e) and (f) correspond to (c) and (d) in figure 6.5. (g) Zero-field specific heat capacity $C$ measured on cooling (vertical bars indicate measurement error). The peak value of $C = 0.96$ kJ K$^{-1}$ kg$^{-1}$ at 401.7 K in (g) was used to determine the entropy change in (c), and the temperature change in (f).

transition start and finish temperatures assume the Clausius–Clapeyron gradient $\frac{dT_t}{dE}$ for an anhysteretic transition at $T_t$.

The peak temperature-change measurement of $|\Delta T| \sim 0.90$ K in 12 kV cm$^{-1}$ [figure 6.6 (c)] represents the fully driven transition in sample 1, as electrical polarization data [figure 6.6 (e)] reveal via the indirect method that 12 kV cm$^{-1}$ is sufficient to drive the full transition [figure 6.6 (f)] of $|\Delta S| \sim 2.2$ J K$^{-1}$ kg$^{-1}$ [figure 6.3 (b), bottom panel]. The entropy and temperature scales in figure 6.6 (c, f) may be crudely interconverted using the peak value of the zero-field specific heat capacity $C = 0.96$ kJ K$^{-1}$ kg$^{-1}$ at 401.7 K [figure 6.6 (g)], but the match is not as good as in figure 6.5 as the field dependence of $C$ has been neglected. This mismatch demonstrates the value of direct data for precise measurements of EC temperature change.

Large electrically driven adiabatic changes in temperature can only be driven reversibly at $T \leq T_{h2}$, in order to avoid the hysteretic regime indicated on our schematic phase diagram [figure 6.6 (d)]. The largest reversible temperature change due to our maximum applied field of 12 kV cm$^{-1}$ is $|\Delta T| \sim 0.5$ K at $T_{h2}$ [figure 6.6 (c)]. To reversibly drive the full transition to achieve $|\Delta T| \sim 0.90$ K would require a larger electric field at $T_{h2}$. Above this starting temperature, an even higher field would be required to drive the transition, as seen from the phase diagram.

The EC heat $|Q| \sim 835$ J kg$^{-1}$ measured for the full transition in sample 2 (figure 6.5) is highly consistent with the EC temperature change $|\Delta T| \sim 0.90$ K for the full transition in sample 1 (figure 6.6), as seen by dividing to obtain a value of $C \sim 0.93$ kJ K$^{-1}$ kg$^{-1}$ that closely matches our experimental peak value of c = 0.96 kJ K$^{-1}$ kg$^{-1}$ [figure 6.6 (g)]. Equally, one may use the experimental peak value of $C$ to obtain $|\Delta T| = \frac{|Q|}{C}| \sim 0.87$ K using $|Q| \sim 835$ J kg$^{-1}$, and $|Q| = |C\Delta T| \sim 864$ J kg$^{-1}$ using $|\Delta T| \sim 0.90$ K. A smaller value of $|\Delta T| \sim 0.4$ K has been previously reported [27] for polycrystalline $BaTiO_3$ (table 6.1), suggesting that the applied field did not drive the full transition in the misoriented grains. However, a similar value of $|Q| \sim 910$ J kg$^{-1}$ was measured [194] in polycrystalline $BaTiO_3$ films using a much larger field. Doped $BaTiO_3$, present in commercially available multilayer capacitors, has a reduced peak value [195] of $C = 0.43$ kJ K$^{-1}$ kg$^{-1}$. Therefore a respectable value of $|\Delta T| \sim 0.5$ K was measured, [196] even though the corresponding value of $|Q| \sim 217$ J kg$^{-1}$ is relatively small.

Table 6.1 Comparison of selected EC materials. We compare our two single-crystal $BaTiO_3$ samples (S1 stands for sample 1, and S2 for sample 2) with values from the literature. SC and PC stand for a single crystal and a polycrystalline sample, repectively. Direct measurements of $|Q|$ and $|\Delta T|$ appear in bold, and were used to calculate the corresponding values of $|\Delta T| = |\Delta Q/C|$ and $|\Delta Q| = |C\Delta T|$. For the two prototypical films showing giant EC effects, indirect measurements of $|Q|$ and $|\Delta T|$ appear in brackets. Values of $C$ at $T_C$ were obtained for the three samples in references [27, 197, 198] and from refs., [199–201] respectively. EC strength is parameterized as $\frac{|Q|}{|\Delta E|}$ and $\frac{|\Delta T|}{|\Delta E|}$. For ref. [194] the large value of $|\Delta T|$ = 1.8 K results from using a small value of $C$ . P(VDF-TrFE) = poly(vinylidene fluoride-trifluoroethylene). P(VDF-TrFE-CFE) = poly(vinylidene fluoride-trifloroethylene-chlorofluoroethylene).

| Material | Bulk or film | SC / PC | $T_C$ (K) | $\|Q\|$ (J/kg) | $\|\Delta T\|$ (K) | $\Delta E\|$ (kV/cm) | $\|Q/\Delta E\|$ (J cm / kg kV) | $\|\Delta T/\Delta E\|$ (mK cm / kV) | Reference |
|---|---|---|---|---|---|---|---|---|---|
| $BaTiO_3$ S1 | bulk | SC | 402 | 864 | 0.90 | 12 | 72 | 75 | This section |
| $BaTiO_3$ S2 | bulk | SC | 397 | 835 | 0.87 | 4 | 209 | 220 | This section |
| $BaTiO_3$ | bulk | PC | 391 | 276 | 0.4 | 7.5 | 51 | 53 | [27] |
| $BaTiO_3$ | film | PC | 353 | 910 | 1.8 | 176 | 5 | 10 | [194] |
| Doped $BaTiO_3$ | film | PC | 350 | 217 | 0.5 | 300 | 0.7 | 1.7 | [196] |
| $Pb(Mg_{1/3}Nb_{2/3})_{0.75}Ti_{0.25}O_3$ | bulk | SC | 383 | 400 | 1.1 | 25 | 16 | 44 | [197] |
| $Pb_{0.99}Nb_{0.02}(Zr_{0.75}Sn_{0.20}Ti_{0.05})O_3$ | bulk | PC | 434 | 1885 | 2.5 | 30 | 63 | 83 | [198] |
| $PbZr_{0.95}Ti_{0.05}O_3$ | film | PC | 495 | (4000) | (12) | 500 | 8 | 24 | [3] |
| P(VDF-TrFE) | film | PC | 343 | (19 000) | (12) | 2000 | 10 | 6 | [180] |
| P(VDF-TrFE-CFE) | film | PC | 318 | 17 490 | 12 | 1700 | 10 | 7 | [202] |

The field $|\Delta E| \sim 4$ kV cm$^{-1}$ required to drive the full transition in sample 2 differs from the field $|\Delta E| \sim 12$ kV cm$^{-1}$ required to drive the full transition in sample 1, and the width of the peak in $|\Delta S(T)|$ [figure 6.5 (a,b)] differs from the width of the peak in $|\Delta T(T)|$ [figure 6.6 (c)]. Both of these differences arise due to extrinsic effects such as domain structure, defects, and impurities as seen in a third sample from the same supplier using electron spin resonance [203]. An intermediate field of $|\Delta E| \sim 7.5$ kV cm$^{-1}$ produced [27] the smaller above-mentioned EC effects in polycrystalline $BaTiO_3$, reducing EC strengths $\frac{|Q|}{|\Delta E|}$ and $\frac{|\Delta T|}{|\Delta E|}$ (table 6.1). The polycrystalline [194] and doped [196] films of $BaTiO_3$ show even lower EC strengths, as much larger fields were required to drive the broad transitions (see the Maxwell relation shown earlier). Our two single-crystal samples of $BaTiO_3$ thus show better EC strengths than the polycrystalline samples of the same material (table 6.1). Well-known EC materials show larger values of $|Q|$ and $|\Delta T|$ , but much larger fields $|\Delta E|$ are required, such that our second sample of $BaTiO_3$ shows superlative EC strengths $\frac{|Q|}{|\Delta E|}$ and $\frac{|\Delta T|}{|\Delta E|}$ (table 6.1).

The discrepancies in the electrical polarization measurements of the two samples arise not just because of the extrinsic effects discussed above, but also because sample 2 was measured using a smaller maximum field, in order to avoid exceeding the field that drove the full transition [figure 6.5 (a)]. The resulting predictions of the indirect method are nevertheless reasonable, implying that minor and major ferroelectric hysteresis loops evolve with temperature in a similar manner.

### 6.3.3 Summary and conclusions

In summary, the direct measurements of electrically driven heat and temperature change in single crystal $BaTiO_3$, near the first-order ferroelectric phase transition at $T_C \sim 402$ K, have been presented. The two types of EC measurement are in good agreement with each other, and with the results of the indirect method based on the Maxwell relation. Therefore the indirect method is valid when there is strong electrical hysteresis, just as it is valid [196] for doped $BaTiO_3$ with weak electrical hysteresis. The observed EC effects, which are fully reversible at starting temperatures above the hysteretic regime, show giant EC strengths $\frac{|Q|}{|\Delta E|}$ and $\frac{|\Delta T|}{|\Delta E|}$ that exceed the values reported for other EC samples (table 6.1). This improvement arises due to the sharpness of the transition as seen via the Maxwell relation, and should be even greater for materials that display first-order phase transitions with larger latent heats.

Therefore EC materials may be exploited for applications by operating at temperatures above the hysteretic regime of sharp first-order phase transitions.

## 6.4 The barocaloric effect in $BaTiO_3$

### 6.4.1 Experimental details

We studied powdered $BaTiO_3$ ($\geq$ 99.99%) from Sigma-Aldrich which had a typical grain size of <1 $\mu$m. The powder was first cold-pressed isostatically in air at 10 kbar and then sintered in air at 1673 K for 48 h. The sintered ceramic (2.3 cm in diameter, 0.2 cm in thickness) was cooled down to room temperature at -3 K $min^{-1}$. A small piece ($\sim$ 0.005 $cm^3$) was cut in order to perform temperature-dependent calorimetry and x-ray diffraction at ambient pressure. The larger remaining piece was used for pressure-dependent calorimetry.

Calorimetric measurements at atmospheric pressure were performed using a commercial TA Q2000 differential scanning calorimeter at $\pm$ 2 K $min^{-1}$.

High-resolution x-ray diffraction was performed in transmission-mode using Cu K$\alpha_1$ = 1.5406 Åradiation in an INEL diffractometer, with a curved position-sensitive detector (CPS120), and Debye-Scherrer geometry. The sample was introduced into a 0.3-mm diameter Lindemann capillary to minimise absorption, and temperature was varied using a liquid-nitrogen 700 series Oxford Cryostream Cooler. Lattice parameters were determined by pattern matching using FullProf software [204].

Measurements of $\frac{dQ}{dT}$ under hydrostatic pressure were performed at approximately $\pm$ 2 K $min^{-1}$, using a differential thermal analyzer described in section 3.4. In order to guarantee optimal thermal contact between the heat sensor and the sample, a chromel-alumel thermocouple was inserted inside a hole that was drilled in the centre of the large $BaTiO_3$ ceramic sample. The ceramic sample and thermocouple were then immersed in the pressure-transmitting medium (Caldic silicon oil for high-temperature measurements; DW-Therm, Huber Kältemaschinenbau GmbH for low-temperature measurements).

### 6.4.2 Results and discussion

The first-order structural phase transitions are seen in calorimetry [Figure 6.7 (a)] to be sharp, with a small thermal hysteresis of $\sim$ 4 K (C-T) and $\sim$ 7 K (T-O). Integration of $\frac{dQ}{dT}$ yields the thermally driven entropy change $\Delta S(T)$ [Figure 6.7(b)], with $|\Delta S_t| = 2.4 \pm 0.2$ J $K^{-1}$ $kg^{-1}$ for the full C-T transition and $|\Delta S_t| = 2.0 \pm 0.2$ J $K^{-1}$ $kg^{-1}$ for the full T-O transition. Integration of $\frac{dQ}{dT}$ across the full transition yields heats of $|\Delta H_t| = 960 \pm 90$ J $kg^{-1}$ (C-T)

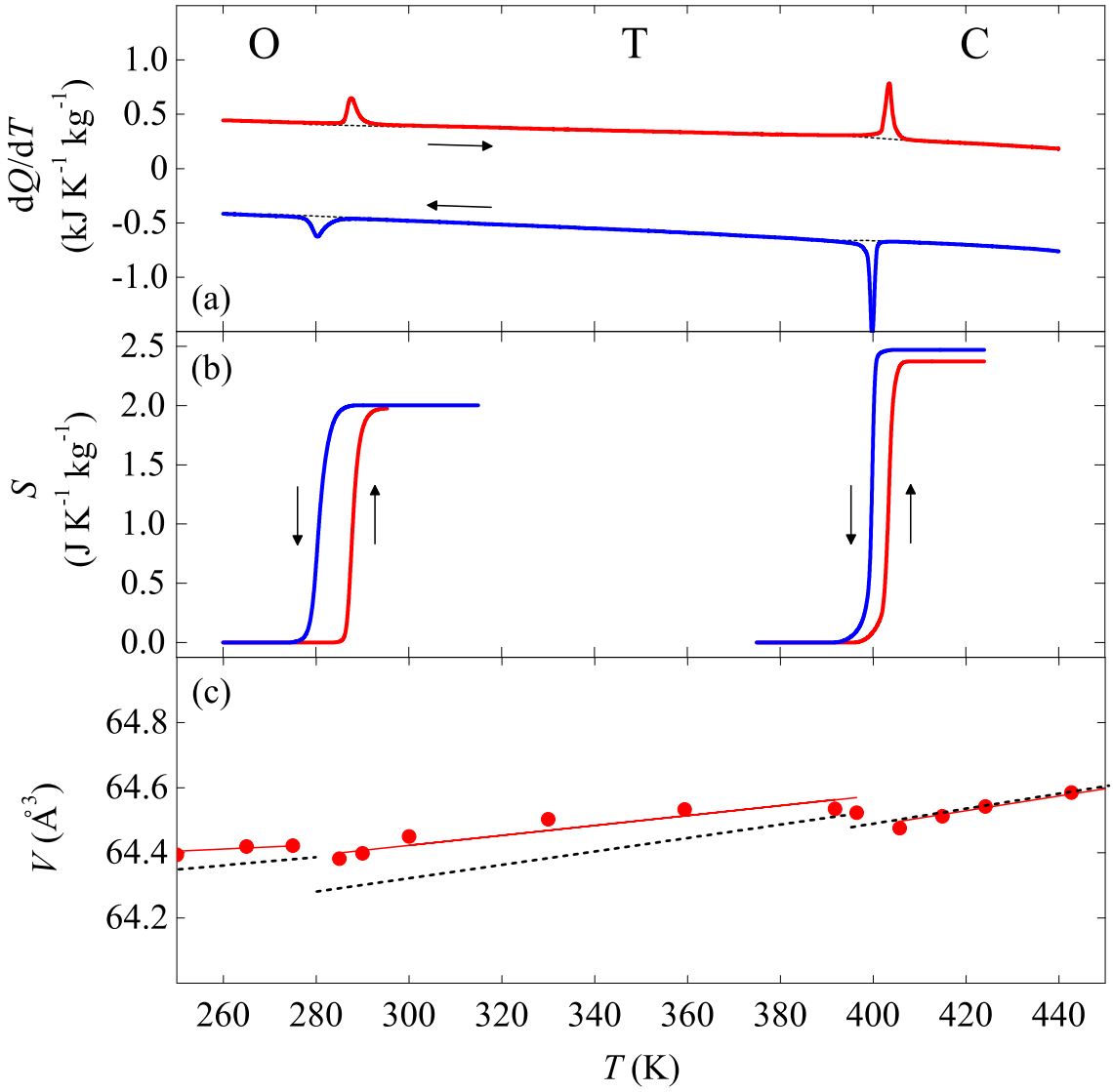


Fig. 6.7 Structural phase transitions in BTO at ambient pressure. (a) $dQ/dT$ on cooling (blue) and heating (red) across the cubic-tetragonal (C-T) and tetragonal-orthorhombic (T-O) transitions. Baselines are black dotted lines, and $dQ/dT > 0$ denotes endothermic processes. (b) Entropy change $\Delta S(T)$ with respect to the low-temperature phase for each transition. Arrows in (a) and (b) show direction of temperature sweep. (c) Unit-cell volume $V(T)$ on heating. Temperature-dependent lattice parameters have been previously shown in figure 6.2 (a). Solid lines represent linear fits. Dashed lines represent the literature data [183, 184]

and $|\Delta H_t| = 560 \pm 60$ J kg$^{-1}$ (T-O). These values are in good agreement with experimental values reported in the previous section and in reference [190] of $|\Delta S_t| \sim 2.4$ J K$^{-1}$ kg$^{-1}$ and $|\Delta H_t| \sim 900$ J kg$^{-1}$ for the C-T transition and are similar to previous values [190, 203] of $|\Delta S_t| \sim 1.6 - 2.3$ J K$^{-1}$ kg$^{-1}$ and $|\Delta H_t| \sim$ 450 - 640 J kg$^{-1}$ for the T-O transition.

On heating through the two transitions, x-ray diffraction data [Figure 1(c)] confirm the expected changes in crystal structure [183, 184]. The unit-cell volume $V$ decreases sharply by $\sim 0.03\%$ (O-T transition, $\Delta V_t = -0.02 \pm 0.01$ Å$^3$) and $\sim 0.11\%$ (T-C, $\Delta V_t$ = -0.07 $\pm$ 0.02 Å$^3$). On either side of each transition, the volume thermal expansion is large [as previously shown in figure 6.2 (b)], implying large additional BC effects [182]. By writing isothermal BC entropy change per unit mass $m$ due to pressure change $\Delta p = p_2 - p_1$ as [1, 182] $\Delta S(p_1 \rightarrow p_2) = -\frac{1}{m}\int_{p_2}^{p_1}\left(\frac{\partial V}{\partial T}\right)_{p'} dp'$ (using the Maxwell relation $\frac{1}{m}\left(\frac{\partial V}{\partial T}\right)_p = -\left(\frac{\partial S}{\partial p}\right)_T$), we therefore anticipate inverse BC effects in the transition regimes where $\left(\frac{\partial V}{\partial T}\right)_{p=0} < 0$, and conventional BC effects outside the transition regimes where $\left(\frac{\partial V}{\partial T}\right)_{p=0} > 0$.

$\frac{dQ}{dT}$ measurements through the two transitions under various applied pressures are shown in figure 6.8. For the C-T transition, there is a strong pressure-induced shift of transition temperature $T_t$, with $\frac{dT_t}{dp} = -5.8 \pm 0.1$ K kbar$^{-1}$ on heating and $\frac{dT_t}{dp} = -5.4 \pm 0.2$ K kbar$^{-1}$ on cooling [Figures 6.8 (a) and (c)]. A larger shift of -7.9 $\pm$ 2.0 K kbar$^{-1}$ on heating is obtained via the Clausius-Clapeyron equation $\frac{dT_t}{dp} = \frac{\Delta v_t}{\Delta S_t}$, using $\Delta S_t = 2.4 \pm 0.2$ J K$^{-1}$ kg$^{-1}$ [figure 6.7 (b)] and specific volume change $\Delta v_t = -(0.19 \pm 0.03) \times 10^{-6}$ m$^3$ kg$^{-1}$ [from Figure 6.7 (c)]. These values of $\frac{dT_t}{dp}$ are similar to those reported for $BaTiO_3$ in the form of single crystals ($\sim \in [-6, -4]$ K kbar$^{-1}$, references [178, 179, 205–210] and ceramics ($\sim \in [-5, -4]$ K kbar$^{-1}$, Refs. [179, 208, 211], and they imply that the narrow first-order transition of width $\sim$4 K may be fully driven using low values of $|\Delta p| \sim 1$ kbar.

For the T-O transition, the pressure-induced shift in $T_t$ is weaker, with $\frac{dT_t}{dp} = -3.5 \pm 0.1$ K kbar$^{-1}$ on heating and $\frac{dT_t}{dp} = -2.6 \pm 0.1$ K kbar$^{-1}$ on cooling [figures 6.8 (b) and (c)]. A similar shift of $\frac{dT_t}{dp} = -2.8 \pm 1.3$ K kbar$^{-1}$ on heating is obtained via the Clausius-Clapeyron equation, using $\Delta S_t = 2.0 \pm 0.2$ J K$^{-1}$ kg$^{-1}$ [figure 6.7 (b)] and specific volume change $\Delta v_t = -(0.06 \pm 0.03) \times 10^{-6}$ m$^3$ kg$^{-1}$ [from figure 6.7 (c)]. These values of $\frac{dT_t}{dp}$ are similar to those reported for single-crystal $BaTiO_3$ ($\sim$ -3 K kbar$^{-1}$, Refs. [179, 207, 209] and

indicate that the wider first-order transition of width ∼7 K may be fully driven using $|\Delta p| \sim$ 2 kbar.

For each of the two transitions, integration of $\frac{1}{T}\frac{dQ}{dT}$ at finite pressure reveals that the entropy change $|\Delta S_t|$ decreases with increasing pressure [Figure 6.8 (d)]. This fall in $|\Delta S_t|$ arises because of additional [182] changes in isothermal entropy $\Delta S_+(p)$ that are conventional, reversible, and opposite in sign with respect to the pressure-driven isothermal entropy changes associated with each transition. These additional changes in entropy are challenging to detect via the calorimetry used for figure 6.8 but may be expressed away from the first-order transitions via $\Delta S_+(p) = -\left[\frac{1}{m}\left(\frac{\partial V}{\partial T}\right)_{p=0}\right] p$, where we have used the aforementioned Maxwell relation with S+ replacing S, and with $\left(\frac{\partial V}{\partial T}\right)_p$ assumed independent of pressure [1, 182].

In order to plot $\Delta S(T,p)$ with respect to the zero-pressure entropy at a temperature $T_+$ above the C-T transition [Figures 6.9 (a) and (b)] and the T-O transition [Figures 6.9 (e) and (f)], we obtained finite-pressure plots of $\Delta S(T)$ from the integration of data in Figures 6.8 (a) and (b)] that we displaced [182] at $T_+$ by evaluating $\Delta S_+(p)$ at this temperature. Note that $\Delta S_+(p)$ was evaluated at $T_+ > T_t(p)$ to avoid the forbidden possibility of $T_t(p)$ falling to $T_+$ at high pressure.

For the C-T transition, our plots in Figure 6.9 (a) of $\Delta S(T,p)$ for $\frac{dQ}{dT}$ data obtained on heating permit us to establish isothermal BC effects on applying pressure [Figure 6.9 (c)], as heating and high pressure both favour the high-temperature cubic phase with smaller volume. Similarly, our plots in Figure 6.9 (b) of $\Delta S(T,p)$ for $\frac{dQ}{dT}$ data obtained on cooling permit us to establish isothermal BC effects on decreasing pressure [Figure 6.9 (d)], as cooling and low pressure both tend to favour the low-temperature tetragonal phase with larger volume. Values of $|\Delta S(T,p)|$ on applying and removing pressure are similar at all temperatures studied. The BC response near the C-T transition is therefore highly reversible, consistent with the low thermal hysteresis of the transition [figure 6.7 (a) and (b)]. The peak isothermal entropy change $|\Delta S| \sim 1.6 \pm 0.2$ J K$^{-1}$ kg$^{-1}$ near ∼ 400 K is achieved with a low value of $|\Delta p| = 1$ kbar [figures 6.9 (c) and (d)], yielding large BC strengths [1], $\frac{|\Delta S|}{|\Delta p|}$ and $\frac{|Q|}{|\Delta p|}$ (table 6.2). Larger pressures extend inverse reversible BC effects to lower temperatures, causing an increase of refrigerant capacity RC [Figure 6.10 (b)], despite the reduction in $|\Delta S_t(p)|$ [figure 6.8 (d)] and thus the peak value of $|\Delta S_t(p)|$ [Figure 6.10 (a)]. Note that recently predicted BC effects ($|\Delta S_t(p)| \sim 3.9$ J K$^{-1}$ kg$^{-1}$ with 10 kbar at 353 K) are larger because additional entropy changes were neglected [187].

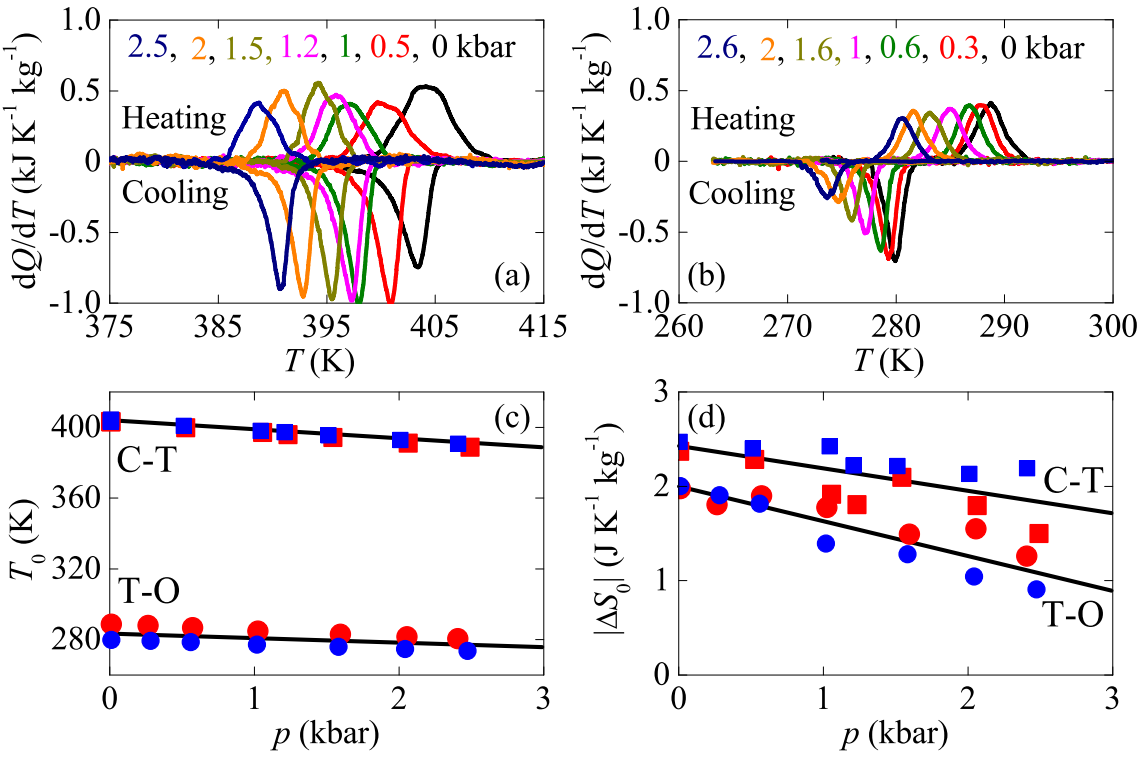


Fig. 6.8 Structural phase transitions in $BaTiO_3$ under pressure. $dQ/dT$ on cooling and heating across (a) the C-T and (b) T-O transitions, after baseline subtraction, for different values of increasing pressure $p$, values of which appear in the same order as the peaks for both heating and cooling. Pressure dependence of (c) transition temperature $T_t$ and (d) entropy change $|\Delta S_t|$, for the C-T transition [square symbols, data from (a)] and the T-O transition [round symbols, data from (b)] on cooling (small blue symbols) and heating (large red symbols). Lines in (c) and (d) are linear fits.

For the T-O transition, our plots in Figures 6.9 (e) and (f) of $\Delta S(T,p)$ for $\dfrac{dQ}{dT}$ data obtained on heating and cooling permit us to establish isothermal BC effects on increasing pressure [Figure 6.9 (g)] and decreasing pressure [Figure 6.9 (h)]. Although the peak entropy change of $|\Delta S| \sim 1.3 \pm 0.2$ J K$^{-1}$ kg$^{-1}$ appears to be similar for $\Delta p = \pm 1$ kbar, the peak occurs at different temperatures, evidencing inverse irreversible BC effects. This irreversibility, which is also seen for conventional EC effects near the T-O transition [212], arises because of the relatively large thermal hysteresis. Therefore caloric effects near the T-O transition are unsuitable for continuous cooling, and so we do not present RC values.

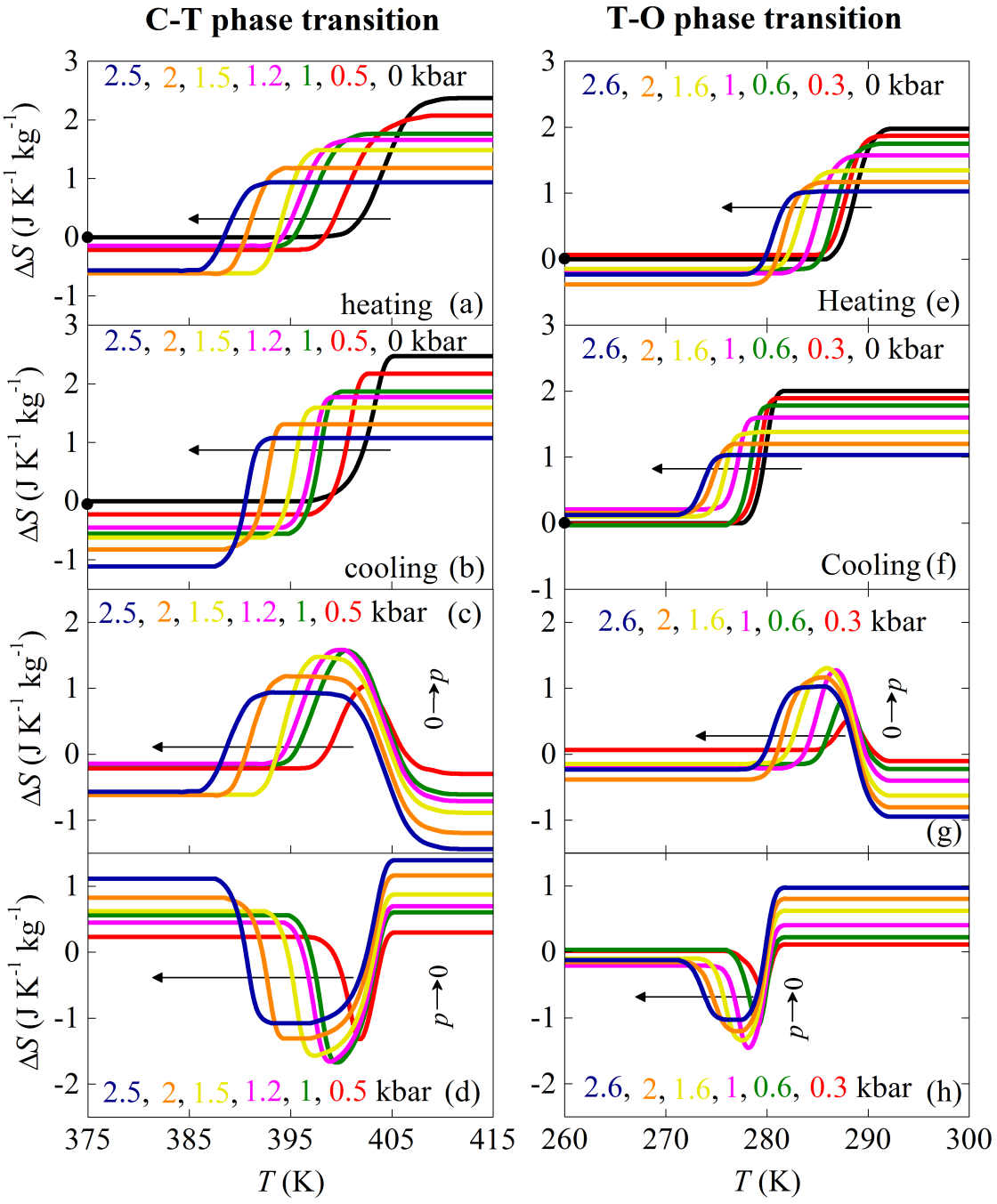


Fig. 6.9 Inverse barocaloric effects in $BaTiO_3$ near the C-T (left panels) and T-O (right panels) phase transitions. For (a, e) heating and (b, f) cooling, we show entropy change $\Delta S(T,p)$ with respect to $S(T=375K, p=0)$ and $S(T=260K, p=0)$ (black dot), offsetting $\Delta S(T)$ at each pressure using additional entropy change $\Delta S_+(p)$ at $T_+ = 410$ K and $T_+ = 292$ K, respectively . Hence isothermal entropy change $\Delta S(p)$ for (c, g) increasing pressure $(0 \to p)$ as deduced from (a, e), and (d, h) decreasing pressure $(p \to 0)$ as deduced from (b, f). In each panel, the given pressure values increase as indicated by the horizontal arrow.

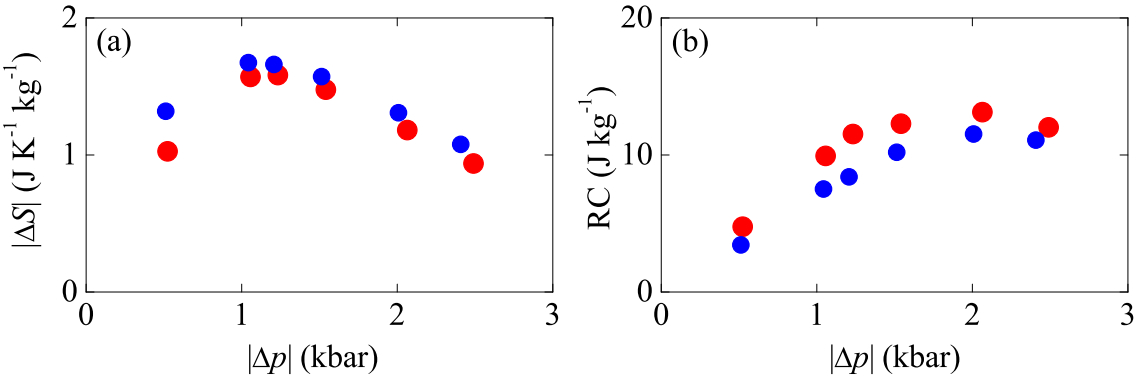


Fig. 6.10 Peak BC response and refrigerant capacity near the C-T phase transition. (a) Peak values $|\Delta S|$ of the temperature-dependent entropy change $\Delta S(T)$ at each measurement pressure $p$, for applying pressure (large red symbols) and removing pressure (small blue symbols). (b) The corresponding refrigerant capacity RC = $|\Delta S| \times$ [FWHM of $\Delta S(T)$] for selected pressure changes of magnitude $|\Delta p| \sim |p|$.

Table 6.2 Comparison of inverse barocaloric effects and conventional electrocaloric effects in $BaTiO_3$. Isothermal entropy change $\Delta S$ and isothermal heat $Q$, at starting temperature $T$, due to changes of hydrostatic pressure $\Delta p$, and change of electric field $\Delta E$. The corresponding strengths are $|\Delta S|/|\Delta p| = 1.6$ J K$^{-1}$ kg$^{-1}$ kbar$^{-1}$ and $|Q|/|\Delta p| = 660$ J kg$^{-1}$ kbar$^{-1}$ for the C-T transition, and $|\Delta S|/|\Delta p| = 1.3$ J K$^{-1}$ kg$^{-1}$ kbar$^{-1}$ and $|Q|/|\Delta p| = 365$ J kg$^{-1}$ kbar$^{-1}$ for the T-O transition. For $\Delta S$ and $Q$, superscripts $^{d}$ and $^{qd}$ refer to the direct and the quasi-direct measurement methods, respectively. For all entries, $Q = T\Delta S$.

| Transition | $T$ (K) | Caloric effect | SC or PC | $\Delta S$ (J / K kg) | $Q$ (J/kg) | $\Delta p$ or $\Delta E$ | Reference |
|---|---|---|---|---|---|---|---|
| C-T | 400 | BC | PC | $1.6^{dq}$ | $660^{qd}$ | 1 kbar | This section |
| | | EC | SC | $-2.1^{d}$ | $-840^{d}$ | 4 kV cm$^{-1}$ | 12 |
| T-O | 280 | BC | PC | $1.3^{qd}$ | $365^{qd}$ | 1 kbar | This section |
| | | EC | SC | $-2.3^{d}$ | $-645^{d}$ | 10 kV cm$^{-1}$ | 43 |

### 6.4.3 Summary and conclusions

In summary, we have combined temperature-dependent x-ray diffraction data with pressure dependent calorimetry to demonstrate BC effects in $BaTiO_3$ ceramic samples. For the T-O phase transition at $\sim$ 280 K, we found small inverse BC effects that are irreversible, whereas for the C-T phase transition at Curie temperature TC $\sim$ 400 K, we found larger inverse BC effects that are reversible.

Our observation of reversible BC effects near the Curie temperature of $BaTiO_3$ should inspire studies of BC effects in a wide range of ferroelectric materials. This should expand the range of BC materials beyond ammonium sulphate [182] and a small number of magnetic materials [5, 41, 84, 89, 90] allowing caloric properties to be exploited in cooling devices without the electrical breakdown that limits EC effects.

# Chapter 7

# Giant electrocaloric effect in $Pb(Sc_{0.5}Ta_{0.5})O_3$

In the present chapter the electrocaloric effect in $Pb(Sc_{0.5}Ta_{0.5})O_3$ (PST) is analysed by direct and quasi-direct experimental evaluation based on consistent calorimetric and infrared imaging measurements. The singular electrostructural features of the room temperature ferroelectric-paraelectric transition with low hysteresis prompt this perovskite oxide to exhibit a great electrocaloric performance, including a large reproducible thermal response of $|\Delta S|$ = 2.8 J $K^{-1}$ $kg^{-1}$ and $|\Delta T| = 2.2$ K driven by particularly low values of electric field ($|\Delta E| = 24.4$ kV $cm^{-1}$). Interestingly, the material is expected to present a great fatigue resistance upon field cycling. The room temperature pyroelectric properties confer to this material the possibility to be applied in new cooling techniques, infrared detectors, thermal imaging and energy harvesting, either in the thin film or in the bulk form [26, 213].

The work presented in this chapter has been realized in collaboration with the Department of Materials Science & Metallurgy of the University of Cambridge (Device Materials group). Specifically, the development of the IR imaging technique and the characterization of the electric field driven values of $\Delta T$ were performed during a research stay at this university (autumn 2015).

## 7.1 Structural and electric properties of $Pb(Sc_{0.5}Ta_{0.5})O_3$

PST compounds have the perovskite $ABO_3$ structure ($Pm\bar{3}m$) described section 6.1, in which A cations are $Pb^{2+}$ and the smaller B cations which occupy the octahedral sites are $Sc^{3+}$ (B') and $Ta^{5+}$ (B") [215]. It has been shown that 1:1 ordering of the B cations in Pb(B', B")$O_3$ perovskites depends on the temperature, the size difference between the B cations

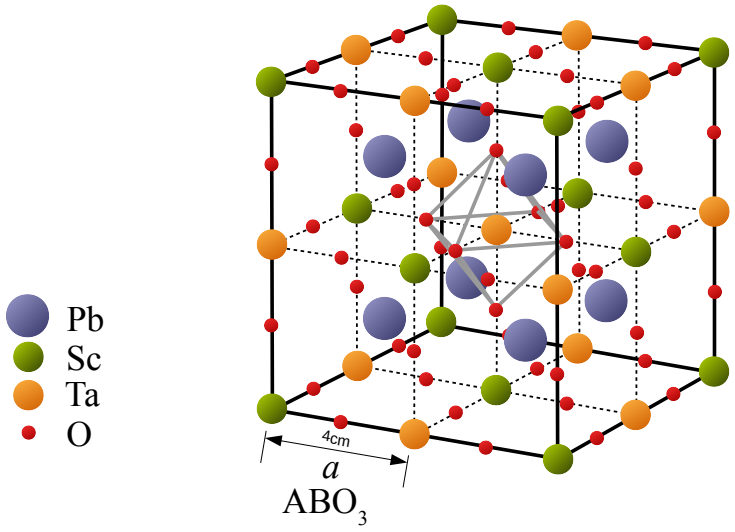


Fig. 7.1 Illustration of the ordered $Pb(Sc_{0.5}Ta_{0.5})O_3$ perovskite crystallographic structure ($Fm\bar{3}m$), adapted from [214]. In perovskites of the A(B'B")$O_3$ type the corresponding lattice parameter doubles that of the $ABO_3$ (indicated by $a$ in the figure) since B and B' atoms alternate at the corners of the simple cubic cell of $ABO_3$ ($Pm\bar{3}m$).

(the larger this difference, the larger the tendency of ordering), and the charge difference between the B cations [215]. This 1:1 order is characterized by an alternate distribution of the B' and B" cations along their positions leading to a doubled unit cell which corresponds to the $Fm\bar{3}m$ space group, as depicted in figure 7.1. In the case of $Pb(Sc_{0.5}Ta_{0.5})O_3$, the ordering of the B cations is close to the limit of stability [19] and the same compound can exhibit different degrees of order at room temperature. These ordering processes occur through nucleation of ordered domains and the corresponding growth by diffusion of the B' and B" cations [215, 216]. Thus, the diameter of the ordered domains increase with the annealing time because at high temperatures the relaxation process occurs in shorter time scales. A subsequent quenching enables the system to remain at the metastable state with a particular degree of order. Accordingly, the degree of order of the PST compounds can be tailored by controlling the annealing time and temperature. Long annealing times at typical temperatures of $T \gtrsim 1000$ ºC lead to highly ordered PST compounds. The degree or order $\Omega$ can be properly characterized by analysing the X-ray spectra and the existence of superlattice lines due to the appearance of the doubled unit cell [20, 217]. The broadening

of these lines is directly related to the dimensions of the domains[1]. Due to minimization of the electrostatic and elastic energies, the ground-state of these perovskite compounds should be the fully ordered structures in which each B cation occupies the corresponding sublattice [216]. The order-disorder transition occurs at temperatures in which the thermal motion is able to destroy this ordering. In PST, it is expected to occur at temperatures between 1450 and 1500 ºC [216, 218].

PST displays a FE-PE phase transition at temperatures typically between 270 to 300 K [19, 219]. The previously described cubic perovskite structure ($Fm\bar{3}m$, $Pm\bar{3}m$) exhibits a PE (or relaxor) behaviour which, upon cooling, transforms to a low-symmetry FE rhombohedral structure ($R3$ or $R3m$) generated by a cooperative distortion of the cubic lattice [20, 220]. The general features of this phase transition are strongly related to the positional disorder, as well as other factors such as the grain size, inhomogeneities, and the presence of defects and vacancies [20, 221–224]. In this regard, relaxors are always associated with common features like certain degrees of chemical disorder, diffuse phase transitions, narrow hysteresis and frequency-dependent dielectric constant in the PE state and weak FE hysteresis below $T_C$ [225]. Accordingly, as the level of atomic disorder in PST is increased the relaxor behaviour of the compounds is enhanced and the FE-PE phase transition shows a more diffuse character with a thermal hysteresis which tends to vanish as $\Omega$ decreases [19, 213, 226]. This behaviour is encompassed by a reduction of the latent heat as the B-cation disorder increases. The transition can be classified as second-order transition for $\Omega \lesssim 0.5$, where the latent heat is expected to vanish [227]. In contrast, for PST compounds with large degrees of order ($\Omega > 0.8$), the first-order character of the transition is strengthened, the transition becomes sharper with a low but well defined hysteresis [218]. In this regard, the associated latent heat increases with the degree of order [19]. It is worth mentioning that even though chemical disorder can be thought as a barrier for the appearance of the long-range dipole coupling responsible of the FE order, the FE phase is present in all PST compounds (for $0 \leq \Omega \leq 1$) [221].

[1] The degree of order can be parametrized by the normalized quantity $\Omega$, where $\Omega = 1$ stands for a completely ordered structure. This parameter can be expressed as a function of the ratio between the intensities of the lattice and superlatice X-ray peaks:

$$\Omega = \sqrt{\frac{\left(I_{\text{lattice}}/I_{\text{superlattice}}\right)_{\text{experiment}}}{\left(I_{\text{lattice}}/I_{\text{superlattice}}\right)_{\text{theory},\Omega=1}}} \tag{7.1}$$

which refers to the fraction between the experimentally obtained values and the calculated values considering $\Omega = 1$.

## 7.2 Experimental details

The PST ceramic sample was prepared by milling $Sc_2O_3$ and $Ta_2O_5$ powders together and prereacting at 900 ºC to form the wolframite phase $ScTaO_4$. The wolframite was then reacted with PbO at 900 ºC to form a single phase perovskite powder. The perovskite powder was then hot-pressed using $Si_3N_4$ tooling and an alumina grit packing medium at 40 MPa and 1200 ºC for 6 hours.

The specimens were prepared with the shape of a thin plate of 0.45 mm thickness. The mass of the specimens for calorimetry and IR imaging was 240.2 and 70 mg, respectively. The electrodes for application of the electric field were built by covering the two principal faces of each specimen by a thin layer of silver paint. The voltage difference $\Delta V$ was applied on each specimen by joining a thin copper wire on each face and connecting them to a Keithley 2410 sourcemeter, which allows application of $\Delta V$ values in the range of 0 – 1.1 kV.

Calorimetric measurements under applied electric fields were performed by the calorimeter described in section 3.2. Isofield and isothermal thermograms were measured at rates $\frac{dT}{dt} = 0.65$ K min$^{-1}$ and $\frac{dE}{dt} = 1.6$ kV cm$^{-1}$ min$^{-1}$. MDSC measurements for the characterization of the heat capacity $C_p$ were conducted using the commercial DSC Q2000 from TA Instruments. For these measurements the signal was modulated with an amplitude of $T_A = 0.8$ K and a period $t_p = 60$ s. Heating and cooling runs were performed at 1 K min$^{-1}$.

The IR imaging technique was carried by means of am infrared camera FLIR ©, model SC7500-MB, and the setup described in section 3.5. The setup allowed proper tracking of the sample temperature during adiabatic electric field cycling, at rates of application and removal of $\sim 200$ kV cm$^{-1}$ s$^{-1}$.

The measurement protocols described in section 3.2 were employed for the isothermal DSC and the IR imaging considering the conventional nature of the caloric effect, as discussed in the following section.

## 7.3 Results and discussion

The isofield thermograms measured at constant values of the applied field up to 20.0 kV cm$^{-1}$ upon heating and cooling are shown figure 7.2 (a) and (b) respectively, together with the heat capacity $C_p$ data [top left inset in panel (a)] and the transition temperature $T_t$ behaviour as a function of the applied electric field [bottom left inset in panel (b)]. The peaks of the thermograms and the $C_p$ plots are associated with the latent heat of the first-order FE-PE transition which spreads over a temperature interval of $\sim 20$ K upon cooling and heating. Interestingly, the calorimetric measurements evidence an enhancement of the sharpness of

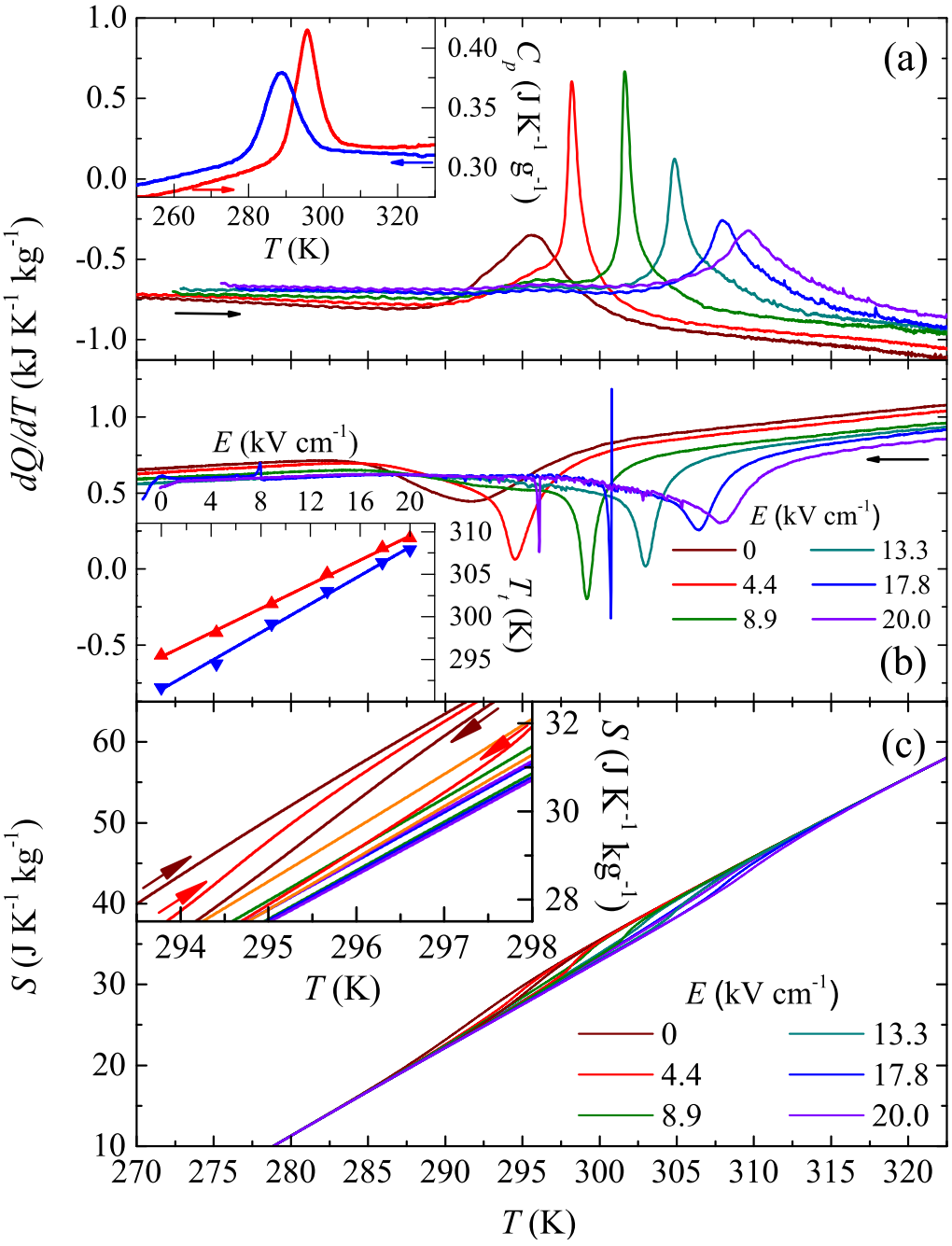


Fig. 7.2 Isofield thermograms obtained upon heating (a) and cooling (b) runs. The inset in (a) displays the heat capacity $C_p$ behaviour at the transition temperature range obtained by conventional MDSC upon heating (red line) and cooling (blue line). The inset in (b) displays the heating (red up triangles) and cooling (blue down triangles) transition temperatures, $T_{th}$ and $T_{tc}$, and the corresponding linear fits. (c) Entropy curves for heating and cooling runs at selected values of the applied electric field. The central part of the plot is magnified in the inset.

Table 7.1 Parameters associated with the PST FE-PE transition. Heating and cooling transitions temperatures, $T_{th}$ and $T_{tc}$; thermal hysteresis, $T_{th} - T_{tc}$; Sensitivity of the transition temperature with the applied electric field upon heating and cooling, $\frac{dT_{th}}{dE}, \frac{dT_{tc}}{dE}$; Electric hysteresis, $\Delta E_H$; Transition entropy change, $\Delta S_t$; Transition enthalpy change, $\Delta H_t$

| $T_{th}, T_{tc}$ (K) | $T_{th} - T_{tc}$ (K) | $\frac{dT_{th}}{dE}, \frac{dT_{tc}}{dE}$ (K cm / kV) | $\Delta E_H$ (kV / cm) | $\lvert\Delta S_t\rvert$ (J / K kg) | $\lvert\Delta H_t\rvert$ (J / g) |
|---|---|---|---|---|---|
| 292, 296 | 4 | 0.71, 0.84 | 3 | 3.0 | 0.9 |

the transition as the electric field is applied. The maximum sharpness is detected at 8.9 kV cm[1] where the transition is seen as a definite peak and spreads over a temperature region of $\sim$ 10 K. Larger values of the applied electric field yields again to a more diffuse transition. The temperature values of the transition peaks upon heating and cooling are associated with the transition temperatures $T_{th}$ and $T_{tc}$, respectively. Table 7.1 shows $T_t$ values at zero field and the sensitivity of the transition to the applied field $\frac{dT_t}{dE}$ obtained from the linear fits of the data shown in bottom left inset in figure 7.2 (b), which agree with the previously reported data [20]. Application of the electric field energetically favours the low-temperature FE phase, thus leading to $\frac{dT_t}{dT} > 0$ which anticipates an electrocaloric effect of conventional nature ($\Delta S < 0$ and $\Delta T > 0$, for $\Delta E > 0$) as explained in section 2.2.2. It is worth noting the reduction of the hysteresis as the applied electric field increases. In temperature regions out of the transition $C_p \sim 0.3$ J g$^{-1}$ and exhibits a modest increase with the temperature, as expected. Integration of the calorimetric curves as described in section 3.1.1 together with the $C_p$ data yields the entropy curves [see equation (3.19)] $S_c(T,E)$ (cooling) and $S_h(T,E)$ (heating) shown in figure 7.2 (c). Within the experimental error, the transition entropy and enthalpy changes are constant at values $\Delta S_t = 3.0 \pm 0.1$ J K$^{-1}$ kg$^{-1}$ and $\Delta H_t = 0.90 \pm 0.05$ J g$^{-1}$, with independence of the applied electric field and the diffusivity of the transition. B-site cation order of the PST sample can be inferred to be $\Omega \sim 0.8$ by correlating the obtained $\Delta H_t$ value with the degree of order by use of the data reported in reference [19], which presents the $\Delta H_t$ behaviour as a function of $\Omega$.

The isothermal calorimetric measurements obtained upon 0 – 24.4 kV cm$^{-1}$ electric field cycling are illustrated in panels (a) and (b) of figure 7.3. Panel (a) shows the heat flow as a function of the scanned electric field at selected temperatures between 287 and 315 K. In each

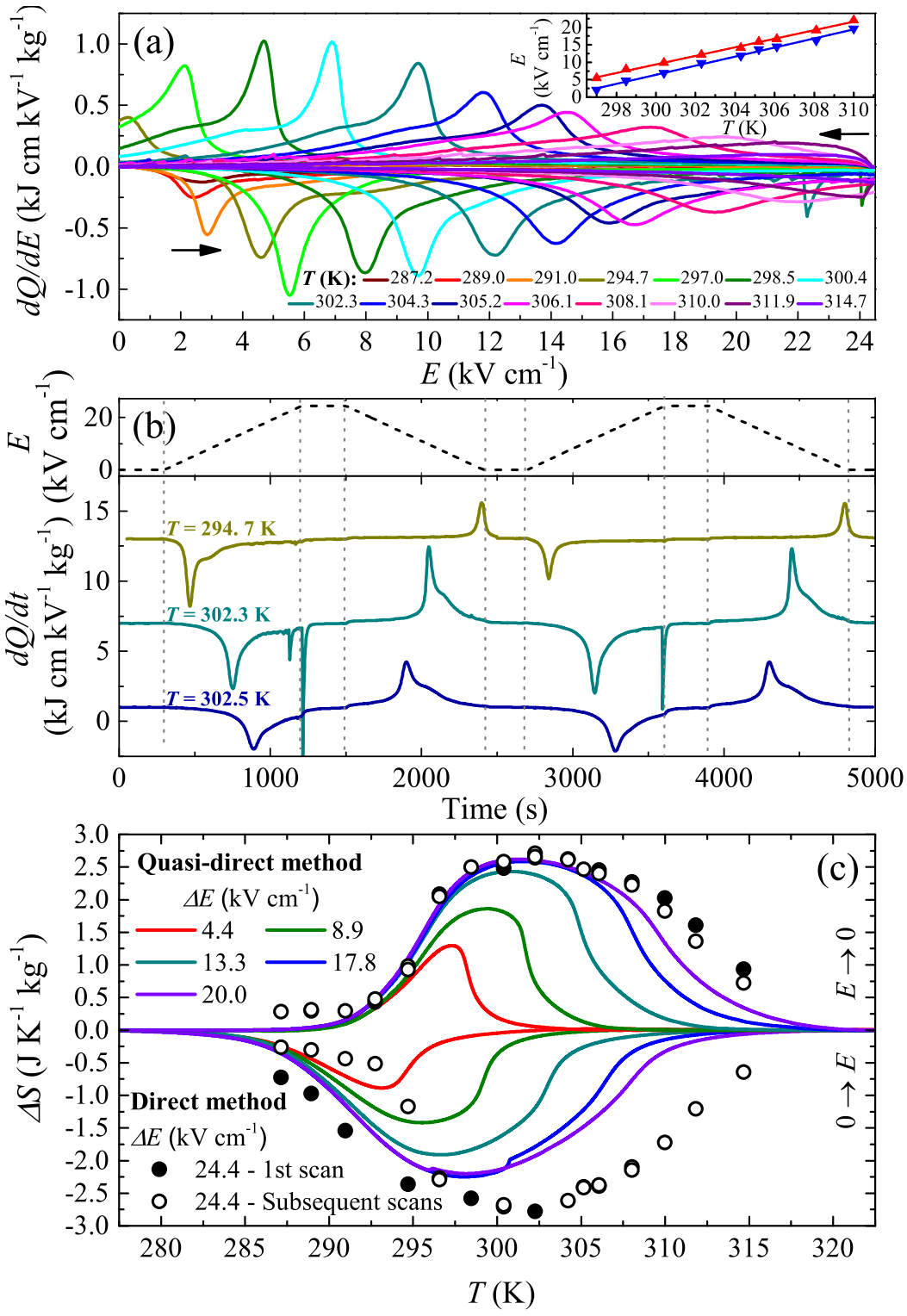


Fig. 7.3 (a) Isothermal thermograms obtained upon application (negative peaks) and removal (positive peaks) of electric field at selected temperatures (see the legend). (b) Illustrative isofield thermograms as a function of time during electric field cycling, as indicated at the top by the plot of the applied electric field as a function of time. (c) Direct (circles) and quasi-direct (lines) estimations of the isothermal entropy change. Solid circles correspond to the first electric field scan and open circles to the subsequent scans.

case, the thermograms illustrate the first two electric field scans, after the previous thermal excursion indicated by the measurement protocols. Again, the sharpness of the transition increases for values of the applied electric between 3 and 10 kV cm$^{-1}$ and decreases for larger values. The calorimetric peak is associated with the critical electric field which drives the transition ($E_{\uparrow}$ and $E_{\downarrow}$ for application and removal of the field, respectively). Values of the critical fields are plotted in the inset of figure 7.3 (a) and the corresponding linear fits provide their thermal sensitivity values, $\frac{dE_{\uparrow}}{dT} = 1.2$ kV cm$^{-1}$ K$^{-1}$ and $\frac{dE_{\downarrow}}{dT} = 1.3$ kV cm$^{-1}$ K$^{-1}$, which are in agreement with those obtained from the isofield measurements written in table 7.1. Interestingly, the electric hysteresis $\Delta E_H$ is reduced at rate $\sim 0.1$ kV cm$^{-1}$ K$^{-1}$ as the critical field increases and the transition takes place at higher temperatures. This supports the idea that under these conditions the transition gains a more diffusive second-order character, although that it is certainly classified as first-order as evidenced by the hysteresis and the latent heat inherent to the transition. This is consistent with the particular degree of order of our sample ($\Omega \sim 0.8$) and the fact that the samples with high B-cation ordering are expected to exhibit a first-order transition, whereas a second-order transition is expected for samples with less ordering [19, 215].

In accordance with the results given in previous chapters, the first electric field scan can drive an irreversible contribution to the caloric effect which is not driven upon subsequent cycles. Thus, the electrocaloric effect accounts solely for the reversible contribution upon further cycling. The irreversible contribution is illustrated by a larger calorimetric peak at the first field scan as can be seen in figure 7.3 (b), which plots the heat flow as a function of time during electric field cycling.

Isothermal and isofield calorimetry confer the direct and quasi-direct characterization of the electrocaloric entropy change $\Delta S$ shown in figure 7.3 (c). The direct estimates are computed by integration of the calorimetric peaks in isothermal thermograms as described in section 3.1.1. The quasi-direct estimates have been computed by subtracting the entropy curves at each field [figure 7.2 (c)] with respect to the reference curve a zero field. The corresponding entropy curves are chosen in accordance with the fact that the PE $\rightarrow$ FE (FE $\rightarrow$ PE) transition can be driven by either cooling (heating) or increasing (decreasing) the applied electric field, i.e. $\Delta S(T, 0 \rightarrow E) = S_c(T,E) - S_c(T,0)$ [$\Delta S(T, E \rightarrow 0) = S_h(T,0) - S_h(T,E)$].

Figure 7.4 shows illustrative IR images at different instants of a cycle in which the electric field is adiabatically applied. The images show one of the lateral faces of the PST sample which is enclosed by the electrodes at the top and bottom sides. The sample lies horizontally on the Peltier thermobattery which is responsible of monitoring the background temperature. As explained in section 3.5, a small piece of black tape is stuck on the measurement surface so that the sample temperature can be calibrated by consideration of its high IR emissivity.

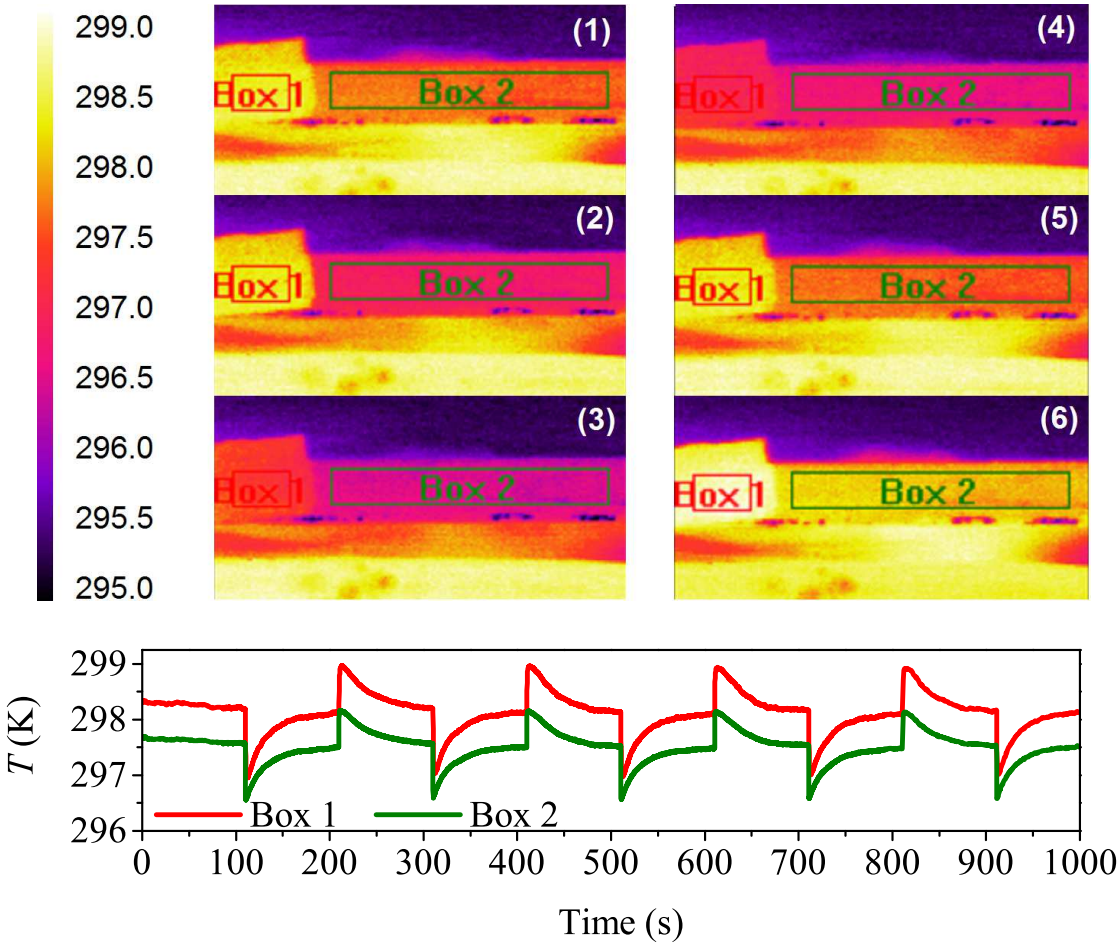


Fig. 7.4 Set of illustrative IR images [panels (1 – 6)] of the sample (box 2) and the black tape portion (box 1). The legend displays the colour-to-temperature conversion. Bottom figure shows an illustrative example of the average temperature behaviour in box 1 (red line) and 2 (green line) upon field cycling

The measured temperatures of the black tape and the sample $T_{bt}$ and $T_s$ are recorded by averaging the values enclosed by box 1 and 2, respectively. The bottom panel in figure 7.4 plots the corresponding evolution during a set of electric field cycles. It is clearly seen that the adiabatic conditions are accomplished because the thermalisation time between the sample and surroundings ($\sim 10^2$ s) is three orders of magnitude larger than the rate at which the electric field is changed ($\sim 10^{-1}$ s).

Illustrative examples of the calibrated signal of the sample temperature are shown in figure 7.5 (a). Each curve departs from different starting temperatures $T_s$ at which the electric field is cycled, after a previous thermal excursion indicated by the measurement protocols. At this point, it is straightforward to compute the temperature change $\Delta T$ related to each adiabatic application or removal of the field and to distinguish the corresponding reproducible values collected after the first field scan by simply identifying the corresponding temperature jumps. The quasi-direct computation is done by inverting the entropy curves at each field shown in 7.2 (c), i.e. $T_c(S,E) = {S_c}^{-1}(T,E)$ and $T_h(S,E) = {S_h}^{-1}(T,E)$, and computing $\Delta T(S,0 \rightarrow E) = T_c(S,E) - T_c(S,0)$ and $\Delta T(S,E \rightarrow 0) = T_h(S,0) - T_h(S,E)$, in analogy with the method described in section 4.3.3 for the magnetocaloric effect in $Fe_{49}Rh_{51}$. Instead of the entropy at which the adiabatic process has been held, it is more convenient to present the $\Delta T$ values as a function of the initial temperature at which the adiabatic temperature change is exhibited, i. e. $\Delta T[T_c(0),0 \rightarrow E]$ and $\Delta T[T_h(E),E \rightarrow 0]$. Figure 7.5 (c) gathers the direct and quasi-direct estimation of the adiabatic temperature change at different values of the applied field. In general, the good concordance between both methods provides high confidence to the obtained results.

Figures 7.3 (c) and 7.5 provide an extended characterization of the ECE in PST. It is shown that a modest value of the applied electric field $|\Delta E| = 24.4$ kV cm$^{-1}$ is able to drive the large values of $|\Delta S| \sim 2.8$ J K$^{-1}$ kg$^{-1}$ and $|\Delta T| \sim 2.2$ J K$^{-1}$. For this field the entropy change is close to $\Delta S_t$ value associated with the transition latent heat, which principally contributes to the caloric effect. The reversibility of the thermal effect is seen for $T \gtrsim 295$ K and the $\Delta T$ maxima obtained upon the first field scan are reproducible for fields $E \gtrsim 6$ kV cm$^{-1}$. As the applied field is increased the ECE and the corresponding reversibility region expand at higher temperatures due to the fact that the transition is shifted towards higher temperatures with the electric field. In agreement with the more second-order character of the transition found at higher temperatures, the effect becomes more reproducible if the transition is driven for larger critical fields (or at higher temperatures), as seen by the direct measurements plotted in figure 7.3 (c) which show a large reproducibility of the first electric field scan when applied at the high temperatures regions. Table 7.2 collects significant parameters related to the ECE exhibited by the analysed ceramic sample in comparison

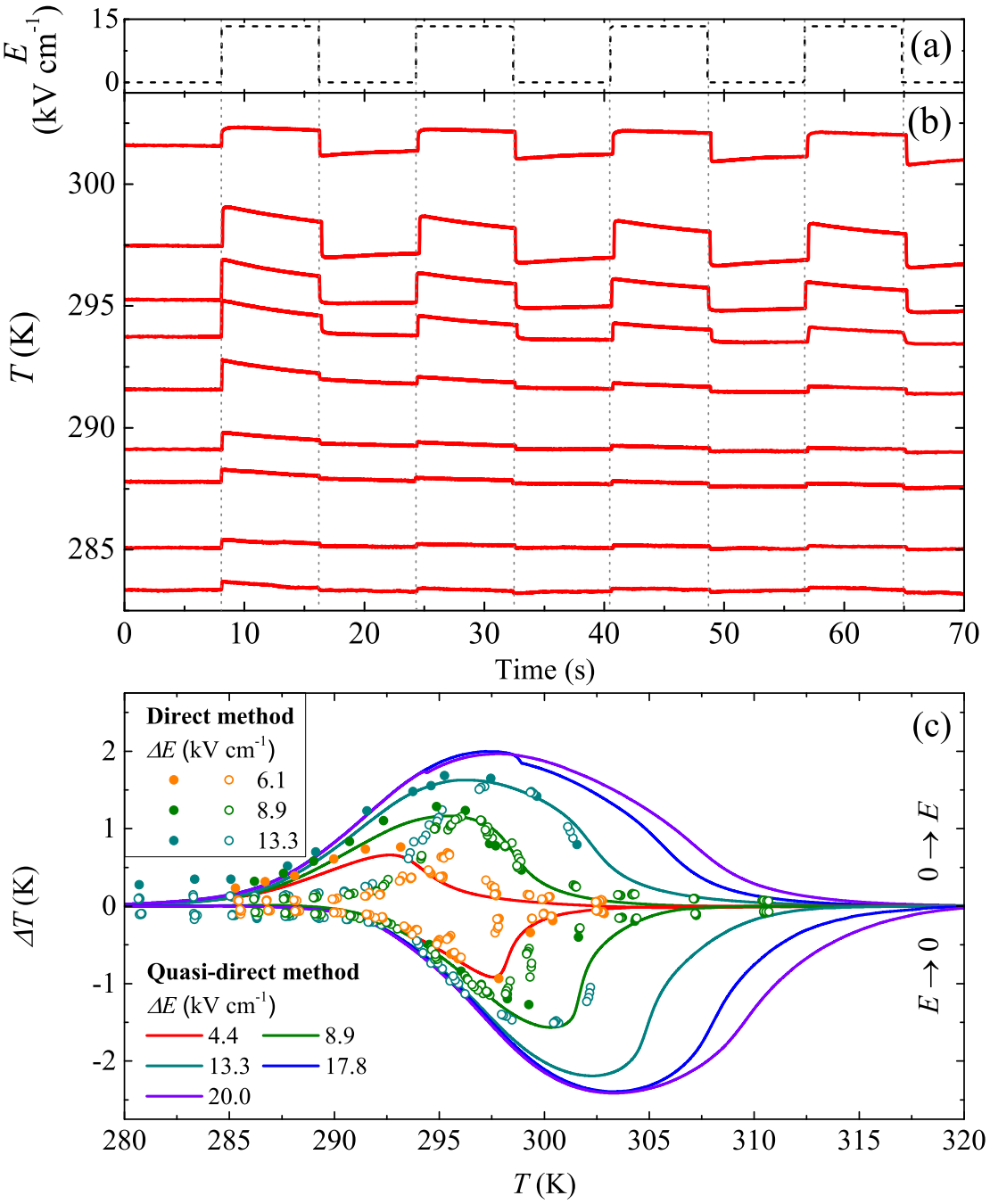


Fig. 7.5 (a) Behaviour of the applied electric field during a set of 0 – 13.3 kV cm$^{-1}$ cycles and the corresponding evolution of the calibrated temperature of the sample departing from different initial temperatures (b). (c) Direct and quasi-direct estimation of the adiabatic temperature change at selected values of the applied electric field. Solid symbols refer to the temperature change upon first application of electric field and open symbols refer to subsequent field scans.

with the results from previous studies. The electrocaloric strength written as $|\Delta S/\Delta E|$ and $|\Delta T/\Delta E|$ is a convenient parameter for describing and comparing the thermal response in relative terms of the applied field. Our direct and quasi-direct results are indicative of a larger ECE in PST ceramic samples if contrasted with the study reported in [226]. The larger thermal response measured in thin films [228] is driven at the expense of giant electric fields and, thus, yielding to poor EC strength values in comparison with the present results.

The fatigue resistance and the persistence of the caloric features upon multiple cycles are interesting aspects to be considered in view of applications to cooling devices. The caloric performance of our sample has been tested for $10^5$ cycles ($0 \leftrightarrow 8.9$ kV cm$^{-1}$). Figure 7.6 (a) displays the measured temperatures behaviour (sample and black tape) at different intervals during the cycling process and (b) shows the corresponding $\Delta T$ values. It is clearly seen that the caloric performance remains unaffected at $\sim 1.4$ K during the cycling process.

## 7.4 Summary and conclusions

We have analysed the giant ECE arising in the vicinity of the first-order FE $\rightarrow$ PE transition in a PST ceramic sample by means of direct and quasi-direct methods. Both methods reveal concordant and consistent results and provide a confident characterization of the relevant quantitites related to the ECE. In PST samples with intermediate degrees of B-cation order the transitions displays a competition between the first and second-order character [218, 219, 227]. The first-order character of the studied transition is consistent with the significant degree of order of our sample ($\Omega \sim 0.8$). In this case, the features associated with the first-order character are enhanced at low values of the applied electric field ($E \lesssim 12$ kV cm$^{-1}$) and for larger $E$ values the transition becomes more diffusive and second-order. The remarkably low hysteresis ($\sim 4$ K) can be attributed to this competition between the first and second order characters. This fact, together with the large caloric contribution associated with the latent heat are ideal conditions for an enhanced reversible thermal response upon field cycling.

It is worth noting the fact that the giant ECE ($|\Delta S| = 2.8$ J K$^{-1}$ kg$^{-1}$ and $|\Delta T| = 2.2$ K) is reversibly driven by modest electric fields ($|\Delta E| = 24.4$ J K$^{-1}$ kg$^{-1}$) which contrasts with the large values of the electric field driving the thermal response in thin films [26, 228]. Interestingly, the performance of the thermal response has been proven to remain unaffected after a large number of electric field cycles ($10^5$). These features prompt the present material for the potential use in cooling technologies.

Table 7.2 Parameters associated with the PST electrocaloric performance. Type of sample (PC: polycrystalline sample); degree of order; temperature; electric field change; EC entropy change; EC temperature change; EC strength in terms of the induced entropy and temperature per applied field. Superscripts refer to the measurement method, $^{d}$: direct, $^{qd}$: quasi-direct, $^{i}$: indirect, $^{c}$: calculated by approximating $\Delta S \sim \frac{C_p \Delta T}{T}$ where $C_p \sim 0.32$ J g$^{-1}$.

| Sample | Ω | $T$ (K) | $\lvert\Delta E\rvert$ (kV / cm) | $\lvert\Delta S\rvert$ (J / K kg) | $\lvert\Delta T\rvert$ (K) | $\lvert\Delta S/\Delta E\rvert$ (mJ cm / K kV kg) | $\lvert\Delta T/\Delta E\rvert$ (mK cm / kV) | Ref. |
|---|---|---|---|---|---|---|---|---|
| Bulk, PC | 0.8 | 298 | 24.4 | $2.8^{d}$ | $2.2^{qd}$ | 110 | 90 | This section |
| | 0.8 | 297 | 13.3 | $2.2^{qd}$ | $1.7^{d}$ | 160 | 130 | This section |
| | 0.8 | 296 | 8.9 | $1.6^{qd}$ | $1.4^{d}$ | 180 | 150 | This section |
| Bulk, PC | 0.85 | 295 | 25 | $1.6^{c}$ | $1.5^{i}$ | 65 | 60 | [226] |
| | 0.34 | 265 | 25 | $0.6^{c}$ | $0.5^{i}$ | 24 | 20 | [226] |
| | 0 | 260 | 25 | $0.1^{c}$ | $0.1^{i}$ | 4.9 | 4 | [226] |
| Thin film (200nm), PC | 0.32 | 337 | 774 | $6^{i}$ | $6.9^{i}$ | 8 | 9 | [228] |
| | 0.32 | 337 | 201 | $1.5^{i}$ | $1.5^{i}$ | 2 | 2 | [228] |

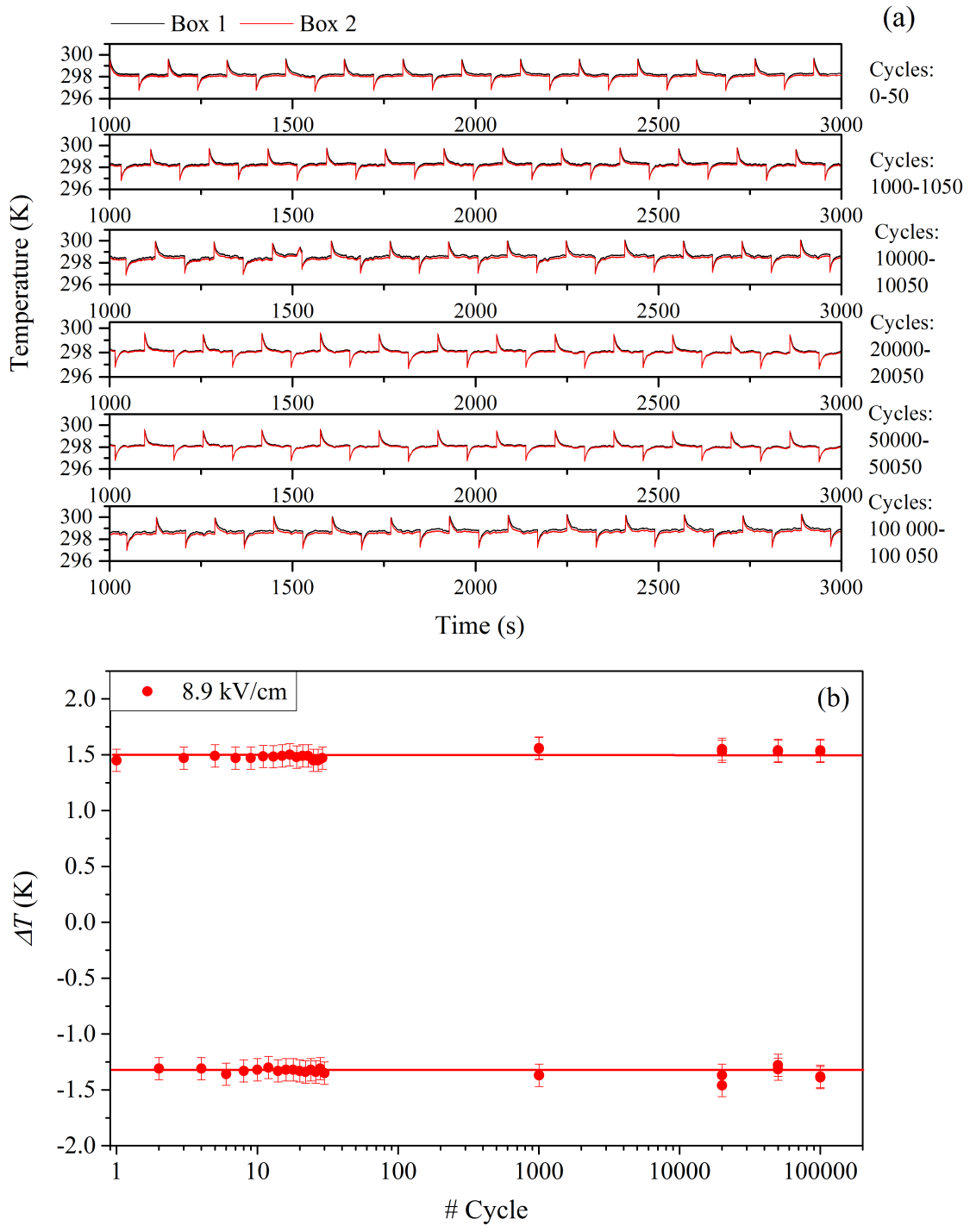


Fig. 7.6 Evaluation of the adiabatic temperature change upon $10^5$ electric field cycles of $0 \leftrightarrow 8.9$ kV cm$^{-1}$ at $T \sim 298$ K. Each row in (a) plots the measured temperature signals during a set of 50 electric field cycles departing from cycle number 1 (1st row), $10^3$ (2nd row), $10^4$ (3rd row), $2 \cdot 10^4$ (4th row), $5 \cdot 10^4$ (5th row), $10^5$ (6th row). As shown in figure 7.4, box 1 (black) stands for the black tape temperature, and box 2 (red) the measured sample temperature. (b) $\Delta T$ values as a function of the number of cycles, in logarithmic scale.

# Chapter 8

# Conclusions and future perspectives

The giant caloric effects arising in the vicinity of first-order transitions with cross-coupled response have been extensively investigated along this dissertation. The work has been done on a significant number of materials belonging to different families in which the corresponding ferroic or multiferroic properties lead to the particular thermal response, being magneto-, mechano- or electrocaloric as a function of the sensitivity of the order parameter with the applied fied (magnetic field, mechanical stress or electric field), and multicaloric when the thermal response is originated by multiple fields. Especial attention has been paid to providing a complete characterization by making use of a series of especially designed experimental techniques. The direct methods for measuring the thermal responses are crucial since results from these techniques are scarce in the literature while they provide a proper frame of results from which physical models can be built and parameters related to the caloric performance are provided with a great degree of reliability. These studies have been carried out by means of the developed calorimetric techniques under applied fields, and thermometry under applied fields by IR imaging and suitable thermocouples. Indirect techniques based on the analysis of the order parameter behaviour in the vicinity of the phase transition have also provided reliable results by application of the suitable thermodynamic relations. Particularly, the validity of the reported indirect results has been proven in each case by comparison with direct and quasi-direct results. In all the studied materials the work has been especially devoted to the study of the reversibility of the thermal response upon field cycling and the search of the physical conditions leading to its enhancement, which is a big issue in view of applications to new cooling devices in which the persistence of the caloric performance upon field cycling is crucial. In addition, the multicaloric properties have also been explored. It has been shown that adding more than one field as a driving force of the caloric effect can significantly enhance its performance and lead to a tailored thermal response by appropriately tuning the magnitude of each field. This is illustrated in figure 8.1 with the analogy of a

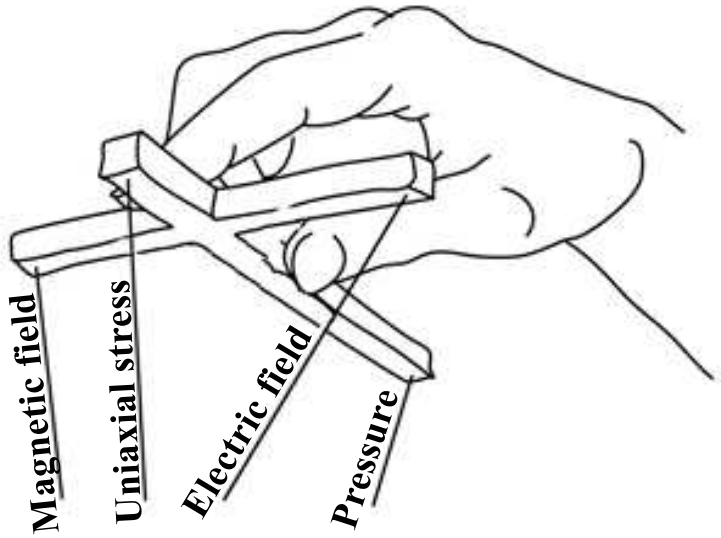


Fig. 8.1 The design of novel caloric materials which are sensitive to distinct external stimuli promise an advanced tailored thermal response by fine tuning the magnitude of each applied field.

hand monitoring a puppet in which each string represents a different field: the length (the magnitude) of each string (each field) is appropriately modified for monitoring the puppet (caloric response of the solid).

The giant caloric effects at the AFM-FM first-order transition in $Fe_{49}Rh_{51}$ have been studied in detail. Since the discovery of its giant MCE in 1990 [10] it has always remained among the best magnetocaloric materials [1, 229]. However, further elucidation regarding the magnitude and the reversibility of the magnetocaloric response was required due to the discrepancy in the reported values. The results given in chapter 4 have been published in [81, 230] and provide great insight into the characterization of the magnetocaloric features. On the one hand, it has been shown that the magnitude of the magnetocaloric entropy change saturates for fields $\mu_0 H \geq 1$ T at the upper bound given by the transition entropy change $\Delta S = 12.5 \pm 1$ J K$^{-1}$ kg$^{-1}$. On the other hand, in contrast with previous considerations certifying the disappearence of the thermal response after the first cycle as a result of its hysteresis of $\sim$ 10 K [2], our direct measurements confirm that great reproducibility of the effect exists for magnetic fields of $\mu_0 H \geq 2$ T. Interestingly, we have reported for the first the time the existence of giant BCE in $Fe_{49}Rh_{51}$. This new caloric effect adds up as a new functional property to be considered in this material. As shown, hydrostatic pressure is the type of mechanical stress which is best adapted to the symmetries of the isotropic expansion associated with the magnetovolumic first-order transition, which contrasts with

the lower sensitivity of the transition to uniaxial stresses ($\frac{dT_t}{d\sigma} \sim \frac{1}{3}\frac{dT_t}{dp}$). The complete description of the MCE and BCE in $Fe_{49}Rh_{51}$ has been a proper framework in preceding the study of the multicaloric response under the influence of magnetic field and hydrostatic pressure or uniaxial stress. Even though the magnitude of the caloric response is still bounded by the value of $\Delta S_t$, the addition of the second field notably enlarges the operation range and enhances the reversibility when the two fields are applied or removed so that both energetically favour the same phase.

The results concerning the giant magnetocaloric and barocaloric responses in Ni-Mn based Heusler materials given in chapter 5 have been published in [50, 84, 230–232]. These thermal phenomena have been analysed in a variety of samples comprising a significant spectrum of Ni-Mn-In, Ni-Co-Mn-Ga-In, and Ni-Cu-Mn-In compositions. First, the magnetocaloric properties in a sample of composition $Ni_{51}Mn_{33.4}In_{15.6}$ are presented. The sample was especially designed to display large enough entropy changes together with a low hysteresis ($\sim$ 4 K) by taking into account the cofactor conditions outlined in section 5.1.1 which involve an optimal compatibility between the parent and the twinned martensite interfaces. Calorimetry under magnetic field has been proven to be a great tool to identify the conditions for the reversibility of the thermal effect. We have shown that this region extends from the start temperature of the forward transition at zero field to the start temperature of the reverse transition under applied field. For a general picture of the caloric performance of this alloy system, the study proceeds with the analysis of a set of low hysteresis samples with tailored compositions so that they exhibit a magnetostructural martensitic transition at different distances to the Curie temperature $T_C$ of the austenite phase, which remains at approximately $\sim$ 304 K. It has been shown that this temperature distance influences the magnetic contribution to the transition entropy change $\Delta S_t$ which has consequences on the features of the caloric response. Hence, this distance appears to be a good parameter to rationalise the behaviour exhibited by the different quantities that characterise the baro- and magnetocaloric responses in these materials, as seen by the $\Delta S$, $\Delta T$, and RC plots in figure 5.24. In a similar manner, the baro- and magnetocaloric effects in the Ni-Co-Mn-Ga-In samples have also been studied. The reversibility emerges from the competition between the hysteresis and the sensitivity of the transition with the applied field. The set of Ni-Co-Mn-Ga-In samples display larger hysteresis ($\sim$ 14–18 K) which indeed compromises the reproducibility of the BCE. However, in the case of the MCE this is compensated by the particularly strong sensitivity of the transition to the magnetic field and good reproducibility is found upon field cycling. It has also been shown that the caloric performance can be tuned by tailoring the composition of the Heusler alloy. Section 5.6 reports the magnetocaloric performance of a Ni-Cu-Mn-In composite composed of fragments with gradual changes in

composition which gradually transform at different temperatures. It has been demonstrated that the development of composites can be highly desirable in view of tailoring the caloric performance with a particular purpose and widening of the operation range. Finally, the nature of the intermartensitic transitions in a Ni-Mn-Ga alloy has been discussed by means of magnetometric and calorimetric measurements which provide relevant information for a thermodynamic study. Our results point out the fact that these changes might occur through a phase transition rather than processes of detwinning of nano-twinned structures.

With regards to the potential multicaloric properties of the studied Heusler systems, it has been evidenced that these materials can display a strong sensitivity of the transition with the applied magnetic field and hydrostatic pressure. However, one should take into account that the thermal response driven by each field can display opposite trends as explained in section 5.4. In comparison with the isotropic $Fe_{49}Rh_{51}$ transition, the shear-like displacements related to the martensitic transitions in Heusler alloys prompt these materials to potentially exhibit large elastocaloric responses [92, 103] and an optimised sensitivity with uniaxial stress if compared with the response upon application of hydrostatic pressure. Both the large magnetic field and uniaxial stress sensitivity of the transition anticipate an exceptional multicaloric response of these materials when driven by these two fields, as already indicated by the preliminary results shown in section 5.8.

We have also studied the electrocaloric response in ferroelectric materials. At a first glance, the advantage of the use of thin films can be evident. In these conditions in which the thicknesses of the materials are typically restricted to $\sim$ 500 nm, the breakdown fields are enlarged in comparison to bulk samples [3, 189] and high values of the applied electric field are accessible. In thin films these fields are usually in the range of $\sim 500\,\mathrm{kV\,cm^{-1}}$ whereas in bulk samples they are of the order of $\sim 50\,\mathrm{kV\,cm^{-1}}$. Under large electric fields, the first-order transitions in electrocaloric materials typically become second-order type [233] leading to an increased reversibility and broadening of the ECE. However, the thin film geometry carries important drawbacks concerning their commercialization as cooling materials. Principally, the low thermal mass of these caloric materials yields to low values of the exchanged heat in absolute terms. In this regard, multilayer capacitors [234] can become highly convenient because they multiply the thermal mass of the caloric material without loosing the benefits of the thin film geometry, even though it results at the expense of a more complex structure with additional difficulties from the engineering point of view. Furthermore, the characterization of the ECE in thin films can be controversial. On the one hand, it usually relies on the indirect derivation obtained from measurements of pyroelectric coefficients. On the other hand, direct methods are especially challenging due to the low thermal mass of the films, deviations from

adiabatic conditions and heat transfer to temperaure measurement devices, substrates and connections [26].

In this dissertation, we have studied the ECE in bulk samples. The ECE in $BaTiO_3$ and $Pb(Sc_{0.5}Ta_{0.5})O_3$ FE-PE transitions is analysed by means of direct, quasi-direct and indirect methods which lead to consistent results. In comparison to the thin films performance, it is demonstrated that the electrocaloric response in bulk samples can also be of giant magnitude and driven by modest values of the applied electric field ($\sim$ 10 kV cm$^{-1}$). The studied materials display large electrocaloric strengths (BTO: $\frac{|Q|}{|\Delta E|} = 209$ J cm kg$^{-1}$ kV$^{-1}$ and $\frac{|\Delta T|}{|\Delta E|} = 220$ mK cm kV$^{-1}$, PST: $\frac{|Q|}{|\Delta E|} = 53$ J cm kg$^{-1}$ kV$^{-1}$ and $\frac{|\Delta T|}{|\Delta E|} = 150$ mK cm kV$^{-1}$) which are one or two orders of magnitude larger than the typical strengths of thin films as shown in tables 6.1 and 7.2. In the case of $BaTiO_3$, we have demonstrated the existence of a giant BCE in the vicinity of the C-T and T-O transitions at 400 K and 280 K. The reported results show that a great barocaloric performance can be found close to the Curie temperature of ferroelectric materials and indicate their great multicaloric potential due to the high sensitivity of the transition to both mechanical stresses and electric fields, which is in line with other studies [233, 235–237].

Recently, the giant barocaloric effect in ammonium sulphate [$(NH_4)_2SO_4$] near its ferrielectric phase transition [238, 239] has been reported [182]. The paper reported an outstanding barocaloric performance in this inexpensive material which currently has a big number of commercial applications, and opened the way of finding new caloric materials in other ferroelectric salts with similar features as well as exploring their multicaloric performance under the influence of electric field and mechanical stresses [233].

After attracting intense scientific attention in the last two decades, the topic of caloric materials has notably progressed. Nowadays, it covers a wide spectrum of research fields which put effort in many areas, from the physical understanding of the involved phase transitions to the engineering point of view for the design of an alternative refrigerator with novel materials. This has allowed the development of materials with advanced caloric and physical properties, including large reversible thermal responses driven by relatively modest values of the applied fields, strong fatigue resistance upon field cycling, and appropriate values of the thermal conductivity. In parallel, new promising refrigerator prototypes have also been presented [240, 241], even though their cost of implementation is still far to become competitive with the conventional vapor-compression technology, just as the finding of proper efficient materials with reduced environmental impact is still unresolved. Therefore, there are still numerous efforts to be made before their use on a large scale and this topic promises further progress in the next years.

# References


[1] X. Moya, S. Kar-Narayan, and N. D. Mathur. Caloric materials near ferroic phase transitions. *Nature Materials*, (5):439–450, 2014.

[2] V. K. Pecharsky and K. A. Gschneidner, Jr. Giant Magnetocaloric Effect in $Gd_5(Si_2Ge_2)$. *Phys. Rev. Lett.*, 78:4494–4497, Jun 1997.

[3] A. S. Mischenko, Q. Zhang, J. F. Scott, R. W. Whatmore, and N. D. Mathur. Giant electrocaloric effect in thin-film $PbZr_{0.95}Ti_{0.05}O_3$. *Science*, 311(5765):1270–1271, 2006.

[4] Erell Bonnot, Ricardo Romero, Lluís Mañosa, Eduard Vives, and Antoni Planes. Elastocaloric effect associated with the martensitic transition in shape-memory alloys. *Phys. Rev. Lett.*, 100:125901, Mar 2008.

[5] Lluís Mañosa, David González-Alonso, Antoni Planes, Erell Bonnot, Maria Barrio, Josep-Lluís Tamarit, Seda Aksoy, and Mehmet Acet. Giant solid-state barocaloric effect in the Ni-Mn-In magnetic shape-memory alloy. *Nature materials*, 9(6):478–481, 2010.

[6] A. Planes, T. Castán, and A. Saxena. Thermodynamics of multicaloric effects in multiferroics. *Philosophical Magazine*, 94(17):1893–1908, 2014.

[7] Oliver Gutfleisch, Matthew A. Willard, Ekkes Brück, Christina H. Chen, S. G. Sankar, and J. Ping Liu. Magnetic materials and devices for the 21st century: Stronger, lighter, and more energy efficient. *Advanced Materials*, 23(7):821–842, 2011.

[8] G Shirane, R Nathans, and CW Chen. Magnetic moments and unpaired spin densities in the Fe-Rh alloys. *Physical Review*, 134(6A):A1547, 1964.

[9] M. Fallot. Les alliages du fer avec les métaux de la famille du platine. *Ann. Phys.*, 10(291), 1938.

[10] S. A. Nikitin, G. Myalikgulyev, A. M. Tishin, M. P. Annaorazov, K. A. Asatryan, and A. L. Tyurin. The magnetocaloric effect in $Fe_{49}Rh_{51}$ compound. *Physics Letters A*, 148:363–366, 1990.

[11] Tanja Graf, Claudia Felser, and Stuart SP Parkin. Simple rules for the understanding of Heusler compounds. *Progress in solid state chemistry*, 39(1):1–50, 2011.

[12] J Kübler, AR William, and CB Sommers. Formation and coupling of magnetic moments in Heusler alloys. *Physical Review B*, 28(4):1745, 1983.

[13] Antoni Planes, Lluís Mañosa, and Mehmet Acet. Magnetocaloric effect and its relation to shape-memory properties in ferromagnetic Heusler alloys. *Journal of Physics: Condensed Matter*, 21(23):233201, 2009.

[14] Aslı Çakır, Lara Righi, Franca Albertini, Mehmet Acet, Michael Farle, and Selçuk Aktürk. Extended investigation of intermartensitic transitions in Ni-Mn-Ga magnetic shape memory alloys: A detailed phase diagram determination. *Journal of Applied Physics*, 114(18):183912, 2013.

[15] Zongbin Li, Nan Xu, Yudong Zhang, Claude Esling, Jean-Marc Raulot, Xiang Zhao, and Liang Zuo. Composition-dependent ground state of martensite in Ni–Mn–Ga alloys. *Acta Materialia*, 61(10):3858–3865, 2013.

[16] Franco Jona and Gen Shirane. *Ferroelectric crystals*, volume 1. Pergamon, 1962.

[17] Walter J. Merz. The electric and optical behavior of $BaTiO_3$ single-domain crystals. *Phys. Rev.*, 76:1221–1225, Oct 1949.

[18] Charles Kittel. *Introduction to Solid State Physics*. Wiley, 2005.

[19] N. Setter and L. E. Cross. The role of B-site cation disorder in diffuse phase transition behavior of perovskite ferroelectrics. *Journal of Applied Physics*, 51(8), 1980.

[20] L. A. Shebanov, E. H. Birks, and K. J. Borman. X-ray studies of electrocaloric lead-scandium tantalate ordered solid solutions. *Ferroelectrics*, 90(1):165–172, 1989.

[21] J. A Gough. A description of a property of caoutchouc or Indian rubber; with some reflections on the cause of the elasticity of this substance. *Phys. Rev.*, 1:288–295, 1805.

[22] E. Warburg. Magnetische Untersuchungen. *Annalen der Physik*, 249(5):141–164, 1881.

[23] Anders Smith. Who discovered the magnetocaloric effect? *The European Physical Journal H*, 38(4):507–517, 2013.

[24] P. Kobeko and J. Kurtschatov. Dielektrische Eigenschaften der Seignettesalzkristalle. *Zeitschrift für Physik*, 66(3):192–205, 1930.

[25] J. F. Scott. Electrocaloric materials. *Annual Review of Materials Research*, 41:229–40, 2011.

[26] T. Correia and Q Zhang. *Electrocaloric Materials. New Generation of Coolers*, volume 34. 2014.

[27] AI Karchevskii. Electrocaloric effect in polycrystalline barium titanate. *Soviet Physics-Solid State*, 3(10):2249–2254, 1962.

[28] S. Blundell. *Magnetism in Condensed Matter*. Oxford Master Series in Condensed Matter Physics. OUP Oxford, 2001.

[29] W. F. Giauque and D. P. MacDougall. Attainment of temperatures below 1° absolute by demagnetization of $Gd_2(SO_4)_3{\cdot}8H_2O$. *Phys. Rev.*, 43:768–768, May 1933.

[30] G. V. Brown. Magnetic heat pumping near room temperature. *Journal of Applied Physics*, 47(8):3673–3680, 1976.

[31] Osmann Sari and Mohamed Balli. From conventional to magnetic refrigerator technology. *International Journal of Refrigeration*, 37:8 – 15, 2014. New Developments in Magnetic Refrigeration.

[32] S.A. Nikitin, G. Myalikgulyev, M.P. Annaorazov, A.L. Tyurin, R.W. Myndyev, and S.A. Akopyan. Giant elastocaloric effect in FeRh alloy. *Physics Letters A*, 171(3–4):234 – 236, 1992.

[33] M. W. Zemansky and R. H. Dittman. *Heat and Thermodynamics: An Intermediate Textbook*. McGraw-Hill, New York, 1981.

[34] Lev Davidovich Landau. 29 - On the theory of phase transitions. In D. Ter Haar, editor, *Collected Papers of L.D. Landau*, pages 193 – 216. Pergamon, 1965.

[35] N. Goldenfeld. *Lectures on phase transitions and the renormalization group*, volume 85 of *Frontiers in Physics*. 1992.

[36] International Union of Crystallography. Online dictionary of crystallography.

[37] Vinod Wadhawan. *Introduction to ferroic materials*. CRC Press, 2000.

[38] James J Binney, Nigel J Dowrick, Andrew J Fisher, and M Newman. *The theory of critical phenomena: an introduction to the renormalization group*. Oxford University Press, Inc., 1992.

[39] A.M. Tishin. Magnetocaloric effect in strong magnetic fields. *Cryogenics*, 30(2):127 – 136, 1990.

[40] Aleksandr M Tishin and Youry I Spichkin. *The magnetocaloric effect and its applications*. Taylor & Francis, 2003.

[41] Lluís Mañosa, David Gonzalez-Alonso, Antoni Planes, Maria Barrio, Josep-Lluís Tamarit, Ivan S Titov, Mehmet Acet, Amitava Bhattacharyya, and Subham Majumdar. Inverse barocaloric effect in the giant magnetocaloric La–Fe–Si–Co compound. *Nature Communications*, 2:595, 2011.

[42] Thorsten Krenke, Eyüp Duman, Mehmet Acet, Eberhard F Wassermann, Xavier Moya, Lluís Mañosa, and Antoni Planes. Inverse magnetocaloric effect in ferromagnetic Ni–Mn–Sn alloys. *Nature materials*, 4(6):450–454, 2005.

[43] Xavier Moya, Emmanuel Defay, Volker Heine, and Neil D Mathur. Too cool to work. *Nature Physics*, 11(3):202–205, 2015.

[44] Emmanuel Defay, Sam Crossley, Sohini Kar-Narayan, Xavier Moya, and Neil D Mathur. The electrocaloric efficiency of ceramic and polymer films. *Advanced Materials*, 25(24):3337–3342, 2013.

[45] M.E. Wood and W.H. Potter. General analysis of magnetic refrigeration and its optimization using a new concept: maximization of refrigerant capacity. *Cryogenics*, 25(12):667 – 683, 1985.

[46] V Franco, JS Blázquez, B Ingale, and A Conde. The magnetocaloric effect and magnetic refrigeration near room temperature: materials and models. *Materials Research*, 42(1):305, 2012.

[47] Virgil Provenzano, Alexander J Shapiro, and Robert D Shull. Reduction of hysteresis losses in the magnetic refrigerant $Gd_5Ge_2Si_2$ by the addition of iron. *Nature*, 429(6994):853–857, 2004.

[48] L. Huang, D. Y. Cong, H. L. Suo, and Y. D. Wang. Giant magnetic refrigeration capacity near room temperature in $Ni_{40}Co_{10}Mn_{40}Sn_{10}$ multifunctional alloy. *Applied Physics Letters*, 104(13):132407, 2014.

[49] Xavier Moya, Enric Stern-Taulats, Sam Crossley, David González-Alonso, Sohini Kar-Narayan, Antoni Planes, Lluís Mañosa, and Neil D. Mathur. Giant electrocaloric strength in single-crystal $BaTiO_3$. *Advanced Materials*, 25(9):1360–1365, 2013.

[50] Baris Emre, Süheyla Yüce, Enric Stern-Taulats, Antoni Planes, Simone Fabbrici, Franca Albertini, and Lluís Mañosa. Large reversible entropy change at the inverse magnetocaloric effect in Ni-Co-Mn-Ga-In magnetic shape memory alloys. *Journal of Applied Physics*, 113(21):213905, 2013.

[51] L. Caron, Z.Q. Ou, T.T. Nguyen, D.T. Cam Thanh, O. Tegus, and E. Brück. On the determination of the magnetic entropy change in materials with first-order transitions. *Journal of Magnetism and Magnetic Materials*, 321(21):3559 – 3566, 2009. Current Perspectives: Magnetocaloric Materials.

[52] George T. Armstrong. The calorimeter and its influence on the development of chemistry. *Journal of Chemical Education*, 41(6):297, 1964.

[53] Richard Williams. The mystery of disappearing heat. *Weatherwise*, 49(4):28–29, 1996.

[54] Jean Rouquerol, I. Wadsö, T.J. Lever, and P.J. Haines. Chapter 2. Developments in nomenclature. In Michael E. Brown and Patrick K. Gallagher, editors, *Recent Advances, Techniques and Applications*, volume 5 of *Handbook of Thermal Analysis and Calorimetry*, pages 13 – 54. Elsevier Science B.V., 2008.

[55] W Zielenkiewicz. Towards classification of calorimeters. *Journal of Thermal Analysis and Calorimetry*, 91(2):663–671, 2007.

[56] Jordi Marcos, Fèlix Casanova, Xavier Batlle, Amílcar Labarta, Antoni Planes, and Lluís Mañosa. A high-sensitivity differential scanning calorimeter with magnetic field for magnetostructural transitions. *Review of Scientific Instruments*, 74(11):4768–4771, 2003.

[57] Lluís Mañosa, Marc Bou, Carme Calles, and Albert Cirera. Low-cost differential scanning calorimeter. *American Journal of Physics*, 64(3), 1996.

[58] Günther Höhne, Wolfgang F Hemminger, and H-J Flammersheim. *Differential scanning calorimetry*. Springer Science & Business Media, 2013.

[59] A Würflinger. Differential thermal analysis under high pressure iv: Low-temperature dta of solid-solid and solid-liquid transitions of several hydrocarbons up to 3 kbar. *Berichte der Bunsengesellschaft für physikalische Chemie*, 79(12):1195–1201, 1975.

[60] R.K. Pathria and P.D. Beale. *Statistical Mechanics*. Elsevier Science, 1996.

[61] MJ O'neill. Measurement of Specific Heat Functions by Differential Scanning Calorimetry. *Analytical Chemistry*, 38(10):1331–1336, 1966.

[62] DA Ditmars, S Ishihara, SS Chang, G Bernstein, and ED West. Enthalpy and heat-capacity standard reference material: synthetic sapphire ($\alpha$-$Al_2O_3$) from 10 to 2250 k. *J. Res. Natl. Bur. Stand*, 87(2):159–163, 1982.

[63] John Clarke and Alex I Braginski. The squid handbook: fundamentals and technology of SQUIDs and SQUID Systems, Volume i, 2004.

[64] Reinhold Kleiner, Dieter Koelle, Frank Ludwig, and John Clarke. Superconducting quantum interference devices: State of the art and applications. *Proceedings of the IEEE*, 92(10):1534–1548, 2004.

[65] Reinhold Kleiner and Werner Buckel. *Superconductivity: An Introduction*. John Wiley & Sons, 2015.

[66] K Gramm, L Lundgren, and O Beckman. Squid magnetometer for mangetization measurements. *Physica Scripta*, 13(2):93, 1976.

[67] Easylab mcell 10 product details.

[68] L. J. Swartzendruber. The Fe - Rh (Iron - Rhodium) system. *Bulletin of Alloy Phase Diagrams*, 5(5):456–462, 1984.

[69] Simon Oddsson Mariager, F Pressacco, G Ingold, A Caviezel, E Möhr-Vorobeva, P Beaud, SL Johnson, CJ Milne, E Mancini, S Moyerman, et al. Structural and magnetic dynamics of a laser induced phase transition in FeRh. *Physical Review Letters*, 108(8):087201, 2012.

[70] AX Gray, DW Cooke, Peter Krüger, C Bordel, AM Kaiser, S Moyerman, EE Fullerton, S Ueda, Y Yamashita, A Gloskovskii, et al. Electronic structure changes across the metamagnetic transition in FeRh via hard X-ray photoemission. *Physical review letters*, 108(25):257208, 2012.

[71] PM Derlet. Landau-Heisenberg Hamiltonian model for FeRh. *Physical Review B*, 85(17):174431, 2012.

[72] David W. Cooke, F. Hellman, C. Baldasseroni, C. Bordel, S. Moyerman, and E. E. Fullerton. Thermodynamic measurements of Fe-Rh alloys. *Phys. Rev. Lett.*, 109:255901, Dec 2012.

[73] MA De Vries, M Loving, AP Mihai, LH Lewis, D Heiman, and CH Marrows. Hall-effect characterization of the metamagnetic transition in FeRh. *New Journal of Physics*, 15(1):013008, 2013.

[74] JB Staunton, Rudra Banerjee, M dos Santos Dias, A Deak, and L Szunyogh. Fluctuating local moments, itinerant electrons, and the magnetocaloric effect: Compositional hypersensitivity of FeRh. *Physical Review B*, 89(5):054427, 2014.

[75] Jan-Ulrich Thiele, Stefan Maat, and Eric E Fullerton. FeRh/FePt exchange spring films for thermally assisted magnetic recording media. *Applied Physics Letters*, 82(17):2859–2861, 2003.

[76] M. P. Annaorazov, S. A. Nikitin, A. L. Tyurin, K. A. Asatryan, and A. Kh. Dovletov. Anomalously high entropy change in FeRh alloy. *Journal of Applied Physics*, 79(3):1689–1695, 1996.

[77] V. K. Pecharsky and K. A. Gschneidner. Tunable magnetic regenerator alloys with a giant magnetocaloric effect for magnetic refrigeration from $\sim$ 20 to $\sim$ 290 K. *Applied Physics Letters*, 70(24), 1997.

[78] Meghmalhar Manekar and SB Roy. Reproducible room temperature giant magnetocaloric effect in Fe–Rh. *Journal of Physics D: Applied Physics*, 41(19):192004, 2008.

[79] R. C. Wayne. Pressure dependence of the magnetic transitions in Fe-Rh alloys. *Phys. Rev.*, 170:523–527, Jun 1968.

[80] Pallavi Kushwaha, Pallab Bag, R Rawat, and P Chaddah. First-order antiferro–ferromagnetic transition in $Fe_{49}(Rh_{0.93}Pd_{0.07})_{51}$ under simultaneous application of magnetic field and external pressure. *Journal of Physics: Condensed Matter*, 24(9):096005, 2012.

[81] Enric Stern-Taulats, Antoni Planes, Pol Lloveras, Maria Barrio, Josep-Lluís Tamarit, Sabyasachi Pramanick, Subham Majumdar, Carlos Frontera, and Lluís Mañosa. Barocaloric and magnetocaloric effects in $Fe_{49}Rh_{51}$. *Phys. Rev. B*, 89:214105, Jun 2014.

[82] Enric Stern-Taulats, Adrià Gràcia-Condal, Antoni Planes, Pol Lloveras, Maria Barrio, Josep-Lluís Tamarit, Sabyasachi Pramanick, Subham Majumdar, and Lluís Mañosa. Reversible adiabatic temperature changes at the magnetocaloric and barocaloric effects in $Fe_{49}Rh_{51}$. *Applied Physics Letters*, 107(15), 2015.

[83] Fèlix Casanova, Amílcar Labarta, Xavier Batlle, Francisco J. Pérez-Reche, Eduard Vives, Lluís Mañosa, and Antoni Planes. Direct observation of the magnetic-field-induced entropy change in $Gd_5(Si_xGe_{1-x})_4$ giant magnetocaloric alloys. *Applied Physics Letters*, 86(26), 2005.

[84] Enric Stern-Taulats, Pedro O. Castillo-Villa, Lluís Mañosa, Carlos Frontera, Sabyasachi Pramanick, Subham Majumdar, and Antoni Planes. Magnetocaloric effect in the low hysteresis Ni-Mn-In metamagnetic shape-memory Heusler alloy. *Journal of Applied Physics*, 115(17), 2014.

[85] M.J. Richardson, D. Melville, and J.A. Ricodeau. Specific heat measurements on an FeRh alloy. *Physics Letters A*, 46(2):153 – 154, 1973.

[86] Fèlix Casanova, Amílcar Labarta, Xavier Batlle, Jordi Marcos, Lluís Mañosa, Antoni Planes, and Sophie de Brion. Effect of a magnetic field on the magnetostructural phase transition in $Gd_5(Si_xGe_{1-x})_4$. *Physical Review B*, 69(10):104416, 2004.

[87] V Recarte, JI Pérez-Landazábal, S Kustov, and E Cesari. Entropy change linked to the magnetic field induced martensitic transformation in a Ni–Mn–In–Co shape memory alloy. *Journal of Applied Physics*, 107(5):053501, 2010.

[88] Fèlix Casanova, Xavier Batlle, Amílcar Labarta, Jordi Marcos, Lluís Mañosa, and Antoni Planes. Entropy change and magnetocaloric effect in $Gd_5(Si_xGe_{1-x})_4$. *Physical Review B*, 66(10):100401, 2002.

[89] Süheyla Yüce, Maria Barrio, Baris Emre, Enric Stern-Taulats, Antoni Planes, Josep-Lluís Tamarit, Yaroslav Mudryk, Jr. Karl A. Gschneidner, Vitalij K. Pecharsky, and Lluís Mañosa. Barocaloric effect in the magnetocaloric prototype $Gd_5Si_2Ge_2$. *Applied Physics Letters*, 101(7):071906, 2012.

[90] Daichi Matsunami, Asaya Fujita, Koshi Takenaka, and Mika Kano. Giant barocaloric effect enhanced by the frustration of the antiferromagnetic phase in $Mn_3GaN$. *Nature materials*, 14(1):73–78, 2015.

[91] Jian Liu, Tino Gottschall, Konstantin P Skokov, James D Moore, and Oliver Gutfleisch. Giant magnetocaloric effect driven by structural transitions. *Nature materials*, 11(7):620–626, 2012.

[92] Lluís Mañosa and Antoni Planes. Materials with giant mechanocaloric effects: Cooling by strength. *Advanced Materials*, pages 1603607–n/a, 2016. 1603607.

[93] T. Graf, J. Winterlik, L. Müchler, G. H. Fecher, C. Felser, and S. S. P. Parkin. Magnetic Heusler Compounds. In Kurt H Jürgen Buschow, editor, *Handbook of magnetic materials*, volume 21. Elsevier, 2013.

[94] Fr Heusler, W Starck, and E Haupt. Magnetic-chemical studies. *Verh. Dtsch. Phys. Ges*, 5:219–223, 1903.

[95] P. G. van Engen, K. H. J. Buschow, R. Jongebreur, and M. Erman. PtMnSb, a material with very high magneto-optical Kerr effect. *Applied Physics Letters*, 42(2), 1983.

[96] Tanja Graf, Claudia Felser, and Stuart SP Parkin. Heusler compounds: Applications in spintronics. *Handbook of Spintronics*, pages 335–364, 2016.

[97] Stanislav Chadov, Xiaoliang Qi, Jürgen Kübler, Gerhard H Fecher, Claudia Felser, and Shou Cheng Zhang. Tunable multifunctional topological insulators in ternary Heusler compounds. *Nature materials*, 9(7):541–545, 2010.

[98] T. Klimczuk, C. H. Wang, K. Gofryk, F. Ronning, J. Winterlik, G. H. Fecher, J.-C. Griveau, E. Colineau, C. Felser, J. D. Thompson, D. J. Safarik, and R. J. Cava. Superconductivity in the Heusler family of intermetallics. *Phys. Rev. B*, 85:174505, May 2012.

[99] S Sakurada and N Shutoh. Effect of Ti substitution on the thermoelectric properties of (Zr, Hf) NiSn half-Heusler compounds. *Applied Physics Letters*, 86(8):082105, 2005.

[100] Seda Aksoy, Thorsten Krenke, Mehmet Acet, Eberhard F. Wassermann, Xavier Moya, Lluís Mañosa, and Antoni Planes. Magnetization easy axis in martensitic Heusler alloys estimated by strain measurements under magnetic field. *Applied Physics Letters*, 91(25), 2007.

[101] Franca Albertini, Lara Righi, Antonio Paoluzi, Massimo Solzi, David Serrate, Simone Fabbrici, Pedro Algarabel, Jiri Kamarad, Zdenek Arnold, Giacomo Porcari, and Chiara Pernechele. Reverse magnetostructural transitions by Co and In doping NiMnGa alloys: Structural, magnetic, and magnetoelastic properties. *Materials Science Forum*, 684:151–163, 7 2011.

[102] Feng-xia Hu, Bao-gen Shen, and Ji-rong Sun. Magnetic entropy change in $Ni_{51.5}Mn_{22.7}Ga_{25.8}$ alloy. *Applied Physics Letters*, 76:3460, 2000.

[103] Rubén Millán-Solsona, Enric Stern-Taulats, Eduard Vives, Antoni Planes, Jyoti Sharma, Ajaya K. Nayak, K. G. Suresh, and Lluís Mañosa. Large entropy change associated with the elastocaloric effect in polycrystalline Ni-Mn-Sb-Co magnetic shape memory alloys. *Applied Physics Letters*, 105(24), 2014.

[104] A. Hirohata, M. Kikuchi, N. Tezuka, K. Inomata, J.S. Claydon, Y.B. Xu, and G. van der Laan. Heusler alloy/semiconductor hybrid structures. *Current Opinion in Solid State and Materials Science*, 10(2):93 – 107, 2006.

[105] Xavier Moya. *Comportament vibracional i magnètic d'aliatges funcionals tipus Heusler*. PhD thesis, University of Barcelona, 2008.

[106] Seda Aksoy. *Magnetic interactions in martensitic Ni-Mn-based Heusler systems*. PhD thesis, Universität Duisburg-Essen, Fakultät für Physik» Experimentalphysik, 2010.

[107] S. Kaufmann, U. K. Rößler, O. Heczko, M. Wuttig, J. Buschbeck, L. Schultz, and S. Fähler. Adaptive modulations of martensites. *Phys. Rev. Lett.*, 104:145702, Apr 2010.

[108] VA Chernenko, J Pons, C Seguı, and E Cesari. Premartensitic phenomena and other phase transformations in Ni–Mn–Ga alloys studied by dynamical mechanical analysis and electron diffraction. *Acta Materialia*, 50(1):53–60, 2002.

[109] P Entel, VD Buchelnikov, VV Khovailo, AT Zayak, WA Adeagbo, ME Gruner, HC Herper, and EF Wassermann. Modelling the phase diagram of magnetic shape memory Heusler alloys. *Journal of Physics D: Applied Physics*, 39(5):865, 2006.

[110] E Şaşıoğlu, LM Sandratskii, and P Bruno. First-principles calculation of the intersublattice exchange interactions and curie temperatures of the full Heusler alloys $Ni_2$ Mn X (X= Ga, In, Sn, Sb). *Physical Review B*, 70(2):024427, 2004.

[111] Stefan Kaufmann, Robert Niemann, Thomas Thersleff, Ulrich K Rößler, Oleg Heczko, Jörg Buschbeck, Bernhard Holzapfel, Ludwig Schultz, and Sebastian Fähler. Modulated martensite: why it forms and why it deforms easily. *New Journal of Physics*, 13(5):053029, 2011.

[112] Alexei Sozinov, AA Likhachev, N Lanska, and Kari Ullakko. Giant magnetic-field-induced strain in NiMnGa seven-layered martensitic phase. *Applied Physics Letters*, 80(10):1746–1748, 2002.

[113] Kazuhiro Otsuka and Clarence Marvin Wayman. *Shape memory materials*. Cambridge university press, 1999.

[114] O. Gutfleisch, T. Gottschall, M. Fries, D. Benke, I. Radulov, K. P. Skokov, H. Wende, M. Gruner, M. Acet, P. Entel, and M. Farle. Mastering hysteresis in magnetocaloric materials. *Philosophical Transactions of the Royal Society of London A: Mathematical, Physical and Engineering Sciences*, 374(2074), 2016.

[115] Tino Gottschall. *On the magnetocaloric properties of Heusler compounds: Reversible, time- and size-dependent effects of the martensitic phase transition*. PhD thesis, Technische Universität Darmstadt, 2016.

[116] R Niemann, S Hahn, A Diestel, A Backen, L Schultz, K Nielsch, MF-X Wagner, and S Fähler. Reducing the nucleation barrier in magnetocaloric Heusler alloys by nanoindentation. *APL Materials*, 4(6):064101, 2016.

[117] Zhiyong Zhang, Richard D. James, and Stefan Müller. Energy barriers and hysteresis in martensitic phase transformations. *Acta Materialia*, 57(15):4332 – 4352, 2009.

[118] Vijay Srivastava, Xian Chen, and Richard D James. Hysteresis and unusual magnetic properties in the singular Heusler alloy $Ni_{45}Co_5Mn_{40}Sn_{10}$. *Appl. Phys. Lett*, 97(1):014101, 2010.

[119] Yintao Song, Xian Chen, Vivekanand Dabade, Thomas W Shield, and Richard D James. Enhanced reversibility and unusual microstructure of a phase-transforming material. *Nature*, 502(7469):85–88, 2013.

[120] RD James and Zhiyong Zhang. A way to search for multiferroic materials with "unlikely" combinations of physical properties. In *Magnetism and structure in functional materials*, pages 159–175. Springer, 2005.

[121] Jing-Han Chen, Nickolaus M. Bruno, Ibrahim Karaman, Yujin Huang, Jianguo Li, and Joseph H. Ross. Calorimetric and magnetic study for $Ni_{50}Mn_{36}In_{14}$ and relative cooling power in paramagnetic inverse magnetocaloric systems. *Journal of Applied Physics*, 116(20), 2014.

[122] Xian Chen, Vijay Srivastava, Vivekanand Dabade, and Richard D. James. Study of the cofactor conditions: Conditions of supercompatibility between phases. *Journal of the Mechanics and Physics of Solids*, 61(12):2566 – 2587, 2013.

[123] John C Slater. Cohesion in monovalent metals. *Physical Review*, 35(5):509, 1930.

[124] Ersoy Şaşıoğlu. *First-principles study of the exchange interactions and Curie temperature in Heusler alloys*. PhD thesis, Doctoral Thesis, Mathematisch–Naturwissens chaftlich–Technischen Fakultät der Martin–Luther–Universität Halle, Wittenberg, 1975.

[125] Parijat Borgohain and Munima B Sahariah. Effect of compositional and antisite disorder on the electronic and magnetic properties of Ni–Mn–In heusler alloy. *Journal of Physics: Condensed Matter*, 27(17):175502, 2015.

[126] Iosif Galanakis. *Theory of Heusler and Full-Heusler Compounds*, pages 3–36. Springer International Publishing, Cham, 2016.

[127] E Şaşıoğlu, Leonid M Sandratskii, and Patrick Bruno. Role of conduction electrons in mediating exchange interactions in Mn-based Heusler alloys. *Physical Review B*, 77(6):064417, 2008.

[128] Antoni Planes. Viewpoint: Controlling the martensitic transition in Heusler shape-memory materials. *Physics*, 3:36, 2010.

[129] Kurt Heinz Jürgen Buschow, Frank R Boer, et al. *Physics of magnetism and magnetic materials*, volume 92. Springer, 2003.

[130] J.M.D. Coey. *Magnetism and Magnetic Materials*. Magnetism and Magnetic Materials. Cambridge University Press, 2010.

[131] I Galanakis, PH Dederichs, and N Papanikolaou. Slater-Pauling behavior and origin of the half-metallicity of the full-Heusler alloys. *Physical Review B*, 66(17):174429, 2002.

[132] F. X. Hu, J. Wang, J. Shen, B. Gao, J. R. Sun, and B. G. Shen. Large magnetic entropy change with small thermal hysteresis near room temperature in metamagnetic alloys $Ni_{51}Mn_{49-x}In_{16}$. *Journal of Applied Physics*, 105(7):–, 2009.

[133] I Titov, M Acet, M Farle, D Gonzalez-Alonso, L Mañosa, A Planes, and T Krenke. Hysteresis effects in the inverse magnetocaloric effect in martensitic Ni-Mn-In and Ni-Mn-Sn. *Journal of Applied Physics*, 112(7):073914, 2012.

[134] Hailemichael M Seyoum, Mohammadreza Ghahremani, Hatem ElBidweihy, Lawrence H Bennett, Edward Della Torre, Francis Johnson, and Min Zuo. Metastability in the magnetic structure of $Ni_{51}Mn_{33.4}In_{15.6}$ Heusler alloy. *IEEE Magnetics Letters*, 4:6000204–6000204, 2013.

[135] W Ito, Y Imano, R Kainuma, Y Sutou, K Oikawa, and K Ishida. Martensitic and magnetic transformation behaviors in Heusler-type NiMnIn and NiCoMnIn metamagnetic shape memory alloys. *Metallurgical and Materials Transactions A*, 38(4):759–766, 2007.

[136] S Kustov, ML Corró, J Pons, and E Cesari. Entropy change and effect of magnetic field on martensitic transformation in a metamagnetic Ni–Co–Mn–In shape memory alloy. *Applied Physics Letters*, 94(19):191901, 2009.

[137] Antoni Planes, Lluís Mañosa, and Mehmet Acet. Recent progress and future perspectives in magnetic and metamagnetic shape-memory heusler alloys. In *Materials Science Forum*, volume 738, pages 391–399. Trans Tech Publ, 2013.

[138] T Kihara, X Xu, W Ito, R Kainuma, and M Tokunaga. Direct measurements of inverse magnetocaloric effects in metamagnetic shape-memory alloy NiCoMnIn. *Physical Review B*, 90(21):214409, 2014.

[139] Tino Gottschall, Konstantin P. Skokov, Dimitri Benke, Markus E. Gruner, and Oliver Gutfleisch. Contradictory role of the magnetic contribution in inverse magnetocaloric Heusler materials. *Phys. Rev. B*, 93:184431, May 2016.

[140] Lluís Mañosa, Xavier Moya, Antoni Planes, Oliver Gutfleisch, Julia Lyubina, Maria Barrio, Josep-Lluís Tamarit, Seda Aksoy, Thorsten Krenke, and Mehmet Acet. Effects of hydrostatic pressure on the magnetism and martensitic transition of Ni–Mn–In magnetic superelastic alloys. *Applied Physics Letters*, 92(1), 2008.

[141] T. Miyamoto, W. Ito, R.Y. Umetsu, R. Kainuma, T. Kanomata, and K. Ishida. Phase stability and magnetic properties of $Ni_{50}Mn_{50-x}In_x$ Heusler-type alloys. *Scripta Materialia*, 62(3):151 – 154, 2010.

[142] Chun-Mei Li, Hu-Bin Luo, Qing-Miao Hu, Rui Yang, Börje Johansson, and Levente Vitos. Role of magnetic and atomic ordering in the martensitic transformation of Ni-Mn-In from a first-principles study. *Phys. Rev. B*, 86:214205, Dec 2012.

[143] AK Nayak, C Salazar Mejia, SW D'Souza, S Chadov, Y Skourski, C Felser, and M Nicklas. Large field-induced irreversibility in Ni-Mn based Heusler shape-memory alloys: A pulsed magnetic field study. *Physical Review B*, 90(22):220408, 2014.

[144] S. Aksoy, M. Acet, P. P. Deen, L. Mañosa, and A. Planes. Magnetic correlations in martensitic Ni-Mn-based Heusler shape-memory alloys: Neutron polarization analysis. *Phys. Rev. B*, 79:212401, Jun 2009.

[145] M. Ghorbani Zavareh, C. Salazar Mejía, A. K. Nayak, Y. Skourski, J. Wosnitza, C. Felser, and M. Nicklas. Direct measurements of the magnetocaloric effect in pulsed magnetic fields: The example of the Heusler alloy $Ni_{50}Mn_{35}In_{15}$. *Applied Physics Letters*, 106(7), 2015.

[146] Takashi Fukuda, Tomoyuki Kakeshita, and Yong hee Lee. An interpretation of the kinetics of martensitic transformation in a $Ni_{45}Co_5Mn_{36.5}In_{13.5}$ alloy. *Acta Materialia*, 81:121 – 127, 2014.

[147] Wataru Ito, Kouhei Ito, Rie Y. Umetsu, Ryosuke Kainuma, Keiichi Koyama, Kazuo Watanabe, Asaya Fujita, Katsunari Oikawa, Kiyohito Ishida, and Takeshi Kanomata. Kinetic arrest of martensitic transformation in the NiCoMnIn metamagnetic shape memory alloy. *Applied Physics Letters*, 92(2), 2008.

[148] V. Recarte, J.I. Pérez-Landazábal, V. Sánchez-Alarcos, V. Zablotskii, E. Cesari, and S. Kustov. Entropy change linked to the martensitic transformation in metamagnetic shape memory alloys. *Acta Materialia*, 60(6–7):3168 – 3175, 2012.

[149] S. Fabbrici, F. Albertini, A. Paoluzi, F. Bolzoni, R. Cabassi, M. Solzi, L. Righi, and G. Calestani. Reverse magnetostructural transformation in Co-doped NiMnGa multifunctional alloys. *Applied Physics Letters*, 95(2), 2009.

[150] G. Porcari, S. Fabbrici, C. Pernechele, F. Albertini, M. Buzzi, A. Paoluzi, J. Kamarad, Z. Arnold, and M. Solzi. Reverse magnetostructural transformation and adiabatic temperature change in Co- and In-substituted Ni-Mn-Ga alloys. *Phys. Rev. B*, 85:024414, Jan 2012.

[151] Simone Fabbrici, Giacomo Porcari, Francesco Cugini, Massimo Solzi, Jiri Kamarad, Zdenek Arnold, Riccardo Cabassi, and Franca Albertini. Co and in doped ni-mn-ga magnetic shape memory alloys: A thorough structural, magnetic and magnetocaloric study. *Entropy*, 16(4):2204–2222, 2014.

[152] Francisco-José Pérez-Reche, Marcelo Stipcich, Eduard Vives, Lluís Mañosa, Antoni Planes, and Michel Morin. Kinetics of martensitic transitions in Cu-Al-Mn under thermal cycling: Analysis at multiple length scales. *Phys. Rev. B*, 69:064101, Feb 2004.

[153] Ekkes Brück. Developments in magnetocaloric refrigeration. *Journal of Physics D: Applied Physics*, 38(23):R381, 2005.

[154] Lluís Mañosa, Antoni Planes, and Mehmet Acet. Advanced materials for solid-state refrigeration. *Journal of Materials Chemistry A*, 2013.

[155] Melvin M Vopson. Theory of giant-caloric effects in multiferroic materials. *Journal of Physics D: Applied Physics*, 46(34):345304, 2013.

[156] Ch. Binek and V. Burobina. Near-room-temperature refrigeration through voltage-controlled entropy change in multiferroics. *Applied Physics Letters*, 102(3), 2013.

[157] J. S. Amaral and V. S. Amaral. Disorder effects in giant magnetocaloric materials. *Physica Status Solidi (a)*, 211(5):971–974, 2014.

[158] J. L. Sánchez Llamazares, H. Flores-Zuñiga, C. Sánchez-Valdes, C. A. Ross, and C. García. Refrigerant capacity of austenite in as-quenched and annealed $Ni_{51.1}Mn_{31.2}In_{17.7}$ melt spun ribbons. *Journal of Applied Physics*, 111(7), 2012.

[159] S.C. Paticopoulos, R. Caballero-Flores, V. Franco, J.S. Blázquez, A. Conde, K.E. Knipling, and M.A. Willard. Enhancement of the magnetocaloric effect in composites: Experimental validation. *Solid State Communications*, 152(16):1590 – 1594, 2012.

[160] A. M. Gomes, J. R. Proveti, A. Y. Takeuchi, E. C. Passamani, C. Larica, and A. P. Guimarães. $La(Fe_{1-x}Co_x)_{11.44}Al_{1.56}$: A composite system for Ericsson-cycle-based magnetic refrigerators. *Journal of Applied Physics*, 99(11), 2006.

[161] Mohamed Balli, Daniel Fruchart, and Damien Gignoux. The $LaFe_{11.2}Co_{0.7}Si_{1.1}C_x$ carbides for magnetic refrigeration close to room temperature. *Applied Physics Letters*, 92(23), 2008.

[162] Pablo Álvarez, Pedro Gorria, José L. Sánchez Llamazares, and Jesús A. Blanco. Searching the conditions for a table-like shape of the magnetic entropy in magnetocaloric materials. *Journal of Alloys and Compounds*, 568:98 – 101, 2013.

[163] H. Fu, Z. Ma, X. J. Zhang, D. H. Wang, B. H. Teng, and E. Agurgo Balfour. Table-like magnetocaloric effect in the Gd-Co-Al alloys with multi-phase structure. *Applied Physics Letters*, 104(7), 2014.

[164] M. Ye, A. Kimura, Y. Miura, M. Shirai, Y. T. Cui, K. Shimada, H. Namatame, M. Taniguchi, S. Ueda, K. Kobayashi, R. Kainuma, T. Shishido, K. Fukushima, and T. Kanomata. Role of electronic structure in the martensitic phase transition of $Ni_2Mn_{1+x}Sn_{1-x}$ studied by hard-X-ray photoelectron spectroscopy and *Ab Initio* calculation. *Phys. Rev. Lett.*, 104:176401, Apr 2010.

[165] Thorsten Krenke, Mehmet Acet, Eberhard F. Wassermann, Xavier Moya, Lluís Mañosa, and Antoni Planes. Ferromagnetism in the austenitic and martensitic states of Ni-Mn-In alloys. *Phys. Rev. B*, 73:174413, May 2006.

[166] VV Martynov and VV Kokorin. The crystal structure of thermally-and stress-induced martensites in $Ni_2MnGa$ single crystals. *Journal de Physique III*, 2(5):739–749, 1992.

[167] AN Vasil'ev, A Kaiper V V Kokorin, VA Chernenko, J Tani, et al. Structural phase transitions induced in $Ni_2MnGa$ by low-temperature uniaxial compression. *Soviet Journal of Experimental and Theoretical Physics Letters*, 58:306, 1993.

[168] VA Chernenko, C Segui, E Cesari, J Pons, and VV Kokorin. Sequence of martensitic transformations in Ni-Mn-Ga alloys. *Physical Review B*, 57(5):2659, 1998.

[169] C Segui, VA Chernenko, J Pons, E Cesari, V Khovailo, and T Takagi. Low temperature-induced intermartensitic phase transformations in Ni–Mn–Ga single crystal. *Acta Materialia*, 53(1):111–120, 2005.

[170] Juan-Pablo Camarillo, Christian-Omar Aguilar-Ortiz, Horacio Flores-Zúñiga, David Ríos-Jara, Daniel-Enrique Soto-Parra, Enric Stern-Taulats, Lluís Mañosa, and Antoni Planes. Large reversible elastocaloric effect near room temperature in Ga-doped Ni-Mn-In metamagnetic shape-memory alloy. *Functional Materials Letters*, 0(ja):null, 2017.

[171] Julio A Gonzalo and Basilio Jiménez. *Ferroelectricity: The Fundamentals Collection*. John Wiley & Sons, 2008.

[172] KM Rabe, CH Ahn, and JM Triscone. Physics of ferroelectrics: A modern perspective. 2007.

[173] MM Vijatović, JD Bobić, and BD Stojanović. History and challenges of barium titanate: Part ii. *Science of Sintering*, 40(3):235–244, 2008.

[174] Yang Liu, Lee C Phillips, Richard Mattana, Manuel Bibes, Agnès Barthélémy, and Brahim Dkhil. Large reversible caloric effect in FeRh thin films via a dual-stimulus multicaloric cycle. *Nature Communications*, 7, 2016.

[175] Zhibo Yan, Yanyan Guo, Guoquan Zhang, and J.-M. Liu. High-performance programmable memory devices based on Co-Doped $BaTiO_3$. *Advanced Materials*, 23(11):1351–1355, 2011.

[176] CH Ahn, KM Rabe, and J-M Triscone. Ferroelectricity at the nanoscale: local polarization in oxide thin films and heterostructures. *Science*, 303(5657):488–491, 2004.

[177] Michael W Lufaso. Crystal structures, modeling, and dielectric property relationships of 2: 1 ordered $Ba_3MM'_2O_9$ (M= Mg, Ni, Zn; M'= Nb, Ta) perovskites. *Chemistry of materials*, 16(11):2148–2156, 2004.

[178] R Clarke and L Benguigui. The tricritical point in $BaTiO_3$. *Journal of Physics C: Solid State Physics*, 10(11):1963, 1977.

[179] T. Ishidate, S. Abe, H. Takahashi, and N. Môri. Phase diagram of $BaTiO_3$. *Phys. Rev. Lett.*, 78:2397–2400, Mar 1997.

[180] Bret Neese, Baojin Chu, Sheng-Guo Lu, Yong Wang, E. Furman, and Q. M. Zhang. Large electrocaloric effect in ferroelectric polymers near room temperature. *Science*, 321(5890):821–823, 2008.

[181] S. Crossley, N. D. Mathur, and X. Moya. New developments in caloric materials for cooling applications. *AIP Advances*, 5(6), 2015.

[182] P Lloveras, Enric Stern-Taulats, M Barrio, J-Ll Tamarit, Sam Crossley, Wei Li, Vladimir Pomjakushin, A Planes, Ll Mañosa, ND Mathur, et al. Giant barocaloric effects at low pressure in ferrielectric ammonium sulphate. *Nature Communications*, 6, 2015.

[183] H.F. Kay and P. Vousden. XCV. symmetry changes in barium titanate at low temperatures and their relation to its ferroelectric properties. *The London, Edinburgh, and Dublin Philosophical Magazine and Journal of Science*, 40(309):1019–1040, 1949.

[184] G. H. Kwei, A. C. Lawson, S. J. L. Billinge, and S. W. Cheong. Structures of the ferroelectric phases of barium titanate. *The Journal of Physical Chemistry*, 97(10):2368–2377, 1993.

[185] Gen Shirane, Sadao Hoshino, and Kazuo Suzuki. X-ray study of the phase transition in lead titanate. *Phys. Rev.*, 80:1105–1106, Dec 1950.

[186] E. A. Mikhaleva, I. N. Flerov, M. V. Gorev, M. S. Molokeev, A. V. Cherepakhin, A. V. Kartashev, N. V. Mikhashenok, and K. A. Sablina. Caloric characteristics of $PbTiO_3$ in the temperature range of the ferroelectric phase transition. *Physics of the Solid State*, 54(9):1832–1840, 2012.

[187] Yang Liu, Jie Wei, Pierre-Eymeric Janolin, Ingrid C. Infante, Xiaojie Lou, and Brahim Dkhil. Giant room-temperature barocaloric effect and pressure-mediated electrocaloric effect in $BaTiO_3$ single crystal. *Applied Physics Letters*, 104(16), 2014.

[188] Qi Li, Guangzu Zhang, Xiaoshan Zhang, Shenglin Jiang, Yike Zeng, and Qing Wang. Relaxor ferroelectric-based electrocaloric polymer nanocomposites with a broad operating temperature range and high cooling energy. *Advanced Materials*, 27(13):2236–2241, 2015.

[189] Samuel Crossley. *Electrocaloric materials and devices*. PhD thesis, University of Cambridge, 2013.

[190] G. Shirane, H. Danner, A. Pavlovic, and R. Pepinsky. Phase transitions in ferroelectric $KNbO_3$. *Phys. Rev.*, 93:672–673, Feb 1954.

[191] A.F. Devonshire. XCVI. Theory of barium titanate. *The London, Edinburgh, and Dublin Philosophical Magazine and Journal of Science*, 40(309):1040–1063, 1949.

[192] Walter J. Merz. Double hysteresis loop of $BaTiO_3$ at the curie point. *Phys. Rev.*, 91:513–517, Aug 1953.

[193] J. J. Wang, P. P. Wu, X. Q. Ma, and L. Q. Chen. Temperature-pressure phase diagram and ferroelectric properties of $BaTiO_3$ single crystal based on a modified Landau potential. *Journal of Applied Physics*, 108(11), 2010.

[194] Yang Bai, Guangping Zheng, and Sanqiang Shi. Direct measurement of giant electrocaloric effect in $BaTiO_3$ multilayer thick film structure beyond theoretical prediction. *Applied Physics Letters*, 96(19), 2010.

[195] Y. Park and H.G. Kim. The microstructure analysis of cerium-modified barium titanate having core-shell structured grains. *Ceramics International*, 23(4):329 – 336, 1997.

[196] S Kar-Narayan and N D Mathur. Direct and indirect electrocaloric measurements using multilayer capacitors. *Journal of Physics D: Applied Physics*, 43(3):032002, 2010.

[197] Gael Sebald, Laurence Seveyrat, Daniel Guyomar, Laurent Lebrun, Benoit Guiffard, and Sebastien Pruvost. Electrocaloric and pyroelectric properties of 0.75 $Pb(Mg_{1/3}Nb_{2/3})$ $O_3$–0.25 $PbTiO_3$ single crystals. *Journal of Applied Physics*, 100(12):124112, 2006.

[198] B. A. Tuttle and D. A. Payne. The effects of microstructure on the electrocaloric properties of $Pb(Zr,Sn,Ti)O_3$ ceramics. *Ferroelectrics*, 37(1):603–606, 1981.

[199] Gen Shirane and Akitsu Takeda. Transition energy and volume change at three transitions in barium titanate. *Journal of the Physical Society of Japan*, 7(1):1–4, 1952.

[200] Yanxue Tang, Xiangyong Zhao, Xiqi Feng, Weiqing Jin, and Haosu Luo. Pyroelectric properties of [111]-oriented $Pb(Mg_{1/3}Nb_{2/3})O_3$–$PbTiO_3$ crystals. *Applied Physics Letters*, 86(8), 2005.

[201] T. Yoshida, Y. Moriya, T. Tojo, H. Kawaji, T. Atake, and Y. Kuroiwa. Heat capacity at constant pressure and thermodynamic properties of phase transitions in $PbMO_3$ (M=Ti, Zr and Hf). *Journal of Thermal Analysis and Calorimetry*, 95(2):675–683, 2009.

[202] S. G. Lu, B. Rožič, Q. M. Zhang, Z. Kutnjak, R. Pirc, Minren Lin, Xinyu Li, and Lee Gorny. Comparison of directly and indirectly measured electrocaloric effect in relaxor ferroelectric polymers. *Applied Physics Letters*, 97(20), 2010.

[203] X Moya, LE Hueso, F Maccherozzi, AI Tovstolytkin, DI Podyalovskii, C Ducati, LC Phillips, M Ghidini, O Hovorka, A Berger, et al. Giant and reversible extrinsic magnetocaloric effects in $La_{0.7}Ca_{0.3}MnO_3$ films due to strain. *Nature materials*, 12(1):52–58, 2013.

[204] J Rodriguez-Carvajal, T Roisnel, and J Gonzales-Platas. Fullprof suite (2005 version). *CEA-CNRS, CEN Saclay, France: Laboratoire Léon Brillouin*, 2005.

[205] W. J. Merz. The effect of hydrostatic pressure on the curie point of barium titanate single crystals. *Phys. Rev.*, 78:52–54, Apr 1950.

[206] J. Klimowski. Effect of high hydrostatic pressure on the dielectric properties of $BaTiO_3$ single crystals. *Physica Status Solidi (b)*, 2(4):456–459, 1962.

[207] Shigeru Minomura, Tatsuyuki Kawakubo, Takehiko Nakagawa, and Shozo Sawada. Pressure dependence of curie point and tetragonal-orthorhombic transition point of $BaTiO_3$. *Japanese Journal of Applied Physics*, 3(9):562, 1964.

[208] G. A. Samara. Pressure and temperature dependences of the dielectric properties of the perovskites $BaTiO_3$ and $SrTiO_3$. *Phys. Rev.*, 151:378–386, Nov 1966.

[209] G. A. Samara. Pressure and temperature dependence of the dielectric properties and phase transitions of the ferroelectric perovskites: $PbTiO_3$ and $BaTiO_3$. *Ferroelectrics*, 2(1):277–289, 1971.

[210] M Malinowski, K Łukaszewicz, and S Åsbrink. The influence of high hydrostatic pressure on lattice parameters of a single crystal of BaTiO3. *Journal of Applied Crystallography*, 19(1):7–9, 1986.

[211] J L Zhu, S Lin, S M Feng, F Y Li, L J Wang, C Q Jin, X H Wang, and L T Li. The effects of high pressure on the ferroelectric properties of nano-$BaTiO_3$ ceramics. *Journal of Physics: Conference Series*, 121(16):162005, 2008.

[212] Yang Bai, Kai Ding, Guang-Ping Zheng, San-Qiang Shi, Jiang-Li Cao, and Lijie Qiao. The electrocaloric effect around the orthorhombic-tetragonal first-order phase transition in $BaTiO_3$. *AIP Advances*, 2(2), 2012.

[213] N M Shorrocks, R. W. Whatmore, and P. C. Osbond. Lead scandium tantalate for thermal detector applications. *Ferroelectrics*, 106(1):387–392, 1990.

[214] Francis S Galasso. *Structure, Properties and Preparation of Perovskite-Type Compounds: International Series of Monographs in Solid State Physics*, volume 5. Elsevier, 2013.

[215] C. G. F. Stenger and A. J. Burggraaf. Order–disorder reactions in the ferroelectric perovskites $Pb(Sc_{1/2}Nb_{1/2})O_3$ and $Pb(Sc_{1/2}Ta_{1/2})O_3$. Kinetics of the ordering process. *Physica Status Solidi (a)*, 61(1):275–285, 1980.

[216] Sidney B Lang and Helen LW Chan. *Frontiers of ferroelectricity: a special issue of the journal of materials science*. Springer Science & Business Media, 2007.

[217] L. Shebanovs, K. Borman, W. N. Lawless, and A. Kalvane. Electrocaloric effect in some perovskite ferroelectric ceramics and multilayer capacitors. *Ferroelectrics*, 273(1):137–142, 2002.

[218] CGF Stenger and AJ Burggraaf. Order–disorder reactions in the ferroelectric perovskites $Pb(Sc_{1/2}Nb_{1/2})O_3$ and $Pb(Sc_{1/2}Ta_{1/2})O_3$. II. Relation between ordering and properties. *physica status solidi (a)*, 61(2):653–664, 1980.

[219] C.G.F. Stenger, F.L. Scholten, and A.J. Burggraaf. Ordering and diffuse phase transitions in $Pb(Sc_{0.5}Ta_{0.5})O_3$ ceramics. *Solid State Communications*, 32(11):989–992, 1979.

[220] P. M. Woodward and K. Z. Baba-Kishi. Crystal structures of the relaxor oxide $Pb_2(ScTa)O_6$ in the paraelectric and ferroelectric states. *Journal of Applied Crystallography*, 35(2):233–242, Apr 2002.

[221] Fan Chu, Ian M. Reaney, and Nava Setter. Role of defects in the ferroelectric relaxor lead scandium tantalate. *Journal of the American Ceramic Society*, 78(7):1947–1952, 1995.

[222] L. Shebanovs, A. Sternberg, W. N. Lawless, and K. Borman. Isomorphous ion substitutions and order-disorder phenomena in highly electrocaloric lead-scandium tantalate solid solutions. *Ferroelectrics*, 184(1):239–242, 1996.

[223] F. Chu, N. Setter, and A. K. Tagantsev. The spontaneous relaxor-ferroelectric transition of $Pb(Sc_{0.5}Ta_{0.5})O_3$. *Journal of Applied Physics*, 74(8):5129–5134, 1993.

[224] P. C. Osbond and R W Whatmore. Dic17: High dielectric constant ceramics in the $PbSc_{0.5}Ta_{0.5}O_3$ -$PbZrO_3$ system. *Ferroelectrics*, 133(1):159–161, 1992.

[225] I.W. Chen. Structural origin of relaxor ferroelectrics—revisited. *Journal of Physics and Chemistry of Solids*, 61(2):197 – 208, 2000.

[226] L. Shebanov and K. Borman. On lead-scandium tantalate solid solutions with high electrocaloric effect. *Ferroelectrics*, 127(1):143–148, 1992.

[227] N. Setter and L. E. Cross. The contribution of structural disorder to diffuse phase transitions in ferroelectrics. *Journal of Materials Science*, 15(10):2478–2482, 1980.

[228] T M Correia, S Kar-Narayan, J S Young, J F Scott, N D Mathur, R W Whatmore, and Q Zhang. PST thin films for electrocaloric coolers. *Journal of Physics D: Applied Physics*, 44(16):165407, 2011.

[229] Karl G. Sandeman. Magnetocaloric materials: The search for new systems. *Scripta Materialia*, 67(6):566 – 571, 2012.

[230] Enric Stern-Taulats, Antoni Planes, Pol Lloveras, Maria Barrio, Josep-Lluís Tamarit, Sabyasachi Pramanick, Subham Majumdar, Süheyla Yüce, Baris Emre, Carlos Frontera, and Lluís Mañosa. Tailoring barocaloric and magnetocaloric properties in low-hysteresis magnetic shape memory alloys. *Acta Materialia*, 96:324 – 332, 2015.

[231] Lluís Mañosa, Enric Stern-Taulats, Antoni Planes, Pol Lloveras, Maria Barrio, Josep-Lluís Tamarit, Baris Emre, Suheyla Yüce, Simone Fabbrici, and Franca Albertini. Barocaloric effect in metamagnetic shape memory alloys. *physica status solidi (b)*, 251(10):2114–2119, 2014.

[232] Juan-Pablo Camarillo, Enric Stern-Taulats, Lluís Mañosa, Horacio Flores-Zúñiga, David Ríos-Jara, and Antoni Planes. Expanding the magnetocaloric operation range in Ni–Mn–In Heusler alloys by Cu-doping. *Journal of Physics D: Applied Physics*, 49(12):125006, 2016.

[233] Yang Liu, James F. Scott, and Brahim Dkhil. Some strategies for improving caloric responses with ferroelectrics. *APL Materials*, 4(6):064109, 2016.

[234] S. Kar-Narayan and N. D. Mathur. Predicted cooling powers for multilayer capacitors based on various electrocaloric and electrode materials. *Applied Physics Letters*, 95(24):242903, 2009.

[235] S. Lisenkov, B. K. Mani, C.-M. Chang, J. Almand, and I. Ponomareva. Multicaloric effect in ferroelectric $PbTiO_3$ from first principles. *Phys. Rev. B*, 87:224101, Jun 2013.

[236] Aditya Chauhan, Satyanarayan Patel, and Rahul Vaish. Elastocaloric effect in ferroelectric ceramics. *Applied Physics Letters*, 106(17):172901, 2015.

[237] Yang Liu, Guangzu Zhang, Qi Li, Laurent Bellaiche, James F. Scott, Brahim Dkhil, and Qing Wang. Towards multicaloric effect with ferroelectrics. *Phys. Rev. B*, 94:214113, Dec 2016.

[238] H-G Unruh and U Rüdiger. The ferroelectric transition of $(NH_4)_2SO_4$. *Le Journal de Physique Colloques*, 33(C2):C2–77, 1972.

[239] Akikatsu Sawada, Yutaka Takagi, and Yoshihiro Ishibashi. The origin of the ferroelectric phase transition in ammonium sulfate. *Journal of the Physical Society of Japan*, 34(3):748–754, 1973.

[240] Pradeep Bansal. Latest developments in not-in-kind refrigeration technologies. *Science and Technology for the Built Environment*, 22(5):473–474, 2016.

[241] Jaka Tušek, Kurt Engelbrecht, Dan Eriksen, Stefano Dall'Olio, Janez Tušek, and Nini Pryds. A regenerative elastocaloric heat pump. *Nature Energy*, 1:16134, 2016.

[242] S Timoshenko and JN Goodier. Theory of elasticity, 1970.

[243] Lev Davidovich Landau and Eugin M Lifshitz. *Course of theoretical physics, Theory of elasticity*. Pergamon Press Oxford, 1986.

[244] EG Ponyatovsky, AR Kut-sar, and GT Dubovka. The possibility of the existence of a singular triple point on the pressure-temperature diagram of an iron-rhodium alloy. *Sov. Phys. Crystallogr., july-aug. 1967, 12,–1–, 63-66*, 1967.

[245] AI Zakharov, AM Kadomtseva, RZ Levitin, and EG Ponyatovskii. Magnetic and magnetoelastic properties of a metamagnetic iron–rhodium alloy. *Sov. Phys. JETP*, 19:1348–1353, 1964.

[246] LI Vinokurova, AV Vlasov, and M Pardavi-Horváth. Pressure effects on magnetic phase transitions in FeRh and FeRhIr alloys. *Physica Status Solidi (b)*, 78(1):353–357, 1976.

[247] GT Dubovka. Effect of pressure on magnetic transformations in an iron-rhodium alloy. *Soviet Journal of Experimental and Theoretical Physics*, 38:1140, 1974.

[248] Radhika Barua, Félix Jiménez-Villacorta, and LH Lewis. Predicting magnetostructural trends in FeRh-based ternary systems. *Applied Physics Letters*, 103(10):102407, 2013.

[249] J Kudrnovskỳ, V Drchal, and I Turek. Physical properties of FeRh alloys: The antiferromagnetic to ferromagnetic transition. *Physical Review B*, 91(1):014435, 2015.

[250] RY Gu and VP Antropov. Dominance of the spin-wave contribution to the magnetic phase transition in FeRh. *Physical Review B*, 72(1):012403, 2005.

# Appendix A

# Fundamentals of the elastic solid

A mechanical force acting on a solid tend to change its shape. The following description is restricted to the elastic regime, i.e. the case in which forces do not overcome the particular *yield strength* of the solid from which the solid deforms plastically. We will assume that matter is homogeneously and continuously distributed in our elastic body[1].

Although force $\mathbf{F}$ is a vector, i.e. a first-rank tensor, we need a second-rank tensor for the description of mechanic forces acting on each surface of a three-dimensional solid which are described by the stress tensor $\boldsymbol{\sigma}$. Figure A.1 depicts a volume element of a solid and the components of the force acting on each surface $\sigma_{ij}$. The first subscript $i$ refers to direction normal to the plane direction and the second subscript $j$ refers to the force direction. Hence, the stress tensor can be defined as:

$$\boldsymbol{\sigma} = \begin{pmatrix} \sigma_{xx} & \sigma_{xy} & \sigma_{xz} \\ \sigma_{yx} & \sigma_{yy} & \sigma_{yz} \\ \sigma_{zx} & \sigma_{zy} & \sigma_{zz} \end{pmatrix} \tag{A.1}$$

which is often referred as the *Cauchy stress tensor*.

At this point we shall distinguish the normal stress which refers to the force component which is perpendicular to each plane ($\sigma_{ii}$) and the shear stress ($\sigma_{ij}$, $i \neq j$) which refers to the coplanar components[2]. The body is in equilibrium and the applied stress does not cause any net moment. Therefore, the condition $\sigma_{ij} = \sigma_{ji}$ is accomplished and the tensor $\boldsymbol{\sigma}$ is symmetric. The components $\sigma_{ij}$ are positive if the direction of the force points to the positive direction of the corresponding axis. Accordingly, tensile stress has positive components whereas a compressive stress has negative components. We can define the *principal stresses*

[1] The given description follows the references [242, 243] which provide a detailed study of the theory of elasticity.

[2] Components of shear stress are often denoted as $\tau_{ij}$.

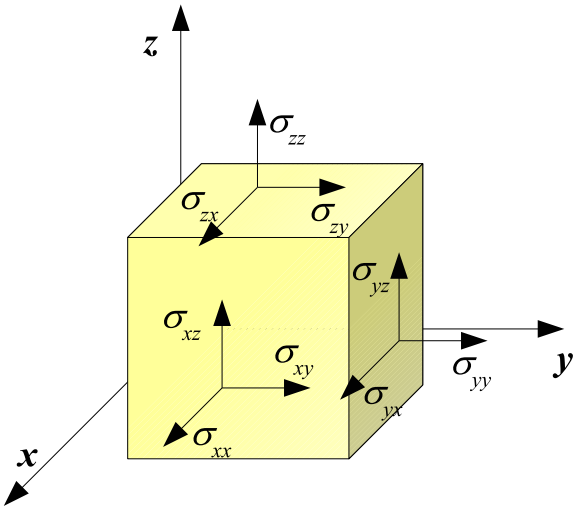


Fig. A.1 Sketch of a volume element at which the strain $\sigma_{ij}$ is applied on each side. The $i$ component of the strain refers to the side at which it is applied and the $j$ component stands for the direction of the mechanical force.

which stand for the three stresses perpendicular to the *principal planes* (principal directions) which maximize the normal stress and usually provide the proper reference framework for the description of the physical problem. The diagonalization of the stress tensor $\boldsymbol{\sigma}$ leads to the eigenvectors and eigenvalues which give the three principal directions and the three principal stresses, respectively. Figure A.2 illustrates special cases in which the material is being loaded in a uniaxial tensile stress (a), a uniaxial compressive stress (b), a hydrostatic pressure (c) and a pure shear stress (d). If the axis of our coordinate system are aligned to the principal directions the components of the tensor $\boldsymbol{\sigma}$ describing each situation in figure A.2 are as follows:

$$\text{(a)}\quad \boldsymbol{\sigma} = \begin{pmatrix} |\sigma| & 0 & 0 \\ 0 & 0 & 0 \\ 0 & 0 & 0 \end{pmatrix} \qquad \text{(b)}\quad \boldsymbol{\sigma} = \begin{pmatrix} -|\sigma| & 0 & 0 \\ 0 & 0 & 0 \\ 0 & 0 & 0 \end{pmatrix}$$

$$\text{(c)}\quad \boldsymbol{\sigma} = \begin{pmatrix} -p & 0 & 0 \\ 0 & -p & 0 \\ 0 & 0 & -p \end{pmatrix} \qquad \text{(d)}\quad \boldsymbol{\sigma} = \begin{pmatrix} 0 & \sigma & 0 \\ \sigma & 0 & 0 \\ 0 & 0 & 0 \end{pmatrix} \tag{A.2}$$

We can proceed now to introduce the strain tensor $\boldsymbol{\varepsilon}$ which accounts for the relative change of shape or size of the body in each direction. The following definitions consider

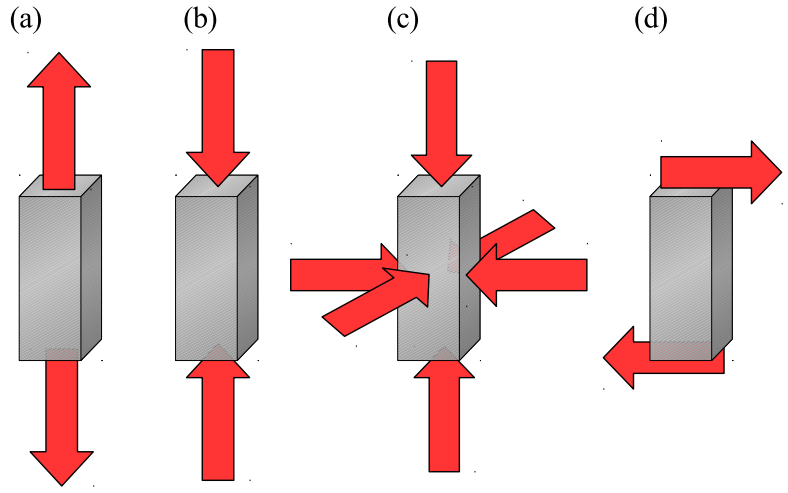


Fig. A.2 Diagram illustrating the different situations in which a stress is applied to a body: a uniaxial tensile stress (a), a uniaxial compression (b), a hydrostatic pressure (c) and a pure shear stress (d). The components of the stress tensor when aligned to the principal directions are expressed in (A.1).

an elastic solid displaying small deformations with enough constraints to prevent the body from moving as a rigid body. We can consider a small volume element of the solid with dimensions $dx \times dy \times dz$ as depicted in figure A.3 (a). The point $O$ of the volume element undergoes displacements with components ($u$, $v$, $w$) as a consequence of the deformation. Figure A.3 (b) illustrates a two-dimensional image of this situation. The length $OA$ varies from $dx$ to:

$$O'A' = \sqrt{\left(dx + \frac{\partial u}{\partial x}dx\right)^2 + \left(\frac{\partial v}{\partial y}dx\right)^2} = dx\sqrt{1 + 2\frac{\partial u}{\partial x} + \left(\frac{\partial u}{\partial x}\right)^2 + \left(\frac{\partial v}{\partial x}\right)^2} \tag{A.3}$$

The Taylor expansion of the last term in equation (A.3) restricted to the first order yields:

$$O'A' \sim dx + \frac{\partial u}{\partial x}dx \tag{A.4}$$

which is a valid approximation for sufficiently small deformations.

The normal strain refers to the relative length change in a particular direction. The normal strain in the $x$ direction is $\varepsilon_x = \dfrac{O'A' - OA}{OA} = \dfrac{\partial u}{\partial x}$. The same analysis for the other segments $O'B'$ and $O'C'$ leads to the following expressions for the normal strain in each direction:

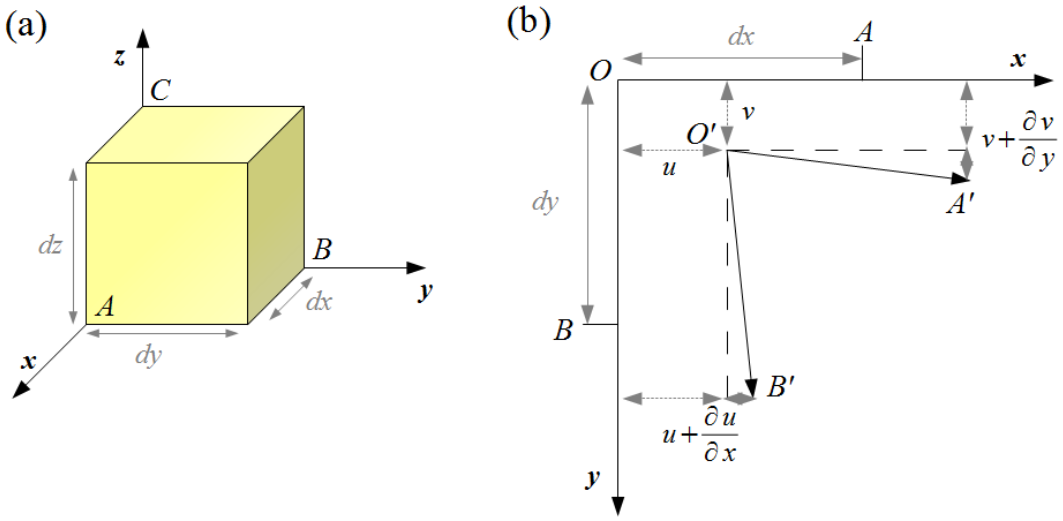


Fig. A.3 Volume element $dx \times dy \times dz$ with corners the A, B and C (a). The corresponding two-dimensional image at the $x-y$ plane shown in (b) illustrates the changes in the segments $OA \rightarrow OA'$ and $OB \rightarrow OB'$ due to the displacements $(u,v)$ for a particular distortion.

$$\varepsilon_x = \frac{\partial u}{\partial x}; \qquad \varepsilon_y = \frac{\partial v}{\partial y}; \qquad \varepsilon_z = \frac{\partial w}{\partial z} \tag{A.5}$$

which are the diagonal terms of $\boldsymbol{\varepsilon}$. The non-diagonal terms are related to the distortion of the angles of the volume element and describe the shearing strain. The angle $\widehat{AOB}$ in figure A.3 (b) results to the new angle $\widehat{A'O'B'}$ after the deformation. The difference between them is the unit shearing strain and is written as $\gamma_{xy} = \alpha + \beta$, where the expressions for $\tan\alpha$ and $\tan\beta$ are defined as:

$$\tan\alpha = \frac{\dfrac{\partial v}{\partial x}dx}{dx + \dfrac{\partial u}{\partial x}dx} = \frac{\dfrac{\partial v}{\partial x}}{1 + \dfrac{\partial u}{\partial x}} \approx \frac{\partial u}{\partial x}; \qquad \tan\beta = \frac{\dfrac{\partial u}{\partial y}dy}{dy + \dfrac{\partial v}{\partial y}dy} = \frac{\dfrac{\partial u}{\partial y}}{1 + \dfrac{\partial v}{\partial y}} \approx \frac{\partial v}{\partial y} \tag{A.6}$$

where the approximation in the last term of each expression is valid for small displacements. Since $\alpha \ll 1$ and $\beta \ll 1$, then $\tan\alpha \approx \alpha$ and $\tan\beta \approx \beta$. According to this, we can write the following relations for the unit shearing stress in other directions as:

$$\gamma_{xy} = \frac{\partial u}{\partial y} + \frac{\partial v}{\partial x}; \qquad \gamma_{xz} = \frac{\partial u}{\partial z} + \frac{\partial w}{\partial x}; \qquad \gamma_{yz} = \frac{\partial v}{\partial z} + \frac{\partial w}{\partial y} \tag{A.7}$$

which fulfill the following generalized expressions:

$$\gamma_{ij} = \frac{\partial u_i}{\partial x_j} + \frac{\partial u_j}{\partial x_i} \gamma_{ij} = \gamma_{ji} \tag{A.8}$$

The components of the strain tensor are defined as $\varepsilon_{ij} = \frac{1}{2}\left(\frac{\partial u_i}{\partial x_j} + \frac{\partial u_j}{\partial x_i}\right)$. Thus, we can write:

$$\boldsymbol{\varepsilon} = \begin{pmatrix} \varepsilon_x & \frac{\gamma_{xy}}{2} & \frac{\gamma_{xz}}{2} \\ \frac{\gamma_{xy}}{2} & \varepsilon_y & \frac{\gamma_{yz}}{2} \\ \frac{\gamma_{xz}}{2} & \frac{\gamma_{yz}}{2} & \varepsilon_z \end{pmatrix} \tag{A.9}$$

Both the stiffness tensor $C_{ijkl}$ and the compliance tensor $S_{ijkl}$ are fourth-rank tensors. They link the applied stress and the strain in the elastic body as follows:

$$\sigma_{ij} = C_{ijkl}\varepsilon_{kl} \qquad \varepsilon_{ij} = S_{ijkl}\sigma_{kl} \tag{A.10}$$

# Appendix B

# Model for FeRh: The phase diagram and multicaloric effects

In this section we provide details of the model developed to describe the magnetoresponsive behavior of FeRh. In summary, the starting point of the model is the partition of the original lattice into four sublattices: two sublattices that are occupied by Fe atoms and two by Rh atoms, with the interatomic interaction extending up to the second nearest neighbours. The model includes a magnetovolumic coupling term to account for the unit cell volume change at the transition. This coupling term is restricted to the minimum order allowed by symmetry and the effect of external fields such as hydrostatic pressure $p$ and magnetic field $H$ are included. The data used to fit the model parameters are the transition temperatures at atmospheric pressure [244], and the value of the pressure where the FM disappears [245, 246]. Moreover, the value of the relative volume change at the magnetostructural transition [247] is taken into account.

We start by dividing the CsCl structure of the equiatomic alloy into four sublattices, two sublattices ($\alpha$ and $\gamma$) occupied by Fe atoms and two sublattices ($\beta$ and $\delta$) occupied by Rh atoms. Next, we define the following magnetic order parameters in terms of the sublattice magnetizations:

$$m_{Fe} = \frac{m_\alpha + m_\gamma}{2}, \;\; m_{Rh} = \frac{m_\beta + m_\delta}{2} \tag{B.1}$$

and

$$\eta_{Fe} = \frac{m_\alpha - m_\gamma}{2}. \tag{B.2}$$

Where $m_{Fe}$ and $m_{Rh}$ represent the ferromagnetic order parameters of Fe and Rh respectively while $\eta_{Fe}$ is the antiferromagnetic order parameter of Fe. Thus, the total magnetization is given by $M = m_{Fe} + m_{Rh}$.

Considering interactions up to second nearest neighbours, the purely magnetic free energy per magnetic atom can be written as:

$$\begin{aligned} f_{mag}(T,m_{Fe},m_{Rh},\eta_{Fe}) = -\frac{z}{2}J^{(1)}_{Fe-Rh}m_{Fe}m_{Rh} - \frac{y}{4}J^{(2)}_{Fe-Fe}({m_{Fe}}^2 - {\eta_{Fe}}^2 - \\ +\frac{k_BT}{8}[(1+m_{Fe}+\eta_{Fe})\ln(1+m_{Fe}+\eta_{Fe}) + (1-m_{Fe}-\eta_{Fe})\ln(1-m_{Fe}-\eta_{Fe}) \\ +(1+m_{Fe}-\eta_{Fe})\ln(1+m_{Fe}-\eta_{Fe}) + (1-m_{Fe}+\eta_{Fe})\ln(1-m_{Fe}+\eta_{Fe}) \\ +2(1+m_{Rh})\ln(1+m_{Rh}) + 2(1-m_{Rh})\ln(1-m_{Rh}) - 8\ln 2], \end{aligned} \tag{B.3}$$

where the superscripts (1) and (2) of the effective interaction parameters $J$ represent nearest and next nearest neighbours atomic pairs respectively. We require $J^{(1)}_{Fe-Rh} > 0$ and we have set $J^{(2)}_{Rh-Rh} = 0$ without loss of generality. In equation (B.3), $z$ and $y$ are the coordination numbers for nearest and next nearest neighbours respectively. To account for the unit cell volume variation at the magnetostructural transition we incorporate the following (magnetovolumic) coupling terms between the magnetic order parameters and the volume change $w$ (relative to a reference volume $\Omega_0$), restricted to the minimum order allowed by symmetry:

$$f_{coupling} = \frac{1}{2}\alpha_0\omega^2 - \alpha_1\omega(m_{Fe}+m_{Rh})^2 - \alpha_2\omega{\eta_{Fe}}^2, \tag{B.4}$$

with $\alpha_1$ and $\alpha_2$ as magnetostriction coefficients and $\alpha_0$ as the inverse of the compressibility. Thus the total free energy of the system is $f = f_{mag} + f_{coupling}$.

Furthermore, it is necessary to include the effect of external magnetic and hydrostatic fields which yields the following expression for the total Gibbs free energy of the system in reduced units:

$$\begin{aligned} g^* = &\frac{g}{zJ^{(1)}_{FeRh}} = -\frac{1}{2}m_{Fe}m_{Rh} - \frac{J^*}{4}({m_{Fe}}^2 - {\eta_{Fe}}^2) \\ &+ \frac{T^*}{8}[(1+m_{Fe}+\eta_{Fe})\ln(1+m_{Fe}+\eta Fe) + (1-mFe-\eta_{Fe})ln(1-m_{Fe}-\eta_{Fe}) \\ &+ (1+m_{Fe}-\eta_{Fe})\ln(1+m_{Fe}-\eta_{Fe}) + (1-mFe+\eta_{Fe})\ln(1-m_{Fe}+\eta_{Fe}) \\ &+ 2(1+m_{Rh})ln(1+m_{Rh}) + 2(1-m_{Rh})ln(1-m_{Rh}) - 8ln2] \\ &+ \frac{1}{2}\alpha^*_0\omega^2 - \alpha^*_1\omega(m_{Fe}+m_{Rh})^2 - \alpha^*_2\omega\eta^2_{Fe} - H^*(m_{Fe}+m_{Rh}) + P\Omega^*_0\omega. \end{aligned} \tag{B.5}$$

The superscript ($^*$) indicates that the corresponding term magnitude is given in units of ($zJ^{(1)}_{Fe-Rh}$). In the present work, the expression for the total Gibbs free energy of the model

(B.5) has been solved for $\alpha_1^* = 0.30$, $\alpha_2^* = -0.4241$ and $J^* = -0.96$. It is worth mentioning that the equilibrium magnetic order configurations have been obtained by requiring the Rh magnetic moment in the AFM phase to be $\mu_{Rh} = 0$. Accordingly, we have considered that the number of magnetic atoms in the FM phase is twice that of the AFM phase. Moreover, the model has been fitted to experimental data for the transition temperatures of equiatomic and nearly equiatomic FeRh both at atmospheric pressure and at the applied pressure where the FM disappears [244–246, 81], and to the relative volume change at the FM-AFM magnetostructural transition. We have obtained the following estimates for the effective exchange constant $J^{(1)}_{Fe-Rh} = 10.2$ meV and for the unit cell volume $\Omega_0 = 17.9 \cdot 10^{-30}$ m$^3$, in good agreement with previously reported values [248–250]. Figure 4.3 in chapter 4 shows the theoretical results (continuous lines) for the phase diagram as a function of the pressure (a) and the magnetic field (b), compared with available experimental data [244–246, 81].

The model described above may be used to study multicaloric effects in FeRh. Indeed, the entropy S of the system can be directly computed from expression (B.5) by employing the definition of S as below in equation (B.6)

$$\begin{aligned} S = \left[\frac{\partial g^*}{\partial T^*}\right]_{p,H} =& [\frac{1}{8}[(1+m_{Fe}+\eta_{Fe})\ln(1+m_{Fe}+\eta_{Fe}) + (1-m_{Fe}-\eta_{Fe})\ln(1-m_{Fe}-\eta_{Fe}) \\ &+ (1+m_{Fe}-\eta_{Fe})\ln(1+m_{Fe}-\eta_{Fe}) + (1-m_{Fe}+\eta_{Fe})\ln(1-m_{Fe}+\eta_{Fe}) \\ &+ 2(1+m_{Rh})ln(1+m_{Rh}) + 2(1-m_{Rh})\ln(1-m_{Rh}) - 8\ln 2] = S_{Fe} + S_{Rh} \end{aligned} \tag{B.6}$$

where $m_{Fe}(T,H,p)$, $m_{Rh}(T,H,p)$ and $\eta_{Fe}(T,H,p)$ are the equilibrium order parameters obtained after minimization of the free energy (B.5). The isothermal entropy change for the multicaloric effect can be calculated from

$$\Delta S(T, 0 \to H, 0 \to p) = S(T,H,p) - S(T, H = 0, p = 0) \tag{B.7}$$

Results are shown in figure 4.26 of the text, and they nicely reveal that, for a particular combination of applied magnetic field and hydrostatic pressure, the total multicaloric entropy change reverses its sign.

# Appendix C

# Computation of the multicaloric effect in $Fe_{49}Rh_{51}$

In section 4.4, a detailed study of the multicaloric entropy change driven by either hystrostatic pressures and magnetic fields at the AFM-FM transition in $Fe_{49}Rh_{51}$ alloy is presented. The present appendix includes the Fortran code which has been employed for the indirect computation of the multicaloric effect. The code incorporates the particular definition of the magnetization taken from the analytic functions and generates a large matrix of $M(T_i, H_j, p_k)$ values from which it computes the different matrices of the entropy change data.

---

```
      program multicaloricFeRh

       real*8 f, y, der, s1, s2, s3, s4, H, d1, d2, d3, factor, p, dt,s5
       real*8 t, t0, a, b, w, x, dmdp, dmdh, trang, s, rao1, rao2, ts
       integer i, j, n, m, k, l, o, q
       parameter (n=10,m=2000,l=2000, r=0.6, trang=0.1)
       DIMENSION y(0:n,0:m,0:l), der(0:n,0:m,0:l), s1(0:n,0:m,0:l)
       DIMENSION s2(0:n,0:m,0:l), s3(0:n,0:m,0:l), s4(0:n,0:m,0:l)
       DIMENSION dt(0:n,0:m,0:l), s5(0:n,0:m,0:l)

!  LIST OF VARIABLES
!
!  y     = Magnetization, M(T,H,p)
!  der   = Derivative of the magnetization with respect to temperature,
    (dM/dT)
```

```
!  dmdp  = Derivative of the magnetization with respect to pressure, (dM/dp)
!  dmdh  = Derivative of the magnetization with respect to magnetic field,
    (dM/dH)
!  t     = Variable for the temperature (K).
!  H     = Variable for the magnetic field (T).
!  p     = Variable for the pressure (kbar).
!  x     = Transition temperature (function of magnetic field and pressure),
    (T_t)
!  trang = Temperature interval at which the entropy change is computed.
!  n,m,l = Parameters bounding the dimensions of the (T,H,p) matrices,
    respectively
!  i,j,k = Labels of the matrices components, i=0,n. j=0,m. k=0,l.
!  r     = (T-T_t) distance at which the exp function is coupled with the
    tanh(x)
!  s1    = Magnetocaloric entropy change (driven by a change in H), at p=ct
!  s2    = Barocaloric entropy change (driven by a change in p), at H=ct
!  s3,s4 = Intermediate terms which are defined for the computation of s5.
!  dt    = Coupling term
!  s5    = Multicalori! entropy change (driven by a change in H and p).
!
!  LIST OF TUNABLE VARIABLES, (AS A CONVENIENCE)

       d1=trang/DBLE(n) ! Temperature step
       d2=5/dble(m)     ! Magnetic field step
       d3=5/dble(l)     ! Pressure step
       q=1200           ! Number of times the temperature interval is divided.
       w=1.15           ! Parameter related to the spread of tanh(x) function
       ts=245           ! Starting point of the iteration (temperature bottom
           limit)


! This factor is defined for the coupling between the exp and tanh(x)
    functions
        factor=(1-((exp(r/w)-exp(-r/w))/(exp(r/w)+exp(-r/w)))**2)/(2*w)

! Integration of the entropy change is repeated q times, so that a total
    temperature
! range of q*trang is covered. This procedure saves memory because n can be
    a lower
```

```
! value.

      do o=0, q
      t0 = ts + dble(o)*trang

      do k=0,l

! We fix the value of the pressure.
      p = 5*dble(k)/dble(l)

      do j=0,m

! We fix the value of the magnetic field.
        H = 5-5*dble(j)/dble(m)

!      x = 319.525 -9.483*H + 6.223*p ! HEATING. Uncomment it if necessary.
       x = 309.341 -9.864*H + 6.352*p ! COOLING. Uncomment it if necessary.

         do i=0,n

! We first give the magnetization values as a function of the applied fields
    and
! temperature (isofield scans).

         if (H>=0.2) then
         a=6.60764-0.17777*p+1.22188*H          ! AFM state M_{afm}
         b=106.4153267-(2/3)*p+3.3881*H-0.27377*H*H ! FM state M_{fm}
         endif

         t=t0+dble(i)*dble(trang)/dble(n) ! Temperature value
         f=(t-x)/w                        ! Argument of the tanh(x) function

! Magnetization values in the limit where both functions couple (T-T_t = r)
         s=0.5*(a+b+(b-a)*(exp(r/w)-exp(-r/w))/(exp(r/w)+exp(-r/w)))
         sb=0.5*(a+b+(b-a)*(exp(-r/W)-exp(r/w))/(exp(-r/w)+exp(r/w)))

! For the temperature interval at which we use the exp function (lower
    bound):
         if (f < -r/w) then
```

```
    rao1=factor*(b-a)*(t-(x-r))/((sb-a)*5)
         y(i,j,k)=a+(sb-a)*exp(rao1)
         der(i,j,k)=((sb-a)*rao1/(t-(x-r)))*exp(rao1)
         endif

! For the temperature interval at which we use the tanh(x) function:
         if (f >= -r/w .and. f<r/w) then
         y(i,j,k)=0.5*(a+b+(b-a)*(exp(f)-exp(-f))/(exp(f)+exp(-f)))
         der(i,j,k)=(b-a)*(2/(exp(f)+exp(-f)))**2/(2*w)
         endif

! For the temperature interval at which we use the exp function (upper
    bound):
         if (f >= r/w) then
         rao2=factor*(b-a)*(t-(x+r))/((s-b)*5)
         y(i,j,k)=b+(s-b)*exp(rao2)
         der(i,j,k)=-((sb-a)*rao2/(t-(x+r)))*exp(rao2)
         endif

        enddo
       enddo
      enddo

! Computation of the integrals:
      do i=0,n
      do j=0,m
        do k=1,l
      dmdp = (y(i,j,k)-y(i,j,k-1))/d3
      dmdh = (y(i,j,k)-y(i,j-1,k))/d2
      s2(i,j,k)=s2(i,j,k-1)+d3*der(i,j,k)*dmdp/dmdh
      s3(i,j,k)=s3(i,j,k-1)+d3*dmdp
        enddo
      enddo
      enddo

      do i=0,n
      do k=0,l
      do j=1,m
      s1(i,j,k)=s1(i,j-1,k)+d2*(der(i,j,k)+der(i,j-1,k))/2
```

```
      s4(i,j,k)=s4(i,j-1,k)+d2*(s3(i,j,k)+s3(i,j-1,k))/2
      dt(i,j,k)=(s4(i,j,k)-s4(i-1,j,k))/d1
      s5(i,j,k)=dt(i,j,k)+s1(i,j,0)+s2(i,1,k)
      enddo
      enddo
      enddo

! At this point, the code has generated the required matrices of data.
! We can modify the code as a convenience for writing the data.

       open(10,file='s5a.dat',ACCESS ='APPEND',STATUS ='old')
       open(13,file='s5b.dat',ACCESS ='APPEND',STATUS ='old')

       do i=1,n
       t=t0+dble(i)*dble(trang)/dble(n)

        write(10,*) t,s5(i,0,2000),s5(i,40,2000),s5(i,80,2000),   &
     & s5(i,120,2000),s5(i,160,2000),s5(i,200,2000),s5(i,240,2000), &
     & s5(i,280,2000),s5(i,320,2000),s5(i,360,2000),s5(i,400,2000), &
     & s5(i,440,2000),s5(i,480,2000),s5(i,520,2000),s5(i,560,2000), &
     & s5(i,600,2000),s5(i,640,2000),s5(i,680,2000),s5(i,720,2000), &
     & s5(i,760,2000),s5(i,800,2000),s5(i,840,2000),s5(i,880,2000), &
     & s5(i,920,2000),s5(i,960,2000),s5(i,1000,2000),s5(i,1040,2000), &
     & s5(i,1080,2000),s5(i,1120,2000),s5(i,1160,2000),s5(i,1200,2000), &
     & s5(i,1240,2000),s5(i,1280,2000),s5(i,1320,2000),s5(i,1360,2000), &
     & s5(i,1400,2000),s5(i,1440,2000),s5(i,1480,2000),s5(i,1520,2000), &
     & s5(i,1560,2000),s5(i,1600,2000),s5(i,1640,2000),s5(i,1680,2000), &
     & s5(i,1720,2000),s5(i,1760,2000),s5(i,1800,2000),s5(i,1840,2000), &
     & s5(i,1880,2000),s5(i,1920,2000),s5(i,1960,2000),s5(i,2000,2000)

        write(11,*) t,s5(i,2000,0),s5(i,2000,40),s5(i,2000,80),   &
     & s5(i,2000,120),s5(i,2000,160),s5(i,2000,200),s5(i,2000,240), &
     & s5(i,2000,280),s5(i,2000,320),s5(i,2000,360),s5(i,2000,400), &
     & s5(i,2000,440),s5(i,2000,480),s5(i,2000,520),s5(i,2000,560), &
     & s5(i,2000,600),s5(i,2000,640),s5(i,2000,680),s5(i,2000,720), &
     & s5(i,2000,760),s5(i,2000,800),s5(i,2000,840),s5(i,2000,880), &
     & s5(i,2000,920),s5(i,2000,960),s5(i,2000,1000),s5(i,2000,1040), &
     & s5(i,2000,1080),s5(i,2000,1120),s5(i,2000,1160),s5(i,2000,1200), &
     & s5(i,2000,1240),s5(i,2000,1280),s5(i,2000,1320),s5(i,2000,1360), &
```

```
& s5(i,2000,1400),s5(i,2000,1440),s5(i,2000,1480),s5(i,2000,1520), &
& s5(i,2000,1560),s5(i,2000,1600),s5(i,2000,1640),s5(i,2000,1680), &
& s5(i,2000,1720),s5(i,2000,1760),s5(i,2000,1800),s5(i,2000,1840), &
& s5(i,2000,1880),s5(i,2000,1920),s5(i,2000,1960),s5(i,2000,2000)
 enddo

 enddo

  close(10)
  close(11)

  end program
```